Durability of the Solid Oxide Cells for Co-Electrolysis of Steam and Carbon Dioxide under High Current Densities

Tao, Youkun

Publication date:
2013

Document Version
Publisher's PDF, also known as Version of record

Durability of the Solid Oxide Cells for Co-Electrolysis of Steam and Carbon Dioxide under High Current Densities

PhD Thesis

Youkun Tao

Department of Energy Conversion and Storage

Technical University of Denmark

December 2013

Preface

This thesis is submitted to the Technical University of Denmark (DTU) as a partly fulfillment of the requirements for the Ph.D. degree. The work presented in this thesis is the product of three years' work conducted at the Department of Energy Conversion and Storage, Technical University of Denmark. This work deals with the durability of the solid oxide electrolysis cells operated at high current densities for co-electrolysis of steam and carbon dioxide. The focus has been the investigation of the degradation mechanisms by combining the detailed analysis of the electrochemical impedance and the micro-structure/composition. The Ph.D. project was financed by the DTU Mobility Fellowship Program.

I would like to express my gratitude to my supervisors:

Professor Mogens Mogensen, Department of Energy Conversion and Storage, DTU
Senior scientist Sune Ebbesen, Department of Energy Conversion and Storage, DTU

Thank you for your suggestions to the experimental, data analysis and written work. Thank you for so many helpful discussions on weekly supervision meetings. Thank you for all the help, encouragement and guidance throughout my Ph.D. study.

I would also like to thank Dr. Søren Simonsen and Dr. Wei Zhang for the careful TEM/EDS work, which is highly important for the mechanism interpretations. Thanks to Dr. Xiufu Sun for his kind helps with various lab tasks and data analysis. Thanks to Dr. Christopher Graves and Dr. Anne Hauch for the helps with the impedance analysis software.

Thanks to Dr. Nikolaos Bonanos, Dr. Johan Hjelm, Dr. Jimmi Nielsen, Dr. Karl Thydén, Dr. Jens Høgh, Dr. Peter Stanley Jørgensen, Dr. Søren Højgaard Jensen, Dr. Per Hjalmarsson, Dr. Ming Chen, Dr. Martin Søgaard, Prof. Anke Hagen, Prof. Peter Vang Hendriksen and many others for sharing their expertise on cell test, electrochemical or microstructural analysis. Thanks to Søren Koch, Henrik Henriksen, Ole Hansen, Martin Nielsen, Ulla Forsberg and other technical staffs for helping with the test setups and equipments. Thanks to Gregory Johnson, Qiang Hu, Li Han, Shiyang Cheng and other colleagues. Thanks to Heidi, the secretary of our section for her patience and kindness. Thank all the staffs at DTU energy Conversion.

At last, I would like to thank my parents for always giving me support and encouragement, and thank my wife Jing, for her care and help during the last three years.

Youkun Tao

Roskilde, Denmark

15th of December 2013

Abstract

Production of hydrogen and syngas (CO + H_2) using solid oxide electrolysis cells (SOECs) has become increasingly attractive due to high oil price, the capability for conversion and storage of intermittent energy from renewable sources and the general interest in hydrogen energy and carbon-neutral energy sources. Long-term stability of SOECs for high fuel productivity is crucial for the application of this technology.

In this work, a series of galvanostatic durability tests were performed at high current densities (|i| = 1.5 or 2.0 A/cm^2), 850 ^oC for up to about 700 hours for co-electrolysis of steam and CO_2. Two types of Ni-YSZ supported cells, the LSM cell and LSCF cell, respectively with a LSM-YSZ or a LSCF-CGO oxygen electrode were tested using a setup with albite glass as sealing material, and using the gasses as received or in an setup using a glass with less known impurities, and cleaning the inlet gasses. The feed gas to the Ni-YSZ electrode consisted of 45 % H_2O + 45 % CO_2 + 10 % H_2 and the reactant conversion was 45 % or 60 %. Electrochemical and the microstructural analysis were performed to investigate the degradation mechanisms of the tested SOECs.

A significant increase of the ohmic resistance and Ni-YSZ TPB reaction resistance accounted for the main degradations of the SOECs. In contrast to LSCF cells, the LSM cells showed a faster and larger increase of ohmic resistance, indicating some kind of relation between YSZ degradation and type of oxygen electrode. The oxygen electrode itself showed no degradation or only limited degradation. Oxygen electrode delamination from the electrolyte was not observed for any of the tested cells. However, parallel cracks were observed in the electrolyte, which could be ascribed to the internal stress due to a large thermal gradient in YSZ electrolyte perpendicular to cell plane.

Severe percolation loss of Ni occurred for the Ni-YSZ electrode adjacent to the YSZ electrolyte, contributing to the increase of TPB resistance due to decrease of active Ni-YSZ TPB length. The large cathodic polarization of Ni-YSZ electrode led to the more severe percolation loss of Ni particles. The blocking of the Ni-YSZ TPBs by impurities (e.g. SiO_x) also contributed to the fast degradation of SOECs in the initial test period. However, the post-test observation revealed dominating SiO_x inclusions inside the Ni grain close to the electrolyte, instead of segregation at the TPBs or Ni-YSZ interface. A reduction-oxidation process was proposed for the formation of SiO_x inclusions in Ni under large cathodic polarizations.

Formation of zirconia nanoparticles were observed for most of the tested cells close to the TPBs and Ni|YSZ interface for the innermost a few microns thick Ni-YSZ electrode. The nanoparticles are similar to the bulk

YSZ in crystal structure and composition. The zirconia nanoparticles were probably formed by direct structure decomposing of YSZ under strong cathodic polarizations, rather than by a complete reduction to metallic Zr. The nanoparticle formation could impair the Ni-YSZ contact, leading to an increased ohmic and oxygen ion transfer resistance.

Further, cells with different porosity were tested, for relative denser Ni-YSZ structure, carbon (CNT) formation was observed at the Ni-YSZ|YSZ interface, where fuel electrode delamination occurred during co-electrolysis of steam and CO_2 at $|i| \geq 2.0$ A/cm^2. Gas diffusion limitations contribute to the dramatic increase of cell voltage and a very reducing atmosphere at the interface.

Dansk Abstrakt

Produktion af brint og syntesegas (CO + H_2) ved hjælp fastoxid elektrolyseceller (SOECs) er blevet stadig mere attraktiv på grund af den høje oliepris, evnen til at omdanne og opbevare fluktuerende energi fra vedvarende energikilder samt den generelle interesse i brint teknologi og CO_2- neutral energi systemer. Stabiliteten af SOECs er afgørende for anvendelsen af denne teknologi.

I dette arbejde er en række galvanostatiske stabilitets tests blevet udført ved høje strømtætheder på op til 2,0 A/cm2 og ved 850 °C for perioder op til ca. 700 timer. Testene blev udført i en blanding af vanddamp og CO_2, såkaldt co-elektrolyse. To typer af celler blev anvendt til stabilitetstestene, begge med en Ni-YSZ katode, men med enten en LSM-YSZ eller LSCF-CGO anode. Holdbarheden af disse celler blev undersøgt både ved at rense fødegasserne og ved at anvende disse gasser som modtaget. Fødegassen til Ni-YSZ elektroden bestod af 45 % H_2O + 45 % CO_2 + 10 % H_2 og omsætningen var på 45 % eller 60 %. Degraderingen af cellerne er analyseret vha. både elektrokemisk og strukturel karakterisering, både før og efter test.

Den elektrokemiske karakterisering afslørede en betydelig øgning over tid af den ohmske modstand, der hovedsagelig stammer fra elektrolytten, samt modstanden for reaktionen ved trefasegrænserne i Ni-YSZ elektroden. I modsætning til cellerne med LSCF elektroderne, viste cellerne med LSM elektroderne en hurtigere og større stigning i den ohmske modstand, hvilket indikerer en sammenhæng mellem YSZ degraderingen og typen af iltelektrode. Iltelektroden i sig selv degraderede enten slet ikke eller kun svagt. Den delaminerede ikke fra elektrolytten, hvorimod revner i elektrolytten, parallelt med overfladen blev observeret. Årsagen til disse parallelle revner i elektrolytten kan skyldes indre spændinger på grund af den termiske gradient vinkelret i elektrolytten.

Den elektroniske ledningsvej gennem Ni-YSZ elektroden var i betydelig udstrækning brudt i de testede celler, hvilket bidrager til en forøgelse af trefasegrænsemodstanden på grund af en kortere trefasegrænselinje. Tabet af aktiv trefasegrænse kan skyldes den høje katodiske polarisering. Blokeringen af Ni-YSZ trefasegrænser er på grund af urenheder (f. eks. Si) bidrager også til degraderingen, specielt i de første par hundrede timer. I modsætning til tidligere studier, hvor urenhederne hovedsageligt blokerede de aktive trefasegrænser, blev SiO_x hovedsageligt observeret inde i nikkelfasen, og ikke akkumuleret ved trefasegrænserne. Disse SiO_x inklusioner inde i nikkelfasen kan skyldes en reduktion af urenhederne til metallisk form ved trefasegrænsen hvorefter disse kan diffundere ind i nikkelkornene og derefter oxideres langsom igen ved andre betingelser.

Zirconia nanopartikler blev dannet ved Ni-YSZ trefasegrænserne samt mellem nikkel og YSZ i Ni-YSZ elektroden tæt på elektrolytten. Sammensætningen af disse zirconia nanopartikler er næsten identisk med sammensætningen af YSZ i Ni-YSZ strukturen og er derfor højst sandsynligt forsaget af en direkte nedbrydning af YSZ strukturen under høj katodisk polarisering, og ikke via en reduktion til metallisk zirconia, da ilt-partieltrykket ved Ni-YSZ|YSZ grænsefladen ikke er lavt nok til det. Nanopartiklerne kan både medføre øget ohmsk modstand samt hindring af iltion overførslen.

Celler med forskellig porøsitet af Ni-YSZ elektrodestrukturen blev desuden testet. Kulnanofiberdannelse blev observeret ved Ni-YSZ|YSZ grænsefladen for cellerne med en tæt Ni-YSZ struktur. Disse kulnanofiber forårsagede delaminering mellem Ni-YSZ elektroden og YSZ elektrolytten. Gasdiffusionsbegrænsningen gennem Ni-YSZ strukturen forårsager en meget reducerende atmosfære tæt ved elektrolytten. Rent termodynamisk er det usandsynligt at danne disse kulfibre i gassen ved cellernes driftsbetingelser, og desuden blev kulfibrene observeret på zirconia partikler og ikke nikkel, som ellers er en velkendt katalysator for dannelse af kulfibre. Derfor blev disse kulfibre højst sandsynligt dannet via en elektrokatalytisk mekanisme og ikke via en ren heterogen katalytisk reaktion.

Table of contents

Chapter 1 Introduction

1. Introduction

Solid oxide fuel cells (SOFCs) are considered as one of the most promising technologies for high effective conversion of H_2 or hydrocarbon fuels into electricity. The cells can also be operated reversely as the solid oxide electrolysis cells (SOECs) for production of H_2 and synthesis gas (H_2 + CO) by electrolysis of steam or/and CO_2 without consuming fossil fuels. SOEC technology has the potential to be applied for large scale energy conversion and storage in the future for a CO_2-neutral society.

Already in the 1980s, A.O. Isenberg[1] and W. Dönitz et al.[2,3] reported high temperature steam electrolysis using solid oxide cells. During the past a few years, high temperature electrolysis using SOECs[4–15] has gained renewed interest due to the increasing oil prices and the high demand for sustainable energy technologies. Pure hydrogen can be produced at high efficiency by the electrolysis of steam,[4–13] without consuming the non-renewable fuel or emitting CO_2. The co-electrolysis of the mixture and steam and CO_2 at high temperatures provide an efficient way for production of H_2/CO synthesis gas,[11,16–19] which can be further catalyzed into various types of synthesis fuels[4,16,20,21] such as methanol and methane. The carbon containing fuels typically are easier to handle and have a higher energy density than hydrogen. Thus, the synthesis fuel produced by co-electrolysis allows a readily transportation with the existing infrastructures.

The high temperature electrolysis via SOECs can be integrated with the intermittent energy sources such as solar or wind energy[16,20] for fuel production and optimization of the total efficiency. The waste heat and surplus energy from nuclear power can also be utilized for fuel production via high temperature electrolysis of steam or/and CO_2 using SOECs.[10,11,20,22]

Fuel production (H_2/CO) by high temperature electrolysis has a high potential to be cost-effective. According to the economic analysis by S. H. Jensen et al,[4] the H_2 production cost can be decreased to 30 US$/barrel equivalent crude oil using SOECs with a performance of -3.6 A/cm^2 at 950 ^{o}C and 1.48 V based on an electricity price of 1.3 US¢/kWh. The CO production cost is estimated to be 40 US$/barrel equivalent crude oil using the same assumptions.

2. Principle of SOFCs and SOECs

The solid oxide cell (SOC) is an electrochemical device operated at high temperatures (600 ~ 1000 ^{o}C) for energy conversion. Basically, a solid oxide cell consists of a cathode, an anode and an electrolyte. The electrolyte is an ion conductive dense ceramic layer, sandwiched between the porous cathode and anode. The SOCs can be operated as fuel cells, i.e. solid oxide fuel cells (SOFC) for directly converting the chemical energy to electric energy (Figure 1A). The SOCs can also be operated reversibly as the electrolysis cells, i.e. solid oxide electrolysis cells (SOEC) for fuel production/storage by converting the electric energy to chemical energy (Figure 1B).

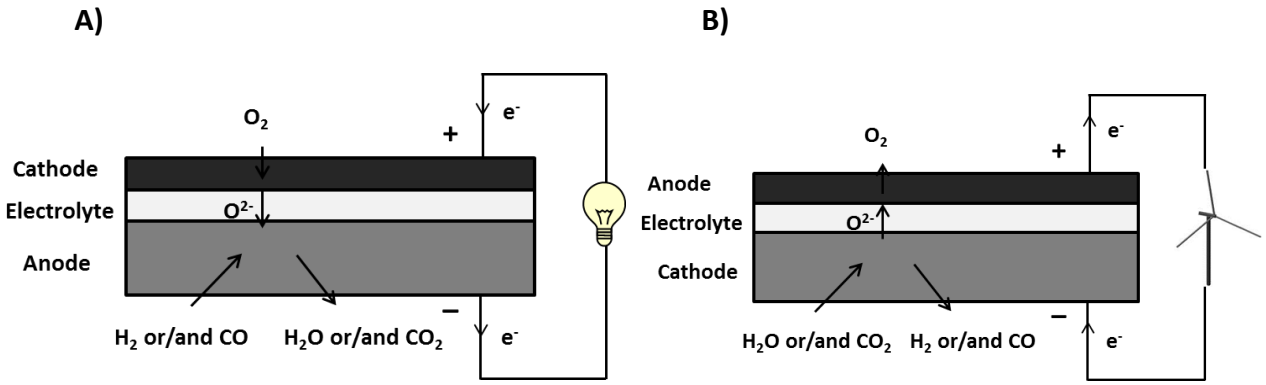

Figure 1 Working principle of a solid oxide cell (SOC). The cell can be operated as A) SOFC (in fuel cell mode) and B) SOEC (in electrolysis cell mode).

For the SOFC operation, O_2 is flown to the oxygen electrode and reduced to oxygen ions, which are transported through the electrolyte to the fuel electrode for the oxidation of H_2/CO. The chemical energy is converted to electrical energy and heat for this operation. The reactions are as follow:

Cathode (O_2 electrode): $½\ O_2 + 2\ e^- \rightarrow O^{2-}$

Anode (Fuel electrode): $O^{2-} + H_2 \rightarrow H_2O + 2\ e^-$; $O^{2-} + CO \rightarrow CO_2 + 2\ e^-$

The total reaction: $½\ O_2 + H_2 \rightarrow H_2O$; $½\ O_2 + CO \rightarrow CO_2$

For the SOEC operation, H_2O/CO_2 is reduced at the fuel electrode to produce H_2/CO. The oxygen ions are conducted through the electrolyte to the oxygen electrode where O_2 is generated. For this operation, heat and electric energy is consumed and converted to chemical energy. The reactions are:

Cathode (Fuel electrode): $H_2O + 2\ e^- \rightarrow O^{2-} + H_2$; $CO_2 + 2\ e^- \rightarrow O^{2-} + CO$

Anode (O_2 electrode): $O^{2-} \rightarrow ½\ O_2 + 2\ e^-$

The total reaction: $H_2O \rightarrow ½\ O_2 + H_2$; $CO_2 \rightarrow ½\ O_2 + CO$;

3. Thermodynamics

The overall reaction for the electrolysis of H_2O or CO_2 is: H_2O (CO_2) + electrical energy (ΔG) + heat (TΔS) → H_2 (CO) + ½ O_2. The high temperature electrolysis of H_2O/CO_2 has a potential for high efficient production of H_2/CO. Figure 2 shows the thermodynamics for both the H_2O and CO_2 electrolysis at ambient pressure. The overall electrolysis reactions become increasingly endothermic with increasing temperature, meanwhile the electric energy demand decreases with temperature. From the thermodynamic point of view, it is more advantageous to operate the solid oxide electrolysis cells at higher temperatures because the larger part of the required energy is provided by thermal energy so that the electrical energy consumption can be reduced. In addition, with increasing temperature both the electrolyte conductivity and the kinetics of the electrode reactions increase so that the cell resistance and electrical energy loss decreases. For a given current density, operating the cell at the higher temperatures decreases the cell voltage and thus the electrical input. On the other hand, for a given cell voltage, the current density and thus the production rate of H_2/CO will be higher at the higher temperatures. The Joule heat produced within the cell during operating can provide part of the energy demand for the electrolysis, which lowers the overall electrical energy demand and reduces the prices of H_2/CO production.

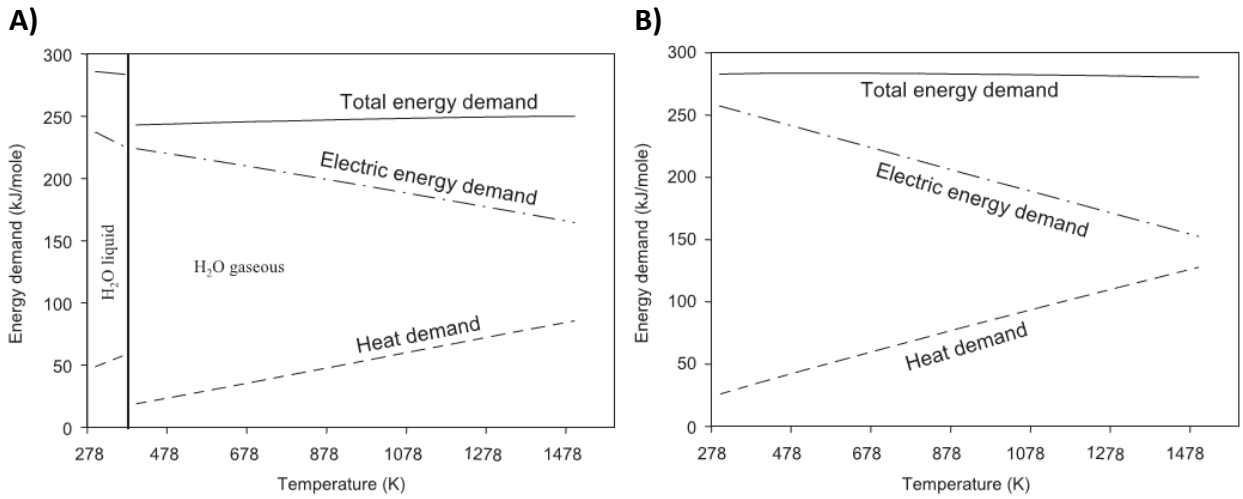

Figure 2 Thermodynamics for H_2O electrolysis and CO_2 electrolysis. Both H_2O and CO_2 electrolysis becomes increasingly endothermic with increasing temperature. (Figure from literature[23])

4. SOCs developments

The most conventional electrolyte of SOCs is Yttria stabilized zirconia (YSZ), which exhibits reasonable oxygen ion conductivity (0.164 S/cm at 1000°C for 8YSZ[24]), good thermal and chemical stability as well as

excellent mechanical properties. Typically, a porous composite consists of Ni and YSZ (Ni-YSZ) is used as the fuel electrode. The strontium-doped lanthanum manganite (LSM) and YSZ (LSM-YSZ) is typically used as the oxygen electrode and better performance can be achieved by using LSCF-CGO, a composite of strontium-doped lanthanum cobalt iron oxide (LSCF) and ceria-gadolinia (CGO). A CGO barrier layer is employed between the LSCF electrode and YSZ electrolyte, in order to avoid the unwanted interfacial reactions between LSCF and YSZ.

Figure 3 shows the three typical designs for the planar type of solid oxide cells, which are categorized by DTU energy conversion (the former Risø National Lab) as different generations according to the development of the cells. The 1st generation SOCs has a thick (typically > 100 µm) electrolyte as the support for the thin electrodes (typically 10 ~ 30 µm thick). The electrolyte supported cells are operated at ~ 1000 ^{o}C in order to lower the ohmic resistance of the thick electrolyte.[25] Reducing the thickness of the electrolyte to ~ 10 µm and employing the high conductive Ni-YSZ cermet as the support, the Ni-YSZ supported cells have been developed. The Ni-YSZ supported cells with a LSM-YSZ electrode is normally operated at 750 ~ 850 ^{o}C.[26,27] An even lower cell resistance can be obtained by employing a better performing LSCF-CGO oxygen electrode so that the cell can be operated at temperatures as low as ~ 650 ^{o}C.

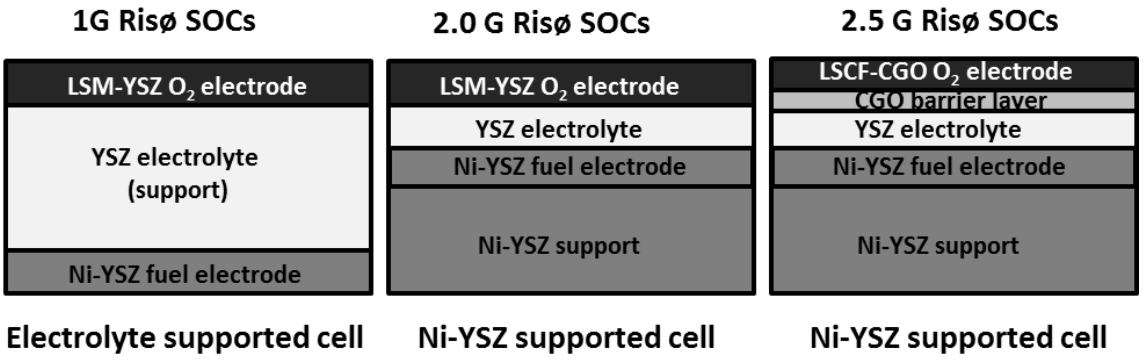

Figure 3 Development of the planar designs of solid oxide cells at DTU energy conversion (the former Risø National Lab)

The typical configuration/microstructure of the state-of-the-art 2.0G Risø SOCs is shown in Figure 4. The Ni-YSZ fuel electrode provides a conductive path for electrons by Ni network and a conductive path for oxygen ions via YSZ network. The electrochemically active region of the Ni-YSZ electrode is the innermost 10 microns Ni-YSZ close to the YSZ electrolyte, limited by the conductivity of YSZ network.[28] The gas molecules get access to the active sites of the electrode reactions, the Ni-YSZ-pore triple phase boundaries (TPBs) by

diffusion though the porous Ni-YSZ structure (~ 30% porosity). Good initial performances, an area-specific resistance (ASR) as low as 0.27 Ωcm^2 at 850 ^oC in 50 % H_2O + 50 % H_2 has been reported for Risø 2.0G cell.[29]

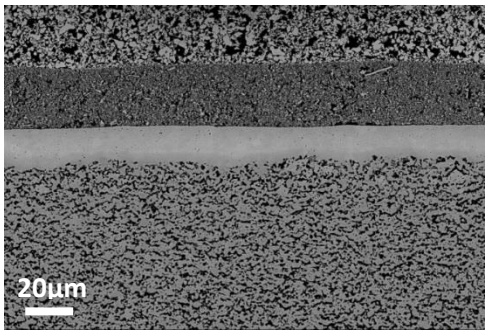

Figure 4 Typical cell structures for a 2.0G Risø cell with a porous Ni-YSZ electrode, a dense YSZ electrolyte and a fine-structured LSM-YSZ electrode. The image was obtained on a cell after reduction of NiO but without durability test.

5. SOECs performance

5.1. Polarization losses

When a load is applied to the SOFCs, the cell voltage (*V)* can be expressed as:

$$V^{SOFC} = E - \eta_{ohm} - \eta_{conc} - \eta_{ct}$$

The open circuit voltage, *E*, is given by the Nernst equation at the given operation conditions. The polarization losses depend on the operating conditions, such as the current density and gas compositions. The cell voltage will be higher than E for the SOECs operations according to:

$$V^{SOEC} = E + \eta_{ohm} + \eta_{conc} + \eta_{act}$$

The different polarizations are termed:[30] ohmic polarization (η_{ohm}), concentration polarization (η_{conc}) and activation polarization (η_{act}). The η_{ohm} includes the contributions from the ohmic resistance of the electrolyte, cathode, anode and also some extent of contact resistances. The electrolyte normally accounts for the major contributions to η_{ohm}, because the oxygen ion conductivity of the electrolyte is typically a few orders lower than the electron conductivity in the electrodes. The concentration or diffusion polarization is caused by the mass transport through the porous electrode to or away from the active sites. The effect of η_{conc} increases with increasing the current density. The η_{conc} also depends on the structural parameters of the porous electrode and the gas diffusivities. Electrode reactions involve charge transfer as a fundamental

step and the activation polarization is also called the charge transfer polarization. It is the over-potential necessary to overcome the energy barrier for the rate determining step in the electrochemical reactions. The electrode reaction mechanisms are dependent of material constituent and microstructures, therefore, the fabrication/operation history and impurity levels of the electrode could play an important role.[30,31] Considering the lack of full reproducibility of the electrodes among different groups and the lack of agreement in the proposed mechanisms, it is difficult to obtain a unified description/understanding of the elementary processes under realistic operating conditions.[30,31]

The performance of the solid oxide cells can be characterized by recording i-V curves and measurement of electrochemical impedance spectroscopy (EIS). The area specific resistance (ASR) of the cell is normally used to represent the cell performance. Because of the lack of consensus about the concept 'ASR', the condition and calculation method has to be specified when use it for characterizations.[32] The ASR can be obtained as the slope of the i-V curves, which reflects the entire cell performance at DC current. ASR can be also obtained by measuring the impedance corresponding to a very low frequency approaching 0 (similar to DC). The impedance spectra are typically measured for a wide range of frequency. The different polarization losses of a SOC can be separated by analysis of the impedance due to the different time constants of the processes.

5.2. State-of-the-art SOEC performance

According to the economic analysis by S. H. Jensen et al,[23] the fuel production cost is sensitive to the electricity price, which accounts for approximately three fourths of the expense. The better cell performance (low resistance) of the SOECs contributes to the less electrical energy loss, making the fuel production more economically attractive.

From the chord of the electrolysis i-V curve, an area-specific resistance (ASR) as low as 0.27 Ωcm^2 at 850 ^oC in 50 % H_2O + 50 % H_2 has been reported for Risø 2.0G cell with a Ni-YSZ fuel electrode and a LSM-YSZ oxygen electrode.[29] For the same type of cells in 50 % CO_2 + 50 % CO, an ASR of 0.30 Ωcm^2 at 850 ^oC was reported by S. Ebbesen et al.[33] The Ni-YSZ electrode has a higher activity for H_2 oxidation than for steam reduction.[5,19,33–35] Some larger resistance and thus lower activity was reported for the Ni-YSZ electrode in CO/CO_2 than in H_2/H_2O.[19,33,36] The fabrication process, the electrode microstructures and impurities highly influence the performance of Ni-YSZ electrode.

6. SOECs degradation

Even though promising initial performances have been demonstrated, the long-term durability of the SOECs was still unsatisfactory,[6,14,15] which is one key issue for the application of this technology. The long-term degradation studies of SOECs performed at different institutes will be reviewed in the following.

The performance and durability of SOFCs and SOECs have been intensively studies at DTU Energy Conversion (the former Risø National Laboratory). The cells operated in SOEC mode generally showed faster degradation rate than the similar cells operated in SOFC mode.[6,33,37–39] A durability test for steam electrolysis (50 % H_2O + 50 % H_2) via SOECs was performed for ~1300 hours, which showed a degradation rate of 2 %/Kh at 850 ^oC, -0.5 A/cm^2.[40] The degradation was mainly attributed to the Ni-YSZ electrode when operating the SOECs at low current densities. The impurities from raw material, sealing or the feed gas can block the Ni-YSZ TPB sites, leading to the decrease of the reaction activity. When operating the cells at high current densities, oxygen bubble was observed at YSZ grain boundaries, accounting for an increase of the ohmic resistance.[39]

An over 2000 hours' durability test was performed at German Aerospace Center (DLR) on the metal supported cells for electrolysis of steam (43 % H_2O in H_2), showing a degradation rate of 3.2 %/Kh at -0.3 A/cm^2 and 800 ^oC.[41] The degradation was attributed to the increase of polarization resistance, relating with the coarsening of Ni particles in the fuel electrode.

A number of long-term tests were performed at European Institute for Energy Research (EIfER) on solid oxide cells and multi-cell stacks for electrolysis of steam.[7–9,42–44] A recent report showed a degradation rate of 3.8 %/Kh based on more than 9000 hours' test for a Ni-YSZ supported solid oxide cell with a LSCF electrode operated at -1.0 A/cm^2. The absolute humidity of the feed gas was 80 vol % and the conversion was 36 % at -1.0 A/cm^2. The dominating ohmic resistance increase can be attributed to the pronounced changes of microstructures: nano-size pores formation along grain boundaries of the YSZ electrolyte and material transport into the ceria barrier layer.[45] Several 5-cell stacks tested at -0.4, -0.8 or -1.0 A/cm^2 for steam electrolysis showed a degradation rate of 3 %/Kh ~ 5 %/Kh.[9]

SOECs tests at Idaho National Lab (INL) were performed for the scandia-stabilized zirconia (SSZ) electrolyte supported SOCs.[10,11,46] Significant degradation of performance was observed for the large-size cells and multi-cell stacks which were used for steam electrolysis. For example, a 25-cell stack tested at 800 ~ 830^oC over approximately 900 hours showed more than 40 % increase for the area-specific resistance (ASR). The degradation mechanisms include the delamination of the oxygen electrode and contamination of the electrodes by Si and Cr, etc.[46,47]

It seems the degradation of SOECs depend on the setup, the initial performance and the operation conditions. Structural and compositional changes of the individual components are responsible for the degradation of cell performance. More details of the degradation will be given below based on literature study. SOECs and SOFCs, being the reversed operations for the same device, could show some common and unique degradation; thus SOFCs will also be referred to in the followings for better understanding the different mechanisms.

6.1. Ni-YSZ fuel electrode

<u>Ni particle coarsening/percolation loss</u>:

The coarsening of Ni particles as a function of time, atmosphere, temperature and catalyst support has been studied by J. Sehested et al for the steam-reforming processes on Ni catalyst.[48,49] An exponent behavior of Ni particle growth at 550 – 750 ^{o}C as a function of the test duration was reported as: $d_{Ni} = d_{Ni,0} + C * (1-\exp(-t/\tau))$, where τ is the time constant for Ni growth ($pH_2O : pH_2$ = 0.2, 1, and 50). Similar trend for the increase of the average particle size of Ni has been reported for the Ni-YSZ electrodes of SOCs.[50–52] A stabilization of the Ni particles growth can be expected due to the spatial limitation of the YSZ skeletons.

Vaßen et al modeled the growth of Ni particles in a porous cermet, assuming the particle size difference as the driving force and surface diffusion as the dominating mechanism.[53] The finer Ni particles have the higher driving force for coarsening, thus, in comparison to the coarser Ni-YSZ cermet, the finer Ni-YSZ structure exhibits a more particle growth.[51,52] Ni particle size increase can be influenced by the steam partial pressures. The higher pH_2O leads to the faster degradation of the Ni-YSZ electrode; however, the final level of the Ni-YSZ degradation seems not to be affected by the pH_2O.[51,54]

The coarsening of Ni particles decreases the TPB length, resulting to the increase of the polarization resistance. The improvement of the FIB-SEM technologies allows the change of TPB length to be quantitatively analyzed.[52,55–57] A decrease of TPB length from 1.84 to 1.38 μm^{-1} was reported by Faes et al. for the Ni-YSZ electrode after ~ 1100 hours' test at 0.28 A/cm^2, 750 – 800 ^{o}C within 3 % H_2O in H_2.[52] The severe coarsening of Ni particles could decrease the percolation of Ni network in the Ni-YSZ electrode, consequently result in decrease of the electrical conductivity.[58,59] The percolated Ni can be differentiated from the un-percolated Ni by the low-voltage SEM imaging method as described by K. Thydén et al.[60]

Ni particle growth has been reported for a SOEC operated at -0.5 A/cm^2, 850^{o}C in 50 % H_2O + 50 % H_2.[40] The mean particle diameter increased from 1.01 ± 0.05 µm for a reference cell to 1.26 ± 0.05 µm after 1300

hours' test. Although Ni particle size increase accounts for some extent of degradation, it is not the main degradation mechanism of SOECs.

Impurity:

Typically, impurities come from the raw materials of the cell components, the sealing materials and the feed gas as received. The accumulation/segregation of impurities in the active Ni-YSZ electrode plays a more important role for the SOEC performance and durability. The TPB site will be inactivated if they are blocked by impurities, corresponding to an increase of the polarization resistance.

Ni-YSZ model electrode studies have revealed the microstructural and electrochemical changes due to impurity segregation.[61–63] For the impure electrode, impurities segregated to the electrode-electrolyte interface, the triple phase boundaries and the surface of YSZ electrolyte, resulting in a significant higher polarization resistance than the pure electrodes.[62,63]

The impurity related performance degradation for the SOECs has been studied by A. Hauch et al[64,65] and S. Ebbesen et al[18]. The impurities originated from the sealing materials and the cell constituents. A degradation rate of 2 %/Kh was obtained for the electrolysis of steam (50 % H_2O + 50 % H_2) via SOECs at 850 ^oC, -0.5 A/cm^2 after ~1300 hours' test. The initial performance passivation of the SOECs within 1st 300 h of test was associated with the Si impurities from the glass sealing. The long-term degradation was mainly caused by an increasing polarization resistance for the fuel electrode, however, the detailed mechanism was not provided.[40] The FIB/TEM examination of the Ni-YSZ electrode close to electrolyte revealed the buildup of impurities containing Si, Al and Na at the TPBs.[65] In another test, Si containing impurities was also observed to segregate at the Ni | YSZ interface, where an impurity rim was formed.[66] Most of the impurities were found for the innermost 2 μm of the Ni-YSZ electrode close to the electrolyte.[66] During the electrolysis of 70 % H_2O + 30 % H_2 at -0.25 and -0.5 A/cm^2, the cell performance decreased mainly for the first 100 hours.[5] However, the initial passivation can be partly activated by either operating reversely in SOFC mode[5] or continuing the electrolysis test for an extended period[5,18,40].

Besides, the impurities (S, P, etc.) in the feed gas, even at extremely low concentration of ppb level, could significantly increase the Ni-YSZ TPB resistance.[18] As a contrast, minor or no degradation of the SOECs was achieved by cleaning the feed gas to the SOECs (operated at the low current density).[18,38] The well-known poisoning effect of sulphur to Ni catalyst is due to the chemisorption of S on the particle surface ($H_2S_{(g)} \leftrightarrow S_{(ads)} + H_{2\ (g)/(ads)}$) thus decrease the catalytic performances.[67–69] The impurity poisoning of the Ni-YSZ electrode will result in a fast voltage increase for SOECs and a moving front of the impurity distribution.[18]

The passivation and activation were reported for the SOECs during electrolysis of CO_2 and steam at mild conditions (-0.25 or -0.5 A/cm^2). However, for the electrolysis of CO_2 solely, cell voltage only showed degradation and no activation was observed. Analysis of the in situ measured impedance spectra revealed a predominant increase in the Ni-YSZ TPB resistance for the cell passivation, with the characteristic frequency shifted from a few KHz to ~ 200 Hz. The ohmic and oxygen ion transfer process were observed to be stable during the electrolysis at -0.25 and -0.5 A/cm^2. For the electrolysis of steam-CO_2 mixtures (without using glass sealing) and the electrolysis of CO_2, the impurities from the feed gas account for most of the polarization resistance increase for the Ni-YSZ electrode.

Possibility of YSZ reduction at the Ni-YSZ|YSZ interface:

The oxygen activity at the fuel electrode and electrolyte interface increases for SOFC operations and decreases for SOEC operations with respect to that at OCV conditions.[70] For the SOFCs, increasing the oxygen activity could lead to the oxidation of nickel at a high anodic over-potential.[14,70] For the SOECs, the decrease of oxygen activity at the Ni-YSZ | YSZ interface with increasing the cathodic over-potential could increase the risk of (partial) reduction of YSZ at the interface. The reduction of YSZ has been observed for the interface of the Ni plate | YSZ electrolyte[71,72] or the Pt pattern electrode | YSZ electrolyte[73] under cathodic polarization. However, the YSZ electrolytes are covered by gas-tight cathode for these cells, different from the typical SOECs, where the electrolyte was covered by porous electrodes with readily gas supply and much faster electrode kinetics. Little investigation on the reduction of YSZ at the cathode | electrolyte interface has been reported for the practical SOEC cells. However, it is still suggested to operate a SOEC within a safe range of electrolysis current to avoid the reduction of YSZ.

6.2. YSZ Electrolyte

Although under normal conditions YSZ is regarded merely as an oxide ion conductor, the transport of electron and hole may be of practical significance for the solid oxide cells operated under large polarizations. The increasing conductivity of the electrons or holes in YSZ has been studied by Park et al as a function of oxygen pressure.[74] Recently, Schefold et al have reported a pronounced electronic conduction through the YSZ electrolyte for a SOEC cell operated at ~ 810 ^oC during steam electrolysis at current densities that corresponded to a steam conversion rate above 100 %, or during cutting off the steam supply while keeping the current at -0.34 A/cm^2.[42]

Taking the electron and hole conductivity of YSZ into account, the oxygen partial pressure and electric potentials across an oxide electrolyte cell was simulated by T. Jacobsen and M. Mogensen.[70] According to

the simulation results, there is a sigmoidal shaped oxygen activity profile (Figure 5) across the YSZ electrolyte at OCV. For a SOFC operation, the oxygen activity will increase at the interface between fuel electrode and electrolyte but decrease at the interface between the oxygen electrode and the electrolyte. As a contrast, for a SOEC operation, the oxygen activity decreases at the interface between the fuel electrode and the electrolyte and increases for the interface between the electrolyte and the oxygen electrode. For both the SOFC and SOEC operations, the oxygen equilibrium pressures inside the electrolyte will always be within the interval of the pressures defined by the electrode potentials. For a SOEC operation, the slope of the electromotive potential at the inflexion point is steeper during operation than at OCV conditions, corresponding to an increase in the hole conductivity of the YSZ close to the oxygen electrode and in the electron conductivity of the YSZ close to the fuel electrode at increased cell voltages. Their theoretical study predicts the possibility of building up detrimental oxygen partial pressures in the YSZ electrolyte for SOEC operations.[70]

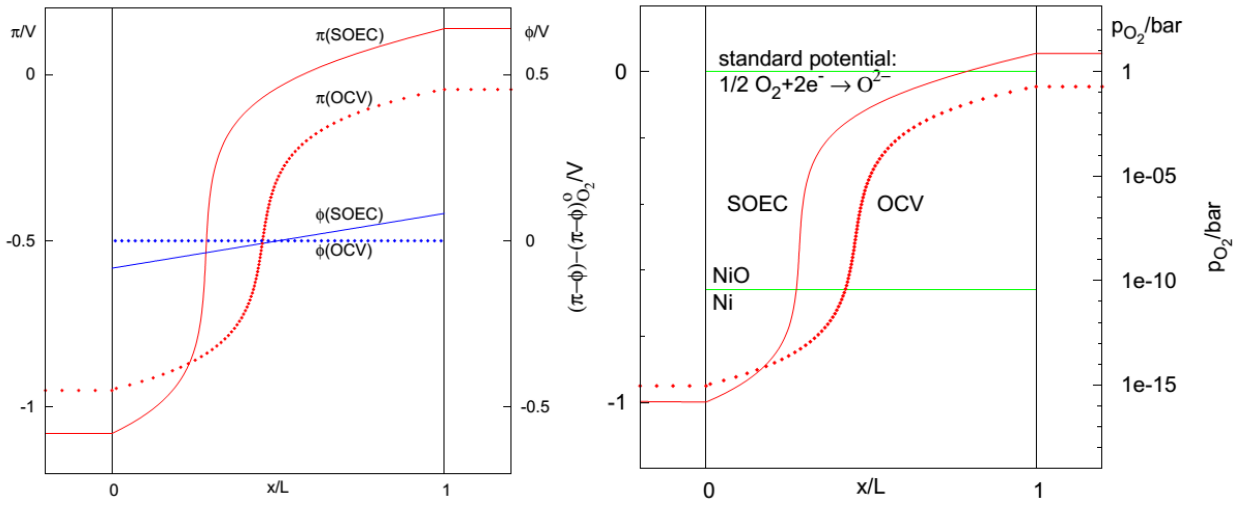

Figure 5 A) The electromotive potentials (π) and Galvani potential (Φ) and B) distribution of electrode potential (π – Φ) and equilibrium oxygen pressure (pO_2) in a SOEC cell under operation compared to OCV conditions at 1000 °C (According to literature[70])

Experimentally, formation of nano scaled oxygen bubbles has been observed at the grain boundaries (GBs) of the YSZ electrolyte adjacent to the oxygen electrode[39] for a SOEC cell after the steam electrolysis operation at a high current density of -2.0 A /cm^2. The oxygen bubbles led to an increase in the ohmic resistance and were ascribed to the buildup of oxygen activity in the electrolyte for a SOEC with a large over-potential on the oxygen electrode.[39,70] The high oxygen pressure at the electrolyte | oxygen electrode interface under SOEC operation could also result in the delamination of the oxygen electrode from the electrolyte[46,47,75–77]

6.3. Oxygen electrode

The degradation of the LSM-YSZ oxygen electrode due to zirconate formation has been reported for the SOFCs.[37,78–84] Zirconate formation is related to the high over-potential of oxygen electrode[37,83,84]. The chemical potential diagrams were employed to study the chemical compatibility of the perovskite electrodes and YSZ by Yokokawa[82]. A safe operation region for avoiding the formation of zirconate ($La_2Zr_2O_7$ and $SrZrO_3$) was suggested by Liu et al according to a T-pO_2 diagram based on thermodynamic calculations.[84] Zirconate is not thermodynamically stable above the critical oxygen partial pressures. Operating the SOCs in electrolysis mode at high current densities leads to an increase in the oxygen activity at the interface between the electrolyte and oxygen electrode due to the anodic polarization. Apparently, for SOEC operations, zirconate formation is not favored for the anodically polarized LSM-YSZ electrode. Delamination of the LSM-YSZ oxygen electrode from the YSZ electrolyte has been reported for both SOFCs[37,83,84]and SOECs[46,47,75–77]. For SOFCs, the higher current density/cathodic over-potential leads to a more pronounced LSM detachment, with the formation of small particles at the contacts and the decrease in the imprint crater size. For the SOECs, the LSM-YSZ oxygen electrode delamination from the electrolyte have been reported as one of the major degradations during steam electrolysis and was ascribed to the oxygen pressure build up at the interface related to a large anodic over-potential.[70]

7. Objective and the layout of the thesis

The long-term degradation is crucial for the application of the SOECs for high efficient production of hydrogen and synthesis fuels. In addition, it is desirable to operate the SOECs at a high current density for a high fuel production rate. There are relatively limited studies on the long-term durability of SOECs operated at high current densities, especially for the co-electrolysis of steam and CO_2. A systematic and comprehensive study on the degradation mechanisms of SOECs based on the combination of structural and electrochemical analysis is still missing.

This PhD project is to provide a thorough analysis of the degradation mechanism through detailed micro structural, compositional, electrochemical studies and the correlation between them. The SOECs in this work were operated at high current densities or accelerated degradation conditions.

The SOECs cell were Ni-YSZ based planar cells with LSM-YSZ and LSCF-CGO oxygen electrodes, tested for co-electrolysis of steam and CO_2 at high current densities ($|i|$ = 1.5 or 2.0 A/cm^2). Detailed analysis of the changes in microstructure and composition of the cell components were performed using scanning and

transmission electron microscopy. Impedance spectra were measured before, during and after the long-term durability tests.

It is found that the SOECs degraded rapidly when operated at high current densities and most of the degradations occurred for the Ni-YSZ electrode and the YSZ electrolyte. This study focuses on the electrochemical performances and microstructural changes of the SOECs operated under heavy load. By correlation of the results of the electrochemical and microstructural analysis, the mechanism of the degradations and a complete picture for the evolution of the individual electrode processes is obtained.

Another issue is the carbon deposition in the SOECs with a relatively dense Ni-YSZ electrode and operated at very high current densities in steam-CO_2 gas mixtures. The diffusion limitation was observed for the SOECs exhibited carbon formations.

Chapter 1 introduces the fundamental, background, progresses and the existing problems of SOECs technology. Chapter 2 describes the experimental set-up, the type and configuration of the solid oxide cells, the test procedure of the SOECs for co-electrolysis of steam and CO_2 and the methods for the electrochemical and microstructural analysis in this study. Chapter 3 includes an electrochemical analysis for characterization of the initial performance and an example of the electrochemical analysis for the entire test period, from OCV condition before durability test to the end of the test. Chapter 4 and Chapter 5 give respectively the detailed electrochemical analysis and post-microstructure analysis for investigation of the durability of SOECs tested under various conditions. The cell performance and the structure changes are correlated to investigate the mechanisms of the cell degradation. Chapter 6 describes the uneven current distribution for the SOECs especially when operating at high current densities and the correlation with the uneven degradation along the cell. Chapter 7 describes the risk of carbon deposition in the Ni-YSZ electrode depending on structure and operating condition during co-electrolysis of steam and CO_2. Detailed TEM characterization for the carbon formed in SOEC is provided in Chapter 8 with a possible mechanism proposed. Finally, Chapter 9 gives the overall conclusion of this work.

Reference

1. A. O. Isenberg, *Solid State Ionics*, **3/4**, 431–437 (1981).

2. W. Dönitz and E. Erdle, *Int. J. Hydrogen Energy*, **10**, 291–295 (1985).

3. W. Dönitz, G. Dietrich, E. Erdle, and R. Streicher, *Int. J. Hydrogen Energy*, **13**, 283–287 (1988).

4. S. H. Jensen, P. H. Larsen, and M. Mogensen, *Int. J. Hydrogen Energy*, **32**, 3253–3257 (2007)

5. A. Hauch, S. H. Jensen, S. Ramousse, and M. Mogensen, *J. Electrochem. Soc.*, **153**, A1741 (2006)

6. A. Hauch, S. D. Ebbesen, S. H. Jensen, and M. Mogensen, *J. Mater. Chem.*, **18**, 2331–2340 (2008)

7. A. Brisse, J. Schefold, and M. Zahid, *Int. J. Hydrogen Energy*, **33**, 5375–5382 (2008)

8. J. Schefold, A. Brisse, and F. Tietz, *J. Electrochem. Soc.*, **159**, A137 (2012)

9. A. Brisse and J. Schefold, *Energy Procedia*, **29**, 53–63 (2012)

10. J. S. Herring et al., *Int. J. Hydrogen Energy*, **32**, 440–450 (2007)

11. C. M. Stoots, J. E. O'Brien, K. G. Condie, and J. J. Hartvigsen, *Int. J. Hydrogen Energy*, **35**, 4861–4870 (2010)

12. X. Yang and J. T. S. Irvine, *J. Mater. Chem.*, **18**, 2349 (2008)

13. X. Yue and J. T. S. Irvine, *Solid State Ionics*, **225**, 131–135 (2012)

14. R. Knibbe, A. Hauch, J. Hjelm, S. D. Ebbesen, and M. Mogensen, *Green*, **1**, 141–169 (2011).

15. M. A. Laguna-Bercero, *J. Power Sources*, **203**, 4–16 (2012)

16. S. D. Ebbesen, C. Graves, and M. Mogensen, *Int. J. Green Energy*, **6**, 646–660 (2009)

17. C. M. Stoots, J. E. O'Brien, J. S. Herring, and J. J. Hartvigsen, *J. Fuel Cell Sci. Technol.*, **6**, 011014 (2009)

18. S. D. Ebbesen, C. Graves, A. Hauch, S. H. Jensen, and M. Mogensen, *J. Electrochem. Soc.*, **157**, B1419–B1429 (2010)

19. S. D. Ebbesen, R. Knibbe, and M. Mogensen, *J. Electrochem. Soc.*, **159**, F482–F489 (2012)

20. C. Graves, S. D. Ebbesen, M. Mogensen, and K. S. Lackner, *Renew. Sustain. Energy Rev.*, **15**, 1–23 (2011)

21. X. Sun et al., *Int. J. Hydrogen Energy*, **37**, 17101–17110 (2012)

22. J. E. O'Brien, M. G. McKellar, E. A. Harvego, and C. M. Stoots, *Int. J. Hydrogen Energy*, **35**, 4808–4819 (2010)

23. S. H. Jensen, P. H. Larsen, and M. Mogensen, *Int. J. Hydrogen Energy*, **32**, 3253–3257 (2007)

24. S. P. S. Badwal, *Solid State Ionics*, **52**, 23–32 (1992).

25. K. Kendall, N. Q. Minh, and S. C. Singhal, *in High Temperature and Solid Oxide Fuel Cells Fundamentals, Design and Applications, edited by* S. C. Singhal and K. Kendal, Editors, 1st ed., Elsevier Ltd., Oxford, UK, (2003)

26. N. Christiansen et al., *Fuel Cells Bull.*, **2006**, 12–15 (2006).

27. S. Linderoth et al., *Mater. Sci. Forum*, **539-543**, 1309–1314 (2007)

28. M. Brown, S. Primdahl, and M. Mogensen, *J. Electrochem. Soc.*, **147**, 475 (2000)

29. A. Hauch, S. H. Jensen, S. Ramousse, and M. Mogensen, *J. Electrochem. Soc.*, **153**, A1741 (2006)

30. E. Ivers-Tiffée and A. V. Virkar, *in High Temperature and Solid Oxide Fuel Cells Fundamentals, Design and Applications, edited by* S. C. Singhal and K. Kendal, Editors, 1st ed., Elsevier Ltd., Oxford, UK, (2003).

31. M. Mogensen, K. V. Jensen, M. J. Jørgensen, and S. Primdahl, *Solid State Ionics*, **150**, 123–129 (2002).

32. M. Mogensen and P. V. Hendriksen, *in High Temperature and Solid Oxide Fuel Cells Fundamentals, Design and Applications, edited by* S. C. Singhal and K. Kendal, Editors, 1st ed., Elsevier Ltd., Oxford, UK, (2003).

33. S. D. Ebbesen and M. Mogensen, *J. Power Sources*, **193**, 349–358 (2009)

34. J. E. O'Brien et al., *J. Fuel Cell Sci. Technol.*, **2**, 156 (2005)

35. S. D. Ebbesen and M. Mogensen, *ECS Trans.*, **50**, 167–182 (2013).

36. P. Holtappels, L. G. J. De Haart, U. Stimming, I. C. Vinke, and M. Mogensen, *J. Appl. Electrochem.*, **29**, 561–568 (1999).

37. A. Hagen, R. Barfod, P. V. Hendriksen, Y.-L. Liu, and S. Ramousse, *J. Electrochem. Soc.*, **153**, A1165 (2006)

38. S. D. Ebbesen and M. Mogensen, *Electrochem. Solid-State Lett.*, **13**, B106 (2010)

39. R. Knibbe, M. L. Traulsen, A. Hauch, S. D. Ebbesen, and M. Mogensen, *J. Electrochem. Soc.*, **157**, B1209 (2010)

40. A. Hauch, S. D. Ebbesen, S. H. Jensen, and M. Mogensen, *J. Electrochem. Soc.*, **155**, B1184 (2008)

41. G. Schiller, A. Ansar, M. Lang, and O. Patz, *J. Appl. Electrochem.*, **39**, 293–301 (2008)

42. J. Schefold, A. Brisse, and M. Zahid, *J. Electrochem. Soc.*, **156**, B897 (2009)

43. J. Schefold, A. Brisse, and M. Zahid, *ECS Trans.*, **28**, 357–367 (2010).

44. J. Schefold, A. Brisse, M. Zahid, J. P. Ouweltjes, and J. U. Nielsen, *ECS Trans.*, **35**, 2915–2927 (2011).

45. F. Tietz, D. Sebold, A. Brisse, and J. Schefold, *J. Power Sources*, **223**, 129–135 (2013)

46. M. S. Sohal et al., *J. Fuel Cell Sci. Technol.*, **9**, 011017 (2012)

47. J. R. Mawdsley, J. David Carter, A. Jeremy Kropf, B. Yildiz, and V. A. Maroni, *Int. J. Hydrogen Energy*, **34**, 4198–4207 (2009)

48. J. Sehested, J. A. P. Gelten, and S. Helveg, *Appl. Catal. A Gen.*, **309**, 237–246 (2006)

49. J. Sehested, *Catal. Today*, **111**, 103–110 (2006)

50. S. P. Jiang, *J. Mater. Sci.*, **38**, 3775–3782 (2003).

51. L. Holzer et al., *J. Power Sources*, **196**, 1279–1294 (2011)

52. A. Faes, A. Hessler-Wyser, D. Presvytes, C. G. Vayenas, and J. Van herle, *Fuel Cells*, **9**, 841–851 (2009)

53. R. Vaßen, D. Simwonis, and D. Stöver, *J. Mater. Sci.*, **36**, 147–151 (2001).

54. A. Hauch, M. Mogensen, and A. Hagen, *Solid State Ionics*, **192**, 547–551 (2011)

55. J. R. Wilson et al., *Nat. Mater.*, **5**, 541–544 (2006)

56. L. Holzer et al., *J. Power Sources*, **196**, 7076–7089 (2011)

57. T. Matsui, R. Kishida, J.-Y. Kim, H. Muroyama, and K. Eguchi, *J. Electrochem. Soc.*, **157**, B776 (2010)

58. H. Yokokawa, H. Tu, B. Iwanschitz, and A. Mai, *J. Power Sources*, **182**, 400–412 (2008)

59. D. Simwonis, F. Tietz, and D. Stover, *Solid State Ionics*, **132**, 241–251 (2000).

60. K. Thydén, Y. L. Liu, and J. B. Bilde-Sørensen, *Solid State Ionics*, **178**, 1984–1989 (2008)

61. K. V. Jensen, S. Primdahl, I. Chorkendorff, and M. Mogensen, *Solid State Ionics*, **144**, 197–209 (2001).

62. K. V. Jensen, R. Wallenberg, I. Chorkendorff, and M. Mogensen, *Solid State Ionics*, **160**, 27–37 (2003)

63. K. V. Hansen, K. Norrman, and M. Mogensen, *J. Electrochem. Soc.*, **151**, A1436 (2004)

64. A. Hauch, S. H. Jensen, J. B. Bilde-Sørensen, and M. Mogensen, *J. Electrochem. Soc.*, **154**, A619 (2007)

65. A. Hauch, J. R. Bowen, L. T. Kuhn, and M. Mogensen, *Electrochem. Solid-State Lett.*, **11**, B38 (2008)

66. A. Hauch, S. H. Jensen, J. B. Bilde-Sørensen, and M. Mogensen, *J. Electrochem. Soc.*, **154**, A619 (2007)

67. M. Gong, X. Liu, J. Trembly, and C. Johnson, *J. Power Sources*, **168**, 289–298 (2007)

68. Z. Cheng and M. Liu, *Solid State Ionics*, **178**, 925–935 (2007)

69. J. R. Rostrup-Nielsen, J. B. Hansen, S. Helveg, N. Christiansen, and A.-K. Jannasch, *Appl. Phys. A*, **85**, 427–430 (2006)

70. T. Jacobsen and M. Mogensen, *ECS Trans.*, **13**, 259–273 (2008).

71. T. Wagner, R. Kirchheim, and M. Rühle, *Acta Met. Mater.*, **40**, S85–S93 (1992).

72. T. Wagner and G. Duscher, *J. Mater. Res.*, **14**, 3340–3345 (1999).

73. B. Luerßen, J. Janek, S. Günther, M. Kiskinova, and R. Imbihl, *Phys. Chem. Chem. Phys.*, **4**, 2673–2679 (2002)

74. J. Park and R. N. Blumenthal, *J. Electrochem. Soc.*, **136**, 2867–2876 (1989).

75. A. Momma, T. Kato, Y. Kaga, and S. Nagata, *J. Ceram. Soc. Japan*, **105**, 369–373 (1997).

76. J. Guan et al., *High Performance Flexible Reversible Solid Oxide Fuel Cell, GE global Research Center Final Report for DOE Cooperative Agreement No. DE-FC36-04GO-14351, NTIS Order No. DE2007-899650*, (2006).

77. M. A. Laguna-Bercero, R. Campana, A. Larrea, J. A. Kilner, and V. M. Orera, *J. Power Sources*, **196**, 8942–8947 (2011)

78. H. Yokokawa, N. Sakai, T. Kawada, and M. Dokiya, *Solid State Ionics*, **40/41**, 398–401 (1990).

79. H. Yokokawa, N. Sakai, T. Kawada, and M. Dokiya, *J. Electrochem. Soc.*, **138**, 2719–2727 (1991).

80. C. Clausen, C. Bagger, J. B. Bilde-sørensen, and A. Horsewell, *Solid State Ionicsstate*, **70/71**, 59–64 (1994).

81. A. Mitterdorfer and L. J. Gauckler, *Solid State Ionics*, **111**, 185–218 (1998).

82. H. Yokokawa, *Annu. Rev. Mater. Res.*, **33**, 581–610 (2003)

83. A. Hagen, Y. L. Liu, R. Barfod, and P. V. Hendriksen, *J. Electrochem. Soc.*, **155**, B1047 (2008)

84. Y. L. Liu et al., *Solid State Ionics*, **180**, 1298–1304 (2009)

Chapter 2 Experimental

1. Cell configurations

Planar Ni-YSZ (YSZ = yttria stabilised zirconia) supported solid oxide cells (SOCs) produced at DTU energy conversion[1–4] were used for all experiments. All the cells were Ni-YSZ supported cells with a YSZ electrolyte. The cells had a dimension of 5×5 cm^2 and the active electrode area is 4×4 cm^2. Two types of different oxygen electrode were used: a composite of YSZ and strontium-doped lanthanum manganate (LSM) electrode, and a composite of strontium-doped lanthanum cobalt iron oxide (LSCF) and ceria-gadolinia (CGO). So, the cells used in this work were categorized into two types: the 'LSM cells' and the 'LSCF cells', according to the oxygen electrode type. The detailed cell configuration was Ni-YSZ support layer (~ 300 µm) | ~ 15 µm Ni-YSZ active electrode | ~ 10 µm YSZ electrolyte | ~ 15 µm LSM-YSZ electrode for the LSM cells and ~ 300 µm Ni-YSZ support | ~ 15 µm Ni-YSZ active electrode | ~ 10 µm YSZ electrolyte | ~ 5 µm CGO | ~ 15 µm LSCF-YSZ electrode for the LSCF cells.

2. Test set-up

The cell test set-up is shown in Figure 6. Current was collected by the Au and Ni foils (current collectors). Four pieces of Pt short wires were used to pick up the current and then it flows through the main current wire. The four Pt wires have a diameter of 1 mm and an equal length of ~ 10 cm. Both the Au and Ni foils are 0.2 mm in thickness, 4 cm in length and 4 cm in width. The Ni-YSZ and LSM gas distributors have a diamension of 1 mm (thickness) x 4 cm x 4 cm. The voltage probes are attached to the surface of the Au and Ni current collectors. The in-plane voltage is caused by the in-plane current through the current collector and the resistance of the current collector that each pair of probes (1 & 2, or 3 & 4) is attached to. The in-plane voltage was measured between the inlet and outlet of the cell. The temperature of the cell at the center and outlet was recorded by two temperature probes which were placed (about 1 mm on top of the oxygen electrode) on the surface of the Au plate.

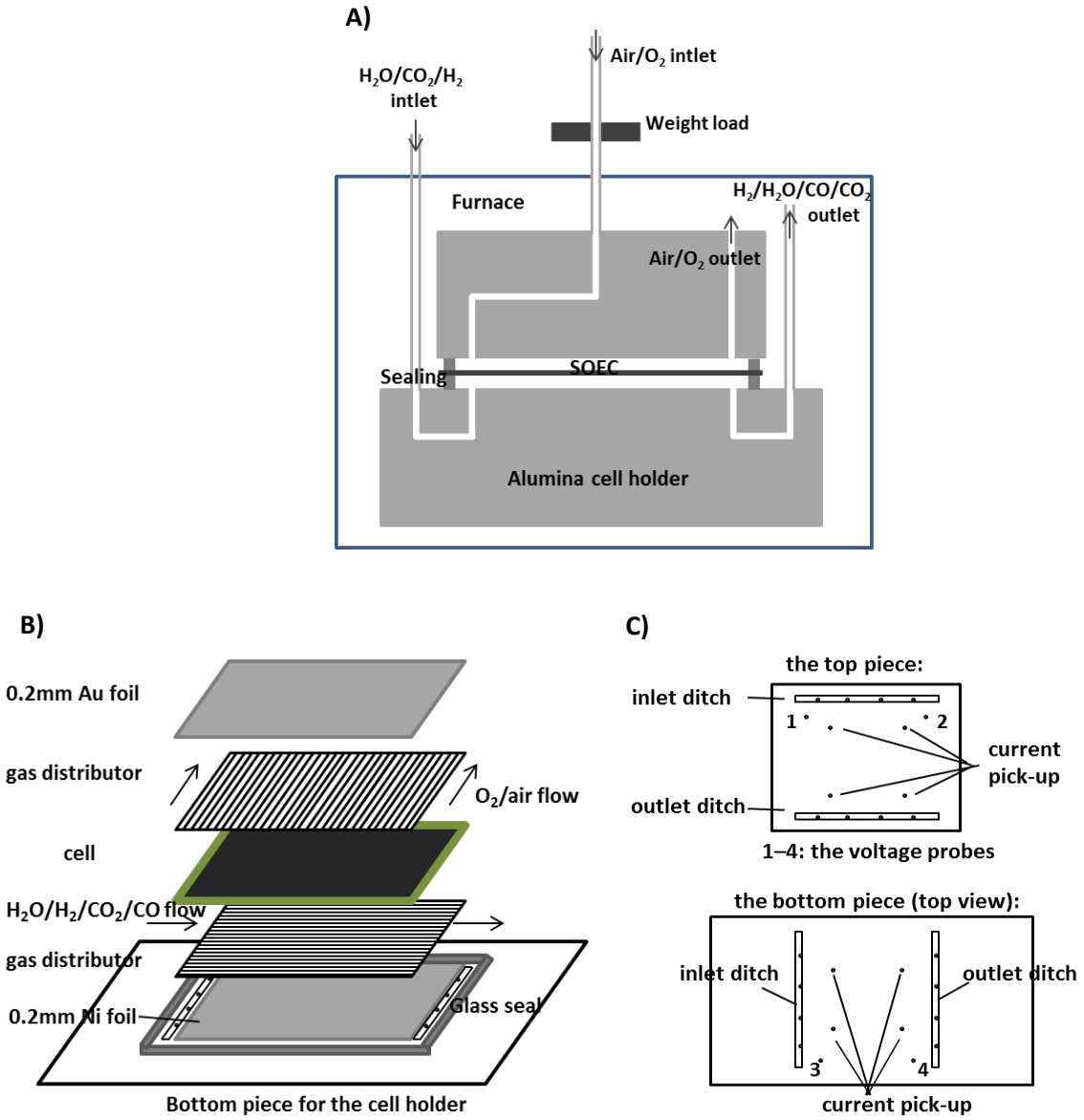

Figure 6 The cell test set-up: A) gas flow though the channels of the cell holder; B) sandwich-setup including the cell, metal foils and the ceramic gas distributors; C) the alumina holder with holes for placing the Pt wires (current pickup and in-plane voltage measurement) and the inlet and outlet ditches for gas flown. Through the holes 1 – 4 the voltage probes are attached to the Au and Ni current collectors. The in-plane voltage is measured between 1 and 2 for the fuel electrode side, or between 3 and 4 for the oxygen electrode side. For each piece of cell holder there are 4 additional holes for placing the current pick-up wires.

3. Test procedures

3.1. Normal test and clean test

The tests can be divided into two categories, the 'normal test' and the 'clean test', according to the types of the set-up and gas processing. For the normal tests, albite glass bars were used as sealing for both the cathode and anode and the cell was exposed to a relatively high level of impurities (Si, etc.). Ni-YSZ or LSM cermet was used respectively on the Ni-YSZ or oxygen electrode side as the gas distributor/current collector. Gas CO_2 and H_2 as received (with S impurities of ~ppb) were flown to the cell directly. For the clean test, metal frame was used as the sealing on both electrodes.[5,6] Ni mesh was used as the contact on the Ni-YSZ electrode and Pt mesh for oxygen electrode. CO_2 and H_2 were cleaned by a gas cleaner to remove the impurities before supplied to the cell.

3.2. Initial cell performance characterization

All the cells were heated up to 1000 ^oC and kept for 2 hours for sealing. Then, 20 L/h 9 % H_2 in N_2 was flown to the cell for 2 hours to obtain Ni-YSZ electrode by the reduction of NiO-YSZ. Afterwards, 25 L/h 4 % H_2O + 96 % H_2 was flown to Ni-YSZ and 140 L/h Air was flown to oxygen electrode for 1 hour. Finally, the cell was cooled down to 850 ^oC for initial performance study.

Characterization of the initial performance include recording of electrochemical impedance spectra (EIS) and i-V curves, with 4 % H_2O + 96 % H_2, 20 % H_2O + 80 % H_2, 50 % H_2O + 50 % H_2, and 45 % H_2O + 45 % CO_2 + 10 % H_2 flown to the Ni-YSZ electrode, and with either air or pure oxygen flown to the LSM-YSZ electrode. The flow rate to the Ni-YSZ electrode was 25 L/h and the flow rate to the LSM-YSZ electrode was 140 L/h in all cases. For each gas atmosphere, EIS measurement was performed at OCV 15 minutes after changing the atmosphere. A Solartron 1255B frequency analyzer was used for measuring the impedance. Then, i-V curves were recorded with the cell voltage decreasing from OCV down to 700 mV or 650 mV in fuel cell mode, and/or increasing up to 1250 mV in electrolysis mode.

3.3. Galvanostatic durability test

After initial performance characterization, the cells were operated at 850 ^oC with 45 % H_2O + 45 % CO_2 +10 % H_2 flown to Ni-YSZ and O_2 to oxygen electrode. The current density was increased by steps to the value at which the galvanostatic test is intended to operate (-1.5 or -2.0 A/cm^2). Impedance was recorded at each step after a hold-time of 15 min. For the LSM cells, after increasing current density from 0 to -1.5 or -2.0 A/cm^2, the cell temperature (T_center probe) could increase to ~ 865 ^oC due to ohmic heating of the cell. For the LSCF cells, the temperature increase was lower due to the lower cell resistance than LSM cells; thus, in order to minimize the contribution of the temperature difference to the cell performance difference, the cell temperature of LSCF cells was lift up to ~ 865 ^oC by control of the furnace temperature. The information

about the test set-up and the operations for the durability tests is given in Table 1. During the long term galvanostatic operation, cell voltage was recorded every 2 minutes and EIS was recorded periodically, e.g. every 6 hours. With the cell degradation, the cell voltage could increase by a few hundred millivolts. The in-plane voltage was recorded during cell degradation in order to study the current distribution along the cell. The tests were stopped when the duration reaching ~ 700 hours or the cell voltage reaching ~ 2000 mV. Due to the cell voltage increase, the cell temperature increased to ~ 875 ^{o}C finally. After the durability test, the current density was stepped down to zero with EIS recorded. For some cells after test, gas variation and EIS measurement were performed at OCV again. The cells were then cooled down with H_2 (> 630 ^{o}C) and 9 % H_2 in N_2 (< 630 ^{o}C) flown to the Ni-YSZ electrode.

Table 1 Set-up and operations for the long term durability tests

Cell Nr.	Current Density (A/cm^2)	Oxygen Electrode	Current Collector & Sealing	Gas Clean	Duration (hours)	Final voltage (mV)
T1	-1.5	LSM-YSZ	Ni-YSZ/LSM; Glass Bar	No	681.5	1785
T2	-2.0	LSM-YSZ	Ni-YSZ/LSM; Glass Bar	No	678.0	2001
T3	-2.0	LSM-YSZ	Ni-YSZ/LSM; Glass Bar	No	501.8	1880
T4	-2.0	LSM-YSZ	Ni-YSZ/LSM; Glass Bar	No	138.3	1765
T5	-2.0	LSM-YSZ	Metal Mesh; Frame	Yes	699.5	1680
T6	-1.5	LSCF-CGO	Ni-YSZ/LSM; Glass Bar	No	707.0	1399
T7	-1.5	LSCF-CGO	Metal Mesh; Frame	Yes	712.4	1193
T8	-2.0	LSCF-CGO	Ni-YSZ/LSM; Glass Bar	No	720.7	1522
T9	-2.0	LSCF-CGO	Metal Mesh; Frame	Yes	682.8	1463

25 L/h 45 % CO_2 + 45 % H_2O + 10 % H_2 to the Ni-YSZ electrode and pure O_2 to the oxygen electrode; Initial cell temperature at ~ 865 ^{o}C under operation and increased to ~ 875 ^{o}C due to degradation;

3.4. Test for investigation of carbon deposition

The performance and durability of SOECs was also investigated on two cells with relative dense Ni-YSZ structure. The same procedure as presented above was used for characterizing the initial performance of the two cells. The cells were tested with 25 L/h 45 % H_2O + 45 % CO_2 + 10 % H_2 flown to the Ni-YSZ cathode at ~ 850 ^{o}C (cell temperature at OCV condition). One cell was operated at -2.0 A/cm^2 for 29.5 hours up to 2.2 V and the other was operated at -2.25 A/cm^2 for 11.2 hours up to 2.0 V. The test duration for the two cells was short because of the fast degradation of cell performance.

4. Electrochemical analysis

4.1. Gas variation for each electrode

The gas atmosphere was varied only for one electrode at one time and the atmosphere of the other electrode was fixed. For gas variations on the Ni-YSZ electrode, impedance was measured with 4 % H_2O + 96 % H_2, 20 % H_2O + 80 % H_2 50 % H_2O + 50 % H_2 and then 45 % H_2O + 45 % CO_2 + 10 % H_2 flown to the Ni-YSZ electrode, while gas composition to the LSM-YSZ electrode was kept constant. Because the electrochemical processes affected by the atmosphere change were related only to the electrode on which the gas variation was performed, the processes corresponding to the LSM-YSZ electrode should keep constant and the change in impedance can be ascribed to the Ni-YSZ electrode only. For gas variations on the LSM-YSZ electrode, impedance was measured with air or O_2 flown to LSM-YSZ and gas condition at Ni-YSZ was kept constant. Gas variations were applied to the LSCF cells in the same way.

4.2. Analysis of the Difference in Impedance (ADIS)

The difference in the impedance measured for the cell at different operation conditions (gas composition, current density, etc.) was analyzed in order to identify the characteristic frequency of the electrode process that affected by the change in conditions. According to equation (1), the ADIS was calculated from the real part of the impedance measured at two different operating conditions. Impedance measured at condition I was regarded as the reference for condition II. For gas variations on the Ni-YSZ electrode, 4 % H_2O + 96 % H_2 or 20 % H_2O + 80 % H_2 was usually set as condition I (reference), while 50 % H_2O + 50 % H_2 and 45 % H_2O + 45 % CO_2 +10 % H_2 was used as condition II. Air and O_2 were usually used for gas variations on the LSM-YSZ electrode. For the current density increase, OCV was used as condition I (reference) and current density i as condition II.

$$\frac{\partial Z'(f)}{\partial \ln(f)} = \frac{(Z'(f_{n+1})_{II} - Z'(f_{n-1})_{II}) - (Z'(f_{n+1})_{I} - Z'(f_{n-1})_{I})}{ln(f_{n+1}) - ln(f_{n-1})}$$

Via ADIS (analysis of the difference in impedance spectra)[7] and DRT (distribution of relaxation times)[8,9] analysis of the impedance spectra recorded during gas variation on one electrode, the characteristic frequency of individual process corresponding to this electrode can be identified. Furthermore, the relative size of the polarization resistance of the electrode processes within various atmospheres can be estimated. This information was then used for the break-down of the impedance for the cell at OCV before and after durability test. ADIS & DRT analysis was also performed for the current increasing/decreasing and more importantly, the galvanostatic operations. Combining with the electrode process and the characteristic frequency identified by gas variations at OCV, it enabled assignment of the increase/decrease in resistance to a specific electrode process as a function of current densities and durations.

4.3. CNLS Fitting of the impedance

In order to break down the total impedance into contributions from individual electrode processes, the impedance spectra need to be fitted to an equivalent circuit with proper physical meaning. The equivalent circuit used for the fitting of the 'LSM cell' was same as the previously developed model for the Ni-YSZ based solid oxide cells at DTU Energy Conversion (former Risø-DTU). It consists of an inductance 'L', a series resistance 'Rs' and five (RQ) elements: L - Rs - $(RQ)_1$ - $(RQ)_2$ - $(RQ)_3$ - $(RQ)_4$ - $(RQ)_5$.[10–12] (RQ) elements 1 to 5 represent respectively the high frequency O^{2-} transfer, the TPB reactions at the Ni-YSZ electrode, the TPB reactions at the LSM-YSZ electrode, the gas diffusion and the gas conversion which are mainly at the Ni-YSZ electrode. Impedance spectra recorded at OCV in 4 % H_2O + 96 % H_2 to the Ni-YSZ electrode and with air to the LSM-YSZ electrode (not shown) was used as a basis for the remaining fit as the published values for the developed model are based on this composition. For the remaining mixtures, first, the contribution to the Ni-YSZ electrode was fitted when changing the gas composition to the Ni-YSZ electrode only, followed by fitting the contribution to the LSM-YSZ electrode. Fitting of all the processes should be in line with the results of ADIS and DRT analysis. The value of 'n', the exponent of the constant phase element, should be kept constant for a specific electrode process. According to the previous work at DTU Energy Conversion, n values of the element $(RQ)_1$ to $(RQ)_5$ were fixed respectively at 0.68, 0.8, 0.87, 0.75 and 0.9 ~ 1 for fitting the impedance[10,11] throughout the durability test. The 'RAVDAV' software was used for the fitting of the impedance spectra.[9] The initial guess of fitting parameters (resistance & frequency) can be facilitated by the previous ADIS & DRT analysis, from which the electrode processes, the characteristic frequency and the relative size of the resistances were estimated. The above information was also used for verification of the fitting results. Accordingly, after repeating many rounds of fitting-feedback-fitting, individual contributions of the electrode processes were identified. The evolution of electrode process obtained from impedance analysis was also correlated with the operation conditions as well as the change in microstructure / composition of the cell component.

For comparisons between the two types of cells (and better consistency), the same equivalent circuit as described above was used for the impedance fitting of the LSCF cells. Regarding to the n values, assuming the nature of the related electrode processes was not totally altered and the better performance was ascribed to the increase of reaction sites (TPB length), the same n values were used for the LSCF cells as for the LSM cells.

5. Microstructural analysis

After test, the cells were dismounted carefully at room temperature for microstructural examination. In order to study the difference in the microstructures of the cell along gas flow direction, fragments of the

cell close to inlet, center and outlet were investigated. Two types of cross-section samples were prepared for each cell: 1) fractured samples, which can provide the intact surface details of the electrodes and 2) polished cross-sections, which were casted in epoxy followed by polishing. The second type of sample was impregnated with epoxy which was hardened for 12 hours, in order to maintain the porous framework and other structure details during polishing. The final polishing procedure were carried out using three kinds of fine diamond sands with decreasing particle size (6, 3 and 1 μm in sequence), in order to get a smooth surface and avoid contaminations from the polishing media. The polished samples were suitable for (Ni) percolation and elemental analysis. The scanning electron microscopy (SEM) (Zeiss Supra 35) and energy dispersive X-ray spectroscopy (EDS) were used for the microstructure and composition analysis. The imaging and EDS analysis was normally performed at 5 ~ 15 KeV and the Ni percolation analysis were performed at 0.9 or 1 KeV in inlens mode.[13]

Transmission electron microscopy (TEM) and EDS analysis under TEM were performed for cell T2 and T3. The sample preparation for TEM analysis includes mechanical polishing and FIB thinning. Two pieces of cell were sandwiched together in epoxy at 140 ^{o}C for 10 min. Then the samples were mechanically polished to a thickness of ~ 20 μm and further thinned to ~ 100 nm by focused ion beam (FIB) milling. The FIB milling was performed using a Carl Zeiss 1540 XB FIB-SEM operating at 30 KV and a probe current of 50 pA. The final step of FIB polishing was carried out at 5 KV and a probe current of 50 pA in order to reduce the amorphous surface layer and Ga-ion implantation. A JEM-3000F microscopy operated at 300 KV was used for the transmission electron microscopy (TEM). Elemental maps and line scan profiles were obtained from EDS analysis of the sample in scanning transmission electron microscopy (STEM) mode with the probe size of ~ 1 nm.

For the SOECs with carbon formation, the nanostructures at the Ni-YSZ|YSZ interface were carefully collected by scraping the bare surface of a delaminated YSZ electrolyte using a sharp steel blade. The collected CNTs and nanoparticles were dispersed in ethanol and loaded onto lacey carbon film supported by copper grid for TEM observation. High-resolution TEM (HRTEM) analysis of the derived CNTs and nanoparticles was performed using a JEM-3000F microscopy equipped with a field-emission gun, operated at 300 kV. The point resolution is 0.19 nm.

References

1. M. J. Jørgensen and M. Mogensen, *J. Electrochem. Soc.*, **148**, A433–A442 (2001)

2. P. H. Larsen et al., in *Proceedings of Solid Oxide Fuel Cell VII (SOFC VII)*, S. C. Singhal and H. Yokokawa, Editors, p. 28–37, Electrochemical Society, Pennington, NJ (2001)

3. S. Linderoth et al., *Mater. Sci. Forum*, **539-543**, 1309–1314 (2007)

4. N. Christiansen et al., *ECS Trans.*, **25**, 133–142 (2009).

5. S. D. Ebbesen, C. Graves, and M. Mogensen, *Int. J. Green Energy*, **6**, 646–660 (2009)

6. S. D. Ebbesen, C. Graves, A. Hauch, S. H. Jensen, and M. Mogensen, *J. Electrochem. Soc.*, **157**, B1419–B1429 (2010)

7. S. H. Jensen et al., *J. Electrochem. Soc.*, **154**, B1325 (2007)

8. H. Schichlein, A. C. Müller, M. Voigts, A. Krügel, and E. Ivers-Tiffée, *J. Appl. Electrochem.*, **32**, 875–882 (2002).

9. C. Graves, RAVDAV data analysis software, version 0.9.7, 2012.

10. R. Barfod et al., *J. Electrochem. Soc.*, **154**, B371 (2007)

11. R. Barfod, a. Hagen, S. Ramousse, P. V. Hendriksen, and M. Mogensen, *Fuel Cells*, **6**, 141–145 (2006)

12. S. D. Ebbesen and M. Mogensen, *ECS Trans.*, **50**, 167–182 (2013).

13. K. Thydén, Y. L. Liu, and J. B. Bilde-Sørensen, *Solid State Ionics*, **178**, 1984–1989 (2008)

Chapter 3 A Durability Study of Solid Oxide Electrolysis Cells Using Impedance Analysis

1 Introduction

In this study, a systematic analysis of the impedance spectra was performed to characterize the cell performance in various gas compositions and under different current densities during co-electrolysis of H_2O and CO_2. The impedance characterization was started in a gas mixture of 4 % H_2O + 96 % H_2, which has been well studied with the established equivalent circuit. Then the steam ratio of the H_2O-H_2 gas mixture was increased to 20% and 50%. Finally, the composition of 45 % H_2O + 45 % CO_2 + 10% H_2 was used for investigation of the co-electrolysis performance. The impedance spectra were first analyzed by ADIS and DRT for the guidance of the fitting process using the equivalent circuits. All the impedance spectra were broke down into individual processes by CNLS fitting using the same equivalent circuit model. The impedance analysis of the overall process is expected to allow a comprehensive description and reliable interpretation of the performance and durability of the cells.

2 Experimental

The solid oxide cells with two different oxygen electrodes, LSM-YSZ and LSCF-CGO, were tested for investigating the initial performance and durability. Two types of contact layer/gas distributor and sealing materials were used for the tests:[1,2] A) the Ni-YSZ ceramic was used as the contact layer and gas distributor while the albite glass bar was use as the sealing; B) the metal mesh served as contact layer and gas distributor while metal frame and a low impurity sealing were employed as the sealing.

All the cells were reduced at 1000 ^{o}C using the same procedure. The cells were cooled down to 850 ^{o}C for characterization of the initial performance at OCV in various gas compositions, 4 % H_2O + 96 % H_2, 20 % H_2O + 80 % H_2, 50 % H_2O + 50 % H_2 and 45 % H_2O + 45 % CO_2 + 10 % H_2 for the Ni-YSZ electrode and air/O_2 for the oxygen electrode. Then the current density was increased step by step to the operating current density intended for the galvanostatic durability test. The impedance of the cell was measured at each step of changing conditions (gas atmosphere and current density). After the durability test, the current was decreased to 0 and the cell was cooled down to room temperature. The impedance characterization in various gas atmospheres was also performed at OCV before cool down for some of the cells.

ADIS and DRT analysis of the impedance were performed and the results were used to guide the breakdown of the impedance by CNLS fitting. The equivalent circuit 'L-Rs-(RQ)1-(RQ)2-(RQ)3-(RQ)4-(RQ)5' was used for the impedance break down.[3–5] L is the inductance, Rs is the serial or ohmic resistance, (RQ) 1 to 5 respectively stands for the high frequency oxygen ion transfer, the Ni-YSZ electrode TPB reaction, the oxygen electrode TPB reaction, the diffusion process and the conversion process. The n value of each process was fixed for all the tests.

Detailed information about the cell configuration, test procedure and method for impedance analysis were described in Chapter 2. Experimental.

3 Results

3.1 Initial performance at OCV in various gas atmospheres

3.1.1 LSM cell: T2

The AIDS and DRT analysis of the impedance spectra were performed for the characterization of the initial performance of LSM cell T2. By varying the gas composition on the Ni-YSZ electrode side (4 % H_2O + 96 % H_2 and 45 % H_2O + 45 % CO_2 + 10 % H_2) and keeping the gas atmosphere on the LSM-YSZ electrode side constant, the characteristic frequency of the Ni-YSZ electrode was revealed to be ~ 6 KHz by ADIS analysis (Figure 7A), which has been ascribed to the characteristic frequency of the Ni-YSZ TPB reaction process.[3,4] Figure 7B shows the DRT analysis results of the impedances measured with 4 % H_2O + 96 % H_2, 20 % H_2O + 80 % H_2, 50 % H_2O + 50 % H_2 and 45 % H_2O + 45 % CO_2 + 10 % H_2 flown to the Ni-YSZ electrode while keeping constant air flow to the LSM-YSZ electrode. A high frequency peak at 20~30 KHz with relatively stable peak height was observed, which was related to the interfacial oxygen ion transfer (major contributions from LSM-YSZ|YSZ interface).[3,4,6] The process at 3 ~ 10 KHz was sensitive to the gas composition in the Ni-YSZ electrode, which is consistent with the results obtained from ADIS (Figure 7A). The peak height of the Ni-YSZ TPB process was observed to decrease with increasing the ratio of steam in the gas mixture from 4% to 20% and 50%, but was similar in 50 % H_2O + 50 % H_2 and 45 % H_2O + 45 % CO_2 + 10 % H_2. As the peak at ~ 800 Hz was not sensitive to gas composition change in the Ni-YSZ side but depended on the gas composition change in the LSM-YSZ side, the process in this frequency range is ascribed to the LSM-YSZ TPB reactions.[3,7] The conversion process was observed at a frequency of a few Hz (Figure 7B) and the peak height decreased with changing the gas composition of Ni-YSZ in the order from 4 % H_2O + 96 % H_2 to 45 % H_2O + 45 % CO_2 + 10 % H_2, 20 % H_2O + 80 % H_2 and 50 % H_2O + 50 % H_2.

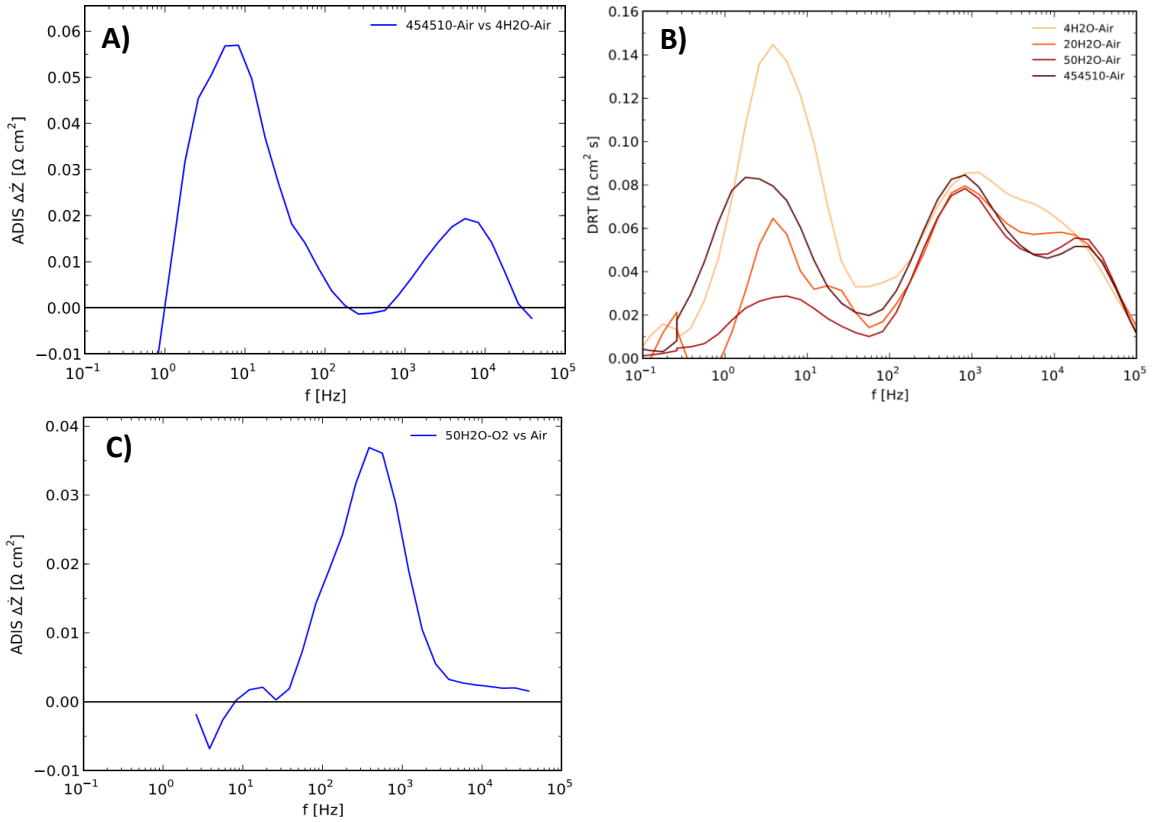

Figure 7 Initial performance characterization for cell T2 at OCV by impedance analysis: A) ADIS analysis with 4 % H_2O + 96 % H_2 and 45 % H_2O + 45 % CO_2 + 10 % H_2 flown to Ni-YSZ (both with air for LSM-YSZ); B) DRT analysis of the cell with 4 % H_2O + 96 % H_2, 20 % H_2O + 80 % H_2, 50 % H_2O + 50 % H_2 or 45 % H_2O + 45 % CO_2 + 10 % H_2 flown to Ni-YSZ and air flown to LSM-YSZ; C) ADIS analysis of LSM-YSZ in air and O_2 (with 50 % H_2O + 50 % H_2 flown to Ni-YSZ)

Base on the ADIS and DRT analysis, the impedance spectra were broken down into individual processes using the model presented in experimental part. As is shown in Figure 8, the Ni-YSZ TPB reaction resistance (R2) decreased with increasing the steam ratio for the gas composition of Ni-YSZ: ~ 0.071 Ωcm^2 for 4 % H_2O + 96 % H_2, ~ 0.062 Ωcm^2 for 20 % H_2O + 80 % H_2 and ~ 0.050 Ωcm^2 for 50 % H_2O + 50 % H_2. In addition, similar values of R2 (~ 0.056 Ωcm^2) were obtained for the Ni-YSZ electrode in 50 % H_2O + 50 % H_2 and 45 % H_2O + 45 % CO_2 + 10 % H_2. The conversion resistance (R5) decreased with changing the gas atmosphere of Ni-YSZ from 4 % H_2O + 96 % H_2 to 45 % H_2O + 45 % CO_2 + 10 % H_2, 20 % H_2O + 80 % H_2 and 50 % H_2O + 50 % H_2. The serial resistance (Rs) and the oxygen ion transfer resistance (R1) were relatively stable and showed no dependence on gas variations. The corresponding summit frequencies of these process were : 20 – 30 KHz for the oxygen ion transfer process, 5 – 9 KHz for the Ni-YSZ TPB reaction process, 600 – 1000 Hz for

the LSM-YSZ TPB process, 10 – 30 Hz for diffusion and 1.9 – 4.9 Hz for the conversion process, close to the values reported in literatures[3–5].

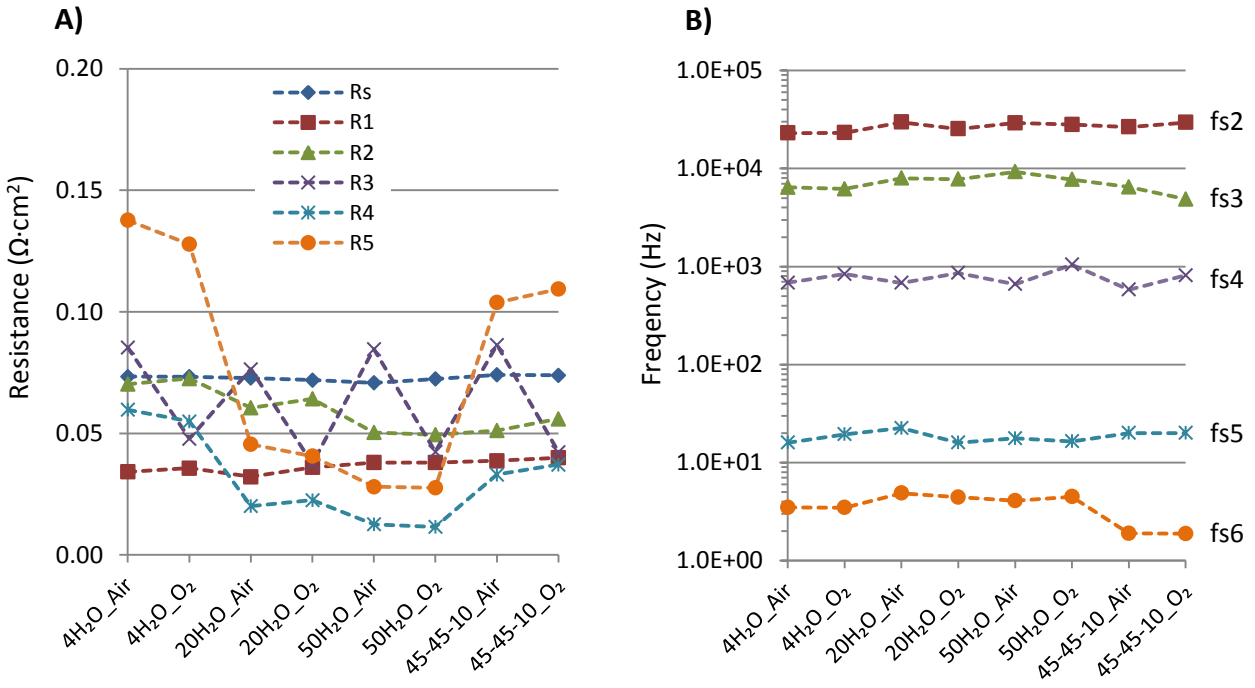

Figure 8 Breakdown of the impedance for cell T2 at OCV in various gas compositions: A) resistance of each process; B) the summit frequency of each process. The xH_2O_Air (or O_2) represents x % H_2O in H_2 was flown to the Ni-YSZ electrode and air (or O_2) flown to oxygen electrode; 45-45-10_Air (O_2) represents that 45 % H_2O + 45 % CO_2 + 10 % H_2 was flown to Ni-YSZ and air (O_2) to oxygen electrode. (Rs: the serial or ohmic resistance; R1 – R3: the oxygen ion transfer, Ni-YSZ and oxygen electrode TPB reaction resistance, respectively; R4: diffusion resistance and R5: conversion resistance. fs 1-5: the summit frequency of the corresponding processes.)

3.1.2 LSCF cell: T7

The impedance analysis was also performed for characterizing the initial performance of the LSCF cells. Figure 9A shows the DRT analysis of LSCF cell T7 with air or O_2 flown to the LSCF-CGO electrode while keeping the atmosphere in the Ni-YSZ electrode side constant (20 % H_2O + 80 % H_2). A high frequency peak was observed at 6 ~ 10 KHz, the similar position of the Ni-YSZ TPB reactions for the LSM cells. Furthermore, the gas variations on Ni-YSZ in Figure 9B showed a characteristic frequency of Ni-YSZ at the similar position (3 ~ 10 KHz). Another peak at a lower frequency of ~ 200 Hz was observed in Figure 9A, which was sensitive to the gas compositions on the LSCF-CGO electrode. The peak height was lower with O_2 flown to LSCF-CGO

compared to air. Thus, it was ascribed to the LSCF-CGO TPB reactions. The peak height of the conversion process (at a few Hz) was slightly higher for the impedance measured with LSCF-CGO in air than in O_2.

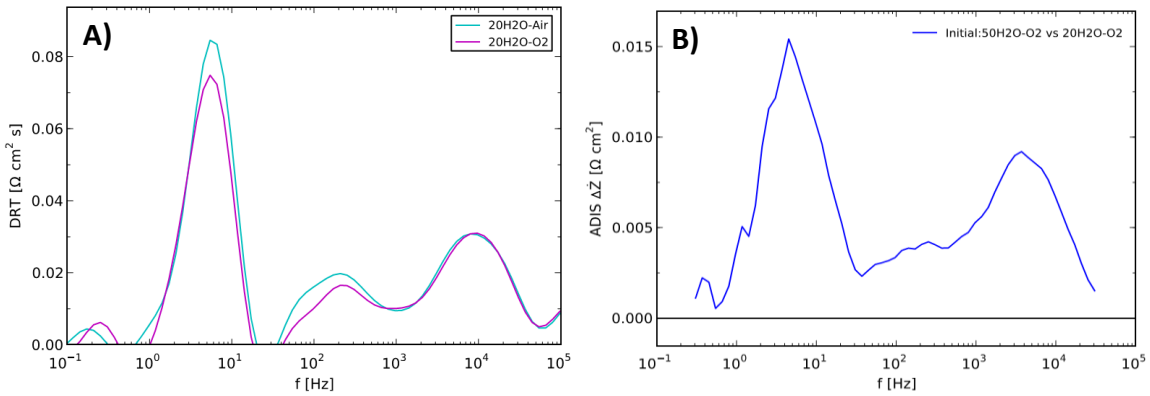

Figure 9 Initial performance characterization for cell T7 at OCV by impedance analysis: A) DRT analysis for the cell with air or O_2 flown to LSM-YSZ while the Ni-YSZ atmosphere was fixed at 20 % H_2O + 80 % H_2; B) ADIS analysis of the cell with 50 % H_2O + 50 % H_2 versus 20 % H_2O + 80 % H_2 flown to Ni-YSZ (O_2 was flown to LSM-YSZ)

The break down results in Figure 10 show that the Ni-YSZ TPB reaction (R2) decreased from ~ 0.055 Ωcm^2 in 4 % H_2O + 96 % H_2 to ~ 0.032 Ωcm^2 in 20 % H_2O + 80 % H_2 and 0.020 Ωcm^2 in 50 % H_2O + 50 % H_2. Similar performance of the Ni-YSZ TPB reactions was observed in 50 % H_2O + 50 % H_2 and 45 % H_2O + 45 % CO_2 + 10 % H_2 at OCV condition. The serial resistance (Rs) and the oxygen ion interfacial transfer resistance (R1) were very stable and showed no dependence on the gas compositions. The conversion resistance (R5) decreased with changing Ni-YSZ gas atmosphere in the order of 4 % H_2O + 96 % H_2 to 45 % H_2O + 45 % CO_2 + 10 % H_2, 20 % H_2O + 80 % H_2 and 50 % H_2O + 50 % H_2. However, the conversion resistance appeared to be influenced by the gas (air/O_2) on the oxygen electrode. Especially, with 4 % H_2O + 96 % H_2 to Ni-YSZ, the R5 value was lower in O_2 than in air (LSCF-CGO); with 45 % H_2O + 45 % CO_2 + 10 % H_2 to Ni-YSZ, the R5 value was higher in O_2 than in air (LSCF-CGO).

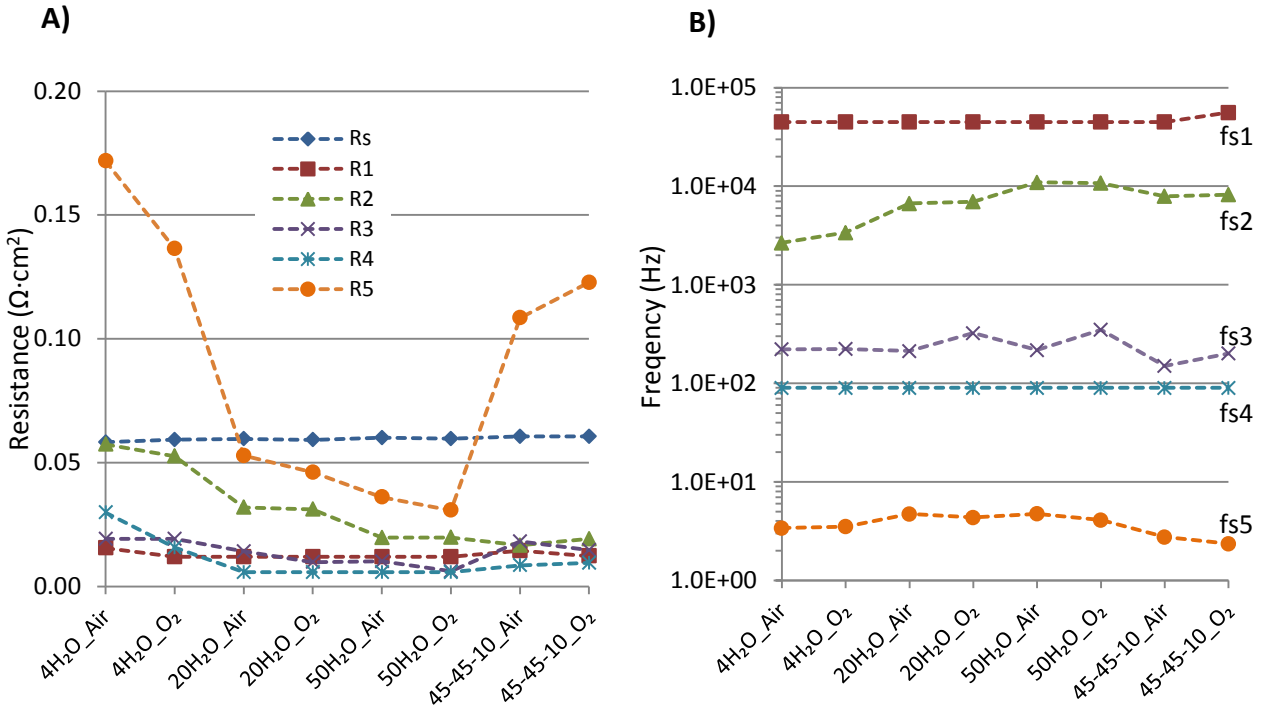

Figure 10 Breakdown of the impedance for cell T7 at OCV in various gas compositions: A) resistance of each process; B) the summit frequency of each process. The xH_2O_Air (or O_2) represents x % H_2O in H_2 was flown to the Ni-YSZ electrode and air (or O_2) flown to oxygen electrode; 45-45-10_Air (O_2) represents that 45 % H_2O + 45 % CO_2 + 10 % H_2 was flown to Ni-YSZ and air (O_2) to oxygen electrode. (Rs: the serial or ohmic resistance; R1 – R3: the oxygen ion transfer, Ni-YSZ and oxygen electrode TPB reaction resistance, respectively; R4: diffusion resistance and R5: conversion resistance. fs 1-5: the summit frequency of the corresponding processes.)

3.2 Polarization performance in 45 % H_2O + 45 % CO_2 + 10 % H_2

Based on the previous analysis of the impedance at OCV, the LSCF-CGO TPB process shows a summit frequency at around 100 ~ 300 Hz, far away from that of the Ni-YSZ TPB reactions (a few KHz). Although the summit frequency of the Ni-YSZ TPB process could shift downward when the polarization was applied, it is still distinct from the position of the LSCF-CGO TPB process. In the case of a LSM cell, the Ni-YSZ process might be overlapped with the LSM-YSZ process when the polarization was applied, as the summit frequency of the latter is around 1 KHz. It is thus more straightforward to identify the effect of polarization on the individual processes for the LSCF cell compared to the LSM cell. In this section, the performance of the individual process is studied by analysing the impedance of the LSCF cells operated in 45 % H_2O + 45 % CO_2 + 10 % H_2 at various current densities.

Cell T7: cell performance *vs.* current density (0 to -1.5 A /cm^2)

The impedance of cell T7 with the current increasing from 0 to the operating current density of -1.5 A/cm^2 was analyzed by the ADIS and DRT methods. As is shown by the Z'' and DRT analysis in Figure 11, a consecutive increase in the peak height with increasing the current was observed at the frequency of a few KHz, which is attributed to the frequency range of the Ni-YSZ TPB reaction based on the results of gas variations at OCV. Correspondingly, the peak position shifted from around 10 KHz to 5 ~ 6 KHz with current increasing from 0 to -1.5 A/cm^2. From the DRT analysis, another peak at ~ 200 Hz was observed, corresponding to the LSCF-CGO TPB reaction process (also based on the gas variations). The LSCF-CGO resistance was observed to be much smaller than the Ni-YSZ TPB reaction resistance and decreased slightly with increasing current. The peak height of the conversion process at a few Hz decreased with the current density increasing from 0 to -1.0 A/cm^2 and then increased slightly with the current density further increased to -1.5 A/cm^2. The above results agreed well with that of the ADIS analysis.

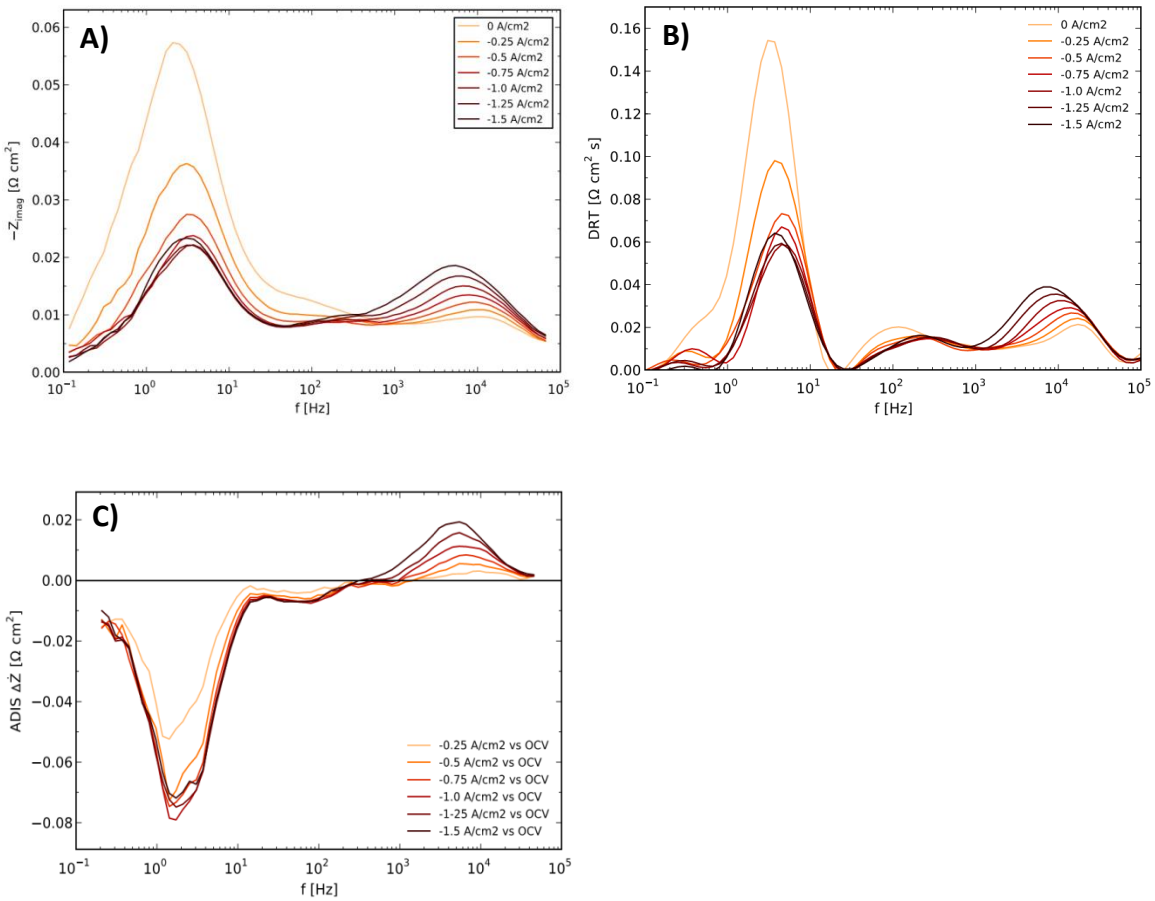

Figure 11 Impedance analysis for cell T7 with current increased from 0 to the operating current density (-1.5 A/cm^2): A) imaginary part (Z''); B) DRT analysis and C) ADIS analysis

The breakdown results of the impedance spectra for cell T7 with increasing current are shown in Figure 12. The cell showed an increasing resistance from 0.019 to 0.045 Ωcm^2 for the Ni-YSZ TPB reaction process. The other obvious change with changing current was observed for the conversion resistance. The conversion resistance reduced significantly when the electrolysis current density (|i|) increased from 0 to 0.5 A/cm^2, but decreased gradually or kept almost constant when the current density exceeded 0.5 A/cm^2. The serial resistance Rs showed a small increase from 0.065 to 0.067 Ωcm^2 with increasing current |i|. A low resistance of the LSCF-CGO TPB reactions was obtained. The summit frequency of the Ni-YSZ TPB reaction process shifted from ~ 10 KHz to ~ 6 KHz. The summit frequency of the LSCF-CGO was between 200 and 300 Hz. The conversion showed a summit frequency at 2.3 – 3.4 Hz. The above breakdown results are consistent with the ADIS and DRT analysis in Figure 11.

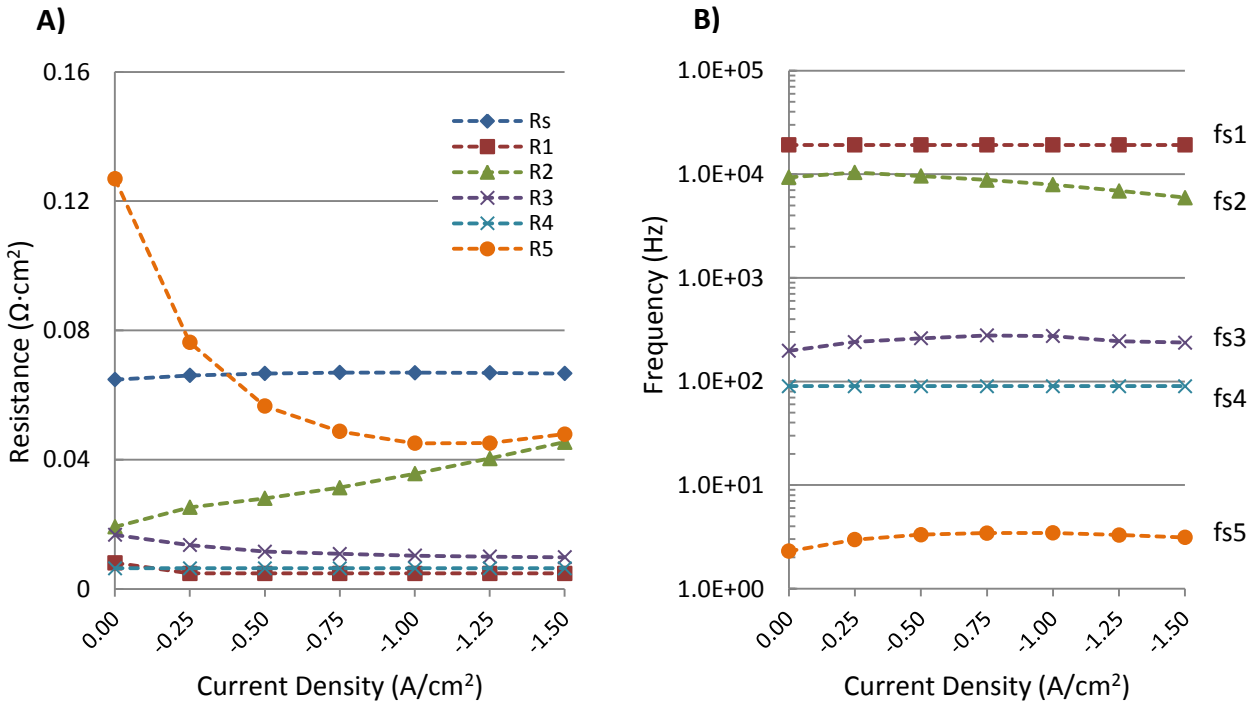

Figure 12 Breakdown of the impedance for cell T7 with current increased from 0 to the operating current density (-1.5 A/cm^2): A) resistance of each process; B) the summit frequency of each process. (Rs: the serial or ohmic resistance; R1 – R3: the oxygen ion transfer, Ni-YSZ and oxygen electrode TPB reaction resistance, respectively; R4: diffusion resistance and R5: conversion resistance. fs 1-5: the summit frequency of the corresponding processes.)

Cell T8: cell performance *vs.* current density (0 to -2.0 A /cm^2)

Cell T8, another LSCF cell, was operated up to a higher current density of -2.0 A/cm^2 compared with cell T7. Figure 13 shows the results of the impedance analysis for cell T8. Generally, the peak height of the Ni-YSZ TPB reaction process was observed to increase with increasing the current density with a slight shift in the peak position to lower frequency. The peak height of the conversion process decreased with electrolysis current density |i| from 0 to 1.0 A/cm^2 and then increased with electrolysis current density |i| above 1.0 A/cm^2. The peak of the LSCF-CGO TPB reaction process, which appeared at the frequency of ~ 200 Hz, decreased slightly with electrolysis current |i| increasing from 0 to 1.5 A/cm^2, but increased to the same level as at OCV with further increasing |i| to 2.0 A/cm^2. The changes in the LSCF-CGO TPB resistance were insignificant regarding to that of the Ni-YSZ TPB process.

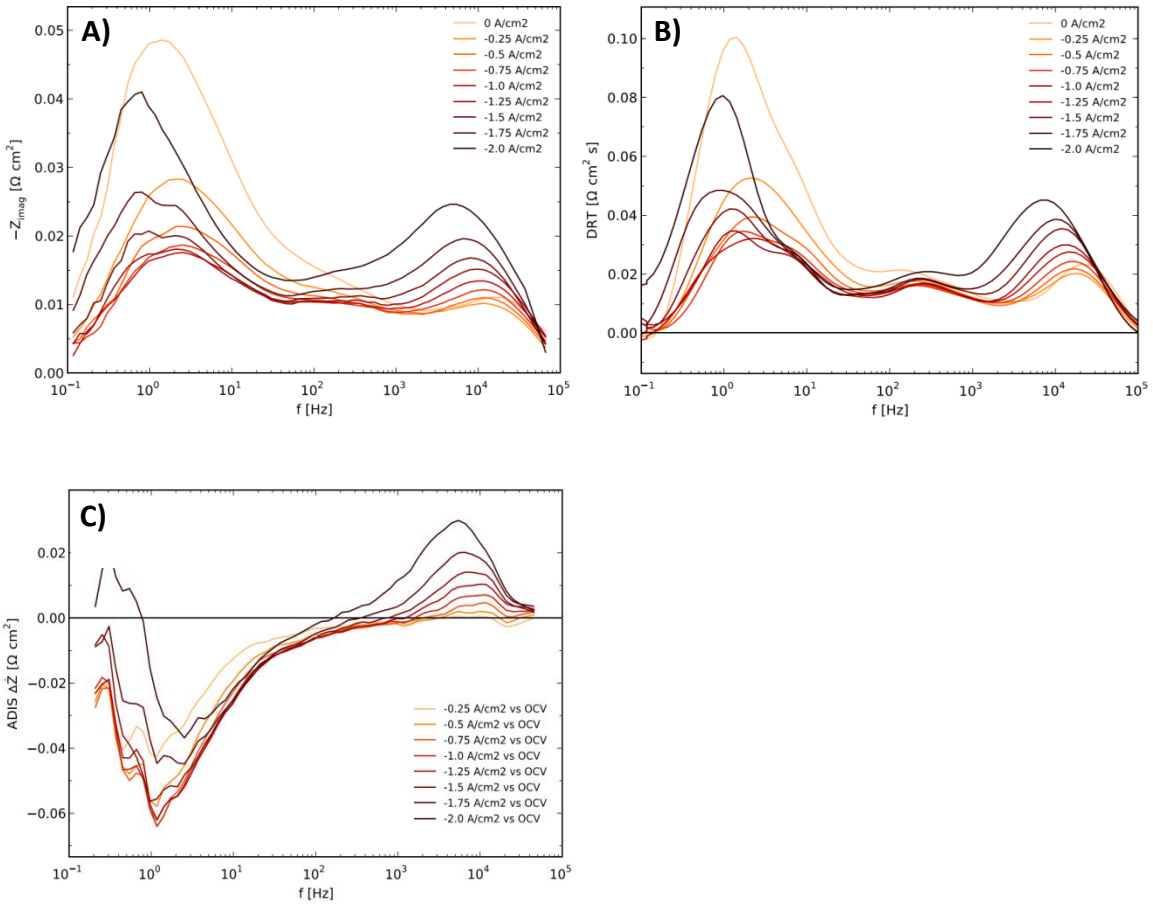

Figure 13 Impedance analysis for cell T8 with current increased from 0 to the operating current density (-2.0 A/cm^2): A) imaginary part (Z''); B) DRT analysis and C) ADIS analysis

The breakdown of the impedance is shown in Figure 14. The serial resistance Rs increased slightly from 0.067 to 0.071 Ωcm^2 with increasing the electrolysis current density. The Ni-YSZ TPB resistance increased from 0.013 to 0.049 Ωcm^2 with the increase in current density. The summit frequency of the Ni-YSZ TPB

reaction process slightly decreased from ~ 8 KHz to ~ 6 KHz with current increase. The conversion resistance decreased from 0.110 Ωcm^2 at OCV to 0.035 Ωcm^2 at the electrolysis current |i| of 1.0 A/cm^2 and increased to 0.089 Ωcm^2 with further increasing the electrolysis current |i| to 2.0 A/cm^2. Similar trend was observed for the changes in the diffusion resistance. The summit frequency of the diffusion and conversion was 10 – 20 Hz and 0.7 – 1.7 Hz, respectively. The oxygen ion transfer resistance and the oxygen electrode TPB resistance were relative stable compared to the other electrode processes. The oxygen ion transfer process showed a summit frequency at above 30 KHz and the LSCF-CGO TPB reaction showed a summit frequency at 200 – 300 Hz.

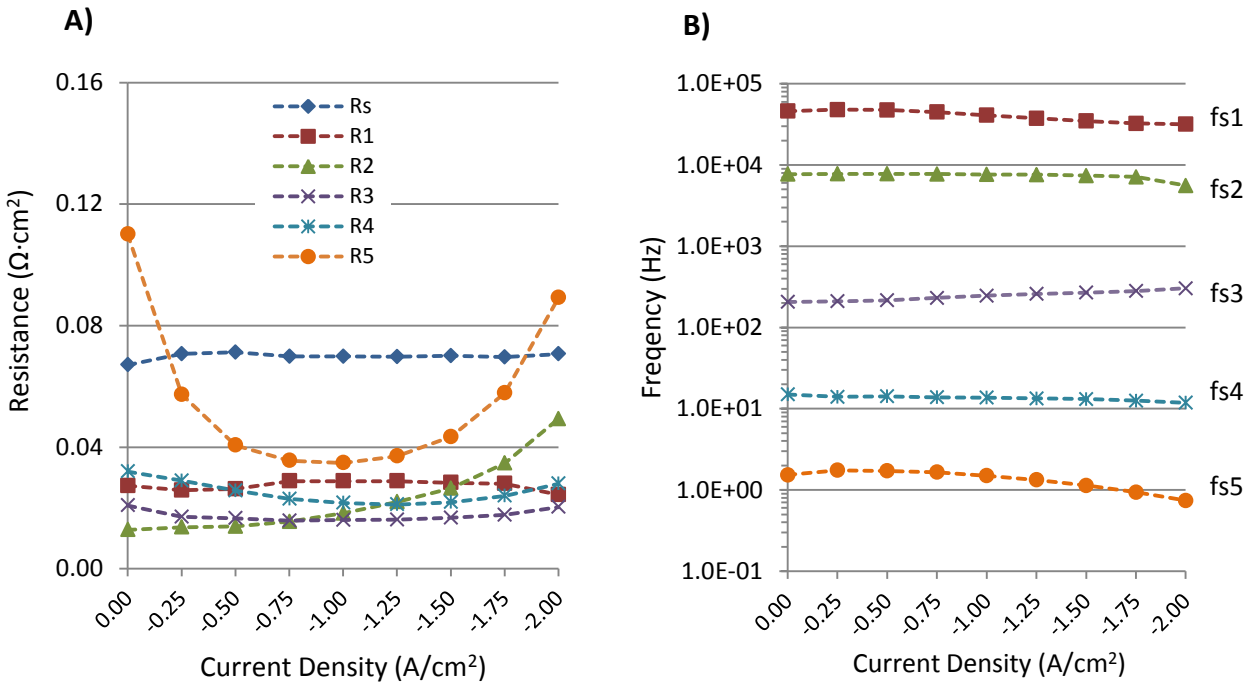

Figure 14 Breakdown of the impedance for cell T8 with current increased from 0 to the operating current density (-2.0 A/cm^2): A) resistance of each process; B) the summit frequency of each process. (Rs: the serial or ohmic resistance; R1 – R3: the oxygen ion transfer, Ni-YSZ and oxygen electrode TPB reaction resistance, respectively; R4: diffusion resistance and R5: conversion resistance. fs 1-5: the summit frequency of the corresponding processes.)

3.3 A consecutive impedance analysis for the overall test

The impedance of the entire test process were analysed in order to trace the evolution of each individual electrode process during the overall test. An example is given below, which shows the impedance analysis of cell T7 in 45 % H_2O +45 % CO_2 +10 % H_2.

Galvanostatic durability test:

As is shown in Figure 15, during the galvanostatic operation for cell T7 at -1.5 A/cm^2, there is a continuous increase in the height of the high frequency peak corresponding to the Ni-YSZ TPB reaction process. The peak position shifted first from ~ 6 KHz to ~ 10 KHz and then slightly decreased to 7 ~ 8 KHz. The peak (at a few hundred Hz) for LSCF-CGO TPB reaction was observed to be relatively stable. With respect to the conversion process, the peak was at a few Hz and the peak height increased during the durability test.

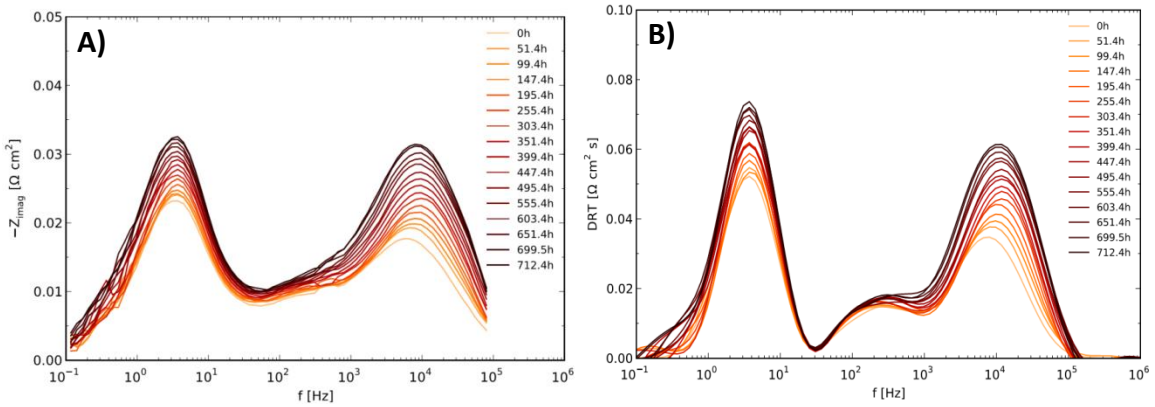

Figure 15 The imaginary part Z'' A) and DRT analysis B) of the impedance spectra of cell T7 during the galvanostatic operation at -1.5 A/cm^2

The breakdown results are shown in Figure 16. The serial resistance, the oxygen ion transfer resistance, the Ni-YSZ TPB reaction resistance and the conversion resistance showed a continuous increase with increasing the operation time. The LSCF-CGO TPB reaction resistance was relative stable. The corresponding summit frequencies of the processes were consistent with those obtained by the DRT analysis.

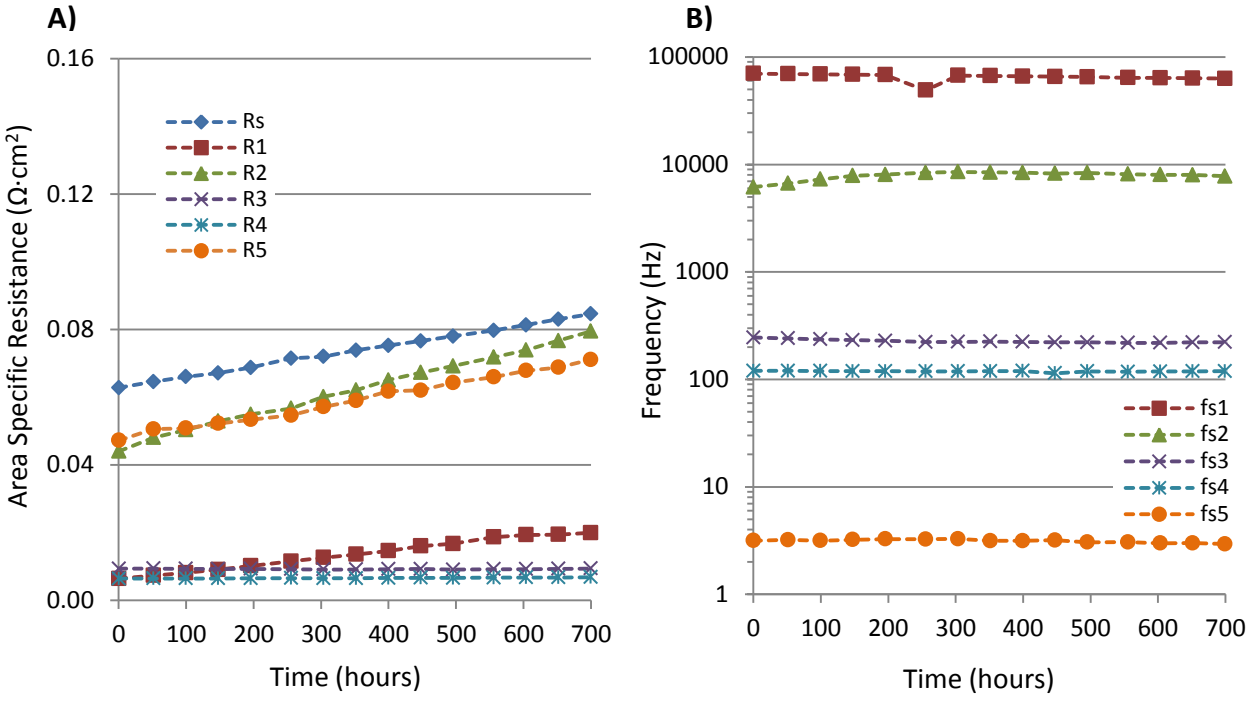

Figure 16 Breakdown of the impedance for cell T7 during galvanostatic durability test at -2.0 A/cm^2: A) resistance of each process; B) the summit frequency of each process. (Rs: the serial or ohmic resistance; R1 – R3: the oxygen ion transfer, Ni-YSZ and oxygen electrode TPB reaction resistance, respectively; R4: diffusion resistance and R5: conversion resistance. fs 1-5: the summit frequency of the corresponding processes.)

Decrease current to 0 after durability test:

After the long-term durability test, the current density was decreased from the operating current (-1.5A/cm^2) to 0. As is shown in Figure 17, the Ni-YSZ TPB reaction process showed a decrease in the peak height with the peak position shifted from 6 ~ 7 KHz upward to above 10 KHz, contrary to the increase in the peak height and decrease in the summit frequency with increasing current density before the durability test. A small increase was observed in the height of the peak at a few tens Hz to a few hundred Hz with decreasing the current. The height of the conversion peak at a few Hz first decreased slightly and then increased significantly with decreasing the current, opposite to the behavior observed before the durability test.

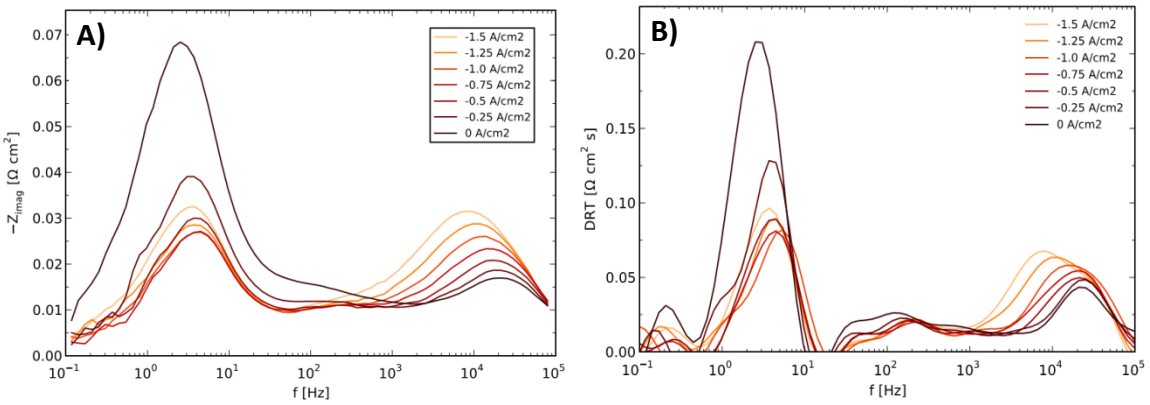

Figure 17 The imaginary part Z'' left) and DRT analysis right) of the impedance spectra of cell T7 with decreasing current from -1.5 A/cm^2 to 0 after durability test.

The breakdown results in Figure 18 showed a continuous decrease in the resistance for Ni-YSZ TPB reaction from 0.079 to 0.038 Ωcm^2 with the summit frequency increased from ~ 8 KHz to ~ 16 KHz when decreased the current density. The conversion resistance decreased slightly from 0.069 Ωcm^2 at -1.5 A/cm^2 to 0.056 Ωcm^2 at -1.0 A/cm^2 and then increase rapidly to 0.142 Ωcm^2 at OCV. The oxygen electrode showed a small increase in the TPB reaction resistance and the summit frequency was 200 – 300 Hz.

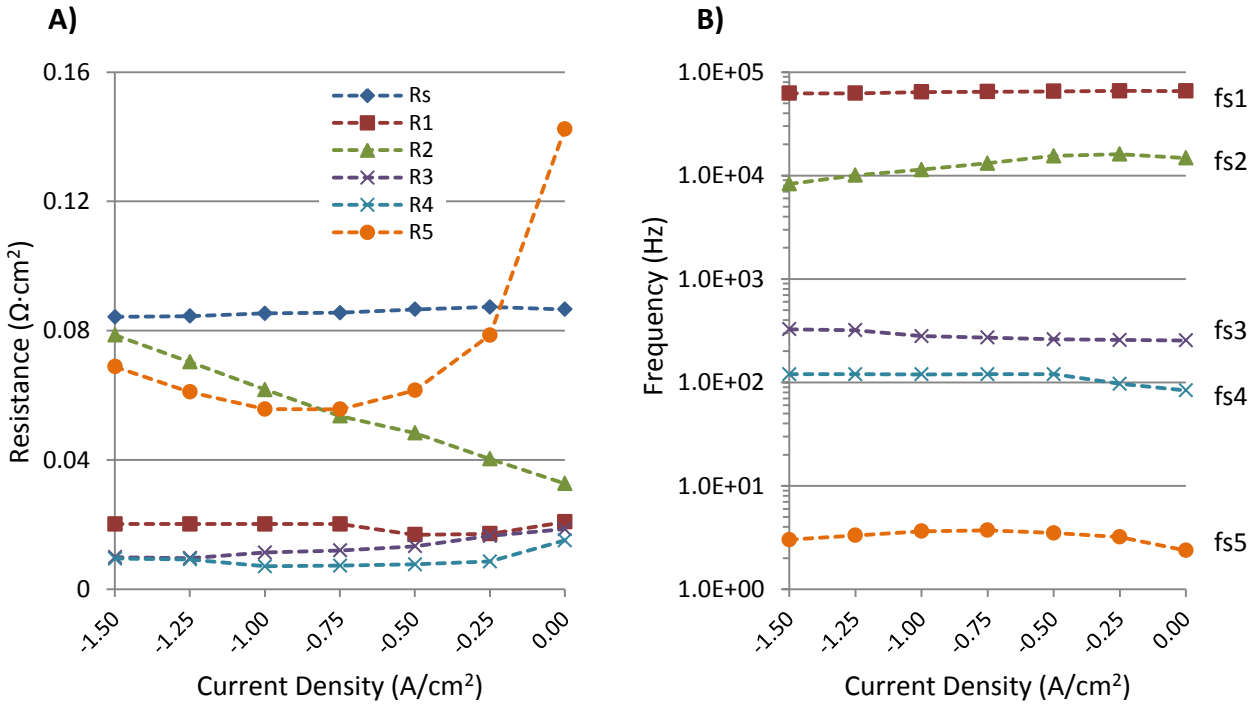

Figure 18 Breakdown of the impedance spectra with decreasing current from -1.5 A/cm^2 to 0 for cell T7 after long-term durability test. (Rs: the serial or ohmic resistance; R1 – R3: the oxygen ion transfer, Ni-YSZ

and oxygen electrode TPB reaction resistance, respectively; R4: diffusion resistance and R5: conversion resistance. fs 1-5: the summit frequency of the corresponding processes.)

A global view of the performance evolution for the individual processes:

Figure 19 shows the overall impedance analysis for cell T7 in 45 % H_2O +45 % CO_2 +10 % H_2, with increasing current from 0 to -1.5 A/cm^2, followed by galvanostatic durability test and finally decreasing current to OCV, as a summary of the above analysis. The resistance of each individual process is observed to change consecutively with changing operating conditions throughout the test. Because the ohmic heating of the LSCF cells was lower than that of the LSM cells, the operation temperature was increased by ~ 6 ^oC after increasing the electrolysis current |i| to 1.5 A/cm^2 in order to maintain the cell temperature the same as that of the LSM cell. The slightly better performance at 0 h during the durability test can be ascribed to this small increase in temperature. Throughout the whole test, the changes in the individual process of the cell were consistent to the results of the ADIS and DRT analysis. The test was started and ended in the same gas atmospheres (45 % H_2O + 45 % CO_2 + 10 % H_2 to the Ni-YSZ electrode and O_2 to LSCF-CGO electrode) at OCV condition. The break down results can be further confirmed by ADIS & DRT analysis for the impedances at OCV after durability test and before the durability test (See Appendix).

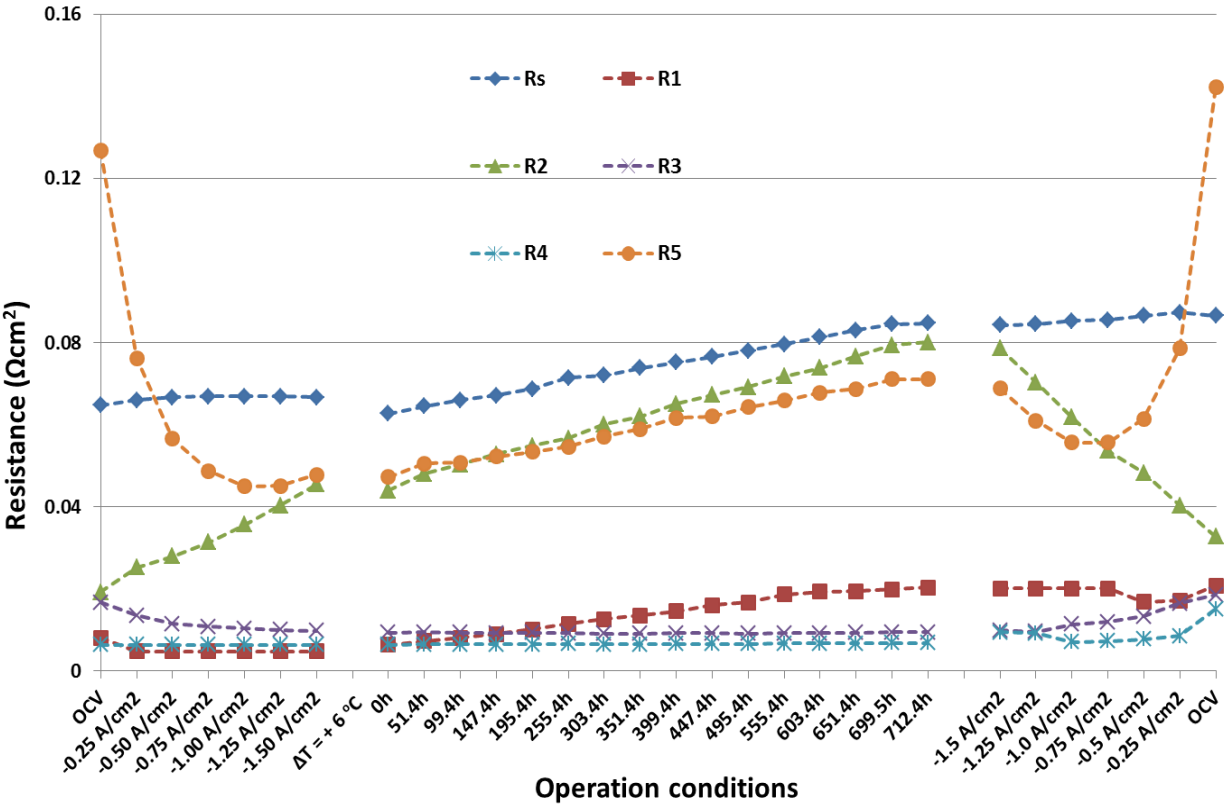

Figure 19 An overall view of the cell performance as a function of cell operation for cell T7: A) increasing current from 0 to the operating current density (-1.5 A/cm^2); B) long-term galvanostatic operation at -1.5 A/cm^2; C) decreasing current from -1.5 A/cm^2 to 0. (Rs: the serial or ohmic resistance; R1 – R3: the oxygen ion transfer, Ni-YSZ and oxygen electrode TPB reaction resistance, respectively; R4: diffusion resistance and R5: conversion resistance. fs 1-5: the summit frequency of the corresponding processes.)

4 Discussions

4.1 Ohmic, O ion transfer and oxygen electrode TPB resistance

Both the ohmic resistance (Rs) and O ion transfer resistance (R1) are temperature dependent, and as expected, they were stable during the gas variations on both the Ni-YSZ electrode and oxygen electrode. In addition, no direct relationship was observed between the ohmic resistance and the polarization on the cell without performing the durability test.

The Rs of LSCF cell T7 (0.06 Ωcm^2) is slightly lower than that of the LSM cell T2 (0.07 Ωcm^2). The resistance of a 20 μm thick LSM-YSZ electrode is estimated to be ~ 10^{-5} Ωcm^2 and that of a ~ 2 mm thick LSM current collector is only ~ 0.001 Ωcm^2. Considering the extra Rs contribution from CGO, the ~ 0.01 Ωcm^2 lower Rs of the LSCF cell T7 indicated an improved contact between the cell and the current collectors for the LSCF than the LSM cell. With increasing the electrolysis current for the cells in 45 % H_2O +45 % CO_2 +10 % H_2, a relative small increase in the Rs could be ascribed to the cooling nature of steam and CO_2 electrolysis.[5]

As a positive correlation is expected between the performance of the oxygen electrode and pO_2, the LSM-YSZ electrode showed much lower TPB resistance (R3) in O_2 than in air. For the LSCF cell, the difference was not as obvious as for the LSM cell, due to the very low resistance of the LSCF-CGO electrode and thus relatively higher error level of fitting.

4.2 Ni-YSZ TPB resistance

OCV performance: pH_2O

The dependence of the Ni-YSZ TPB reaction resistance on the partial pressure of hydrogen (pH_2) and steam (pH_2O) has been reported to be:[8]

$$\frac{1}{R_3} \propto \mathrm{pH_2}^{\mathrm{a}} \cdot \mathrm{pH_2O}^{\mathrm{b}} \qquad (1)$$

Considering the weak dependency (a ~ -0.15 to 0.26) on pH_2 (and controversy in the positive/negative value of 'a'),[8,9] the exponent 'a' was set to 0 for simplification. The dependency on pH_2O 'b' for the Ni-YSZ TPB reaction resistance has been reported to be 0.5 by M. Brown[8] and 0.68 by A. Utz[9].

In this study, based on the break down results for the cells in 4 %, 20 % and 50% H_2O with H_2 as balance, a dependency on pH_2O was observed to be b = 0.39 for the Ni-YSZ TPB reaction resistance of cell T7 (Figure 20). (Assuming an equivalent role between CO_2 and H_2 for the TPB reaction, the gas composition 45 % H_2O +45 % CO_2 +10 % H_2 equals 90 % H_2O + 10 % H_2 for Ni-YSZ TPB process, the exponent b ~ 0.37 will be obtained.)

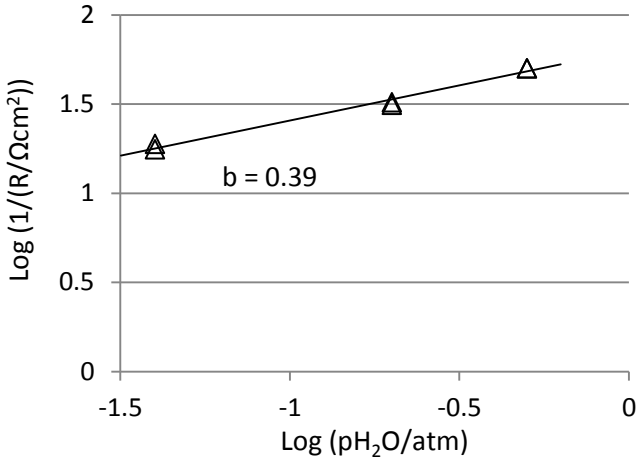

Figure 20 The Ni-YSZ TPB reaction resistance (R3) of cell T7 as a function of the steam partial pressure (pH_2O) in 4 %, 20 % and 50 % H_2O and balance H_2. 'b' is the dependency on pH_2O as defined in relation expression (1).

Polarization performance

The changes of the Ni-YSZ TPB reaction resistances (R3) with increasing electrolysis current in 45 % H_2O + 45 % CO_2 +10 % H_2 for cell T7, T8 and T9 (see Chapter 2 'Experimental' for details) are shown in Figure 21. The Ni-YSZ TPB reaction resistance (R3) increased from 0.019 Ωcm^2 at OCV to 0.045 Ωcm^2 at -1.5 A/cm^2 for cell T7, increased from 0.013 Ωcm^2 at OCV to 0.049 Ωcm^2 at -2.0 A/cm^2 for cell T8 and from 0.016 Ωcm^2 at OCV to 0.051 Ωcm^2 at -2.0 A/cm^2 for cell T9. With the electrolysis current increase, the molar ratio of steam decreases and could contributed to the increase of the Ni-YSZ TPB reaction resistance (R3), according to the relationship found between pH_2O and Ni-YSZ TPB resistance (Figure 20). Considering the complexity of the electrode reaction mechanisms and the focus of this work, it will not be further discussed here.

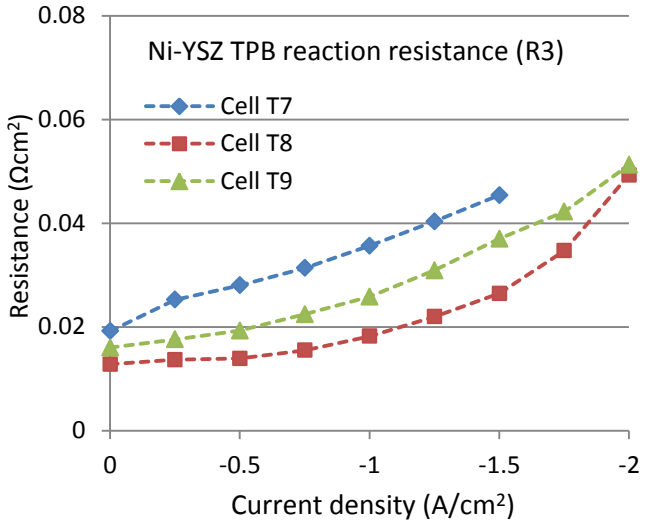

Figure 21 Ni-YSZ TPB reaction resistance (R3) of cell T7, T8 and T9 with increasing electrolysis current for the initial characterization. 25L/h 45 % H_2O + 45 % CO_2 +10 % H_2 was flown to the Ni-YSZ electrode for all the cells.

4.3 Diffusion resistance and conversion resistance

Conversion resistance (R5):

The conversion resistance was observed to decrease with changing the gas composition at OCV in the order of: 4 % H_2O + 96 % H_2 to 45 % H_2O +45 % CO_2 + 10 % H_2, 20 % H_2O + 80 % H_2 and 50 % H_2O + 50 % H_2, as shown in Figure 8 and Figure 10.

Using a continuous stirred tank reactor (CSTR) model, the impedance caused by gas conversion of the H_2O-H_2 mixtures in Ni-YSZ electrode can be expressed by the simplified equation:[10]

$$R_{conv} = \frac{RT}{4F^2 J_i}\left(\frac{1}{X_{i,H_2O}} + \frac{1}{X_{i,H_2}}\right) \qquad (2)$$

Where R_{conv} is the conversion resistance, R is the gas constant, T is the temperature in Kelvin, F is Faradays constant, J_i is the inlet area specific flow rate in mol/m^{2}s, X_i,H_2O and X_i,H_2 are the inlet mole fractions of steam and hydrogen. The above equation can be applied when the changes in the concentration during the AC perturbations of the impedance measurement is insignificant compared to the changes in the inlet concentrations.

Using a plug flow model, the conversion resistance for the H_2O-H_2 mixtures can be expressed in Eq. (3) with the same variables defined as above.[11] Equation (3) is valid when the current resulted concentration change is insignificant compared with the changes in the inlet concentrations.

$$R_{conv} = \frac{RT}{8F^2 J_i}\left(\frac{1}{X_{i,\,H_2O}} + \frac{1}{X_{i,\,H_2}}\right) \qquad (3)$$

For both models, the expressions indicate that the conversion resistance was the lowest when the ratio of H_2O to H_2 equals one and will increase with the ratio moving away from one. Therefore, the conversion resistance was observed to decrease with increasing the steam ratio from 4 % to 50 % for H_2O-H_2 mixtures at OCV. For CO_2-CO mixtures, the expressions of the conversion resistance in the Ni-YSZ electrode can be obtained by directly substituting the concentrations of H_2O and H_2 by that of CO_2 and CO and the same trend can be obtained for the conversion resistance with varying the concentrations. For the gas with the composition of 45 % H_2O +45 % CO_2 + 10 % H_2, the fraction of H_2O + CO_2 is 90 % and H_2 + CO is 10 %, so the conversion resistance was lower than that for 4 % H_2O + 96 % H_2 and higher than for 20 % H_2O + 80 % H_2. In addition, the lower conversion resistance for 4 % H_2O + 96 % H_2 (Ni-YSZ) – O_2 (oxygen electrode) than for – air (oxygen electrode) in Figure 8 and Figure 10 was due to a slightly higher faction of H_2O due to the leakage of O_2 into the Ni-YSZ electrode. It also lead to a higher conversion resistance in 45 % H_2O +45 % CO_2 + 10 % H_2 – O_2 (oxygen electrode) than – air (oxygen electrode).

Under electrolysis operations, the changes in the conversion resistance for cell T7, T8 and T9 in 45 % H_2O +45 % CO_2 + 10 % H_2 are shown in Figure 22. The outlet molar fraction of H_2O+ CO_2 decreases from 90 % at OCV to 50 % at -1.5 A/cm^2 and 36 % at -2.0 A/cm^2. Accordingly, the conversion resistance should decrease with increasing the electrolysis current and reach the minimum at -1.5 A/cm^2. The conversion resistance should increase symmetrically with further increasing the current. In general, the experimental results followed this trend, except that the minimum was observed at -1.0 A/cm^2 instead of -1.5 A/cm^2 and the value increased fast from -1.5 to -2.0 A/cm^2. The conversion resistance depends on the gas composition at the Ni-YSZ active electrode. The theoretical resistance is based on an ideal gas mixing for the bulk gas and the gas at the active electrode. However, the gas composition at Ni-YSZ active electrode could be altered due to gas diffusions.[5] Because the H_2O + CO_2 fraction was lower at active electrode than in bulk gas due to diffusion, the minimum conversion resistance would be observed at an electrolysis current lower than the theoretical value. At high electrolysis current / conversions, the faster increase in the conversion resistance was observed in the experiment, due to the increasing importance of the gas transportation. An example of significantly larger conversion resistances at -2.0 A/cm^2 due to gas diffusion limitations is shown for cell 4 and 5 in chapter 7 'Carbon deposition'. Besides, the flow rate could also play a role. There could be some

gas unavailable to the Ni-YSZ active electrode for electrolysis reactions due to the high flow rate, resulting in a larger conversion resistance than expected.

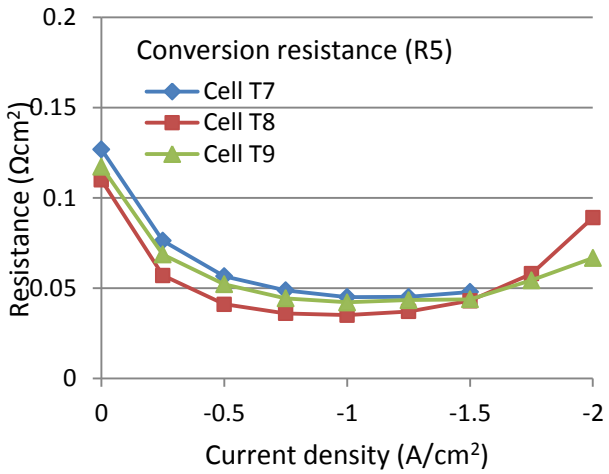

Figure 22 The conversion resistance (R5) as a function of electrolysis current for the cells (T7, T8 and T9) with 45 % H_2O +45 % CO_2 + 10 % H_2 flown to the Ni-YSZ electrode.

<u>Diffusion resistance (R4):</u>

The diffusion resistance of the Ni-YSZ electrode can be expressed as:[12]

$$R_{diff} = \frac{R^2T^2}{4F^2}\frac{l}{PD_{eff}}\left(\frac{1}{X_{B,H_2O}} + \frac{1}{X_{B,H_2}}\right) \qquad (4)$$

Where R_{diff} is the diffusion resistance, F is the Faraday constant, R is the gas constant, T is the temperature in Kelvin, l is the thickness of stagnant layer, P is the pressure, D_{eff} is the effective diffusion coefficient, X_{B,H_2O} and X_{B,H_2} denote respectively the molar fraction of H_2O and H_2 in the bulk gas.

According to the expressions of the diffusion and conversion resistance, the tendency for changes in the diffusion resistance should be similar to that in the conversion resistance with varying concentrations. Therefore, following the changes in conversion resistance, the diffusion resistance decreased in the gas atmosphere in the order of: 4 % H_2O + 96 % H_2 to 45 % H_2O +45 % CO_2 + 10 % H_2, 20 % H_2O + 80 % H_2 and 50 % H_2O + 50 % H_2, as was observed in Figure 8 and Figure 10.

Moreover, it has been observed that the diffusion resistance of cell T7 in Figure 10 is much lower than that of cell T2 as shown in Figure 8. This is mainly ascribed to the difference in the two types of test set-ups for the two cells. A porous Ni-YSZ ceramic current collector and gas distributor (Figure 23A) was used for cell T2

and metal meshes (Figure 23B) were used for cell T7. Apart from the channels for gas flow, there is approximately 50% of the electrode area covered directly by the ribs of the Ni-YSZ ceramic gas distributor. Even though the Ni-YSZ ceramic is very porous, it takes much longer routes for the gas diffusion from the bulk gas to the Ni-YSZ active electrode through the ribs than through the channels. This difference could be significant if one considers the large width of the ribs (~ 1 mm) compared to that of the Ni-YSZ support (~ 300 µm). For the cell tested using metal meshes as the gas distributor, diffusion takes place in the ~ 300 µm Ni-YSZ supports for the whole electrode area. The lower diffusion resistance was observed for all the cells tested using metal meshes compared with the cells with Ni-YSZ ceramic gas distributors.

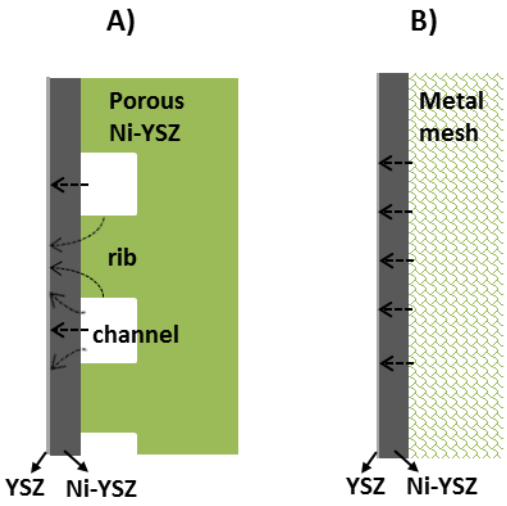

Figure 23 Gas diffusion routes toward the Ni-YSZ|YSZ interface for the cell tested with A) a Ni-YSZ ceramic and B) metal mesh current collector and gas distributor.

4.4 The comprehensive analysis of impedance spectra

A good fitting of the impedance with reasonable physical meanings requires that the same equivalent circuit can be applied to all the impedance measured for the same type of cell and similar electrode reactions. The physical meaning has to be found from the relations to the varied parameters in the study. The circuit elements should have specific physical meaning for each process. The exponent (n) of the constant phase element (RQ) should be constant for a specific process. In addition, the changes in the individual process should be consistent with the results of ADIS and DRT analysis. For the impedance analysis in this study, the above requirements were well satisfied. Furthermore, an example of the impedance analysis for the entire test process was given in Figure 19. The results indicate a good interpretation of the impedance both qualitatively and quantitatively. The comprehensive analysis of the impedance spectra provides a reliable way for the study of cell performance and durability.

5 Conclusions

The initial performances of solid oxide cells at OCV condition in various gas compositions were studied by impedance analysis. Based on the results of the ADIS and DRT analysis, the impedance were broken down into different individual processes by CNLS fitting, which consists of an inductance, an ohmic resistance, an oxygen ion transfer process, a Ni-YSZ TPB reaction process, an oxygen electrode TPB reaction process, a diffusion process and a conversion process. The Ni-YSZ TPB reaction resistance decreased with increasing steam fraction from 4 % to 20 % and 50 % for H_2O-H_2 mixtures. An exponent of 0.39 was observed for the dependency of the Ni-YSZ TPB resistance on pH_2O. The Ni-YSZ TPB resistance for 45 % H_2O + 45 % CO_2 + 10 % H_2 was close to that for 50 % H_2O +50 % H_2. The conversion resistance decreased with changing gas composition from 4 % H_2O + 96 % H_2 to 45 % H_2O + 45 % CO_2 + 10 % H_2, 20 % H_2O + 80 % H_2 and 50 % H_2O + 50 % H_2.

The cell performance in 45 % H_2O + 45 % CO_2 + 10 % H_2 as a function of electrolysis current density was also studied by impedance analysis. The Ni-YSZ TPB reaction resistance was observed to increase with increasing the electrolysis current. Apart from the electrode polarization, the change in gas composition due to conversion could also contribute to the increase in TPB reaction resistance. The conversion resistance first decreased and then increased with electrolysis current increase. The conversion resistance can be altered to some extent by gas diffusions.

The electrochemical impedance was measured for the overall test of co-electrolysis of steam and CO_2 via a solid oxide cell which has a LSCF-CGO oxygen electrode. The impedance spectra were analysed by ADIS/DRT/fitting methods in order to investigate the degradation of individual processes. The performance degradation was mainly ascribed to the increase in the ohmic resistance, the oxygen ion interfacial transfer resistance and the Ni-YSZ TPB reaction resistance.

References

1. S. D. Ebbesen, C. Graves, and M. Mogensen, *Int. J. Green Energy*, **6**, 646–660 (2009).

2. S. D. Ebbesen, C. Graves, A. Hauch, S. H. Jensen, and M. Mogensen, *J. Electrochem. Soc.*, **157**, B1419–B1429 (2010).

3. R. Barfod et al., *J. Electrochem. Soc.*, **154**, B371 (2007).

4. R. Barfod, a. Hagen, S. Ramousse, P. V. Hendriksen, and M. Mogensen, *Fuel Cells*, **6**, 141–145 (2006)

5. S. D. Ebbesen and M. Mogensen, *ECS Trans.*, **50**, 167–182 (2013).

6. M. J. Jørgensen and M. Mogensen, *J. Electrochem. Soc.*, **148**, A433–A442 (2001).

7. S. H. Jensen et al., *J. Electrochem. Soc.*, **154**, B1325 (2007).

8. M. Brown, S. Primdahl, and M. Mogensen, *J. Electrochem. Soc.*, **147**, 475 (2000).

9. A. Utz, H. Störmer, A. Leonide, A. Weber, and E. Ivers-Tiffée, *J. Electrochem. Soc.*, **157**, B920 (2010).

10. S. Primdahl and M. Mogensen, *J. Electrochem. Soc.*, **145**, 2431–2438 (1998).

11. S. H. Jensen, A. Hauch, P. V. Hendriksen, and M. Mogensen, *J. Electrochem. Soc.*, **156**, B757 (2009).

12. S. Primdahl and M. Mogensen, *J. Electrochem. Soc.*, **146**, 2827–2833 (1999).

Appendix. Extra results of the Impedance analysis of the SOCs

Cell T2: OCV before

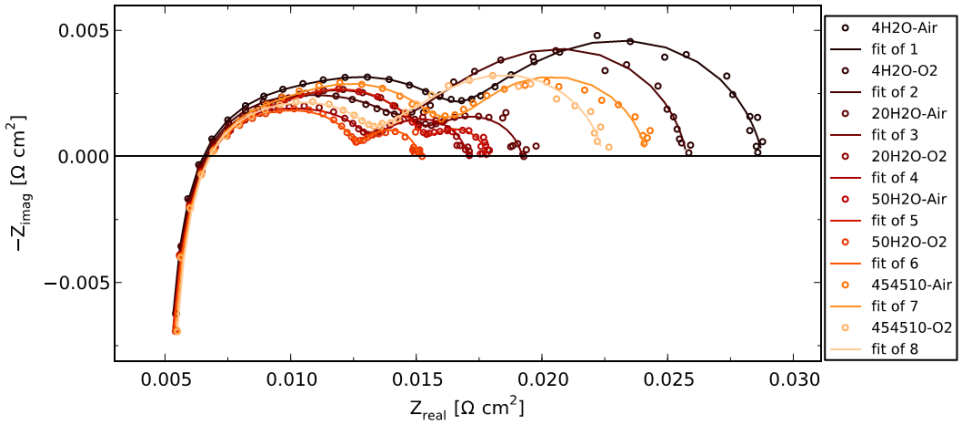

Figure A3-1: Fitting of the impedance spectra measured at OCV for initial performance characterization of LSM cell T2 at ~ 850 °C: 4 % H_2O + 96 % H_2, 20 % H_2O + 80 % H_2, 50 % H_2O + 50 % H_2 or 45 % H_2O + 45 % CO_2 +10 % H_2 were flown to the Ni-YSZ electrode; air or O_2 was flown to the oxygen electrode.

Cell T7: OCV before

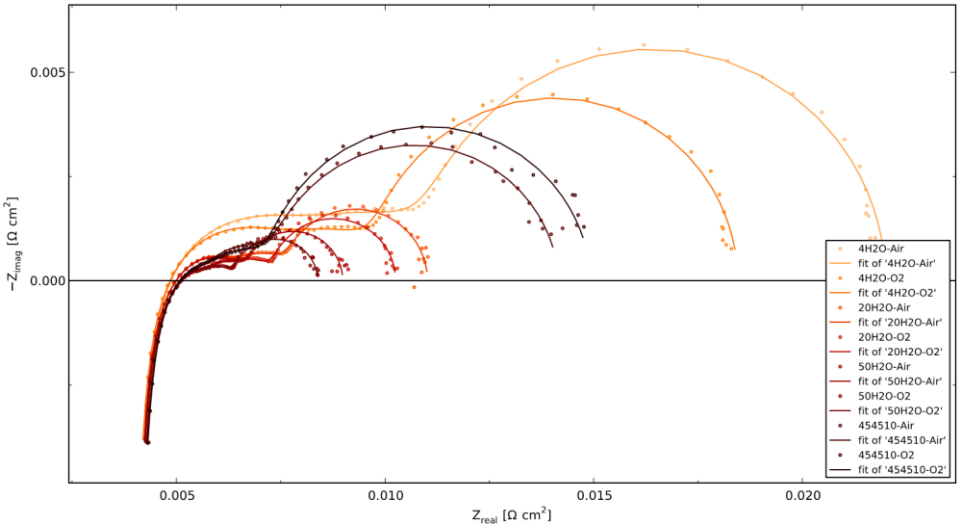

Figure A3-2: Fitting of the impedance spectra measured at OCV for initial performance characterization of LSCF cell T7 at ~ 850 °C: 4 % H_2O + 96 % H_2, 20 % H_2O + 80 % H_2, 50 % H_2O + 50 % H_2 or 45 % H_2O + 45 % CO_2 +10 % H_2 were flown to the Ni-YSZ electrode; air or O_2 was flown to the oxygen electrode.

Cell T7: OCV_ After vs. OCV_Before

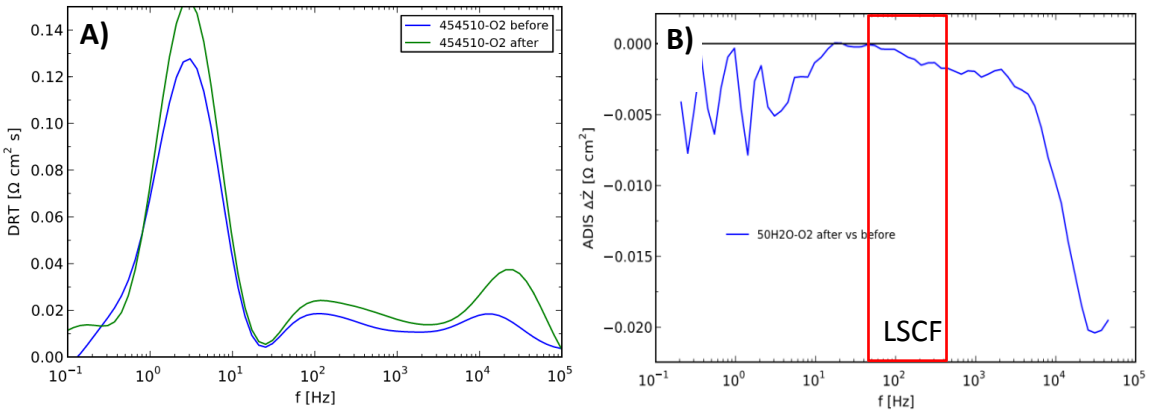

Figure A3-3. The comparisons of the impedance measured at OCV and ~ 850 °C for cell T7 before and after long-term durability test. A) DRT analysis for the cell with 45 % H_2O + 45 % CO_2 +10 % H_2 flown to the Ni-YSZ electrode and O_2 flown to the oxygen electrode; B) ADIS analysis for the cell in 50 % H_2O +50 % H_2 and O_2 before and after durability test.

The DRT and ADIS analysis showed the most degradation occurred at the frequency above 6 KHz, which was ascribed to the Ni-YSZ TPB reaction and the oxygen ion transfer processes. A small degradation was also observed at a few hundred Hz, corresponding to the LSCF-CGO TPB reaction process.

Cell T4: OCV before

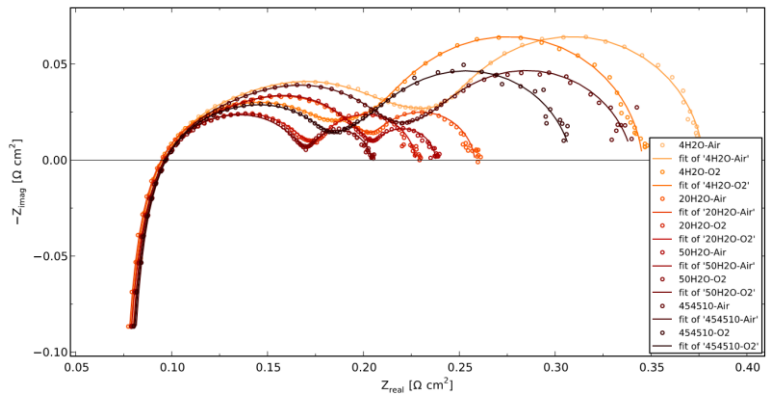

Figure A3-4: Fitting of the impedance spectra measured for cell T4 at OCV for initial performance characterization at ~ 850 °C: 4 % H_2O + 96 % H_2, 20 % H_2O + 80 % H_2, 50 % H_2O + 50 % H_2 or 45 % H_2O + 45 % CO_2 +10 % H_2 were flown to the Ni-YSZ electrode; air or O_2 was flown to the oxygen electrode.

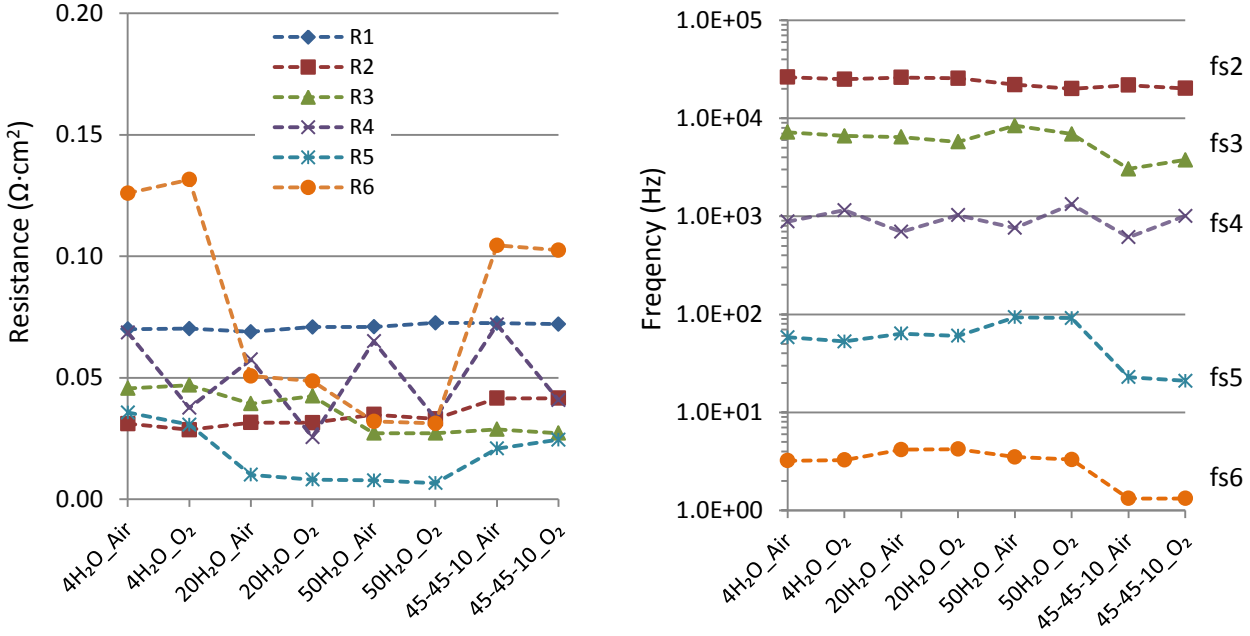

Figure A3-5. Breakdown of the impedance for cell T4 at OCV in various gas compositions: left) resistance of each process; B) the summit frequency of each process. The xH_2O_Air (or O_2) represents x % H_2O in H_2 was flown to the Ni-YSZ electrode and air (or O_2) was flown to oxygen electrode; 45-45-10_Air (O_2) represents that 45 % H_2O + 45 % CO_2 + 10 % H_2 was flown to Ni-YSZ and air (O_2) to oxygen electrode. (Rs: the serial or ohmic resistance; R1 – R3: the oxygen ion transfer, Ni-YSZ and oxygen electrode TPB reaction resistance, respectively; R4: diffusion resistance and R5: conversion resistance. fs 1-5: the summit frequency of the corresponding processes.)

<u>Cell T6: Gas variations at OCV before test</u>

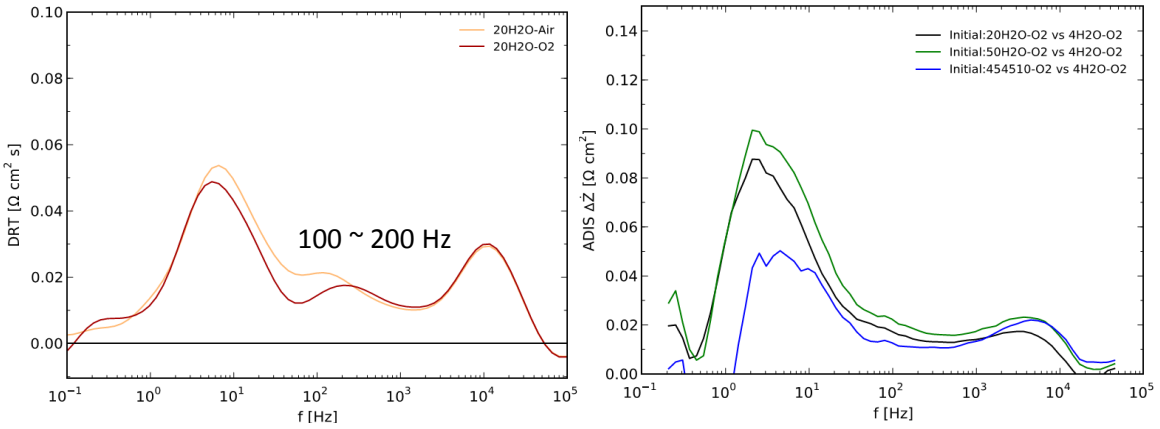

Figure A3-6. Initial performance characterization for cell T6 at OCV by impedance analysis: A) DRT analysis by shifting the gas composition in LSCF-CGO between air and O2 with 20 % H_2O + 80 % H_2 flow to Ni-YSZ; B)

DRT analysis of the cell performance with 20 % H_2O + 80 % H_2, 50 % H_2O + 50 % H_2 or 45 % H_2O + 45 % CO_2 + 10 % H_2 flown to Ni-YSZ in comparison to 4 % H_2O + 96 % H_2; constant O_2 was flown to LSCF-CGO. The LSCF-CGO oxygen electrode showed a characteristic frequency of 100 ~ 200 Hz.

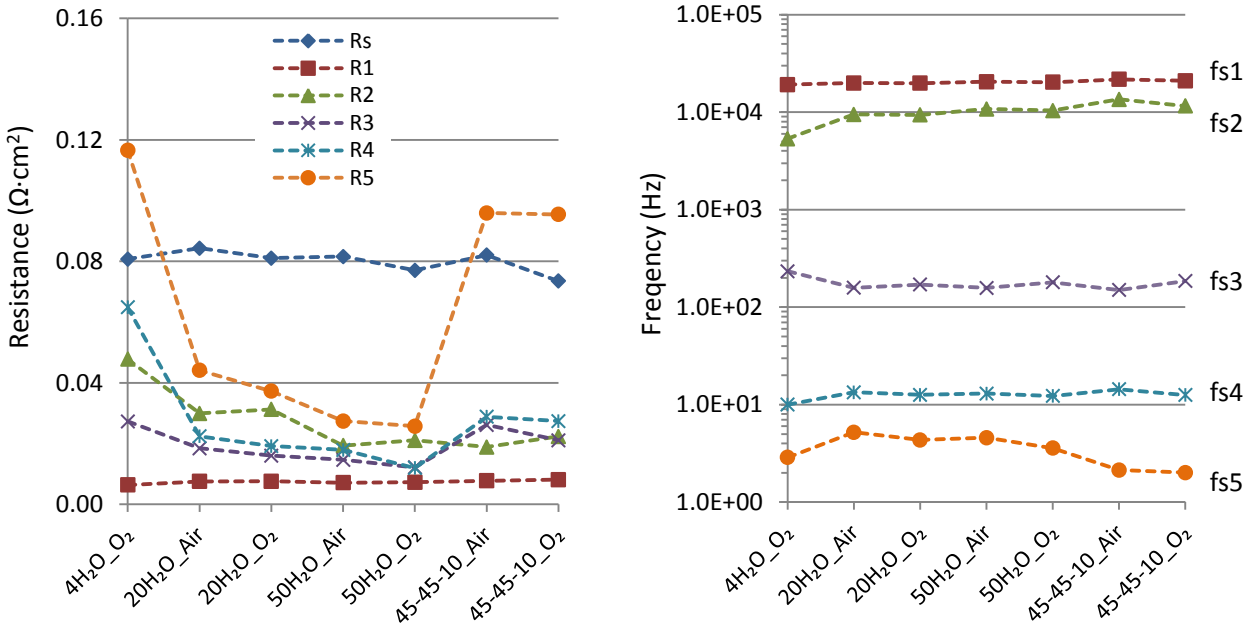

Figure A3-7. Breakdown of the impedance for cell T6 at OCV in various gas compositions: A) resistance of each process; B) the summit frequency of each process. The xH_2O_Air (or O_2) represents x % H_2O in H_2 was flown to the Ni-YSZ electrode and air (or O_2) was flown to oxygen electrode; 45-45-10_Air (O_2) represents that 45 % H_2O + 45 % CO_2 + 10 % H_2 was flown to Ni-YSZ and air (O_2) to oxygen electrode. (Rs: the serial or ohmic resistance; R1 – R3: the oxygen ion transfer, Ni-YSZ and oxygen electrode TPB reaction resistance, respectively; R4: diffusion resistance and R5: conversion resistance. fs 1-5: the summit frequency of the corresponding processes.)

Chapter 4 Durability of SOECs for Co-Electrolysis of H_2O and CO_2 under High Current Densities: I. Electrochemical Analysis

1 Introduction

Over the past a few years, there has been an increasing demand on sustainable energy because of high prices of fossil fuels and severe environmental problems such as air pollutions and CO_2 emissions. Solid oxide electrolysis cells (SOECs) [1–12] is a very promising technology for hydrogen and syngas (CO + H_2) production use the industrial waste heat and excess electricity from intermittent energy sources. The co-electrolysis of steam and CO_2 ($H_2O \rightarrow H_2 + ½ O_2$; $CO_2 \rightarrow CO + ½ O_2$) is of special interest, because the syngas (H_2 + CO) is produced, [8,13–16] which can be further converted to various synthesis fuels [1,13,17,18]. Synthesis fuel production using CO_2 captured from atmosphere or at plants would enable a carbon-neutral fuel cycle. Another advantage is the existing energy infrastructure can be still used for fuel storage and transportation without major modifications. Further, in combination with wind turbines and solar cells, etc.,[13,17] fuel production via SOECs could provide a promising solution to the storage of the fluctuating renewable energy and make the best use of the spare capacity.

Performance and durability are critical issues for the commercialization of SOECs for fuel production. Although the high initial performance of the state-of-the-art solid oxide cells has been demonstrated, [3,19] the long term stability (e.g. 5 years) of the SOECs under operation is still a major problem. It is therefore of great significance to investigate the mechanism of SOECs degradation. It has been reported that impurities (S or Si, Al, etc.)[15,20,21] from raw materials of the cell, feed gas or sealing, play a major role in the Ni-YSZ electrode degradation at low current densities (below -1.0 A/cm^2). The impurities were thought to decrease the amount of the reaction sites by blocking the triple phase boundary (TPBs) of the Ni-YSZ electrode. Minor or no degradation has been demonstrated by cleaning the feed gas to the Ni-YSZ electrode.[22] At higher current densities (above -1.0 A/cm^2), additional YSZ electrolyte degradation and/or oxygen electrode delamination have been observed.[23–27] The proposed hypothesis for the mechanism of this degradation is the buildup of oxygen partial pressure at the electrolyte and anode interface due to a large anodic polarization.[28,29]

Most of the durability tests were performed at relative low current densities. With the degradation of the electrodes, the SOEC cells will sooner or later reach a significant higher polarization than that of the initial. However, investigation on the further degradation (evolution, mechanism, lifetime, etc.) requires very long test durations. For a cell running under more harsh conditions, e.g. higher current densities and conversions, the degradation is expected to be accelerated, which would facilitate the durability study by providing sufficient information within shorted period. In addition, operating at high current densities (and conversions) will make fuel production using SOECs more cost-competitive.[1]

More important, electrochemical performance monitored in situ and its interpretation, detailed analysis of the post-test microstructure and composition, as well as the correlation between the two and the operation condition, which are essential for a full disclosure of the evolution and mechanism of SOECs degradation, are still missing. Therefore, in this work, a series of long term co-electrolysis tests was performed at very high current densities (-1.5 and -2.0 A/cm^2) for the systematic investigation of the cell durability. The post-test cell microstructures were examined by high-resolution scanning electron microscopy (HRSEM) and transmission electron microscopy (HRTEM) equipped with energy-dispersive X-ray spectroscopy (EDS). The in situ measured electrochemical impedance spectra (EIS) were carefully analyzed and broken down into individual contributions of electrode processes. Thus the degradation on each cell component, especially the Ni-YSZ electrode, can be analyzed quantitatively. The changes in polarization resistance (Rp) were then correlated with the microstructural change and the operation conditions such as current density and over-potential.

2 Experimental

2.1 Solid oxide cells

Two types of planar solid oxide cells developed at DTU Energy Conversion[30–33] were used for the durability tests. One type of the cells has a configuration of ~ 300 µm Ni-YSZ support | ~ 15 µm Ni-YSZ active electrode | ~ 10 µm YSZ electrolyte | ~ 15 µm LSM-YSZ electrode, which will be referred to as the 'LSM cell' in the latter text. The other type of cells has a configuration of ~ 300 µm Ni-YSZ support | ~ 15 µm Ni-YSZ active electrode | ~ 10 µm YSZ electrolyte | ~ 5 µm CGO | ~ 15 µm LSCF-YSZ electrode, which will be mentioned as the 'LSCF cell'.

2.2 SOECs test: set-up and procedures

2.2.1 Normal test and clean test

The tests can be divided into two categories, the 'normal test' and the 'clean test', according to the types of the set-up and gas processing. For the normal tests, albite glass bars were used as sealing on the both electrodes and the impurities (Si, etc.) were expected to result in contaminations to the TPBs of Ni-YSZ. Ni-YSZ or LSM cermet was used respectively on the Ni-YSZ or oxygen electrode side as the gas distributor/current collector. Gas CO_2 and H_2 as received (with S, etc. impurities of ~ppb) were flown to the cell directly. For the clean test, metal frame was used as the sealing on both electrodes.[13,15] Ni mesh was used as the contact on the Ni-YSZ electrode and Pt mesh for oxygen electrode. CO_2 and H_2 were cleaned by a gas cleaner to remove the impurities before supplied to the cell. All the cells were heated up to 1000 ^oC and kept for 2 hours for sealing at the beginning. Then, 20 L/h 9 % H_2 in N_2 was flown to the cell for 2 hours to obtain Ni-YSZ electrode by the reduction of NiO-YSZ. Afterwards, 25 L/h 4 % H_2O + 96 % H_2 was flown to Ni-YSZ and 140 L/h Air was flown to oxygen electrode for 1 hour. Finally, the cell was cooled down to 850 ^oC for initial performance study.

2.2.2 Initial cell performance characterization

The initial cell performance was characterized by electrochemical measurement with gas variation on each electrode at 850 ^oC (and 800 ^oC & 750 ^oC for some cells). The typical gas atmospheres used for gas variation are: 4 % H_2O + 96 % H_2, 20 % H_2O + 80 % H_2, 50 % H_2O + 50 % H_2 and 45 % H_2O + 45 % CO_2 +10 % H_2 to the Ni-YSZ electrode, while Air and O_2 to the oxygen electrode. For each gas atmosphere, EIS measurement was performed at OCV 15 minutes after changing the atmosphere. Then, i-V curves were recorded with the cell voltage decreasing from OCV down to 700 mV or 650 mV in fuel cell mode, and/or increasing up to 1250 mV in electrolysis mode.

2.2.3 Galvanostatic durability test

The cells were then operated at 850 ^oC with 45 % H_2O + 45 % CO_2 +10 % H_2 flown to Ni-YSZ and O_2 to oxygen electrode. The current density was increased by steps to the value at which the galvanostatic test is intended to operate (-1.5 or -2.0 A/cm^2). Impedance was recorded at each step after a hold-time of 15 min. For the LSM cells, after increasing current density from 0 to -1.5 or -2.0 A/cm^2, the cell temperature (T_center probe) could increase to ~ 865 ^oC due to ohmic heating of the cell. For the LSCF cells, the temperature increase was lower due to the lower cell resistance than LSM cells; thus, in order to minimize the contribution of the temperature difference to the cell performance difference, the cell temperature of LSCF cells was lift up to ~ 865 ^oC by control of the furnace temperature. During the long term galvanostatic operation, cell voltage was recorded every 2 minutes and EIS was recorded periodically, e.g. every 6 hours. With the cell degradation, the cell voltage could increase by a few hundred millivolts. The tests were

stopped when the duration reaching ~ 700 hours or the cell voltage reaching ~ 2000 mV. Due to the cell voltage increase, the cell temperature increased to ~ 875 ^{o}C finally. After the durability test, the current density was stepped down to zero with EIS recorded. For some cells after test, gas variation and EIS measurement were performed at OCV again. The cells were then cooled down with H_2 (> 630 ^{o}C) and 9 % H_2 in N_2 (< 630 ^{o}C) flown to the Ni-YSZ electrode.

Table 2 Set-up for the Long Term Durability Tests

Cell Nr.	Current Density (A/cm^2)	Oxygen Electrode	Current Collector & Sealing	Gas Clean
T1	-1.5	LSM-YSZ	Ni-YSZ/LSM; Glass Bar	No
T2	-2.0	LSM-YSZ	Ni-YSZ/LSM; Glass Bar	No
T3	-2.0	LSM-YSZ	Ni-YSZ/LSM; Glass Bar	No
T4	-2.0	LSM-YSZ	Ni-YSZ/LSM; Glass Bar	No
T5	-2.0	LSM-YSZ	Metal Mesh; Frame	Yes
T6	-1.5	LSCF-CGO	Ni-YSZ/LSM; Glass Bar	No
T7	-1.5	LSCF-CGO	Metal Mesh; Frame	Yes
T8	-2.0	LSCF-CGO	Ni-YSZ/LSM; Glass Bar	No
T9	-2.0	LSCF-CGO	Metal Mesh; Frame	Yes

25 L/h 45 % CO_2 + 45 % H_2O + 10 % H_2 to the Ni-YSZ electrode and pure O_2 to the oxygen electrode; Initial cell temperature at ~ 865 ^{o}C under operation and increased to ~ 875 ^{o}C due to degradation;

2.3 Analysis of the Electrochemical Impedance

2.3.1 Gas variation for each electrode

The gas atmosphere was varied only for one electrode at one time and the atmosphere of the other electrode was fixed. For gas variations on the Ni-YSZ electrode, impedance was measured with 4 % H_2O + 96 % H_2, 20 % H_2O + 80 % H_2 50 % H_2O + 50 % H_2 and then 45 % H_2O + 45 % CO_2 + 10 % H_2 flown to the Ni-YSZ electrode, while gas composition to the LSM-YSZ electrode was kept constant. Because the electrochemical processes affected by the atmosphere change were related only to the electrode on which the gas variation was performed, the processes corresponding to the LSM-YSZ electrode should keep constant and the change in impedance can be ascribed to the Ni-YSZ electrode only. For gas variations on the LSM-YSZ electrode, impedance was measured with air or O_2 flown to LSM-YSZ and gas condition at Ni-YSZ was kept constant. Gas variations were applied to the LSCF cells in the same way.

2.3.2 Analysis of the Difference in Impedance (ADIS) and distribution of relaxation times (DRT)

The difference in the impedance measured for the cell at different operation conditions (gas composition, current density, etc.) was analyzed in order to identify the characteristic frequency of the electrode process that affected by the change in conditions. According to equation (1),[34] the ADIS was calculated from the real part of the impedance measured at two different operating conditions. Impedance measured at condition I was regarded as the reference for condition II. For gas variations on the Ni-YSZ electrode, 4 % H_2O + 96 % H_2 or 20 % H_2O + 80 % H_2 was usually set as condition I (reference), while 50 % H_2O + 50 % H_2 and 45 % H_2O + 45 % CO_2 +10 % H_2 was used as condition II. Air and O_2 were usually used for gas variations on the LSM-YSZ electrode. For the current density increase, OCV was used as condition I (reference) and current density i as condition II.

$$\frac{\partial Z'(f)}{\partial \ln(f)} = \frac{(Z'(f_{n+1})_{II} - Z'(f_{n-1})_{II}) - (Z'(f_{n+1})_{I} - Z'(f_{n-1})_{I})}{ln(f_{n+1}) - ln(f_{n-1})} \qquad (1)$$

Via ADIS and DRT analysis[34,35]of the impedance spectra recorded during gas variation on one electrode, the characteristic frequency of individual process corresponding to this electrode can be identified. Furthermore, the relative size of the polarization resistance of the electrode processes within various atmospheres can be estimated. This information was then used for the break-down of the impedance for the cell at OCV before and after durability test. ADIS & DRT analysis was also performed for the current increasing/decreasing and more importantly, the galvanostatic operations. Combining with the electrode process and the characteristic frequency identified by gas variations at OCV, it enabled assignment of the increase/decrease in resistance to a specific electrode process as a function of current densities and durations.

2.3.3 CNLS Fitting of the impedance

In order to break down the total impedance into contributions from individual electrode processes, the impedance spectra need to be fitted to an equivalent circuit with proper physical meaning. The equivalent circuit used for the fitting of the 'LSM cell' was same as the previously developed model for the Ni-YSZ based solid oxide cells at DTU Energy Conversion (former Risø-DTU). It consists of an inductance 'L', a series resistance 'Rs' and five (RQ) elements[36–38]: L - Rs - $(RQ)_1$ - $(RQ)_2$ - $(RQ)_3$ - $(RQ)_4$ - $(RQ)_5$. (RQ) elements 1 to 5 represent respectively the high frequency O^{2-} transfer, the TPB reactions at the Ni-YSZ electrode, the TPB reactions at the LSM-YSZ electrode, the gas diffusion and the gas conversion which are mainly at the Ni-YSZ electrode. The value of 'n', the exponent of the constant phase element, should be kept constant for a specific electrode process. According to the previous work at DTU Energy Conversion,[36,37] n values of the element $(RQ)_1$ to $(RQ)_5$ were fixed respectively at 0.68, 0.8, 0.87, 0.75 and 0.9 ~ 1 for fitting the impedance

throughout the durability test. The initial guess of fitting parameters (resistance & frequency) can be facilitated by the previous ADIS & DRT analysis, from which the electrode processes, the characteristic frequency and the relative size of the resistances were estimated. The above information was also used for verification of the fitting results. Accordingly, after repeating many rounds of fitting-feedback-fitting, individual contributions of the electrode processes were identified. The evolution of electrode process was then correlated with the operation condition as well as the change in microstructure/composition of the cell component.

In order to facilitate the comparison between the two types of cells (and for a better consistency), the same equivalent circuit as described above was used for the impedance fitting of the LSCF cells. Due to a significant better ionic conductivity of the LSCF-CGO electrode, the O^{2-} transfer resistance (R2) of the LSCF cells could be much smaller. Because of the mixed ionic and electronic conductors of LSCF, the TPBs could be expanded significantly, leading to a much smaller R3 value for LSCF cells at same test conditions. Regarding to the n values, assuming the nature of the related electrode processes was not totally altered and the increase of reaction sites (TPB length) accounted for the better oxygen electrode performance, the same n values were used for the LSCF cells as for the LSM cells.

3 Results – Electrochemical analysis

3.1 Characterization of the initial cell performance at OCV by EIS

3.1.1 LSM cells

Table 3 EIS fitting results for the LSM cells at OCV before test (45 % H_2O + 45 % CO_2 +10 % H_2) at ~ 850 ^oC

Cell Nr.	Rs ($\Omega\cdot cm^2$)	R1 ($\Omega\cdot cm^2$)	fs1 (Hz)	R2 ($\Omega\cdot cm^2$)	fs2 (Hz)	R3 ($\Omega\cdot cm^2$)	fs3 (Hz)	R4 ($\Omega\cdot cm^2$)	fs4 (Hz)	R5 ($\Omega\cdot cm^2$)	fs5 (Hz)	Error chi_sq
T1	0.067	0.061	29628	0.026	3197	0.039	1205	0.051	17	0.122	1.2	8.8E-06
T2	0.074	0.040	29502	0.056	4860	0.042	814	0.037	20	0.109	1.9	9.6E-06
T3	0.069	0.052	33238	0.045	3195	0.027	900	0.040	10	0.097	1.3	3.2E-06
T4	0.072	0.042	20186	0.027	3757	0.041	1010	0.025	21	0.103	1.3	8.9E-06
T5	0.072	0.031	24448	0.031	6519	0.046	782	0.009	95	0.111	2.5	4.6E-06

Rs: ohmic resistance; R1: interfacial O^{2-} transfer resistance; R2: Ni-YSZ TPB reaction resistance; R3: oxygen electrode TPB reaction resistance; R4: diffusion resistance; R5: conversion resistance. fs1 – fs5: the corresponding summit frequencies to the above processes.

Table 3 shows the breakdown of the impedance spectra measured at OCV for the initial characterization of the LSM cells. The serial resistance (Rs) for all the cells was in the range of 0.067 – 0.074 Ω·cm^2. For the oxygen ion interfacial transfer process, the largest resistance (R1) was observed for cell T1 (0.061 Ω·cm^2) and the smallest was observed for cell T5 (0.031 Ω·cm^2). Cell T1 (0.026 Ω·cm^2) and cell T4 (0.027 Ω·cm^2) showed relative lower resistance of the Ni-YSZ TPB reaction (R2) and cell T2 (0.056 Ω·cm^2) showed the largest one. The TPB reaction resistance of the LSM-YSZ electrode (R3) was 0.027 – 0.046 Ω·cm^2. The diffusion resistance (R4) was below 0.01 Ω·cm^2 for cell T5 using a metal mesh contact, which was significantly smaller than that of cell T1 – T4 using the Ni-YSZ contact. The conversion resistance of the cells was 0.10 – 0.12 Ω·cm^2. The summit frequencies of the electrochemical processes (diffusion and conversion process not included) in a descending order were: 20 K – 33 K Hz for the oxygen ion interfacial transfer process, 3.2K – 6.5K Hz for the Ni-YSZ TPB reaction process and 780 – 1200 Hz for the LSM-YSZ TPB reaction process.[36–38] The summit frequency of the gas diffusion process was 10 – 21 Hz for all the other cells except T5 (metal mesh contact), which showed a higher summit frequency of 95 Hz. A summit frequency of the gas conversion process was found to be 1.2 – 2.5 Hz for all the cells.

3.1.2 LSCF cells

Table 4 EIS fitting results for the LSCF cells at OCV before test (45 % H_2O + 45 % CO_2 +10 % H_2) at ~ 850 ^oC

Cell Nr.	Rs (Ω·cm^2)	R1 (Ω·cm^2)	fs1 (Hz)	R2 (Ω·cm^2)	fs2 (Hz)	R3 (Ω·cm^2)	fs3 (Hz)	R4 (Ω·cm^2)	fs4 (Hz)	R5 (Ω·cm^2)	fs5 (Hz)	Error chi_sq
T6	0.073	0.013	46412	0.018	8220	0.020	238	0.033	12	0.093	1.9	6.6E-06
T7	0.061	0.012	55935	0.019	8217	0.015	201	0.010	90	0.123	2.4	4.0E-06
T8	0.067	0.027	46155	0.013	7703	0.021	207	0.032	15	0.110	1.5	2.8E-06
T9	0.071	0.005	26300	0.025	8642	0.020	135	0.002	99	0.107	2.5	1.9E-06

Rs: ohmic resistance; R1: interfacial O^{2-} transfer resistance; R2: Ni-YSZ TPB reaction resistance; R3: oxygen electrode TPB reaction resistance; R4: diffusion resistance; R5: conversion resistance. fs1 – fs5: the corresponding summit frequencies to the above processes.

Table 4 shows the breakdown of the impedance spectra for the LSCF cells at OCV before durability test. The serial resistance (Rs) was 0.061 – 0.074 Ω·cm^2, close to that of the LSM cells. The oxygen ion interfacial transfer process (R1) showed a low resistance of around 0.01 Ω·cm^2, except cell T8 (0.027 Ω·cm^2). The Ni-YSZ TPB reaction (R2) was 0.013 – 0.025 Ω·cm^2 and the TPB reaction resistance of the LSCF-CGO electrode (R3) was 0.015–0.021 Ω·cm^2. The diffusion resistance (R4) was much larger for cell T6 and T8 (~ 0.03 Ω·cm^2) than T7 and T9 (≤ 0.01 Ω·cm^2). Note the value of R4 for cell T9 obtained from the fitting can only be used for a qualitative rather than a quantitative analysis, because of the higher error level for the less significant process (with a very small resistance). The conversion resistance of the cells was 0.10 – 0.12 Ω·cm^2. The

summit frequencies of the processes above ~ 100 Hz were: 21K – 56K Hz for the oxygen ion interfacial transfer process, 7.7K – 11.6K Hz for the Ni-YSZ TPB reaction process and 140 – 210 Hz for the LSCF-CGO TPB reaction process. The summit frequency of the gas diffusion process was 10 – 20 Hz for cell T6 and T8. Cell T7 and T9 (using mesh contact) showed a higher summit frequency of 90 – 100 Hz. The gas conversion process had a summit frequency of 1.5 – 2.5 Hz.

3.2 Cell voltage evolution during durability test

The evolution of the cell voltages for the LSM and LSCF cells during galvanostatic durability test were shown in Figure 24. LSM cell T1 was tested at -1.5 A/cm^2 and the other LSM cells (T2 – T5) were tested at -2.0 A/cm^2. During the short-term (138 hours) test, the voltage changes of cell T4 was almost overlapped with that of cell T3.

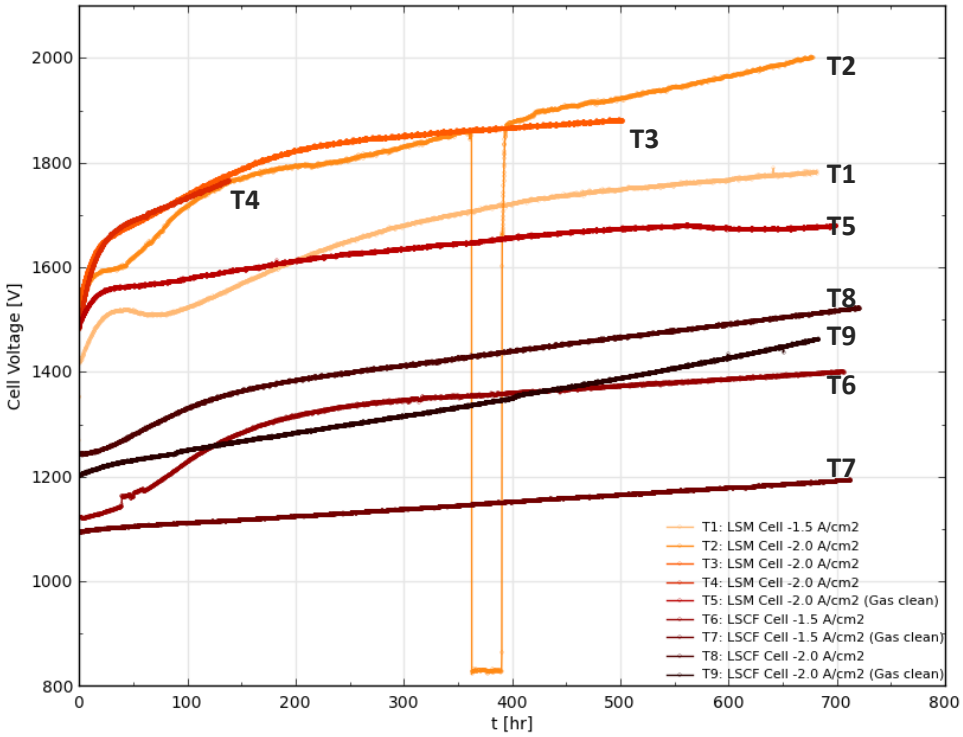

Figure 24 Durability of solid oxide cells for electrolysis of 45 % H_2O + 45 % CO_2 +10 % H_2 under current densities of -1.5 or -2.0 A/cm^2; initially the cell temperature was ~ 865 ^oC (under operation) and finally increased to ~ 875 ^oC.

3.2.1 LSM cells

Table 5 Long Term Durability of LSM cells

Cell Nr.	Current Density (A/cm^2)	Duration (h)	Initial Volt. (mV)	Final Volt. (mV)	Degra.Rate_from 300h till end (mV/Kh)	Degra.Rate_ final 100h (mV/Kh)	Gas & Sealing Clean	Nano-particle formation
T1	-1.5	681.5	1418	1785	275	210	No	Yes
T2	-2.0	678	1502	2001	452	460	No	Yes
T3	-2.0	501.8	1529	1880	149	140	No	Yes
T4	-2.0	138.3	1480	1765	–	(890)	No	Yes
T5	-2.0	699.5	1483	1680	115	60	Yes	Yes

25 L/h 45 % CO_2 + 45 % H_2O + 10 % H_2 flown to the Ni-YSZ electrode and pure oxygen to the oxygen electrode; Initial cell temperature at ~ 865 ^{o}C (under operation) and finally increased to ~ 875 ^{o}C;

3.2.2 LSCF cells

Table 6 Long Term Durability of LSCF cells

Cell Nr.	Current Density (A/cm^2)	Duration (h)	Initial Volt. (mV)	Final Volt. (mV)	Degra.Rate_from 300h till end (mV/Kh)	Degra.Rate_ final 100h (mV/Kh)	Gas & Sealing Clean	Nano-particle formation
T6	-1.5	707	1123	1399	130	120	No	Yes
T7	-1.5	712.4	1096	1193	136	130	Yes	No
T8	-2.0	720.7	1243	1522	261	260	No	Yes
T9	-2.0	682.8	1205	1463	386	430	Yes	–

25 L/h 45 % CO_2 + 45 % H_2O + 10 % H_2 flown to the Ni-YSZ electrode and pure oxygen to the oxygen electrode; Initial cell temperature at ~ 865 ^{o}C (under operation) and finally increased to ~ 875 ^{o}C;

3.3 Analysis of the EIS measured during durability test

3.3.1 LSM cells

The in situ impedance spectra of the LSM cell T1 – T5 during the durability tests were broken down into individual processes using the method described in the Experimental part. The area specific resistances and characteristic frequencies as a function of time are shown in Figure 25 – Figure 29 and described as followings:

Cell performance of T1 during durability test: (-1.5 A/cm^2; 681.5h; normal test)

LSM Cell T1 was tested for 681.5 hours under a constant current density of -1.5 A/cm^2 using the 'normal' set-up (higher impurity level than 'clean' test). As is shown in Figure 25, the series resistance (Rs) dominated the cell resistance throughout the test. Rs increased from 0.150 (at 25 hour) to 0.323 Ω·cm^2 at 681.5 hours. The Rs degradation can be roughly separated into two periods according to the increase rate: in the first ~ 200 hours Rs increased rapidly with an average rate of 0.552 Ω·cm^2/Kh; in the later periods the degradation rate slowed down and stabilized at approximately 0.157 Ω·cm^2/Kh. The polarization resistance (Rp) of TPB reaction at Ni-YSZ electrode (R2) also increased significantly and can be separated into two stages: in the first stage, R2 increased from 0.053 Ω·cm^2 at 25h to 0.141 Ω·cm^2 at 399.7 hours; in the second stage, R2 almost leveled off at around 0.14 Ω·cm^2 for the later periods. The characteristic or summit frequency relating to this process decreased from 6K ~ 7K Hz to ~ 1.4K Hz after 681.5 hours' test. Minor degradation was found for the interfacial oxygen ion transfer (R1) with a summit frequency above 20K Hz and the TPB reaction at LSM-YSZ electrode (R3) with the summit frequency decreasing from ~ 600 Hz to ~ 350 Hz. The diffusion resistance (R4) was stable and the summit frequency was between 16 and 27 Hz. The cell showed an increasing conversion resistance (R5) from the start to ~ 300 h, which then decreased gradually for the later period (300 h ~ 700 h). The final conversion resistance is still larger than the initial value. The summit frequency of the conversion arc was 1.0 – 1.6 Hz.

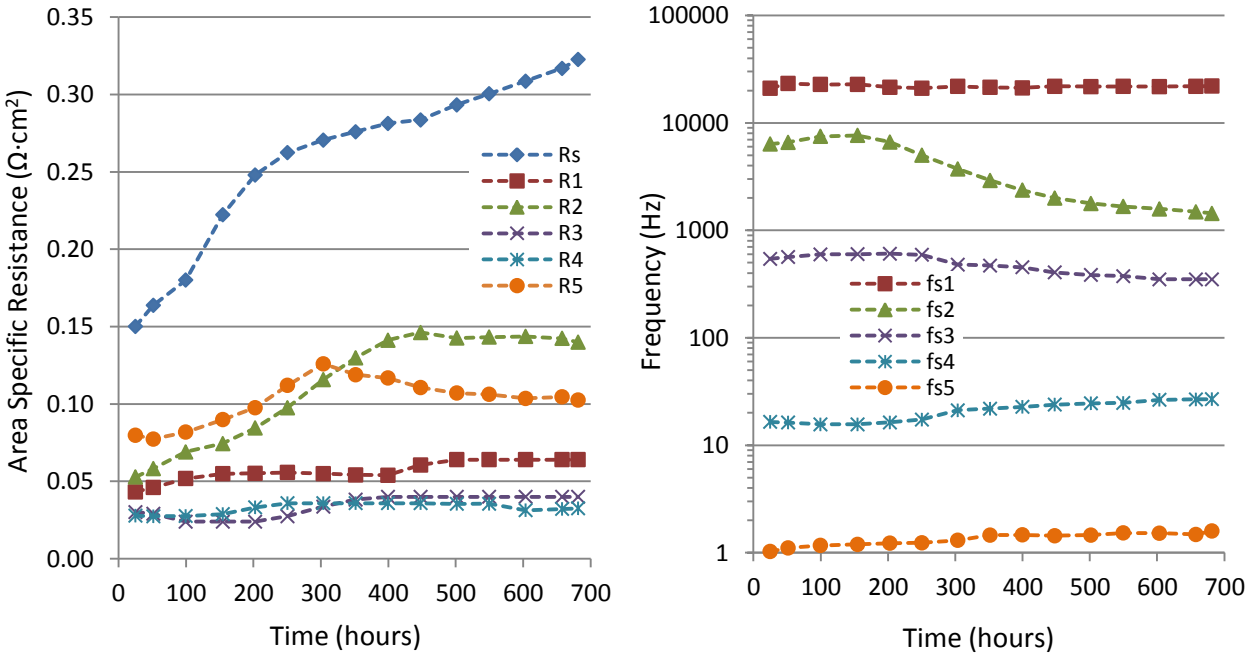

Figure 25 Breakdown of the impedance spectra measured on cell T1 during the galvanostatic test (-1.5 A/cm^2; normal test): area specific resistance of each process vs. time (left) and the corresponding characteristic frequency vs. time (right). Rs: ohmic resistance; R1: interfacial O^{2-} transfer resistance; R2: Ni-

YSZ TPB reaction resistance; R3: oxygen electrode TPB reaction resistance; R4: diffusion resistance; R5: conversion resistance. fs1 – fs5: the summit frequency corresponding to the above processes.

Cell performance of T2 during durability test: (-2.0 A/cm^2; 676.7h; normal test)

LSM Cell T2 was tested for 676.7 hours under -2.0 A/cm^2 using the 'normal' set-up. As is shown in Figure 26, Rs increased dramatically from 0.089 Ω·cm^2 at the start to 0.207 Ω·cm^2 at 124.7 hours. For the later periods, the degradation of Rs slowed down to an almost linear increase rate of 0.201 Ω·cm^2/Kh (the simple average) and the final value of Rs after 676.7 hours' test was 0.318 Ω·cm^2. Resistance for the Ni-YSZ electrode TPB reaction (R2) increased from the initial value of 0.044 Ω·cm^2 to 0.096 Ω·cm^2 at 178.7 hour. For the later periods, R2 almost leveled off at ~ 0.10 Ω·cm^2. Corresponding to the increasing and level off of R2, the summit frequency of Ni-YSZ TPB process decreased rapidly from 5K ~ 6K Hz at the beginning to 1.6 KHz at 154.7 hour, and then continued to decrease slowly to ~ 1.1K Hz at 676.7 hour. Smaller degradation was found for interfacial oxygen ion transfer resistance (R1), which had a summit frequency of ~ 20K Hz. The LSM-YSZ TPB reaction resistance (R3) showed minor degradation and a summit frequency of between ~ 450 Hz and ~ 700 Hz. The diffusion resistance (R4) was relative stable and the summit frequency was 9 to 18 Hz. The conversion resistance (R5) firstly showed an increase from start to the 178.7 hour. Then R5 decreased and stabilized finally at a lower value than the initial one. The summit frequency of the conversion arc was 0.9 – 1.6 Hz.

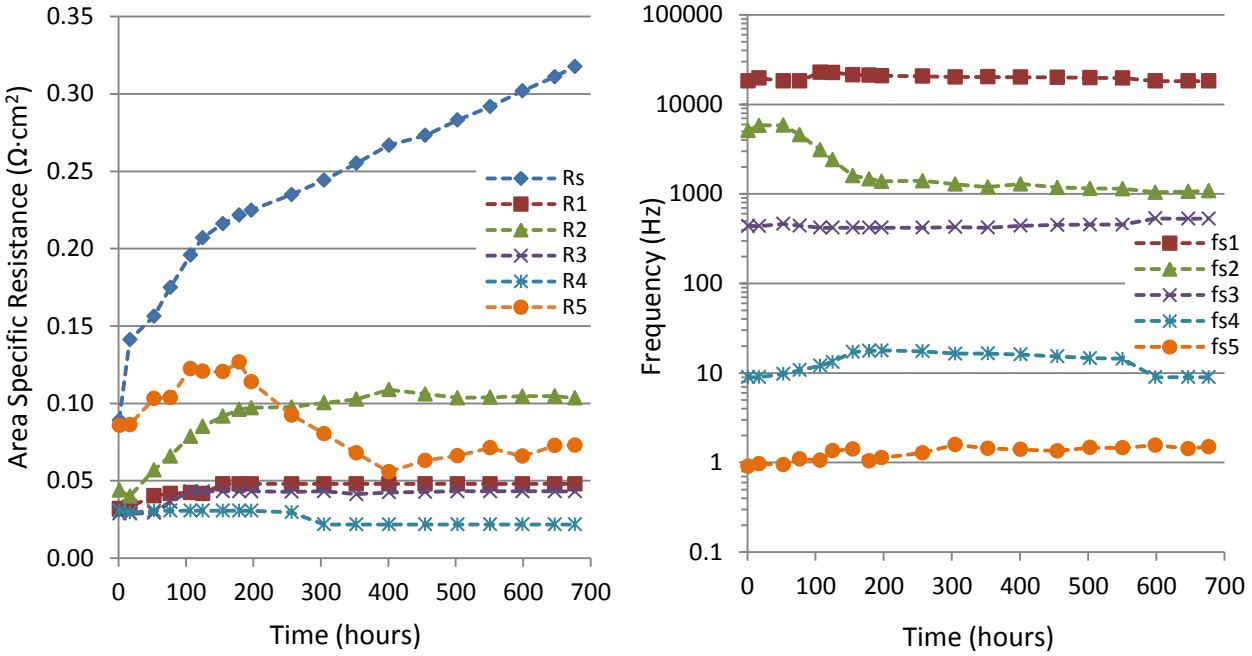

Figure 26 Breakdown of the impedance spectra measured on cell T2 during the galvanostatic test (-2.0 A/cm^2; normal test): area specific resistance of each process vs. time (left) and the corresponding characteristic frequency vs. time (right). Rs: ohmic resistance; R1: interfacial O^{2-} transfer resistance; R2: Ni-YSZ TPB reaction resistance; R3: oxygen electrode TPB reaction resistance; R4: diffusion resistance; R5: conversion resistance. fs1 – fs5: the summit frequency corresponding to the above processes.

Cell performance of T3 during durability test: (-2.0 A/cm^2; 501.8h; normal test)

LSM Cell T3 was tested for 501.8 hours under -2.0 A/cm^2 using the 'normal' set-up. As is shown in Figure 27, Rs was almost doubled within 102.4 hours from the initial value of 0.107 Ω·cm^2 to 0.205 Ω·cm^2. Then Rs continued to increase to 0.249 Ω·cm^2 at 501.8 h in a slower rate of 0.110 Ω·cm^2/Kh (average). Rs accounted for the largest part of cell resistance throughout the test and the degradation of Rs contributed the most to the cell resistance increase. The TPB reaction resistance of the Ni-YSZ electrode (R2) increased from 0.024 Ω·cm^2 at the start to 0.083 Ω·cm^2 after 246.7 hours' operation, then R2 almost leveled off at ~ 0.09 Ω·cm^2. The summit frequency showed a decrease from ~ 6K Hz to ~ 700 Hz after 501.8 hours' test. Relative smaller degradation from 0.064 to 0.072 Ω·cm^2 was found for the interfacial oxygen ion transfer resistance (R1), which had a summit frequency of ~ 20K Hz. TPB reaction resistance of the LSM-YSZ electrode (R3) increase from 0.019 to 0.042 Ω·cm^2 and the summit frequency was between ~ 400 Hz and ~ 800 Hz. The diffusion resistance (R4) was stable and the summit frequency was ~ 10 Hz. The conversion resistance (R5) was found to increase generally in the first 200 hours and decrease in the later periods. The conversion arc had a summit frequency of 0.8 – 1.4 Hz.

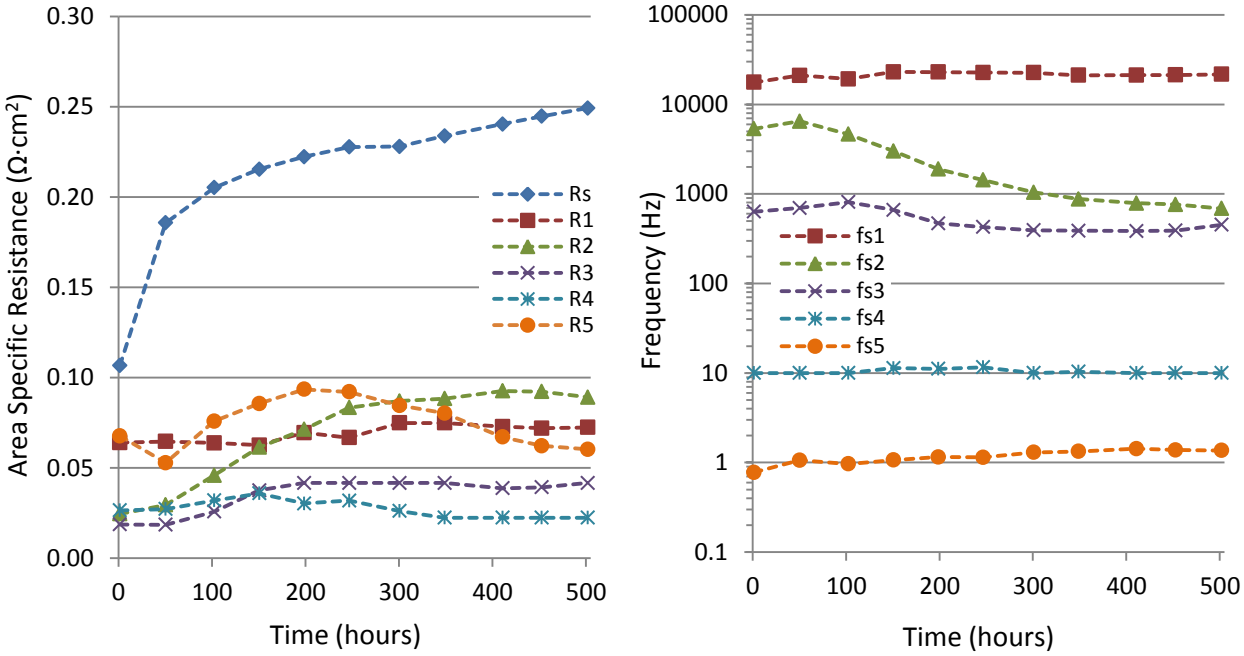

Figure 27 Breakdown of the impedance spectra measured on cell T3 during the galvanostatic test (-2.0 A/cm^2; normal test): area specific resistance of each process vs. time (left) and the corresponding characteristic frequency vs. time (right). Rs: ohmic resistance; R1: interfacial O^{2-} transfer resistance; R2: Ni-YSZ TPB reaction resistance; R3: oxygen electrode TPB reaction resistance; R4: diffusion resistance; R5: conversion resistance. fs1 – fs5: the summit frequency corresponding to the above processes.

<u>Cell performance of T4 during durability test:</u> (-2.0 A/cm^2; 138h; normal test)

LSM Cell T4 was tested under -2.0 A/cm^2 using the 'normal' set-up. In order to investigate the evolution of the cell components during cell degradation, especially the initial stage of rapid degradation, this test was performed within a short duration (138 hours). As is shown in Figure 28, the increase of Rs was much larger than that of the other processes. Rs increased dramatically from 0.078 Ω·cm^2 at the start to 0.186 Ω·cm^2 at 50.2 hour (simple average: 2.15 Ω·cm^2/Kh) (and 0.196 Ω·cm^2 at 87.5 hour). Finally, Rs increased in a lower rate of 0.191 Ω·cm^2/Kh (average) to 0.203 Ω·cm^2 at 138 hour, 160 % larger than the initial value. After 138 hours' operation, the TPB reaction resistance of the Ni-YSZ electrode (R2) increased by 83 % from the initial 0.029 Ω·cm^2 to 0.053 Ω·cm^2 with the summit frequency decreased from 6K ~ 7K Hz to ~ 2.8K Hz. An increase from 0.044 to 0.067 Ω·cm^2 was found for the interfacial oxygen ion transfer resistance (R1), which had a summit frequency at above 20K Hz. From the EIS analysis, a stable TPB reaction resistance of the LSM-YSZ electrode (R3) was found at ~0.023 Ω·cm^2 with the summit frequency of ~ 600 Hz. The diffusion resistance (R4) and conversion resistance (R5) were also stable during this short test. The summit frequency was about 10 Hz for the diffusion and 0.8 to 1.4 Hz for the conversion arc.

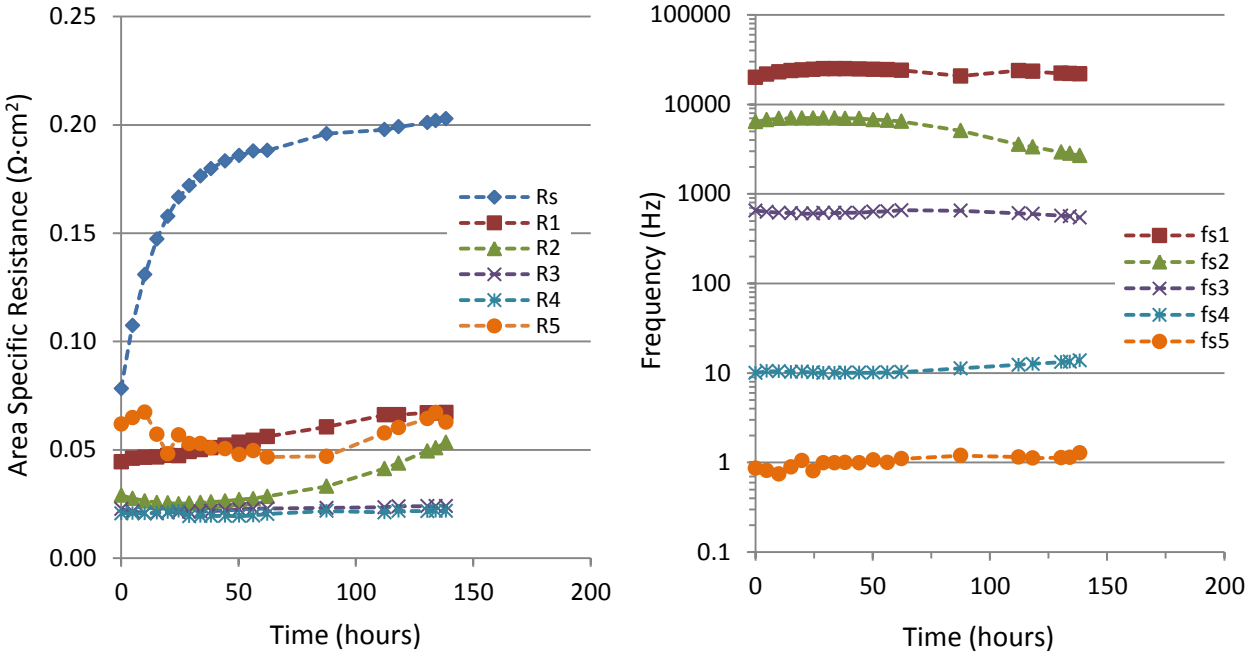

Figure 28 Breakdown of the impedance spectra measured on cell T4 during the galvanostatic test (-2.0 A/cm^2; normal test): area specific resistance of each process vs. time (left) and the corresponding characteristic frequency vs. time (right). Rs: ohmic resistance; R1: interfacial O^{2-} transfer resistance; R2: Ni-YSZ TPB reaction resistance; R3: oxygen electrode TPB reaction resistance; R4: diffusion resistance; R5: conversion resistance. fs1 – fs5: the summit frequency corresponding to the above processes.

Cell performance of T5 during durability test: (-2.0 A/cm^2; 699.5h; clean test)

LSM Cell T5 was tested for 699.5 hours under -2.0 A/cm^2 using the 'clean' set-up for which the impurities from the sealing material and feed gas had been minimized. As is shown in Figure 29, Rs increased from 0.080 Ω·cm^2 at the start (by 109 % to 0.167 Ω·cm^2 at 201.4 hour) by 114 % to 0.171 Ω·cm^2 at 249.4 hour. Finally, the increase of Rs stabilized to a slower degradation rate of 0.019 Ω·cm^2/Kh. The final Rs value was 0.180 Ω·cm^2, 125 % larger than the initial Rs. The TPB reaction resistance of the Ni-YSZ electrode (R2) increased from the initial 0.079 Ω·cm^2 to 0.101 Ω·cm^2 after 297.5 hours' operation and finally stabilized at 0.10 to 0.11 Ω·cm^2. The summit frequency was between 3.9K Hz and 2.4K Hz. The interfacial oxygen ion transfer resistance (R1) was found to increase from 0.035 to 0.071 Ω·cm^2 and the summit frequency was above 20K Hz. A stable TPB reaction resistance of the LSM-YSZ electrode (R3) was found at approximately 0.03 Ω·cm^2 with the summit frequency at around 500 Hz. The diffusion resistance (R4) was around 0.01 Ω·cm^2 and the summit frequency was around 110 Hz. The conversion resistance increased slightly and the summit frequency was between 2.1 and 2.7 Hz.

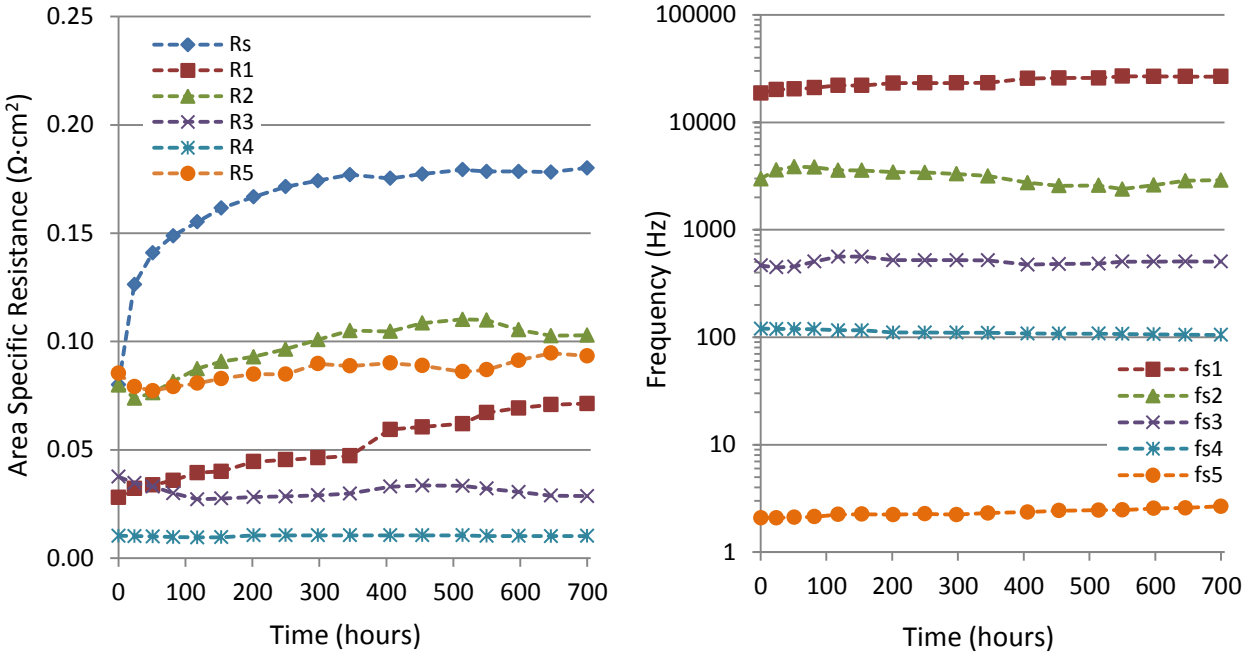

Figure 29 Breakdown of the impedance spectra measured on cell T5 during the galvanostatic test (-2.0 A/cm^2; clean test): area specific resistance of each process vs. time (left) and the corresponding characteristic frequency vs. time (right). Rs: ohmic resistance; R1: interfacial O^{2-} transfer resistance; R2: Ni-YSZ TPB reaction resistance; R3: oxygen electrode TPB reaction resistance; R4: diffusion resistance; R5: conversion resistance. fs1 – fs5: the summit frequency corresponding to the above processes.

3.3.2 LSCF cells

The in situ measured impedance spectra for the LSCF cell T6 – T9 during the durability tests were broken down into individual processes (See Appendix) and the results (Figure 30 – Figure 33) are described as followings:

Cell performance of T6 during durability test: (-1.5 A/cm^2; 701h; normal test)

LSCF Cell T6 was tested for 701 hours under a constant current density of -1.5 A/cm^2 using the 'normal' set-up. From Figure 30, Rs increased gradually throughout the test (by 91 %) from 0.074 Ω·cm^2 at the start to 0.127 Ω·cm^2 after 701 hours' operation. Simply dividing the increase of Rs by test duration, the average degradation rate was 0.076 Ω·cm^2 /Kh. The change in the TPB reaction resistance of the Ni-YSZ electrode (R2) can be roughly divided into two periods: R2 increased fast from the initial 0.024 Ω·cm^2 to 0.186 Ω·cm^2 within 251 hours, then R2 showed much slower change for the later periods. A slight decrease in R2 from the maximum of 0.192 Ω·cm^2 (at 299 hour) to 0.186 Ω·cm^2 was observed (confirmed by ADIS & DRT). Corresponding to the changes of R2, the summit frequency of Ni-YSZ TPB process firstly decreased fast

from 9.5K to 790 Hz then continued to decrease slowly to 610 Hz. The interfacial oxygen ion transfer resistance (R1) showed a small degradation from 0.011 to 0.034 Ω·cm^2. The summit frequency of the high frequency O^{2-} transfer process was 20K to 38K Hz. There was also small degradation from 0.016 to 0.024 Ω·cm^2 for the TPB reaction at the LSCF-CGO electrode (R3) which had a summit frequency between 240 and 360 Hz. A diffusion resistance (R4) was found at about 0.02 Ω·cm^2 at the beginning and decreased slowly with the test. The conversion resistance (R5) increased in the first 200 hours and then decrease to about its initial value. The summit frequency of conversion arc was 1.2 to 1.7 Hz.

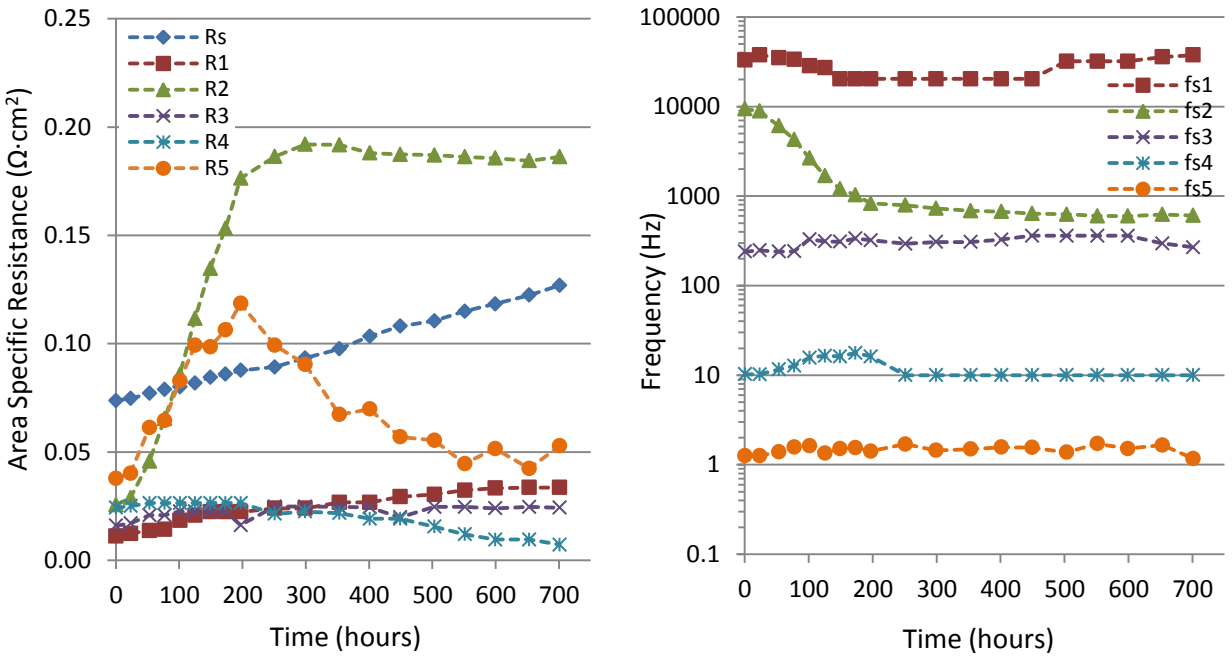

Figure 30 Breakdown of the impedance spectra measured on cell T6 during durability test (-1.5 A/cm^2; normal test): area specific resistance of each process vs. time (left) and the corresponding characteristic frequency vs. time (right). Rs: ohmic resistance; R1: interfacial O^{2-} transfer resistance; R2: Ni-YSZ TPB reaction resistance; R3: oxygen electrode TPB reaction resistance; R4: diffusion resistance; R5: conversion resistance. fs1 – fs5: the summit frequency corresponding to the above processes.

<u>Cell performance of T7 during durability test:</u> (-1.5 A/cm^2; 699.5h; clean test)

LSCF Cell T7 was tested for 699.5 hours under a constant current density of -1.5 A/cm^2 using the 'clean' set-up. From Figure 31, Rs increased (by 35 %) almost linearly from 0.063 Ω·cm^2 at the start to 0.085 Ω·cm^2 after 699.5 hours' test. The average degradation rate of Rs was calculated to be 0.031 Ω·cm^2/Kh using the total increase of Rs divided by the test duration. The TPB reaction resistance of the Ni-YSZ electrode (R2) increased from the initial value of 0.044 Ω·cm^2 gradually to 0.079 Ω·cm^2 at last. The summit frequency was

6.2K to 8.5K Hz. Based on the fitting of the impedance, the interfacial oxygen ion transfer resistance (R1) increased from 0.0064 to 0.02 Ω·cm^2 and the summit frequency was ~ 60K Hz. Little degradation was attributed to the TPB reaction at the LSCF-CGO electrode, which had an almost constant resistance (R3) at ~ 0.009 Ω·cm^2 and summit frequency at 220 to 250 Hz. The diffusion resistance (R4) was also stable, with a size of between 0.006 and 0.007 Ω·cm^2. The conversion resistance (R5) increased throughout the test and the summit frequency was 2.9 – 3.3 Hz.

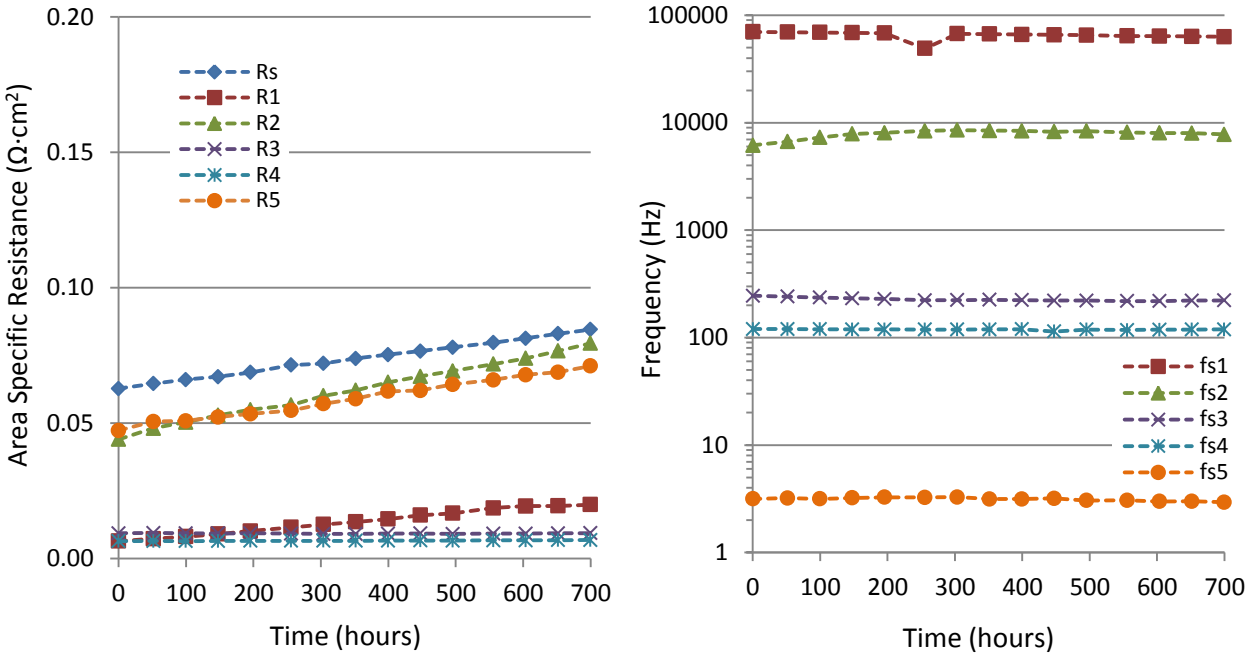

Figure 31 Breakdown of the impedance spectra measured on cell T7 during durability test (-1.5 A/cm^2; clean test): area specific resistance of each process vs. time (left) and the corresponding characteristic frequency vs. time (right). Rs: ohmic resistance; R1: interfacial O^{2-} transfer resistance; R2: Ni-YSZ TPB reaction resistance; R3: oxygen electrode TPB reaction resistance; R4: diffusion resistance; R5: conversion resistance. fs1 – fs5: the summit frequency corresponding to the above processes.

<u>Cell performance of T8 during durability test:</u> (-2.0 A/cm^2; 716.5 h; normal test)

LSCF Cell T8 was tested using the 'normal' set-up for 716.5 hours under a constant current density of -2.0 A/cm^2. From Figure 32, Rs increased slowly from 0.070 Ω·cm^2 at the start to 0.079 Ω·cm^2 after 266 hours' test. For the later periods, the increase of Rs turned faster and the average degradation rate in the final 451 hours was 0.113 Ω·cm^2/Kh. The final Rs value was 0.130 Ω·cm^2, 85.7 % larger than the initial value. The TPB reaction resistance of the Ni-YSZ electrode (R2) increased rapidly from 0.045 Ω·cm^2 at the beginning to 0.118 Ω·cm^2 in 170 hours, then changed little and stabilized at around 0.12 Ω·cm^2 for the later periods

(confirmed by ADIS & DRT). The corresponding summit frequency decreased from 5.2K at the beginning to 800 Hz finally. The interfacial oxygen ion transfer resistance (R1) was 0.021 Ω·cm^2 at the beginning and 0.040 Ω·cm^2 at the end. The summit frequency was about 20K – 33K Hz. The TPB reaction at the LSCF-CGO electrode (R3) also showed a degradation from 0.017 to 0.027 Ω·cm^2 while the summit frequency was between 200 and 350 Hz. A diffusion resistance (R4) was found at 0.029 Ω·cm^2 at the beginning and decreased with the test (confirmed by the ADIS & DRT). The conversion resistance increased fast (0 – 170 h) and later decreased gradually to even lower than the initial value. The summit frequency of conversion process was between 0.8 and 1.1 Hz.

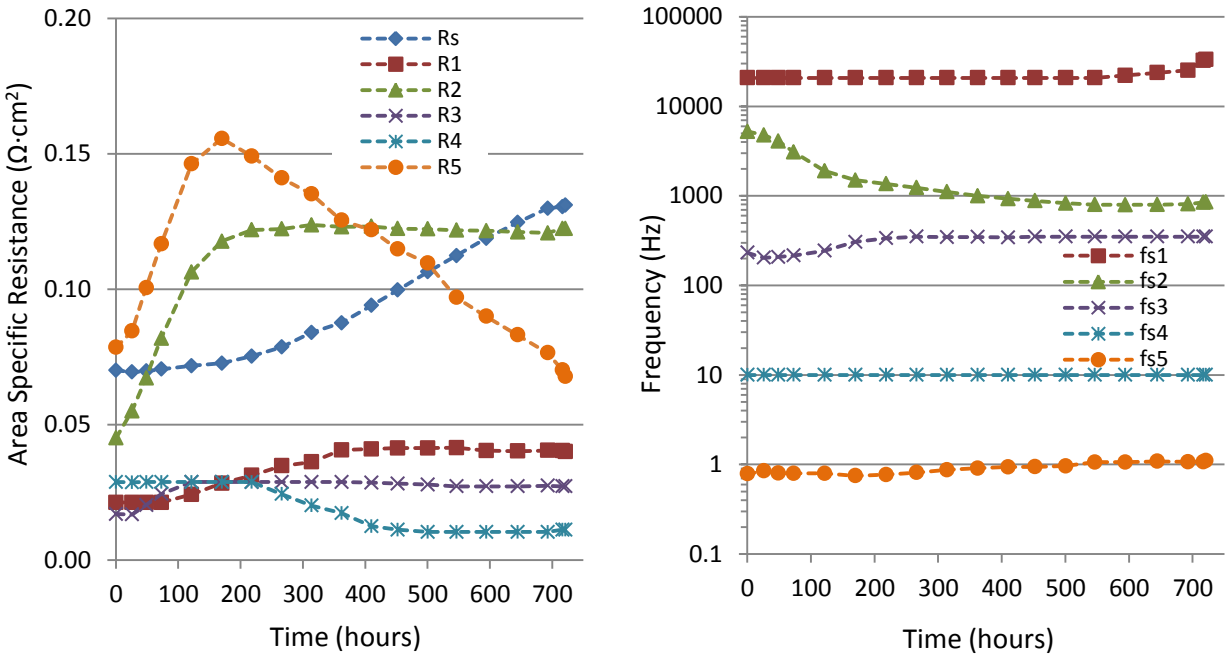

Figure 32 Breakdown of the impedance spectra measured on cell T8 during durability test (-2.0 A/cm^2; normal test): area specific resistance of each process vs. time (left) and the corresponding characteristic frequency vs. time (right). Rs: ohmic resistance; R1: interfacial O^{2-} transfer resistance; R2: Ni-YSZ TPB reaction resistance; R3: oxygen electrode TPB reaction resistance; R4: diffusion resistance; R5: conversion resistance. fs1 – fs5: the summit frequency corresponding to the above processes.

Cell performance of T9 during durability test: (-2.0 A/cm^2; 682.8 h; clean test)

LSCF Cell T9 was tested for 682.8 hours under a constant current density of -2.0 A/cm^2 using the 'clean' set-up. Figure 33 shows that Rs increased slowly from 0.070 Ω·cm^2 to 0.083 Ω·cm^2 for the period of 0 – 250 hour. For the later periods, the increase of Rs turned faster and the average degradation rate in the final 84 hours was 0.177 Ω·cm^2/Kh. The total increase in Rs was 74 %. The TPB reaction resistance of the Ni-YSZ

electrode (R2) increased by 163 % from 0.049 Ω·cm^2 at the start to 0.129 Ω·cm^2 at the end. The average degradation rate of R2 was 0.117 Ω·cm^2/Kh for the whole test duration. The corresponding summit frequency decreased from 4.5K to 1.7K Hz. The interfacial oxygen ion transfer resistance (R1) was 0.010 Ω·cm^2 at the beginning and 0.019 Ω·cm^2 at the end. The summit frequency was between 19K and 28K Hz. A stable TPB reaction at the LSCF-CGO electrode (R3) of 0.016 – 0.019 Ω·cm^2 was obtained from impedance fitting while the summit frequency was 250 – 500 Hz. The diffusion resistance (R4) was 0.006 – 0.007 Ω·cm^2 during the test. The conversion resistance increased for the period of 0 – 450 h and decreased for the later test. The summit frequency of conversion process was 1.9 – 2.4 Hz.

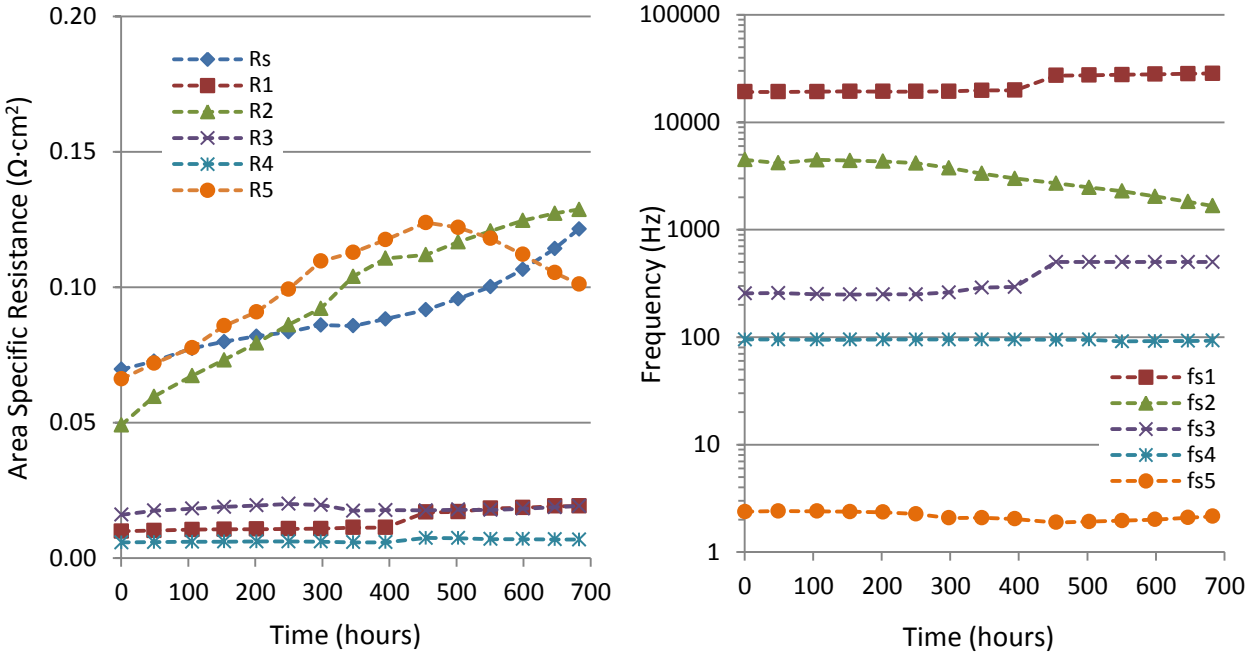

Figure 33 Breakdown of the impedance spectra measured on cell T9 during durability test (-2.0 A/cm^2; clean test): area specific resistance of each process vs. time (left) and the corresponding characteristic frequency vs. time (right). Rs: ohmic resistance; R1: interfacial O^{2-} transfer resistance; R2: Ni-YSZ TPB reaction resistance; R3: oxygen electrode TPB reaction resistance; R4: diffusion resistance; R5: conversion resistance. fs1 – fs5: the summit frequency corresponding to the above processes.

3.4 EIS analysis of the cell at OCV after durability test

Based on the ADIS & DRT analysis, the impedance spectra at OCV after durability test were broke down. The break-down of the impedance for the LSM cells (T1, T4 & T5) and LSCF cells (T6, T7 & T8) measured in 45 % H_2O + 45 % CO_2 +10 % H_2 can be found in Table 7 & Table 8. The impedance fitting were not

performed for the remaining cells at OCV after test because the OCV was too low (T2) or the impedance has not been measured (T3 & T9).

As expected, the Rs values for the cells after test were much larger than the initial ones. After a test of ~ 700 hours at -2.0 A/cm^2, LSM cell T5 showed larger Rs at OCV than LSCF cell T8. For the LSM cell T4 tested for a short duration (138 hours), the final Rs value was close to that of LSCF cell T8 which was operated for a long period (~700 hours). The oxygen ion interfacial transfer resistance was also larger for the LSM cells than the LSCF cells. Similar Ni-YSZ TPB reaction resistance (0.62 – 0.72 Ω·cm^2) were observed at OCV for the cells (LSM cell T4, T5 and LSCF cell T8) tested at a same current density of -2.0 A/cm^2. For the cells tested at -1.5 A/cm^2, lower Ni-YSZ TPB resistance (R2) was found for LSCF cell T6 (0.047 Ωcm^2) and for cell T7 (0.033 Ωcm^2); higher value was observed for LSM cell T1 (0.064 Ωcm^2). LSCF cell T7 showed the best cell performance (the lowest value for Rs and electrochemical process R1, R2 and R3) after test.

Table 7 EIS fitting results for the LSM cells at OCV after test (45 % H_2O + 45 % CO_2 +10 % H_2 & O_2)

Cell Nr.	Rs (Ω·cm^2)	R1 (Ω·cm^2)	fs1 (Hz)	R2 (Ω·cm^2)	fs2 (Hz)	R3 (Ω·cm^2)	fs3 (Hz)	R4 (Ω·cm^2)	fs4 (Hz)	R5 (Ω·cm^2)	fs5 (Hz)	Error chi_sq
T1	0.183	0.140	45030	0.064	5850	0.038	720	0.062	27	0.143	2.1	1.5E-05
T4	0.121	0.081	51689	0.064	8246	0.041	1440	0.029	12	0.091	1.2	4.7E-06
T5	0.200	0.209	35732	0.062	3193	0.048	574	0.015	54	0.139	2.7	4.1E-06

Test history: T4 was tested using normal set-up at -2.0 A/cm^2 for 138 hours; T5 was tested using clean set-up at -2.0 A/cm^2 for 700 hours.

Table 8 EIS fitting results for the LSCF cells at OCV after test (45 % H_2O + 45 % CO_2 +10 % H_2 & O_2)

Cell Nr.	Rs (Ω·cm^2)	R1 (Ω·cm^2)	fs1 (Hz)	R2 (Ω·cm^2)	fs2 (Hz)	R3 (Ω·cm^2)	fs3 (Hz)	R4 (Ω·cm^2)	fs4 (Hz)	R5 (Ω·cm^2)	fs5 (Hz)	Error chi_sq
T6	0.129	0.034	36751	0.047	3834	0.023	174	0.041	11	0.093	1.4	8.0E-06
T7	0.087	0.021	65456	0.033	14760	0.019	254	0.015	84	0.142	2.4	3.2E-06
T8	0.136	0.080	33497	0.072	1371	0.030	205	0.034	18	0.109	1.6	3.2E-05

Test history: T6 was tested using normal set-up at -1.5 A/cm^2 for 707 hours; T7 was tested using clean set-up at -1.5 A/cm^2 for 712 hours; T8 was tested using normal set-up at -2.0 A/cm^2 for 721 hours.

4 Discussions

4.1 Cell performance at OCV before and after durability test

Based on the breakdown results of the impedance measured at OCV for the cell before (Table 3 & Table 4) and after (Table 7 & Table 8) durability test, it is found that most of the degradations come from the serial resistance (Rs), the high frequency interfacial transfer resistance for oxygen ion (R1) and the Ni-YSZ TPB reaction resistance (R2). The changes are clearly shown in Figure 34. The diffusion and conversion resistance were less important and thus not shown in the figure.

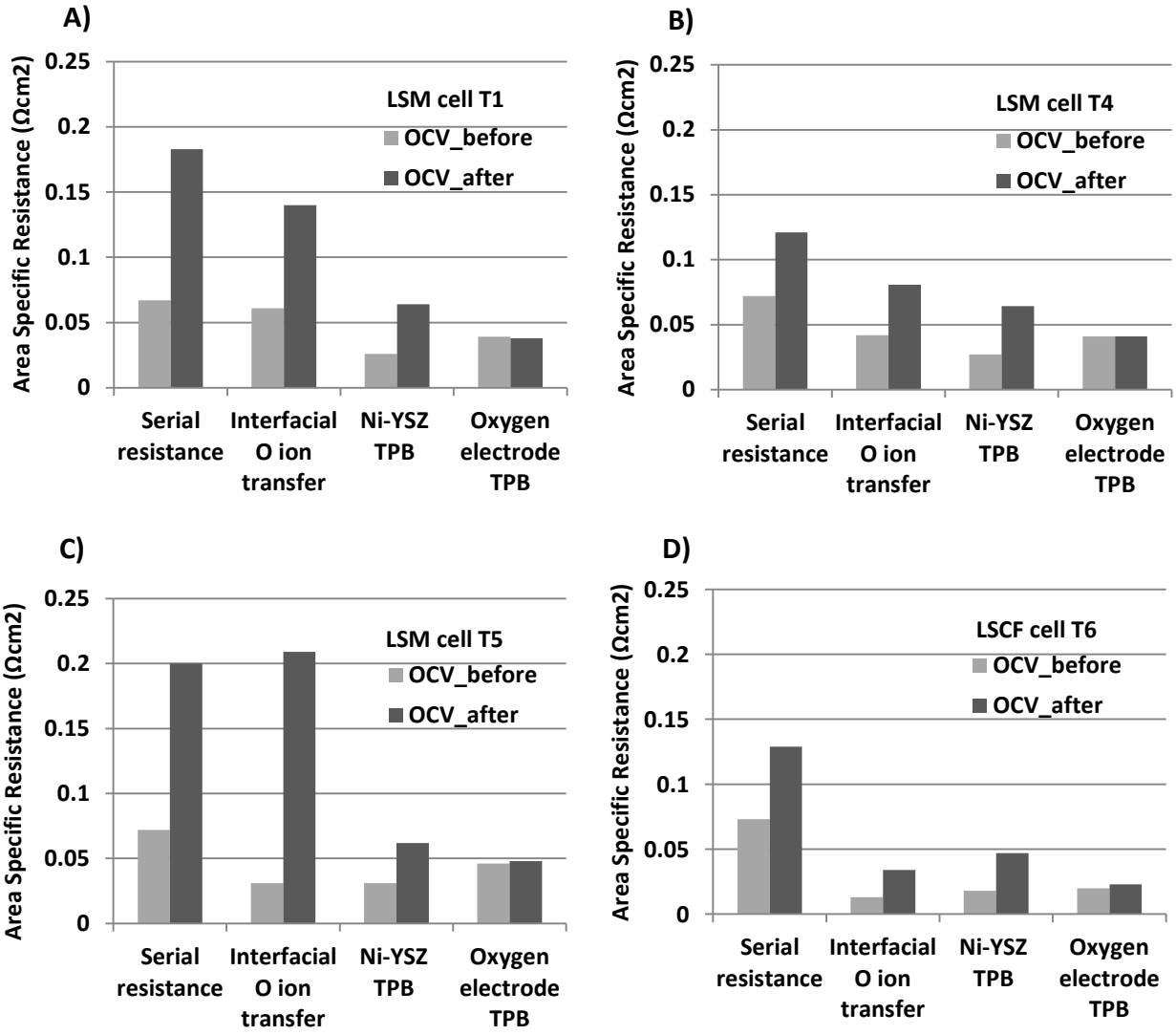

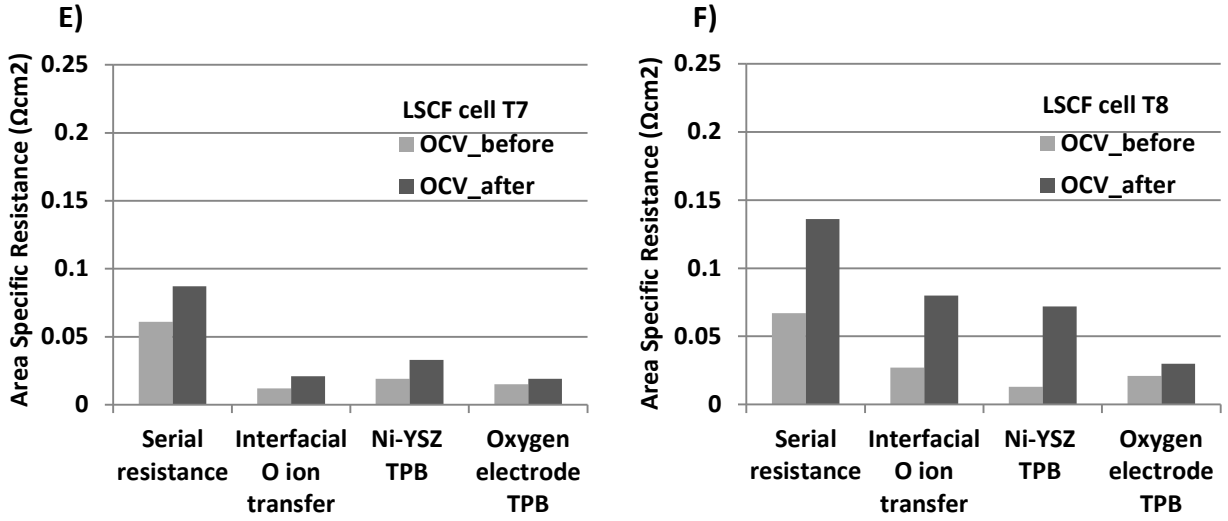

Figure 34. Comparisons of the ohmic and electrochemical processes of the cells in 45 % H_2O + 45 % CO_2 + 10 % H_2 at OCV before and after durability test. A) LSM cell T1 (-1.5 A/cm^2; normal test; 682 h); B) LSM cell T4 (-2.0 A/cm^2; normal test; 138 h); C): LSM cell T5 (-2.0 A/cm^2; clean test; 700 h); D) LSCF cell T6 (-1.5 A/cm^2; normal test; 707 h); E) LSCF cell T7 (-1.5 A/cm^2; clean test; 712 h); F): LSCF cell T8 (-2.0 A/cm^2; normal test; 721 h).

Serial resistance (Rs): The LSM cells and LSCF cells showed close values of the serial resistance (0.06 ~ 0.07 Ωcm^2) at OCV before the test. However, after a similar test period of ~ 700 hours and operation at the same current density, the LSM cells showed more severe degradation in the serial resistance than the LSCF cells: LSM cell T1 (0.18 Ωcm^2) vs. LSCF cell T6 (0.13 Ωcm^2) or T7 (0.09 Ωcm^2) after operation at -1.5 A/cm^2, and LSM cell T5 (0.20 Ωcm^2) vs. LSCF cell T8 (0.14 Ωcm^2) after operation at -2.0 A/cm^2. Another LSM cell (T4) showed a fast increase of Rs to 0.12 Ωcm^2 even after a short duration of 138 hours. The cells tested at higher current densities showed more severe degradation of Rs. By correlating the impedance during the degradation and the post-test microstructural analysis, the degradations of Rs is ascribed not only to the degradation of the YSZ electrolyte but also Ni-YSZ contact loss (discuss later).

Oxygen ion transfer resistance (R1): The oxygen ion transfer resistances (R1) for all the cells except T7 were significantly larger after test than the initial ones, especially for the cells tested at a larger current density of -2.0 A/cm^2. Based on the post-test microstructural analysis (See Chapter 5 'Microstructure'), the percolation loss of Ni particles, the contact loss between Ni and YSZ and accumulation/segregation of impurities at Ni-YSZ active electrode could contribute to the increase of oxygen ion transfer resistance. It has to be mentioned that the most of the R1 degradation for cell T5 occurred during decreasing current after the galvanostatic test, instead of during the galvanostatic test. The strange drastic increase of R1

cannot be explained merely by the decrease of cell temperature (~ 20 ^{o}C) when cutting off current. It is also hypothesized that precipitation of nano-zirconia in the Ni-YSZ electrode occurred with removal of the polarization and resulted in deterioration of the Ni-YSZ interface which contributed to increase of oxygen ion transfer resistance. However, such significant increase of R1 during cutting off current was not clearly observed for the other cells where nano-precipitates were also observed. Further work is still needed for a better interpretation.

Ni-YSZ TPB reaction resistance (R2): All the tested cells except T7 showed substantial increase in the Ni-YSZ TPB reaction resistance at OCV after test than before test. It could be ascribed to the loss of Ni-YSZ TPB reaction active sites due to impurity accumulation, Ni coarsening and Ni percolation loss during the test.

Oxygen electrode TPB resistance (R3): Based on the ADIS and DRT analysis for the impedance at OCV before and after durability test (see Appendix), little or minor degradation was found for the TPB reaction resistance of the LSM-YSZ electrode (Cell T1, T4 and T5). For the LSCF cells (cell T6, T7 and T8), a very small increase (0.003 ~ 0.01 Ωcm^2) of the oxygen electrode TPB reaction resistance was obtained by impedance fitting. However, because of the difficulty in fitting of this process due to the insignificant resistance values, the above numbers can be deemed to reveal only qualitatively rather than precisely the increase of the LSCF-CGO resistance.

Diffusion resistance (R4) and conversion resistance (R5): Higher diffusion resistance was observed for the cells (LSM cell T1 – T4 and LSCF cell T6 & T8) tested using a porous ceramic contact than for the cells (LSM cell T5 and LSCF cell T7 & T9) with a metal mesh contact. The ceramic contact has the embedded grooves as channels of gas flowing across the cell and the porous ceramic still directly covered a significant ~50 % of the surface area of the electrode, where the mass transport was by means of gas diffusion. In comparison to a metal mesh contact, the porous ceramic contact has a much lower porosity and smaller pore size. Therefore, the cells using a ceramic contact showed a larger diffusion resistance, despite of the macro-scale gas channel working as well as the metal mesh contact. In addition, cell T5 and T7 showed a little bit larger conversion resistance (~0.14 Ωcm^2) at OCV after test than the other cells (0.09 ~ 0.11 Ωcm^2). Theoretically, the conversion resistance should be of minimum at 1: 1 for the ratio of $H_2O + CO_2$ to $H_2 + CO$ and will increase with moving away from this ratio.[39] The relative lower OCV of cell T5 (811 mV) and T7 (822 mV) indicate a higher ratio of $H_2O + CO_2$ than that of the feed gas (45 % H_2O + 45 % CO_2 +10 % H_2) due to gas leakage. Therefore, the conversion resistance was larger for the two cells.

Rs and R2 after removing the polarization after durability test:

Ohmic resistance (Rs) – relaxation: With current decreasing to 0 after the durability test, the ohmic resistance of the YSZ electrolyte should have increase due to the major decrease of cell temperature (ohmic heat). However, significant decrease of Rs was observed on a few LSM cells (Figure 25, Figure 28 and Table 7: T1 and T4) during current decreasing to 0, but not for any of the LSCF cells. Thus, the Rs decrease (relaxation) related probably with the LSM electrode, which has a larger over-potential. YSZ degradation (Rs increase) has been reported for SOECs during steam electrolysis under high current densities and was ascribed to the oxygen bubble formation in YSZ electrolyte due to large oxygen electrode over-potentials[28,29]. Contrary, when decreasing the current, a structural relaxation of the YSZ electrolyte could occur and result to a reduced Rs.

Ni-YSZ TPB resistance (R2) – up & down: Other than the unexpected Rs relaxation, a strange Ni-YSZ TPB resistance (R2) first increasing then decreasing was observed for LSM cell T4 during decreasing current from the operating current (-2.0 A/cm^2) to 0. However, the occurrence of this strange change of R2 was not dependent on Rs relaxation, because it has been observed also for LSCF cell T8 (-2.0 A/cm^2), which hadn't shown a reduced Rs after the removal of polarization. The increase of R2 with decreasing current from 2.0 A/cm^2 to ~1.0 A/cm2 could be partly due to the decrease of cell temperature. In addition, large cathodic polarizations[40] could lead to some extent of electronic conductivity of YSZ[41] and thus a decrease in the Ni-YSZ TPB resistance (R2), which would increase again with the removal of the polarization. R2 was observed to decrease with decreasing the current further to 0, which is in accordance to its dependence on interfacial pO_2 / cathodic polarization.

4.2 Durability test

4.2.1 Performance & durability: comparisons among the LSM cells

During the durability test, the two most important electrochemical processes for cell degradation were the serial resistance (Rs) and the Ni-YSZ TPB reactions (R2). The two processes were summarized and listed in Table 9 and Table 10 for comparisons.

Table 9 Degradation of the serial resistance (Rs) for the LSM cells during galvanostatic durability test.

Cell Nr.	Current density (A/cm^2) & set-up	1st stage_Rs (hour)	Rs increase ($\Omega \cdot cm^2$)	Degra. Rate[(1)(2)] ($\Omega \cdot cm^2/Kh$)	2nd stage_Rs (hour)	Rs_final ($\Omega \cdot cm^2$)	Degra. Rate[(1)] ($\Omega \cdot cm^2/Kh$)	Degra. Rate[(1)]_ final near-linear period of Rs ($\Omega \cdot cm^2/Kh$ & hours)
T1	-1.5; normal	0 – 202.5 or 250.5	0.15(25h) – 0.248 or 0.262	0.552 or 0.497	– 682	0.323	0.157 or 0.142	0.167; 234
T2	-2.0; normal	0 – 124.7h	0.089(1h) – 0.207	0.954	– 677	0.318	0.201	0.201; 552
T3	-2.0; normal	0 – 102.4	0.107(1h) – 0.205	0.969	– 502	0.249	0.110	0.104; 201
T4	-2.0; normal	0 – 50.2	0.078 – 0.186	2.151	– 138	0.203	0.193	0.137; 51
T5	-2.0; clean	0 – 201.4	0.080 –0.167	0.432	– 700	0.180	0.026	0.017; 294

[(1)] Calculated as the difference of the initial and final resistance divided by the duration;

[(2)] Only can be viewed as a simple estimation due to the deviation from a linear change for the Rs in the 1st stage.

Table 10 Degradation of Ni-YSZ TPB reaction resistance (R2) for the LSM cells during galvanostatic test.

Cell Nr.	Current density (A/cm^2) & set-up	1st stage_R2 (hour)	R2 increase ($\Omega \cdot cm^2$)	Degra. Rate[(1)] ($\Omega \cdot cm^2/Kh$)	2nd stage_ R2 plateau (hour)	R2_final ($\Omega \cdot cm^2$)
T1	-1.5; normal	0 – 399.7	0.053 – 0.141	0.220	– 681.5	– 0.140
T2	-2.0; normal	0 – 178.7	0.044 – 0.096	0.291	– 676.7	– 0.104
T3	-2.0; normal	0 – 246.7	0.024 – 0.083	0.239	– 501.8	– 0.089
T4	-2.0; normal	0 – 138	0.029 – 0.053	0.174	–	–
T5	-2.0; clean	0 – 297.5	0.079 – 0.101	0.074	– 699.5	– 0.103

[(1)] The difference between the initial and final resistance divided by the duration

Degradations and evolutions of Rs: As is revealed by the impedance analysis, the serial resistance (Rs) accounted for the largest part of the cell resistance throughout the test. Rs also showed the largest degradation among all the processes. Base on the initial and finial values of Rs, an increase of 115 % to 257 % was observed for the LSM cells during the tests. The increase of Rs can be separated roughly into two periods. The 1st stage is a period of about 100 – 200 hours from the start of the galvanostatic test, where significant increase of Rs can be clearly observed in the 1st stage for all the tested LSM cells. Rs continued to increase but in a much slower rate for the later period of the test, i.e. the 2nd stage (Table 9).

Rs contribution from the YSZ electrolyte: The dramatic increase of Rs generally observed for the LSM cells in the early period of the test was not observed for the LSCF cells. In comparison to the LSCF-CGO electrode, the larger oxygen electrode resistance of LSM-YSZ could play an important role for the faster increase of

the ohmic resistance of the YSZ electrolyte. The degradation of the YSZ electrolyte has been reported for a steam electrolyzer operated under high current densities at DTU Energy Conversion[29] and Julich[42]. The increase of serial resistance was attributed to the oxygen bubbles formed at the YSZ grain boundaries at the YSZ|LSM interface, which was hypothesized to be caused by the large over-potentials of the oxygen electrode.[28,29] The larger oxygen electrode over-potentials (η_{ox}) of the LSM cells could account for the more severe Rs degradation than the LSCF cells. Interestingly, when removing the polarization for LSM cells after test significant decrease of Rs (relaxation) can be observed (e.g. LSM cell T2 & T4). This respond of Rs to current density (polarization) is probably due to a transient change of the YSZ electrolyte caused by large η_{ox} of LSM cells. However, the details are unclear yet.

Rs & Ni-YSZ electrode degradation: Apart from the increase of ohmic resistance for YSZ electrolyte under large oxygen electrode over-potentials, severe Ni-Ni percolation loss, and more important, the contact loss between the Ni particles and YSZ electrolyte could also result into an increase of the ohmic resistance. The faster (near-linear) increase of Rs can be found later than 400 ~ 450 h for cell T1, later than 150 ~ 200 h for cell T2 and later than 200 ~ 300 h for cell T3, at the same turning point when the Ni-YSZ TPB reaction resistance started to be stabilized. Among all the cells, cell T2 showed the highest Rs degradation rate for the final period of near-linear Rs increase, corresponding to SEM revealed the most severe structure changes of Ni-YSZ (large amount of nano-particle formation and gaps between Ni and YSZ). The lowest degradation rate for the final Rs increase was observed on cell T5, where limited amount of nano-particles were found in the Ni-YSZ electrolyte for the Ni particles only next to the YSZ electrolyte. Therefore, based on the correlation between the electrochemical and the microstructural analysis, the precipitation of zirconia nanoparticles and the Ni-YSZ contact loss was likely to account for significant part of the increase of Rs for the late periods of durability test.

Degradation of Ni-YSZ TPB reaction resistance & current density: Generally, the evolution of the Ni-YSZ TPB reaction resistance (R2) of the cells could be divided into two stages, according to the breakdown results of the in situ measured impedance. (Note the two-stage divide for the Ni-YSZ TPB reaction is not necessarily same with the Rs evolution. The 1st stage of Rs evolution is normally shorter than that of Ni-YSZ TPB process.) R2 increases very fast in the 1st stage, which starts from the initiation of the galvanostatic test and lasts typically 150 – 300 hours. For the later period, i.e. the 2nd stage, the R2 value will be stabilized after reaching the plateau. Based on the fitting results, it is found that the higher current density, the faster the Ni-YSZ TPB reaction resistance reaches the maximum. For example, a current density of -1.5 A/cm^2 was applied to cell T1 and it took about 400 hours for R2 value to reach a plateau. As a contrast, cell T2 and T3 were tested using the same test set-up but at a higher current density of -2.0 A/cm^2, corresponding to a

shorter time of the 1st stage (150 ~ 250h). For the same current density and test set-up, the worse initial performance of the Ni-YSZ TPB reactions tended to result in a shorter duration of the 1st stage. In comparison to cell T3 and T4, cell T2 had a larger initial resistance of Ni-YSZ TPB (R2) and correspondingly, R2 of cell T2 increased to the level off value within a shorter time (150 ~ 200 hours).

Degradation of Ni-YSZ TPB reaction resistance & impurity: The poisoning effect to the Ni-YSZ electrode by the impurities has been reported by A. Hauch[20,21] and S.D. Ebbesen et al.[15] Impurities such as Si could accumulate at the TPBs of the Ni-YSZ electrode, blocking the reaction sites and therefore reduce the activity of the electrode. The impurities originate from the raw materials of the cell components and more importantly, from the normally Si containing sealing materials and feed gas flows, which contains S etc. impurities of ppb level. Compared with the normal set-up, the clean test is regarded to have a negligible impurity level in this work. Cell T5 (clean test) showed a slower increase in the Ni-YSZ TPB reaction resistance at the same current density of -2.0 A/cm^2 than cell 2 and 3 (higher level of impurities). A lower impurity level of the test would lead to a slower degradation so that longer time is needed for the Ni-YSZ TPB resistance to reach the plateau. However, it seems that the impurity level hadn't influence the final TPB resistance of Ni-YSZ electrode.

The plateau for the Ni-YSZ TPB reaction resistance: Interestingly, all the LSM cells except T4 showed a similar Ni-YSZ TPB reaction resistance (R2) at around 0.1 Ω·cm^2 independent of the initial values. (The final value of R2 at 138 hour for cell T4 was only ~ 0.05 Ω·cm^2 and it hadn't reached a plateau probably because the test duration was not long enough.) With the durability test, the increase of cell resistance slowed down due to the stabilization of the Ni-YSZ TPB resistance (plus a relatively slower increase of Rs), resulting in a relatively slower degradation of the cell voltage, as was shown previously. The stable electrochemical performance of Ni-YSZ in the 2nd stage indicates that either the electrode had not experienced any microstructural and compositional change, or a stabilization mechanism had been reached by balancing the active and the passive factors for the electrochemical performance. Further analysis will be carried out later correlating the impedance and microstructure of the LSCF cells.

At the 2nd stage (the plateau), cell T2, T3 and T5, which were tested at a higher current density of -2.0 A/cm^2 showed a lower Ni-YSZ TPB resistance (~ 0.1 Ω·cm^2) than that of cell T1 (~ 0.14 Ω·cm^2), which was tested at -1.5 A/cm^2. It is considered not due to the difference in gas compositions under different conversions. The ratio of (H_2O +CO_2) to (H_2 + CO) is about 50 % : 50 % when operating at -1.5 A/cm^2 and 36 % : 64 % at -2.0 A/cm^2, thus the cell operated at -1.5 A/cm^2 should have showed a smaller Ni-YSZ TPB resistance due to the higher ratio of the oxidant. The lower temperature could contribute to a higher

electrode resistance, but such a difference (40 %) in resistance is unlikely due to merely the small difference in cell temperatures (less than 8 ^{o}C). One possible explanation for the lower Ni-YSZ TPB resistance of the cells operated at higher current density of -2.0 A/cm^2 is that the active sites for electrode reactions were enlarged due to the larger cathodic polarizations. Normally, YSZ has negligible electronic conductivity and is regarded as a pure ionic conductor only. For the SOECs, the cathodic polarization could cause a partially reduction of the YSZ at Ni-YSZ interface. Thus, the electronic conduction[40]/ oxygen vacancy could be increased and result into a better performance by expanding the active sites further from the original TPB lines of the Ni-YSZ electrode.

4.2.2 Performance & durability: comparisons among the LSCF cells

The serial resistance (Rs) and Ni-YSZ TPB reaction resistance (R2) for the LSCF cells were summarized in Table 11 and Table 12.

Table 11 Degradation of the serial resistance (Rs) for the LSCF cells during galvanostatic durability test.

Cell Nr.	Current density (A/cm^2) & set-up	1st stage_Rs (hour)	Rs increase (Ω·cm^2)	Degra. Rate$^{(1)}$ (Ω·cm^2/Kh)	2nd stage_Rs (hour)	Rs_final (Ω·cm^2)	Degra. Rate$^{(1)}$ (Ω·cm^2/Kh)
T6	-1.5; normal	0 – 251 (0 – 701)	0.074 – 0.089 (0.074 – 0.127)	0.060	– 701	0.127	0.084 (0.076)
T7	-1.5; clean	0 – 700	0.063 – 0.085	0.031	–	0.085	0.031
T8	-2.0; normal	0 – 266	0.070 – 0.079	0.034	– 717	0.130	0.113
T9	-2.0; clean	0 – 394	0.066 – 0.088	0.056	– 683	0.121	0.114

(1) The difference between the initial and final resistance divided by the duration

Table 12 Degradation of Ni-YSZ TPB reaction resistance (R2) for the LSCF cells during galvanostatic test.

Cell Nr.	Current density (A/cm^2) & set-up	1st stage_R2 (hour)	R2 increase (Ω·cm^2)	Degra. Rate$^{(1)}$ (Ω·cm^2/Kh)	2nd stage_R2 plateau (hour)	R2_final (Ω·cm^2)
T6	-1.5; normal	0 – 251	0.024 – 0.186	0.645	– 701	– 0.186
T7	-1.5; clean	0 – 700	0.044 – 0.079	0.050	–	–
T8	-2.0; normal	0 – 170	0.045 – 0.118	0.430	– 717	– 0.122
T9	-2.0; clean	0 – 683	0.049 – 0.129	0.117	–	–

(1) The difference between the initial and final resistance divided by the duration

Degradations and evolutions of Rs: From the breakdown of in situ measured impedance during the test, significant increase of Rs can be found for all the LSCF cells and Rs was one of the two processes where the most severe degradations occurred. For example, the Rs of LSCF cell T8 (-2.0 A/cm^2; normal test) was 0.070 Ω·cm^2 at the beginning, accounting for 27 % of the ASR (0.261 Ω·cm^2); after 716.5 hours' operation the Rs increased by 89 % to 0.137 Ω·cm^2, accounting for 34 % of the ASR (0.402 Ω·cm^2).

In contrast to LSM cells, the LSCF cells showed a different profile for the increase of Rs during the test. The two cells (T6 and T7) operated at a current density of -1.5 A/cm^2 showed an almost linear increase of Rs throughout the test. The evolution of Rs degradation for the two cells tested at -2.0 A/cm^2 (cell T8 and T9) could be roughly divided into two stages: the 1st stage is ~300 hours from the beginning, where a slow increase of Rs can be observed, while for the later test periods, i.e. in the 2nd stage, the increase of Rs turned faster than in the 1st stage. This evolution of Rs was demonstrated by LSCF cell T6, T8 and T9 and a turning point (300 – 400 hours) was observed. For the 1st stage of Rs degradation, cell T6 (0.060 Ω·cm^2/Kh), T8 (0.034 Ω·cm^2/Kh) and T9 (0.056 Ω·cm^2/Kh) showed a low degradation rate, which is also of the same level with that of cell T7 (0.031 Ω·cm^2/Kh). However, in the 2nd stage, the Rs degradation of cell T6 (0.084 Ω·cm^2/Kh), especially T8 (0.113 Ω·cm^2/Kh) and T9 (0.114 Ω·cm^2/Kh) speeded up clearly. The distinct two stages for the evolution of Rs with test probably indicate two different mechanisms for Rs degradation.

Rs & oxygen electrode over-potential **(η_{ox}):** The YSZ degradation for SOECs operated under high current densities was hypothesized to be dependent of the large over-potentials at oxygen electrode.[29,43] Based on the equivalent circuit model used in this work, the oxygen electrode resistance consists of the oxygen ion transfer resistance (R1, mainly attributed to the oxygen electrode) and the TPB reaction resistance (R3). The (initial) oxygen electrode resistance was calculated to be 0.02 ~ 0.04 Ωcm^2 for the LSCF cells, only ⅓ to ½ of that of the LSM cells (0.06 ~ 0.08 Ωcm^2). Correspondingly, the η_{ox} of LSCF-CGO was significantly smaller than that of the LSM-YSZ electrode at the same current densities. This may imply that for a given η_{ox} without causing YSZ degradation, the LSCF cells could be operated at a current density two or three times higher than LSM cells. No significant increase of Rs has been reported for the similar SOECs at DTU Energy Conversion with a LSM-YSZ electrode tested at -0.5 or -0.75 A/cm^2, thus, with a better performing LSCF-YSZ electrode the SOEC cells are expected to be safely operated at -1.5 or -2.0 A/cm^2 without causing destructive build-up of pO_2 in YSZ electrolyte.

Rs & Ni-YSZ electrode degradation: Based on the post-test microstructure analysis, the YSZ electrolyte|CGO barrier layer|LSCF-CGO electrode interfaces were found to be intact. Thus, the oxygen electrode and the YSZ electrolyte were unlikely to make major contributions to such a significant increase of Rs. However, distinct microstructure changes were observed for the active Ni-YSZ electrodes: percolation loss of Ni particles was found for all the tested cells, no matter the current densities or impurity levels; besides, nano-particles formation (and Ni-YSZ contact loss) was observed for the other cells except T7 after similar durations. Ni percolation loss will result into an increase of the Ni-YSZ TPB resistance and even increase of Rs if the Ni-Ni connection loss is severe enough. The LVSEM images revealed that Ni particles lost almost all the percolations for the immediate a few microns thick Ni-YSZ electrode to the YSZ

electrolyte (thus forming a 'dead' zone), indicating probably an important contribution to the increase of Rs. Assuming an average of 3 µm thick layer for the 'dead' Ni-YSZ electrode with a porosity of 20 vol % and equal volume of Ni and YSZ, as well as a ionic conductivity of 0.05 S/cm for bulk YSZ, according to the Bruggeman's asymmetric media equation (insulator dispersion and conductor host)[44–46]:

$$\sigma_m = \sigma_h * (1 - f)^{3/2} \qquad (2)$$

where σ_m and σ_h is the conductivity of the composite and high conductivity phase respectively and f is the volume fraction of the poor conductivity phase, the increase of the ohmic resistance is estimated to be 0.023 Ω·cm^2, close to the Rs increase of cell T7 (ΔRs = 0.022 Ω·cm^2). Thus, the linear increase of Rs for cell T7 throughout the test could be mainly ascribed to Ni percolation loss, the only clearly observed structural changes for cell T7. And it is likely the major contribution to the Rs increase in the 1st stage for the other LSCF cells. However, the faster Rs increase in the 2nd stage indicates an additional influence to the cell. Nano-zirconia precipitating in the Ni-YSZ electrode of cell T6, T8 and T9 could result in contact loss between Ni particles and YSZ framework, thus contribute to the increase of ohmic resistance. (See Chapter 5 'Microstructure') Coincidently, according to the impedance break down for the durability tests, faster increase of Rs is observed at the same period when Ni-YSZ TPB reaction resistance leveled off (cell T6 & T8) or slowing down (cell T9), indicating a correlation between the degradation of Rs and Ni-YSZ TPB resistance. And the leveling off or slowing increases of the Ni-YSZ TPB resistance was proposed to closely relate to the precipitation of the nanoparticles (See Chapter 5 'Microstructure').

Degradation of Ni-YSZ TPB reaction: Apart from the degradation of Rs, significant increase of the Ni-YSZ TPB reaction resistance was observed for all the LSCF cells during the galvanostatic test. For example, the R2 of LSCF cell T8 (-2.0 A/cm^2; normal test) was 0.044 Ω·cm^2 at the beginning, accounting for 17 % of the ASR (0.261 Ω·cm^2); after 716.5 hours' operation the R2 increased by 145 % to 0.108 Ω·cm^2, accounting for 27 % of the ASR (0.402 Ω·cm^2), which increased by 54 % during the test.

Degradation of Ni-YSZ TPB reaction resistance & impurity: For LSCF cell T6 and T8 (higher impurity levels), the Ni-YSZ TPB reaction resistance (R2) increased fast and then reached a plateau after 250 hours' (cell T6) or 170 hours' operation (cell T8). As a contrast, cell T 7 and cell T9, which were tested using a clean set-up, showed slower but continuous increase of the Ni-YSZ TPB reaction resistance, without reaching a plateau. The difference of the R2 evolution indicates the impurities accelerated the degradation of Ni-YSZ TPB reaction process. The accumulation /segregation of impurities can decrease the numbers of the active sites by blocking the TPBs, resulting into a lower performance for electrode TPB reactions.

Degradation of Ni-YSZ TPB reaction resistance & current density: Using the same set-ups with a low impurity level, the cell operated at lower current densities showed a slower increase of R2 (cell T7, -1.5 A/cm^2; 0.05 Ω·cm^2/Kh) in comparison to the cell operated at higher current densities (cell T9, -2.0 A/cm^2, 0.12 Ω·cm^2/Kh). For the cells tested with the high impurity level, longer time was needed for R2 increasing to the plateau when operated at a lower current density, e.g. LSCF cell T6 (-1.5 A/cm^2, ~ 250 h) vs. LSCF cell T8 (-2.0 A/cm^2, ~ 170 h).

The plateau for the Ni-YSZ TPB reaction resistance: The Ni-YSZ TPB reaction resistance of cell T6 (-1.5 A/cm^2) finally leveled off at 0.18 ~ 0.19 Ω·cm^2, higher than that of cell T8 (0.12 Ω·cm^2), which operated at a higher current density of -2.0 A/cm^2. Apart from a higher cell temperature ($\Delta T < 5\ ^oC$), the lower plateau of R2 for the cell (T8) operated at the larger current could be mainly ascribed to the expansion of TPB length due to electronic conduction of YSZ locally at harsher operations as discussed before (lower pO_2 or larger polarizations of the Ni-YSZ electrode; note the polarizations resistance is the sum of R2, R4 and R5 rather than merely R2).

Cell T9, which was also tested at 2.0 A/cm^2 but with a low impurity level, showed a Ni-YSZ TPB resistance keeping increasing to 0.13 Ω·cm^2 without a plateau. However, the R2 increase of cell T9 slowed down for the final period, implying that it may finally level off for an extension of the duration, as was observed for cell T8, which was operated at the same current density but a higher impurity level. Comparing the Ni-YSZ TPB reaction resistance of cell T8 with that of T9, the impurities were found to shorten the time needed for R2 to level off but not result into a higher value of the final plateau. Based on the correlation of the electrochemical and microstructural analysis, it is proposed that activation of the Ni-YSZ TPB reactions by precipitating of the nano-zirconia compensated to some extent the degradation due to other factors.

4.2.3 Performance & durability: summary/comparison of LSM & LSCF cells

Degradation of Rs for LSCF cells vs. LSM cells: Based on the impedance analysis, the increase of Rs for the LSCF cells was much slower than that of the LSM cells at same conditions. For example, the Rs of LSCF cell T8 (-2.0 A/cm^2; normal test) increased by 89 % from 0.070 to 0.137 Ω·cm^2 after 716.5 hours operation, while a LSM cell T2 operated under the same condition for 676.7 hours showed 257 % increase of the Rs from 0.089 to 0.318 Ω·cm^2. Both LSCF cell T9 and LSM cell T5 were tested at -2.0 A/cm^2 with a clean set-up, however, the former showed an increase of Rs by 73 % from 0.070 to 0.121 Ω·cm^2 in 683 hours, while the later showed Rs increasing by 125 % from 0.080 to 0.180 Ω·cm^2 in 700 hours.

Oxygen electrode over-potential (η_{ox})*:* The more severe degradation of Rs for the LSM cells than the LSCF cells, especially the dramatic Rs increase in the initial period of ~ 100 hours after starting the test, could be related to the difference in the performance of the oxygen electrodes. Assuming the total polarization of the oxygen electrode consists the oxygen ion transfer resistance R1 and oxygen electrode TPB resistance R3, the (initial) oxygen electrode resistance is calculated to be 0.06 ~ 0.08 Ωcm^2 for the LSM cells and only 0.02 ~ 0.04 Ωcm^2 for the LSCF cells. As discussed before, the higher η_{ox} of LSM cells could contribute to a faster Rs increase with degradation of YSZ electrolyte.

Nanoparticle precipitation and Ni-YSZ contact: In addition, as discussed for the LSCF cells, the final stage of Rs increase is likely ascribed to the contact loss between Ni and YSZ, which is proposed to be mainly resulted from the precipitation of zirconia nanoparticles. Zirconia nanoparticles observed for all the other LSCF cells except T7 could account for the significant larger Rs degradation of these cells than that of cell T7. In comparison to other LSM cells (also LSCF cells), cell T5 showed significant slower Rs degradation for the final stage. The above explanation for LSCF cells seems also apply to the results of LSM cells: SEM observations confirmed that only limited amount of zirconia nanoparticles formed at Ni-YSZ|YSZ interface for LSM cell T5, while more nanoparticles were observed for the other LSM cells that showed larger degradations.

The plateau of the Ni-YSZ TPB reaction resistance: The first step of Ni-YSZ electrode degradation likely involved the impurity accumulation and segregation, Ni particle coarsening and Ni percolation loss. Notice that no matter the initial value of Ni-YSZ TPB reaction resistance, it increased and stabilized at a similar level after degradation under the same operations. It is hypothesized that when the critical condition (local pO_2, e.g.) was reached, the zirconia nanoparticle precipitation would result into a self-compensation effect, stabilizing the polarization resistance of the Ni-YSZ electrode. However, before reaching the plateau the precipitation of zirconia could already start, as revealed by LSM cell T4. The more degradation of Ni-YSZ due to any other factors would lead to the larger amount of nano-zirconia precipitation thus finally the stabilization of the performance.

Summit frequency for the Ni-YSZ TPB reaction process: Corresponding to the increase of the Ni-YSZ TPB reaction resistance for the LSM cells during the galvanostatic operation, a peak position was observed to shift from a few KHz, the initial peak position of the Ni-YSZ TPB process, towards ~1 KHz (LSM cell T1 or T2) or even lower to ~ 700 Hz (LSM cell T3), which was close to peak position of the LSM-YSZ TPB reaction process. Because of the close peak position for the LSM-YSZ and Ni-YSZ TPB processes under operations, it is not straightforward to attribute the peak position shift to which of two electrodes. However, based on

the analysis for the LSCF cells, which showed peak position of the oxygen electrode far away from that of Ni-YSZ TPB process, the peak position shift during test is readily attributed to Ni-YSZ rather the oxygen electrode.

4.3 Nano-zirconia precipitation

The critical condition for nano-zirconia precipitation: Based on the experimental results, the precipitation of the nano-zirconia was likely to be dependent on the cell performance (e.g. polarization and current density) under galvanostatic operation. The over-potential thus the oxygen partial pressure (pO_2) at the Ni-YSZ|YSZ interface can be estimated based on the final electrochemical performance. As was observed for cell T4, the zirconia nanoparticles could start for some regions already before the Ni-YSZ TPB resistance of the total cell reaching a plateau. Assuming a constant ohmic resistance Rs, oxygen ion transfer resistance R1 and LSM-YSZ TPB resistance R3 for the current-voltage relationship of the cell, deducting the voltage drop due to the Rs (0.203 $\Omega\cdot cm^2$), the R1 (0.044 $\Omega\cdot cm^2$) and the R3 (0.024 $\Omega\cdot cm^2$) from the final cell voltage (1765 mV) of cell T4 under galvanostatic operation at -2.0 A/cm^2, the potential difference of the Ni-YSZ electrode vs. 1 atm O_2 was calculated to be 1123 mV, corresponding to a $pO_2 \sim 10^{-22}$ atm versus 1 atm O_2 for the oxygen electrode at 875 ^oC. The final value of the Rs and R3 was used for the calculation; however, the initial value of the R1 was still used as the final contribution of LSM-YSZ|YSZ interface, because the degradation of the oxygen ion transfer for entire cell was mainly ascribed to the Ni-YSZ|YSZ interface while the LSM-YSZ|YSZ appeared to change little. The Ni-YSZ|YSZ interfacial pO_2 was calculated for all the other cells and the results are given in Table 13. Cell T7, on which no zirconia nanoparticle was observed, showed a Ni-YSZ interfacial pO_2 ($\sim 10^{-19}$) 2 ~ 3 orders higher than that of the other cells. Corresponding to the occurrence of nano-zirconia precipitation, all the other cells showed a close level of Ni-YSZ interfacial pO_2 at $10^{-21} \sim 10^{-22}$ atm, no matter the cell type or test set-up. Therefore, the critical condition for precipitation of zirconia nanoparticles in the Ni-YSZ electrode as tested is derived to be a potential difference larger enough ($\sim 1.19 \pm 0.03$ V) for the Ni-YSZ electrode versus oxygen electrode in 1 atm. O_2, or a sufficient low pO_2 ($10^{-21} \sim 10^{-22}$ atm) at the Ni-YSZ|YSZ interface under cathodic polarization. It should be noted that this is a significantly higher pO_2 than the pO_2 necessary to reduce ZrO_2 to metallic Zr: the reduction of to metallic Zr corresponds to a pO_2 of 10^{-41} atm. based on the Gibbs energy of ZrO_2 and Nernst equation. Even the calculation of the thermodynamic phase diagram of Ni-ZrO_2 predicts a pO_2 ($\sim 10^{-29}$ atm.)[47] still much lower than the experimental value presented above.

Table 13 Estimation of the Ni-YSZ|YSZ interfacial oxygen partial pressure (pO_2) based on the final cell performance under galvanostatic operation. Note both the measured impedance and the calculations below represent the average of the performance for the entire cell area.

Cell Nr.	Current density_i (A/cm^2)	Final cell voltage_V (mV)	Ohmic resistance & Oxygen electrode polarization_R' (R' = Rs + [(1)] R1 + R3) ($\Omega \cdot cm^2$)	Derived voltage contribution of Ni-YSZ_V_{Ni} ([(2)] V_{Ni} =V – i * R') (mV)	Ni-YSZ|YSZ interfacial [(3)] pO_2 vs. 1atm O_2 (atm.)
T1	-1.5	1785	0.406	1176	2.2E-21
T2	-2.0	2001	0.393	1215	4.6E-22
T3	-2.0	1880	0.355	1170	2.8E-21
T4	-2.0	1765	0.271	1223	3.3E-22
T5	-2.0	1680	0.237	1206	6.6E-22
T6	-1.5	1399	0.162	1156	5.0E-21
T7	-1.5	1193	0.100	1043	4.8E-19
T8	-2.0	1522	0.178	1166	3.3E-21
T9	-2.0	1463	0.150	1163	3.8E-21

[(1)] Assuming a constant contribution from the LSM-YSZ|YSZ interface to the oxygen ion transfer resistance since the degradation of the oxygen ion transfer was mainly due to the Ni-YSZ|YSZ instead of the LSM-YSZ|YSZ interface;

[(2)] The voltage The EIS measured under current represents the local slope of the i-V curves at that current. Because Rs, R1 and R3 are not sensitive to the cell polarization (See Chapter 3), the voltage due to Rs, R1 and R3 can be simply calculated as the product of current and resistance. As a consequence, the contribution from the Ni-YSZ electrode the cell to voltage can be obtained by subtracting the remaining contributions (Rs, R1 and R3) from the cell voltage. The voltage contribution of Ni-YSZ electrode cannot be directly calculated as the product of current and resistance because the resistance of the Ni-YSZ electrode changes upon current density (See Chapter 3). It can be calculated by an integration method, which is unfeasible here however.

[(3)] Calculation corresponding to the cell temperature at 875 ^oC.

5 Conclusions

Galvanostatic co-electrolysis of steam and carbon dioxide was performed on solid oxide cells under high current densities of -1.5 and -2.0 A/cm^2 at ~ 875 ^oC. Two types of cells with different oxygen electrodes and two set-ups with different impurity level were used for the electrolysis test. Except the short-term ones for studying the degradation evolutions, most of the tests were performed for approximately700 hours. The LSM cells generally showed a faster and larger increase in cell voltage than the LSCF cells. The cells with lower impurity levels showed a slower and smaller increase in cell voltage than the cells with higher impurity levels.

According to a comprehensive electrochemical analysis, the degradation of the cell performances was mainly due to the increase in the serial resistance (Rs) and the Ni-YSZ TPB reaction resistance (R2). The interfacial oxygen ion transfer resistance (R1) also increased after the degradation test, but minor increase was observed for the oxygen electrode TPB reaction resistance (R3).

Significant increase in Rs was observed at the beginning of the test for LSM cells, which could be ascribed to the ohmic resistance increase of the YSZ electrolyte under large over-potential of the oxygen electrode (LSM-YSZ) during electrolysis. Corresponding to the dramatic increase of Rs at the beginning, significant decrease of Rs (relaxation) was observed when removing the polarization for LSM cells after test. When applying current again, the Rs rapidly rose up to the previous level. This responding of Rs to current density (polarization) could be ascribed to the transient change in the YSZ electrolyte under large over-potential of oxygen electrode for the LSM cells. The exact mechanism requires a detailed study in future. Increase in Rs for the later period of the test was also ascribed to a severe percolation loss of Ni particles and contact loss between the Ni and YSZ at the active cathode close to YSZ electrolyte.

The increase in the high frequency oxygen ion transfer resistance could be due to the structural change in the interface between the Ni and YSZ rather than that in the interface between the oxygen electrode and electrolyte, as the latter was observed to be almost unchanged by post-test microstructural observations.

The increase in the Ni-YSZ TPB reaction resistance was due to the accumulation/segregation of impurity from internal and external sources, the coarsening and percolation loss of Ni particles. The above structural/compensational changes were observed primarily at the Ni-YSZ active electrode immediate to the YSZ electrolyte (See Chapter 5 'Microstructure'). The faster increase in the Ni-YSZ TPB reaction resistance at the early stage of the durability test was mainly ascribed to the higher impurity level and the higher current density /cathodic over-potential. The higher impurity level accelerated the degradation rate at the beginning but did not affect the final values of the Ni-YSZ TPB resistance significantly. The reason could be that the impurity blocking the Ni-YSZ TPBs was finally removed from the TPBs by reduction and incorporation into the Ni grains under large cathodic polarization (See Chapter 5 'Microstructure'), apart from removal by the gas flow.

Slowing down of the increase or a plateau of the Ni-YSZ TPB resistance was observed during the test and a stabilization mechanism was proposed: the inclusion of the impurities in Ni grains and more importantly, the self-mediated precipitation of the zirconia nanoparticles resulted in a compensating effect for the degradation of the Ni-YSZ electrode. Corresponding to the fast increase in the Ni-YSZ TPB reaction

resistance, the summit frequency generally decreased rapidly from a few KHz to 1 ~ 2 KHz. As the Ni-YSZ TPB resistance leveling off, the summit frequency finally stabilized at ~ 1 KHz or even as low as ~ 600 Hz.

Last, the critical conditions for the precipitation of zirconia nanoparticles in the Ni-YSZ electrode at ~ 875 ^{o}C was estimated to be: an oxygen partial pressure as low as 10^{-21} ~ 10^{-22} atm at the Ni-YSZ|YSZ interface versus 1 atm O_2 for oxygen electrode, or a large cathodic over-potential on the Ni-YSZ electrode equivalent to a potential difference of ~ 1.19 ± 0.03 V versus oxygen electrode in 1 atm O_2.

References

1. S. H. Jensen, P. H. Larsen, and M. Mogensen, *Int. J. Hydrogen Energy*, **32**, 3253–3257 (2007)

2. A. Hauch, S. H. Jensen, S. Ramousse, and M. Mogensen, *J. Electrochem. Soc.*, **153**, A1741 (2006)

3. A. Hauch, S. D. Ebbesen, S. H. Jensen, and M. Mogensen, *J. Mater. Chem.*, **18**, 2331–2340 (2008)

4. A. Brisse, J. Schefold, and M. Zahid, *Int. J. Hydrogen Energy*, **33**, 5375–5382 (2008)

5. J. Schefold, A. Brisse, and F. Tietz, *J. Electrochem. Soc.*, **159**, A137 (2012)

6. A. Brisse and J. Schefold, *Energy Procedia*, **29**, 53–63 (2012)

7. J. S. Herring et al., *Int. J. Hydrogen Energy*, **32**, 440–450 (2007)

8. C. M. Stoots, J. E. O'Brien, K. G. Condie, and J. J. Hartvigsen, *Int. J. Hydrogen Energy*, **35**, 4861–4870 (2010)

9. X. Yang and J. T. S. Irvine, *J. Mater. Chem.*, **18**, 2349 (2008)

10. X. Yue and J. T. S. Irvine, *Solid State Ionics*, **225**, 131–135 (2012) 11. R. Knibbe, A. Hauch, J. Hjelm, S. D. Ebbesen, and M. Mogensen, *Green*, **1**, 141–169 (2011).

12. M. A. Laguna-Bercero, *J. Power Sources*, **203**, 4–16 (2012)

13. S. D. Ebbesen, C. Graves, and M. Mogensen, *Int. J. Green Energy*, **6**, 646–660 (2009)

14. C. M. Stoots, J. E. O'Brien, J. S. Herring, and J. J. Hartvigsen, *J. Fuel Cell Sci. Technol.*, **6**, 011014 (2009)

15. S. D. Ebbesen, C. Graves, A. Hauch, S. H. Jensen, and M. Mogensen, *J. Electrochem. Soc.*, **157**, B1419–B1429 (2010)

16. S. D. Ebbesen, R. Knibbe, and M. Mogensen, *J. Electrochem. Soc.*, **159**, F482–F489 (2012)

17. C. Graves, S. D. Ebbesen, M. Mogensen, and K. S. Lackner, *Renew. Sustain. Energy Rev.*, **15**, 1–23 (2011)

18. X. Sun et al., *Int. J. Hydrogen Energy*, **37**, 17101–17110 (2012)

19. A. Hauch, S. H. Jensen, S. Ramousse, and M. Mogensen, *J. Electrochem. Soc.*, **153**, A1741 (2006)

20. A. Hauch, S. H. Jensen, J. B. Bilde-Sørensen, and M. Mogensen, *J. Electrochem. Soc.*, **154**, A619 (2007)

21. A. Hauch, J. R. Bowen, L. T. Kuhn, and M. Mogensen, *Electrochem. Solid-State Lett.*, **11**, B38 (2008)

22. S. D. Ebbesen and M. Mogensen, *Electrochem. Solid-State Lett.*, **13**, B106 (2010)

23. A. Momma, T. Kato, Y. Kaga, and S. Nagata, *J. Ceram. Soc. Japan*, **105**, 369–373 (1997).

24. J. Guan et al., *High Performance Flexible Reversible Solid Oxide Fuel Cell, GE global Research Center Final Report for DOE Cooperative Agreement No. DE-FC36-04GO-14351, NTIS Order No. DE2007-899650*, (2006).

25. J. R. Mawdsley, J. David Carter, A. Jeremy Kropf, B. Yildiz, and V. A. Maroni, *Int. J. Hydrogen Energy*, **34**, 4198–4207 (2009)

26. M. A. Laguna-Bercero, R. Campana, A. Larrea, J. A. Kilner, and V. M. Orera, *J. Power Sources*, **196**, 8942–8947 (2011)

27. M. S. Sohal et al., *J. Fuel Cell Sci. Technol.*, **9**, 011017 (2012)

28. T. Jacobsen and M. Mogensen, *ECS Trans.*, **13**, 259–273 (2008).

29. R. Knibbe, M. L. Traulsen, A. Hauch, S. D. Ebbesen, and M. Mogensen, *J. Electrochem. Soc.*, **157**, B1209 (2010)

30. M. J. Jørgensen and M. Mogensen, *J. Electrochem. Soc.*, **148**, A433–A442 (2001)

31. P. H. Larsen et al., in *Proceedings of Solid Oxide Fuel Cell VII (SOFC VII)*, S. C. Singhal and H. Yokokawa, Editors, p. 28–37, Electrochemical Society, Pennington, NJ (2001)

32. S. Linderoth et al., *Mater. Sci. Forum*, **539-543**, 1309–1314 (2007)

33. N. Christiansen et al., *ECS Trans.*, **25**, 133–142 (2009).

34. S. H. Jensen et al., *J. Electrochem. Soc.*, **154**, B1325 (2007)

35. H. Schichlein, A. C. Müller, M. Voigts, A. Krügel, and E. Ivers-Tiffée, *J. Appl. Electrochem.*, **32**, 875–882 (2002).

36. R. Barfod et al., *J. Electrochem. Soc.*, **154**, B371 (2007)

37. R. Barfod, a. Hagen, S. Ramousse, P. V. Hendriksen, and M. Mogensen, *Fuel Cells*, **6**, 141–145 (2006)

38. S. D. Ebbesen and M. Mogensen, *ECS Trans.*, **50**, 167–182 (2013).

39. S. Primdahl and M. Mogensen, *J. Electrochem. Soc.*, **146**, 2827–2833 (1999).

40. Y. Tao, S. D. Ebbesen, W. Zhang, and M. B. Mogensen, *submitted* (2013).

41. J. Park and R. N. Blumenthal, *J. Electrochem. Soc.*, **136**, 2867–2876 (1989).

42. F. Tietz, D. Sebold, A. Brisse, and J. Schefold, *J. Power Sources*, **223**, 129–135 (2013)

43. T. Jacobsen and M. Mogensen, *ECS Trans.*, **13**, 259–273 (2008).

44. D. W. Dees, T. D. Claar, T. E. Easler, D. C. Fee, and F. C. Mrazek, *J. Electrochem. Soc.*, **134**, 2141 (1987)

45. R. Landauer, in *AIP Conference Proceedings*, J. C. Garland and D. B. Tanner, Editors, vol. 40, p. 2–45, American Institute of Physics, New York (1978)

46. D. S. Mclachlan, M. Blaszkiewicz, and R. E. Newnham, *J. Am. Ceram. Soc.*, **73**, 2187 (1990).

47. M. Chen et al., *J. Electrochem. Soc.*, **160**, F883–F891 (2013).

Appendix: Limited changes for the oxygen electrode

Electrochemical performance of the cell at OCV before and after durability test—Limited changes for the oxygen electrode

1. LSM cell T2: ADIS for the impedance at OCV before vs. OCV after 359 hours' test at -2.0A/cm^2

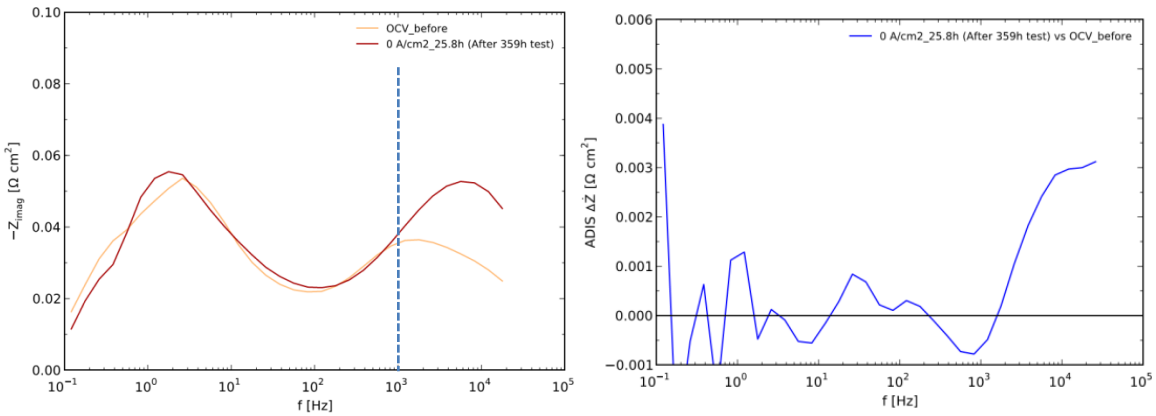

Degradation was observed mainly at frequency above 1 KHz, the frequency range of Ni-YSZ TPB reaction and oxygen ion transfer process; little change was observed for the LSM-YSZ electrode, which had a characteristic frequency of a few hundreds to 1 KHz.

2. LSM cell T4:

LSM gas shift at OCV after test: ~ 700 Hz

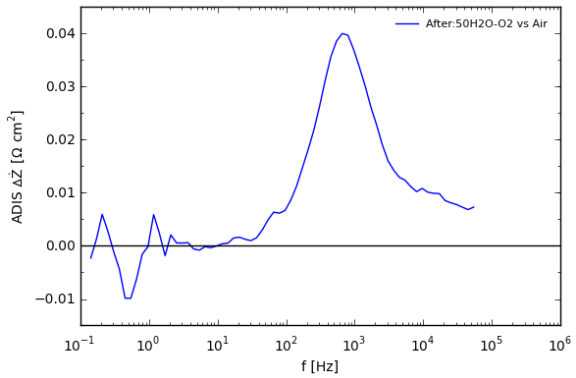

ADIS for the Impedance measured at OCV after vs. before test:

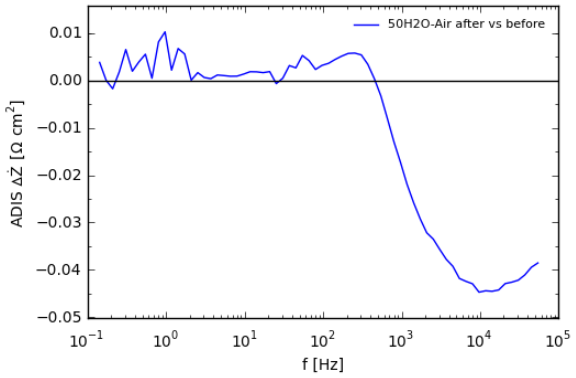

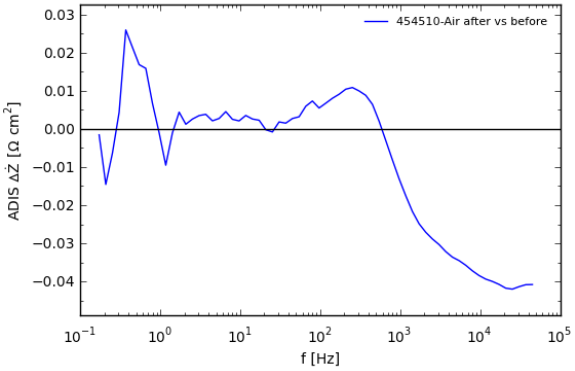

Significant change was observed for the process at above 1 KHz and little change below 1 KHz. Correspondingly, electrode degradation was mainly ascribed to the Ni-YSZ TPB reaction and high frequency oxygen ion transfer process, while little degradation occur at the LSM-YSZ electrode.

3. LSCF cell T7:

LSCF-CGO electrode gas shift at OCV after test: peak frequency ~ 200 Hz

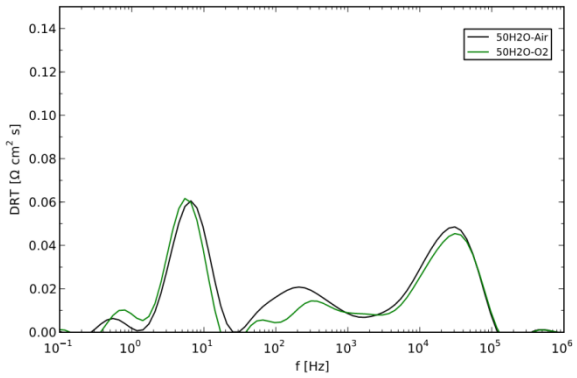

Ni-YSZ electrode gas shift at OCV after test: peak frequency ~ 10 KHz

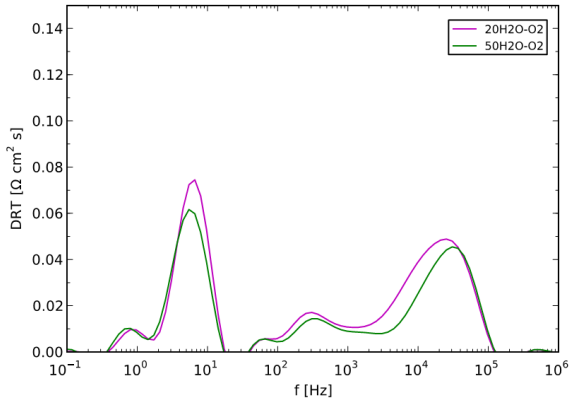

ADIS for the Impedance measured at OCV after vs. before test:

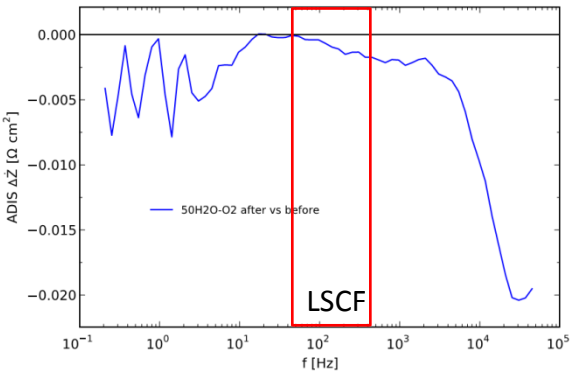

Degradation occurred mainly for the process at above 6 KHz, which was ascribed to Ni-YSZ TPB reaction and high frequency oxygen ion transfer process. Limited changes was observed for the LSCF-CGO electrode, which has a peak frequency of 100 ~ 200 Hz.

4. **Same ADIS results were observed for LSCF cell T6:** OCV before vs. after

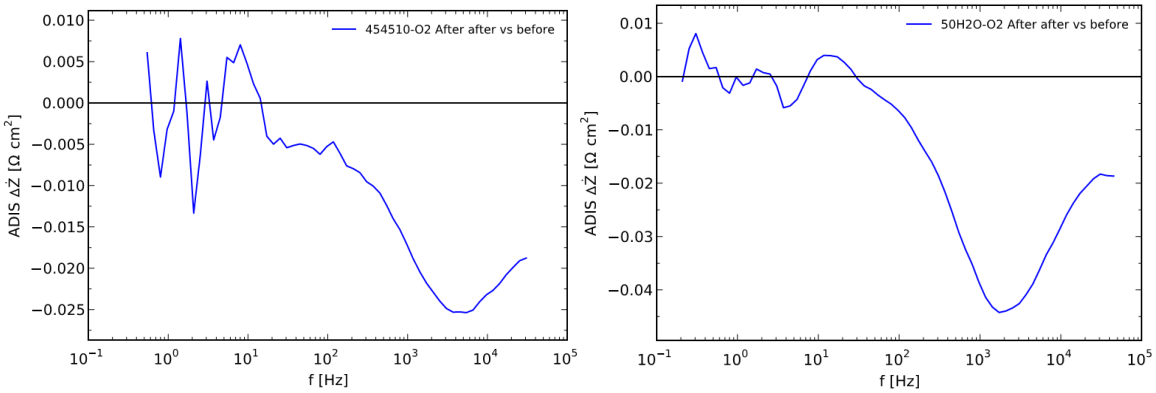

5. Same ADIS results were observed for LSCF cell T8: OCV before vs. after

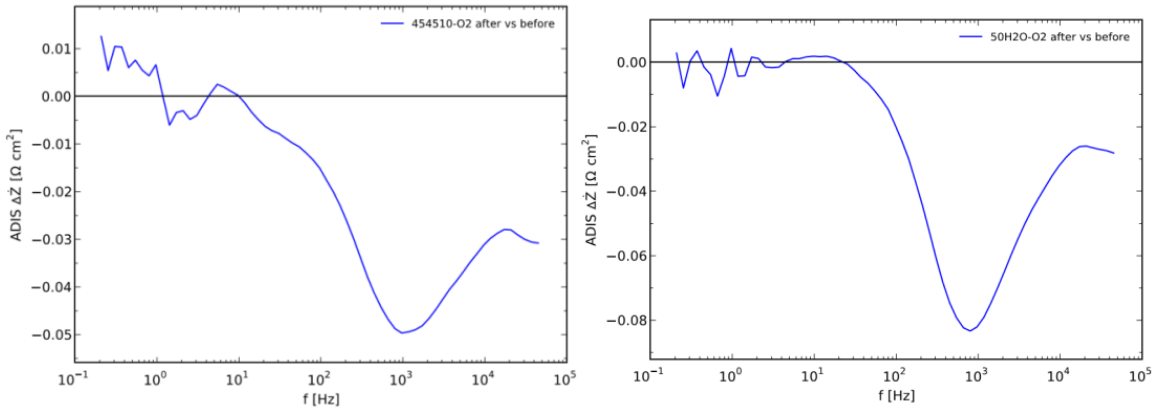

Chapter 5 Durability of SOECs for Co-Electrolysis of H_2O and CO_2 under High Current Densities: II. Microstructural Analysis

1. Introduction

In Chapter 4, the electrochemical analysis was performed for the SOECs (T1 – T9), which were tested at various conditions for investigating the durability of these cells for co-electrolysis of steam and CO_2. The micro-structural and micro-compositional changes of the cells should be responsible for the changes of the electrochemical performance. In this chapter, the analysis of the post-test microstructure/composition was performed for these tested cells. The degradation mechanism of the SOECs will be discussed based on a correlation of the results from the electrochemical and the microstructure/composition analysis.

2. Experimental

2.1 Solid oxide cells:

Two types of planar solid oxide cells developed at DTU Energy Conversion were used for the durability tests. One type of the cells has a configuration of ~ 300 µm Ni-YSZ support | ~ 15 µm Ni-YSZ active electrode | ~ 10 µm YSZ electrolyte | ~ 15 µm LSM-YSZ electrode, which will be referred to as 'LSM cell' in the latter text. The other type of cells has a configuration of ~ 300 µm Ni-YSZ support | ~ 15 µm Ni-YSZ active electrode | ~ 10 µm YSZ electrolyte | ~ 5 µm CGO | ~ 15 µm LSCF-YSZ electrode, which will be mentioned as 'LSCF cell'.

2.2 Normal test and clean test

The tests can be divided into two categories, the 'normal test' and the 'clean test', according to the types of the set-up and gas processing. For the normal tests, albite glass bars were used as sealing for both the cathode and anode and the cell was exposed to a relatively high level of impurities (Si, etc.). Ni-YSZ or LSM cermet was used respectively on the Ni-YSZ or oxygen electrode side as the gas distributor/current collector. Gas CO_2 and H_2 as received (with S, etc. impurities of ~ppb) were flown to the cell directly. For the clean test, metal frame was used as the sealing on both electrodes. Ni mesh was used as the contact on the Ni-YSZ electrode and Pt mesh for oxygen electrode. CO_2 and H_2 were cleaned by a gas cleaner to remove the impurities before supplied to the cell. All the cells were heated up to 1000 ^oC and kept for 2 hours for sealing at the beginning. Then, 20 L/h 9 % H_2 in N_2 was flown to the cell for 2 hours to obtain Ni-YSZ electrode by the reduction of NiO-YSZ. Afterwards, 25 L/h 4 % H_2O + 96 % H_2 was flown to Ni-YSZ and 140

L/h Air was flown to oxygen electrode for 1 hour. Finally, the cell was cooled down to 850 ^{o}C for initial performance study.

2.3 Galvanostatic durability test

The cells were then operated at 850 ^{o}C with 45 % H_2O + 45 % CO_2 +10 % H_2 flown to Ni-YSZ and O_2 to oxygen electrode. The current density was increased by steps to the value at which the galvanostatic test is intended to operate (-1.5 or -2.0 A/cm^2). Impedance was recorded at each step after keeping the cell at that current density for 15 minutes. For the LSM cells, after increasing current density from 0 to -1.5 or -2.0 A/cm^2, the cell temperature (T_center probe) could increase to ~ 865 ^{o}C due to ohmic heating of the cell. For the LSCF cells, the temperature increase was lower due to the lower cell resistance than LSM cells; thus, for direct comparison of the performance between the two different types of cells at a similar cell temperature, cell temperature was lift up to ~ 865 ^{o}C by the control of the furnace temperature. During the long term galvanostatic operation, cell voltage was recorded every 2 minutes and EIS was recorded periodically, e.g. every 6 hours. With the cell degradation, the cell voltage could increase by a few hundred millivolts. The tests were stopped when the duration reaching ~ 700 hours or the cell voltage reaching ~ 2000 mV. Due to the cell voltage increase, the cell temperature increased to ~ 875 ^{o}C finally. A summary of the test information is provided in Table 14. After the durability test, the current density was stepped down to zero with EIS recorded. For some cells after test, gas variation and EIS measurement were performed at OCV again. The cells were then cooled down with H_2 (> 630 ^{o}C) and 9 % H_2 in N_2 (< 630 ^{o}C) flown to the Ni-YSZ electrode.

Table 14 Set-up and operations for the long term durability tests

Cell Nr.	Current Density (A/cm^2)	Oxygen Electrode	Current Collector & Sealing	Gas Clean	Duration (hours)	Final voltage (mV)
T1	-1.5	LSM-YSZ	Ni-YSZ/LSM; Glass Bar	No	681.5	1785
T2	-2.0	LSM-YSZ	Ni-YSZ/LSM; Glass Bar	No	678.0	2001
T3	-2.0	LSM-YSZ	Ni-YSZ/LSM; Glass Bar	No	501.8	1880
T4	-2.0	LSM-YSZ	Ni-YSZ/LSM; Glass Bar	No	138.3	1765
T5	-2.0	LSM-YSZ	Metal Mesh; Frame	Yes	699.5	1680
T6	-1.5	LSCF-CGO	Ni-YSZ/LSM; Glass Bar	No	707.0	1399
T7	-1.5	LSCF-CGO	Metal Mesh; Frame	Yes	712.4	1193
T8	-2.0	LSCF-CGO	Ni-YSZ/LSM; Glass Bar	No	720.7	1522
T9	-2.0	LSCF-CGO	Metal Mesh; Frame	Yes	682.8	1463

25 L/h 45 % CO_2 + 45 % H_2O + 10 % H_2 to the Ni-YSZ electrode and pure O_2 to the oxygen electrode; Initial cell temperature at ~ 865 ^{o}C under operation and increased to ~ 875 ^{o}C due to degradation;

2.4 Analysis of the Post-test Microstructure

After test, the cells were dismounted carefully at room temperature. Then the microstructures for all the other cells except T9 were examined. The microstructures of cell T9 was not relevant to the durability test due to the gas supply problem when stopping the test, therefore the microstructural analysis of cell T9 was not examined. In order to study the difference in the microstructures of the cell along gas flow direction, fragments of the cell close to inlet, center and outlet were investigated. Two types of cross-section samples were prepared for each cell: 1) fractured samples, which can provide the intact surface details of the electrodes and 2) polished cross-sections, which were casted in epoxy followed by polishing. The second type of sample was impregnated with epoxy which was hardened for 12 hours, in order to maintain the porous framework and other structure details during polishing. The final polishing procedure were carried out using three kinds of fine diamond sands with decreasing particle size (6, 3 and 1 μm in sequence), in order to get a smooth surface and avoid contaminations from the polishing media. The polished samples were suitable for (Ni) percolation and elemental analysis. The scanning electron microscopy (SEM) (Zeiss Supra 35) and energy dispersive X-ray spectroscopy (EDS) were used for the microstructure and composition analysis. The imaging and EDS analysis was normally performed at 5 ~ 15 KeV and the Ni percolation analysis were performed at 0.9 or 1 KeV in inlens mode.

Transmission electron microscopy (TEM) and EDS analysis under TEM were performed for cell T2 and T3. The sample preparation for TEM analysis includes mechanical polishing and FIB thinning. Two pieces of cell were sandwiched together in epoxy at 140 ^{o}C for 10 min. Then the samples were mechanically polished to a thickness of ~ 20 μm and further thinned to ~ 100 nm by focused ion beam (FIB) milling. The FIB milling was performed using a Carl Zeiss 1540 XB FIB-SEM operating at 30 KV and a probe current of 50 pA. The final step of FIB 'polishing' was carried out at 5 KV and a probe current of 50 pA in order to reduce the amorphous surface layer and Ga-ion implantation. A JEM-3000F microscopy operated at 300 KV was used for the transmission electron microscopy (TEM). Elemental maps and line scan profiles were obtained from EDS analysis of the sample in scanning transmission electron microscopy (STEM) mode with the probe size of ~ 1 nm.

3. Results—Post-test microstructural analysis

3.1 Ni-YSZ electrode

3.1.1 Normal tests — SEM (T1, T2, T4, T6 & T8)

Cell T1, T2, T4, T6 & T8 were tested using the normal un-cleaned set-up at a current density of -1.5 A/cm^2 or -2.0 A/cm^2 for 140 — 720 hours. (See Chapter Electrochemistry) The structral changes in the Ni-YSZ electrode after test are shown in this section, especially about the nano-scaled precipitates, which were widely observed at Ni-YSZ electrode|YSZ electrolyte interface.

Details & Distributions of the nano-precipitates in the local Ni-YSZ electrode:

Cell T2: Inlet & Outlet

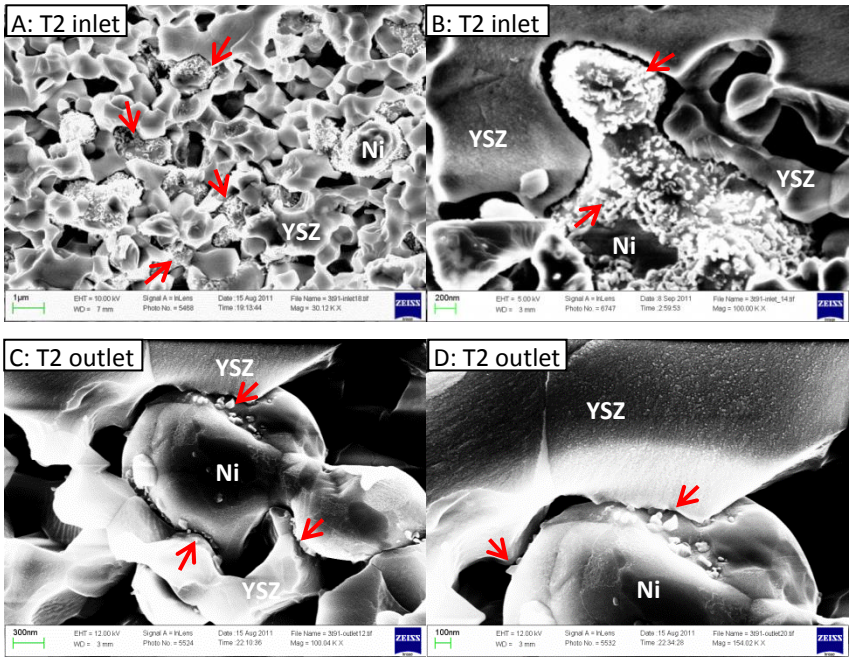

Figure 35. Ni-YSZ electrode of cell T2 after durability test: A) an overview and B) zooming in of the Ni-YSZ electrode at cell inlet; C) & D) Ni-YSZ electrode at cell outlet.

Figure 35 (cell T2) shows a typical Ni-YSZ electrode after durability test. A number of nano-scaled precipitates were found over the Ni surfaces at the Ni-YSZ contacts, the TPBs and the open pores. Generally, the precipitates were less than 100 nm in diameter. Some precipitates appeared to be well binded to the Ni particles while others were loosely connected to the Ni surface. Nano-precipitates were not found on the surfaces of YSZ (or YSZ-pore interface). At the inlet of cell T2, nano-precipitates can be found in the Ni-YSZ electrode up to ~ 8 µm away from the YSZ electrolyte, but most of the precipitates located on the Ni particles within 5 — 6 µm away from the electrolyte. Within this region, no obvious decrease in the amount of the precipitates was found with increasing the distance. When exceeded the 5 — 6 µm limitation, the amount of the precipitates dropped clearly. Gaps with a width of ~ 50 nm were found between Ni and YSZ, indicating a connection loss. At the cell outlet, the precipitates were much fewer and confined within a

region of ~ 3 µm to the YSZ electrolyte. The precipitates were found only at Ni-YSZ contacts or very close neighbouring regions of TPBs, but were rarely seen on the Ni surface at open pores.

Cell T6: Inlet & Outlet

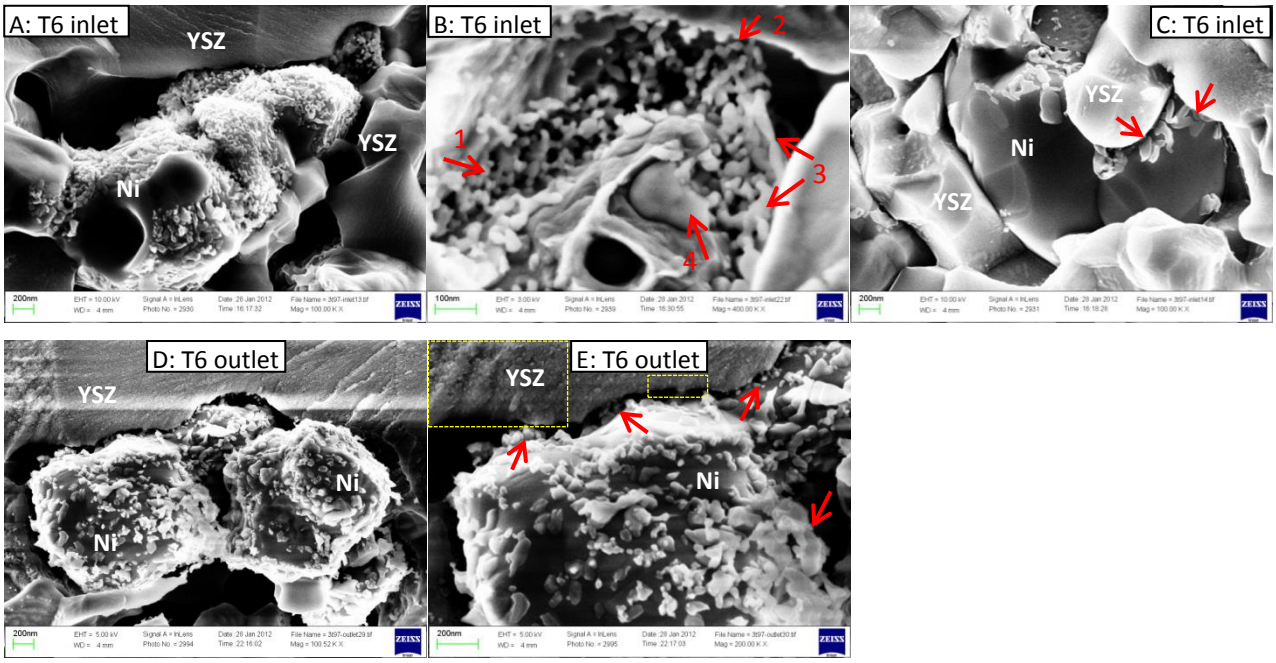

Figure 36. Ni-YSZ electrode of cell T6 after durability test: A) & B) Ni-YSZ electrode close to electrolyte and C) ~ 5 µm to the electrolyte at cell inlet; D) & E) Ni-YSZ electrode and YSZ electrolyte at cell outlet.

Figure 36 reveals a large amount of nano-particles covering the Ni grains in the Ni-YSZ electrode of cell T6 close to the YSZ electrolyte both at the inlet and the outlet. Beside the ones attached closely to the surface of the Ni grains, nanoparticles loosely spreaded on the surfaces of the Ni grains, the YSZ electrolyte, and between them were also observed (indicated as '2' in Figure 36B). The images of high magnification showed a rough YSZ surface at the Ni-YSZ contacting points. The nanoparticles were approximately 20 to 50 nm in diameter. Flake-like particles (indicated as '3') and large agglomerations (indicated as '4') of a few smaller particles were also observed.

Nanoparticles of similar morphology were observed at cell outlet as well. Moreover, the YSZ electrolyte, marked by the yellowsquares, showed a rough surface at the Ni-YSZ|YSZ interface as indicated in Figure 36E. Especially, some larger bumps of YSZ were in the same scale of the smallest nanoparticles covering Ni. Meanwhile, loosely stacked nanoparticles were observed between the Ni grains and YSZ electrolyte (Figure 36E). Significant amounts of nano-precipitates were found at both the inlet and outlet of cell T6.

Cell T4 inlet & cell T8 outlet:

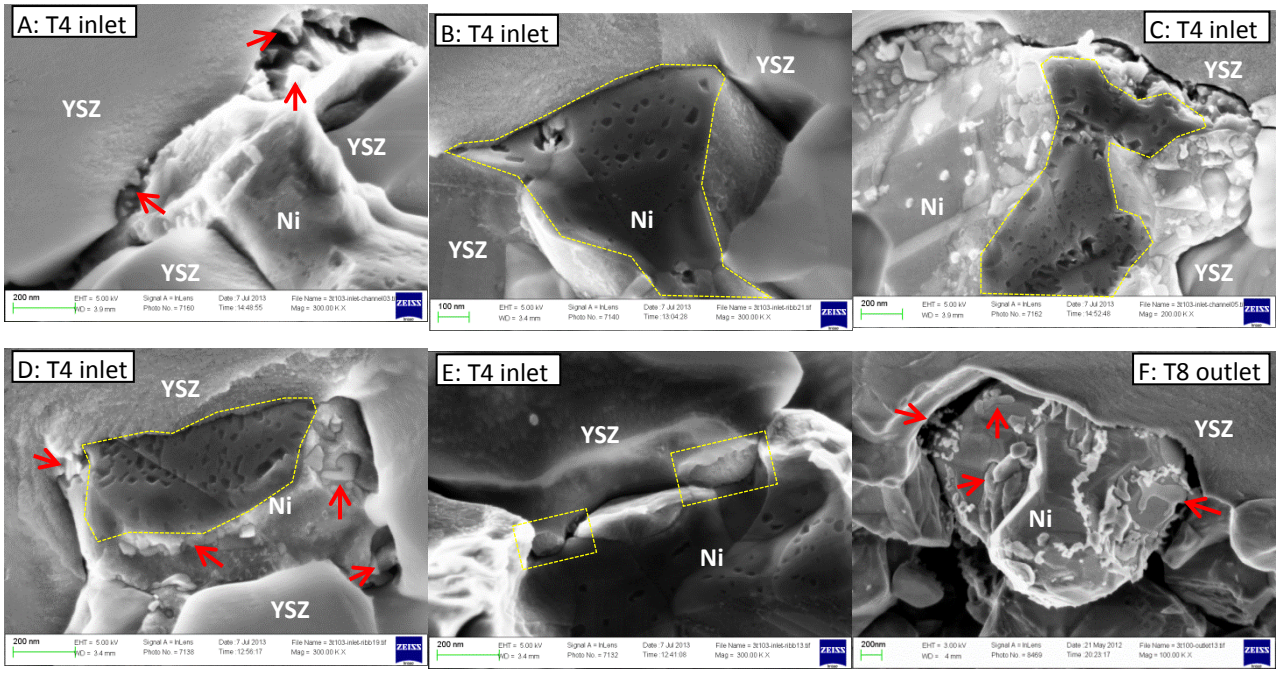

Figure 37. A) – D) Ni-YSZ electrode | YSZ electrolyte at inlet of cell T4 after durability test and E) YSZ at a distance of ~ 1 µm to the electrolyte; F) Ni-YSZ electrode | YSZ electrolyte for cell T8 outlet.

The Ni-YSZ electrode of LSM cell T4, which was tested for a shorter period (138 hours), showed a different post-test structure with other cells tested for a longer duration. As an important feature shown in Figure 37, lots of pits can be observed on Ni at the previous Ni-YSZ contact interface. Because Ni-Ni detachment was hardly found through intensive microstructural observations on the polished cross-sections for all the tested cells, the darker region (encircled by yellow lines in Figure 37B, C & D) on Ni should not be attributed to the Ni-Ni connecting. As a contrary, Ni-YSZ detachment was widely observed for the Ni-YSZ electrodes after test. Thus, the encircled region on Ni was ascribed to the previous interface between Ni and YSZ. The detachment was due to the broken off of the cell for SEM observation. It seems the Ni-YSZ connecting was still very firm before breaking off the cell. The pits appear to be distributed randomly at the interface and the size of the pits was a few tens nanometer (below ~50 nm), close to the particle size of the precipitates normally observed on Ni surface. At the Ni|pore interface (or bare surface of Ni), nanoparticles with a wide size distribution from a few up to ~200 nm were observed (Figure 37C & D). Some of the large particles appeared to be well bound to Ni surface. The amount of the nanoparticles on the Ni surface was found to decrease with increasing the distance to the TPBs. However, in Figure 37B, nanoparticles were hardly observed on the Ni|pore interface.

<u>Nano-precipitates distributions along cell length (from gas inlet to outlet):</u>

Cell T1: Inlet vs. outlet

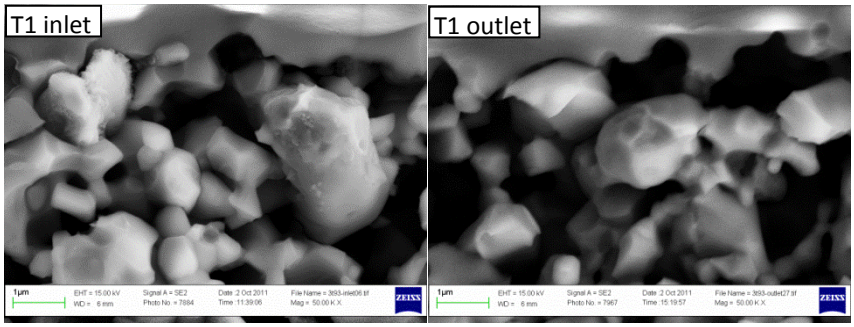

Figure 38. Nano-precipitates in the Ni-YSZ electrode of cell T1 after durability test: left) inlet vs. right) outlet

Cell T2: from inlet to center & outlet

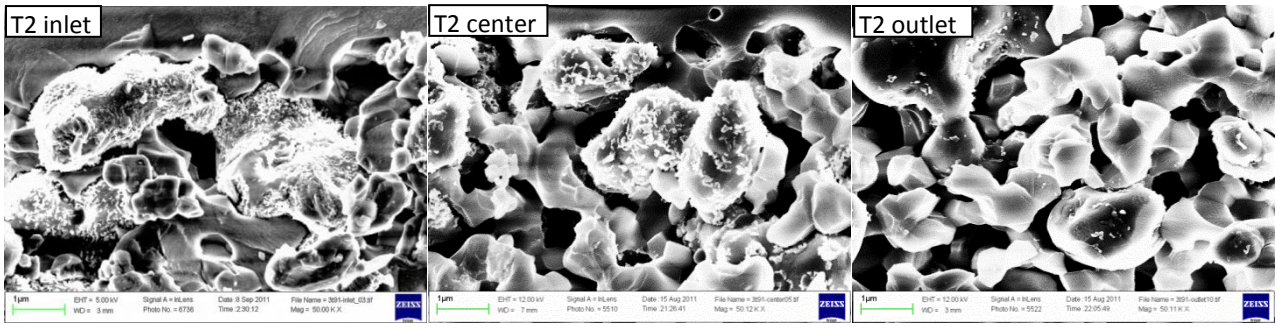

Figure 39. Nano-precipitates in the Ni-YSZ electrode of cell T2 after durability test: left) inlet vs. middle) center vs. right) outlet

The amount of nano-precipitates was different at different regions of the Ni-YSZ electrode. Figure 38 shows that a small amount of nano-precipitates on Ni particles within 2 µm to the interface at the inlet of cell T1, while no such particles were found at the outlet. Figure 39 shows a significant precipitation of nano-particles in the Ni-YSZ electrode for at the inlet of cell T2, a fewer nanoparticles at the center of the cell and the least at the outlet.

Decreasing amount of the nano-precipitates from the inlet to the outlet was also observed on cell T8. Cell T6, however, didn't show the same tendency as on the other cells. Considerable amount of the nano-precipitates was observed both at inlet and outlet of cell.

<u>Ni-YSZ contact loss & nano-precipitates:</u>

Cell T1: Inlet and outlet

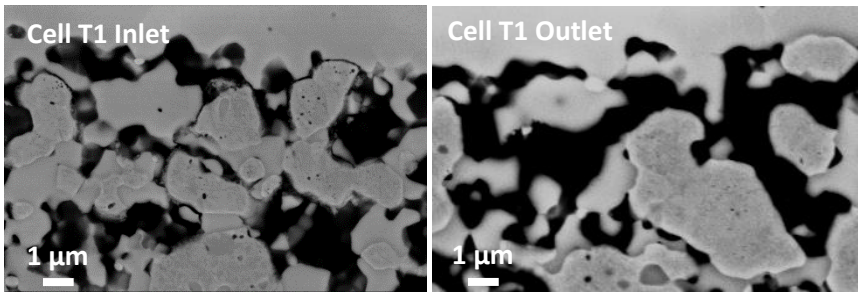

Figure 40. Contact loss between Ni and YSZ electrolyte for cell T1 after durability test

Cell T2: From inlet to outlet

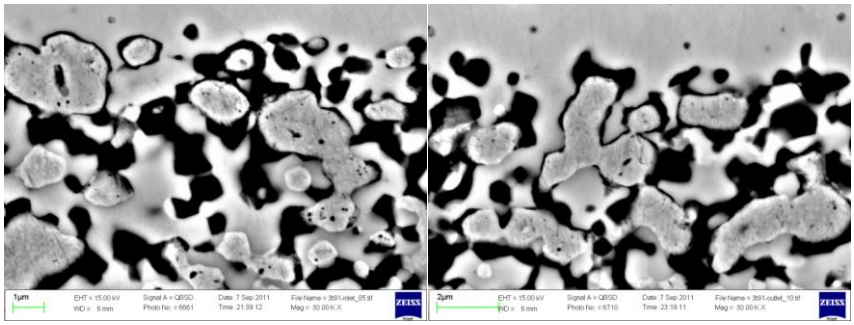

Figure 41. Contact loss between Ni and YSZ for cell T2 after durability test: left) inlet and right) outlet

Cell T8: Inlet vs. outlet

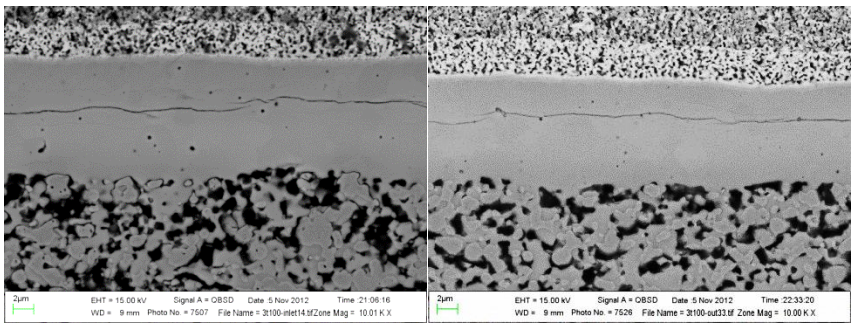

Figure 42. Ni-YSZ electrode and YSZ electrolyte for cell T8 after durability test: left) inlet and right) outlet

Polished cross-sections of the cells were studied under SEM for examining the Ni-YSZ contact. The inlet of cell T1 (Figure 40) showed gaps or detachment between the YSZ electrolyte and the closest Ni particles, indicating a contact loss between the electrode and the electrolyte. The Ni-YSZ contact loss was observed to be much less significant at the outlet of cell T1. Figure 41 shows the Ni-YSZ contact of cell T2 both at the inlet and outlet. The contact loss was more severe for cell T2 compared to T1. Entire detachment of the Ni grains can be observed for the closest Ni grains to the YSZ electrolyte. The Ni-YSZ contact loss can be found a few microns deep into the Ni-YSZ active electrode from the electrolyte. For cell T8 (Figure 42), the Ni-YSZ

contact loss was observed clearly at cell inlet but hardly at outlet. The contact loss at the inlet was also more server than that of cell T1.

Voids/impurities inside Ni grains:

Cell T1 inlet & cell T8 inlet

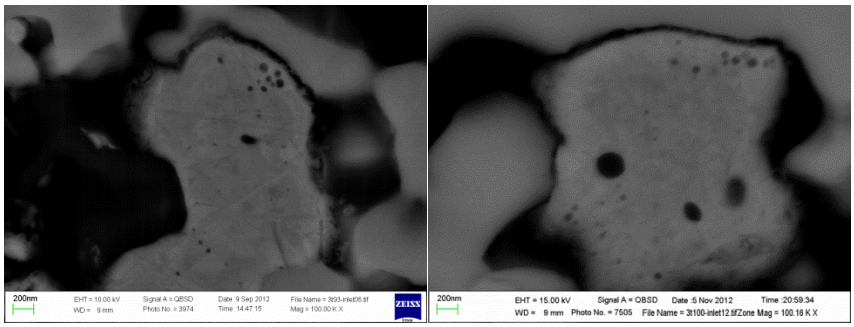

Figure 43. Inclusions in Ni grains after durability test: left) T1 inlet and right) T8 inlet

Inclusions were clearly observed in Ni grains close to YSZ electrolyte after durability test. There were many small inclusions (~50 nm) in Ni close to TPB site and some larger ones up to~200 nm in diameter (Figure 43). More inclusions were found in the Ni grain adjacent to the electrolyte than those with some distance. The inclusions were also found in the Ni grains of the Ni-YSZ support, but to a much less degree. Along the gas flow direction, more inclusions were found at the cell inlet compared to the cell outlet.

Cell T2:

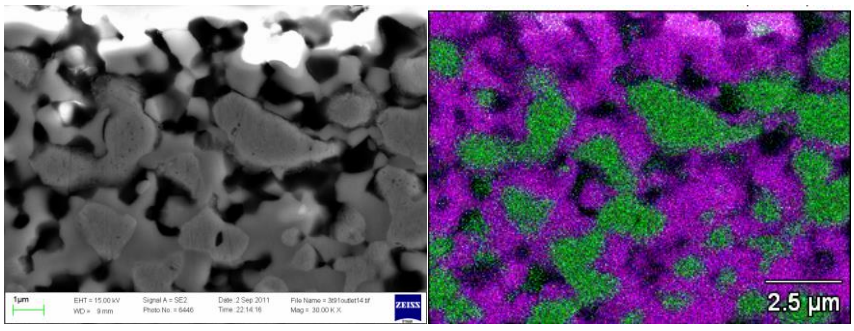

Figure 44. EDS analysis for the Ni-YSZ active electrode of cell T2. The green color indicates Ni and the violet color indicates YSZ.

According the results of EDS analysis, no change in composition was found within the detecting limit of the SEM/EDS (Figure 44). The particle size of Ni near YSZ electrolyte is estimated to be larger than 2 microns.

YSZ particles inside Ni grains or not:

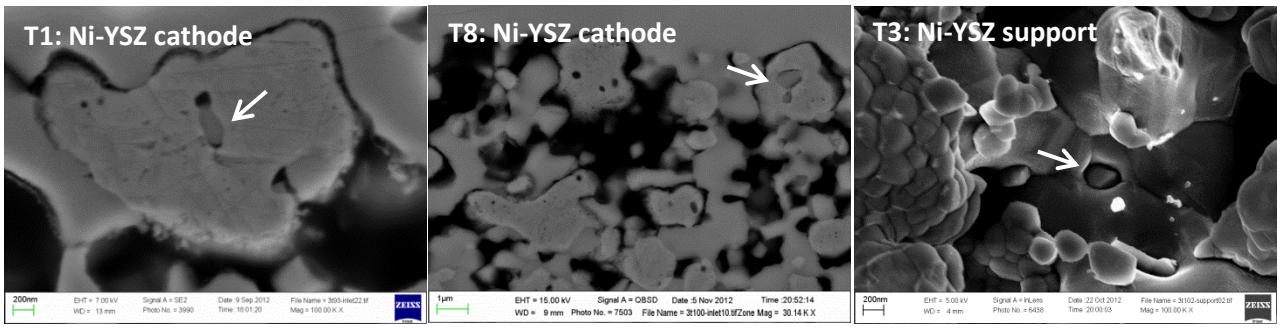

Figure 45. YSZ inclusions in Ni grains of the active Ni-YSZ electrode of left) cell T1 and middle) cell T8; right) YSZ in Ni grains of the Ni-YSZ support

YSZ particles were sometimes observed inside the Ni grains after durability test, as shown in Figure 45 for the inlet of cell T1 and cell T8). As it was only observed in few cases and was also found in the support layer (Figure 45), which should be structurally stable during test, the YSZ inclusion is not considered as a precipitate in Ni due to cell operation and was believed to originate from cell fabrications (processing and sintering).

A reference cell: without durability test

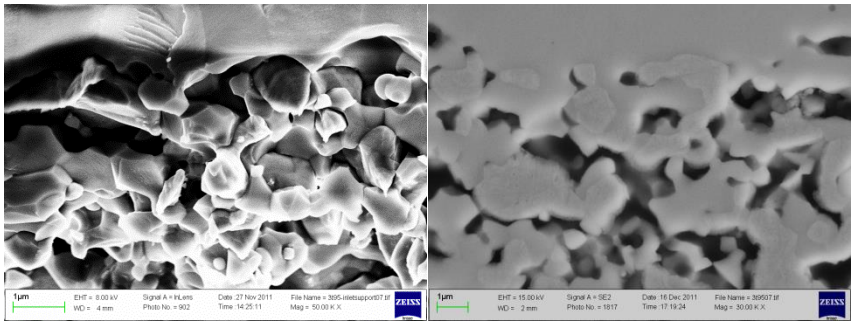

Figure 46. Ni-YSZ electrode for a reference cell without durability test

A similar solid oxide cell with a LSM oxygen electrode was tested for characterization of the initial performance using the same precedure as for cell T1–T9 and then cooled down without performing a durability test. The microstructure of this cell was taken as a reference for that of long-term tested cells. The SEM images (Figure 46) revealed that no nanoparticle precipitated in the Ni-YSZ active electrode. Good Ni-YSZ contact was maintained, with no gaps being observed between Ni and YSZ for the polished cross-sections. No significant inclsuion was observed in the Ni grains.

3.1.2 Clean tests — SEM (Cell T5, T7, T9)

<u>Details & distributions of the precipitates in the local Ni-YSZ electrode:</u>

Cell T5: Inlet

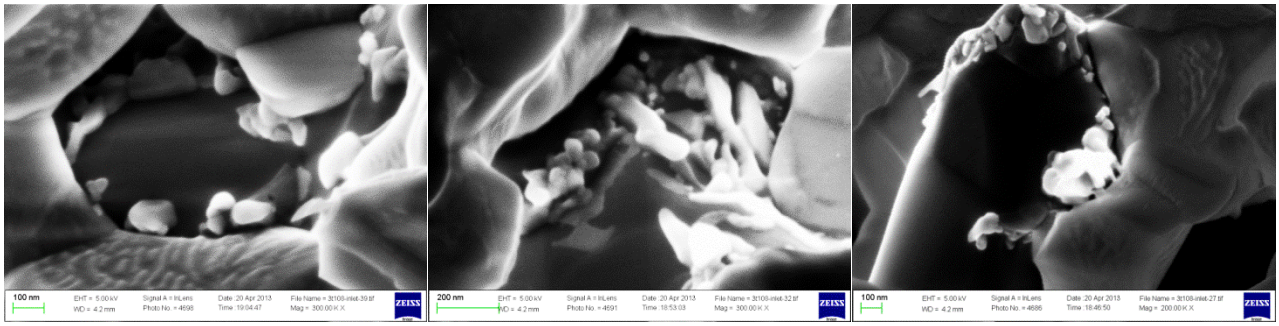

Center:

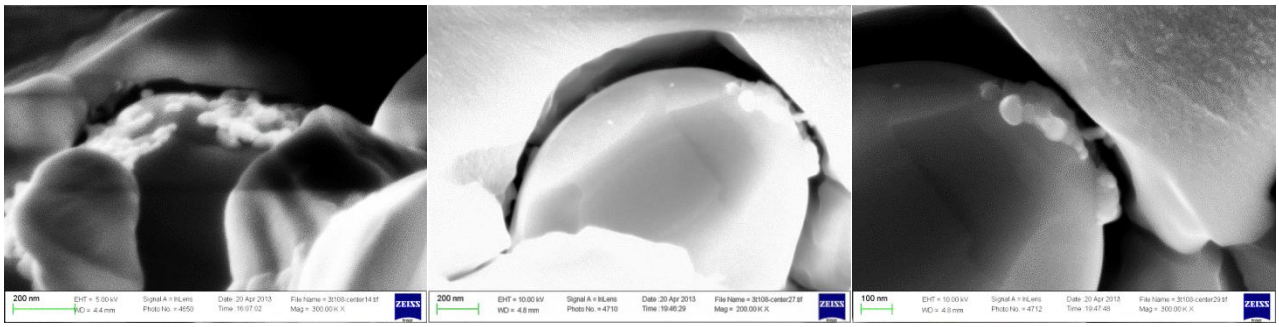

Outlet:

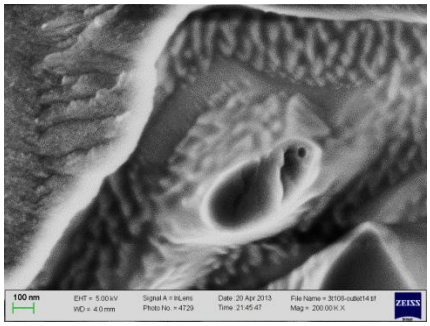

Figure 47. Microstructure of cell T5 after durability test: Ni-YSZ electrode at cell inlet and center; and surface morphology of YSZ at cell outlet.

Cell T5 was tested at -2.0 A/cm^2 for co-electrolysis of CO_2 and H_2O with the clean set-up. The microstructures of the Ni-YSZ electrode after durability test were shown in Figure 47. Nano-precipitates were observed on the surface of the 1st Ni grain next to the YSZ electrolyte at the cell inlet. In general, the nano-precipitates spread along the TPBs and partly covered the surface of Ni. The precipitate for this cell was much less pronounced than that for cell T2, which was tested at a same current density for a similar duration but with a normal set-up (un-cleaned). Fewer nano-precipitates were found in the Ni-YSZ electrode at the cell center along the gas flow direction compared to the inlet. The size of the particles was also smaller for the cell center than that at the inlet. The nanoparticles were located between Ni and YSZ or

on the Ni surface very close to TPBs. At the cell outlet, no nano-particles were observed. However, a rough YSZ surface with a lot of small knobs was observed at YSZ-pore interface close to the electrolyte.

Nano-precipitates distributions along the cell length (from gas inlet to outlet):

Cell T5: From inlet to outlet

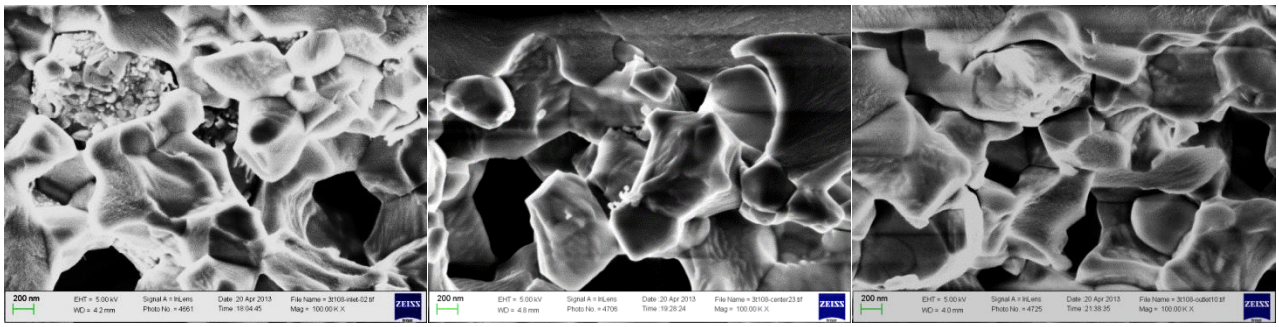

Figure 48. Ni-YSZ electrode of cell T5 after durability test: left) cell inlet, middle) cell center and right) cell outlet

Cell T7: Inlet vs. outlet

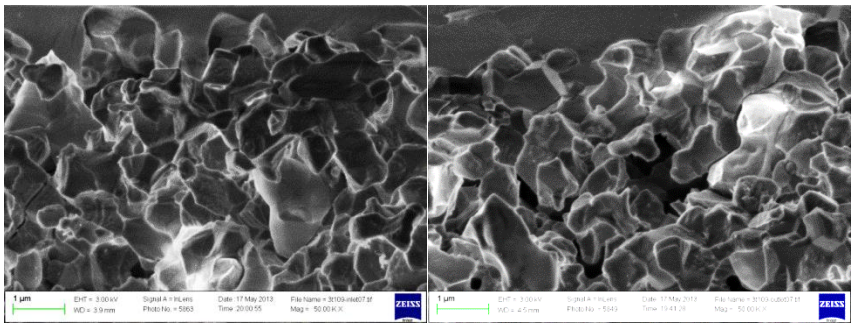

Figure 49. Nano-precipitates in the Ni-YSZ electrode of cell T7 after durability test: left) cell inlet and right) cell T7 outlet

The numbers of the nano-precipitates in the Ni-YSZ electrode were found to decrease from the inlet to the outlet (Figure 48) of the cell T5 (-2.0 A/cm^2). At the inlet, the nano-precipitates were observed only on the Ni grain directly connecting to the YSZ electrolyte. Very limited amount of precipitates were seen in the Ni-YSZ electrode at the cell center and were confined to the contact points of Ni-YSZ or TPBs. No precipitates were found at the cell outlet.

No nano-precipitate was observed in the Ni-YSZ electrode throughout the cell T7 (Figure 49), which was tested at a lower current density (-1.5 A/cm^2) and showed the lowest degradation in cell voltage and Rp.

Ni-YSZ contact loss & nano-precipitates:

Cell T5: Inlet vs. outlet

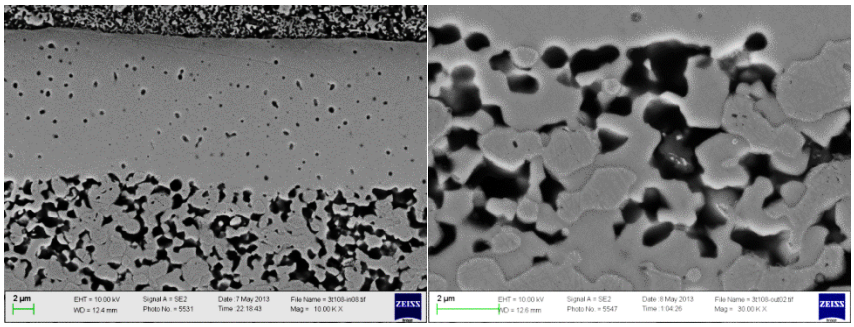

Figure 50. Ni-YSZ electrode of cell T5 after durability test: left) inlet vs. right) outlet

Cell T7: Inlet vs. outlet

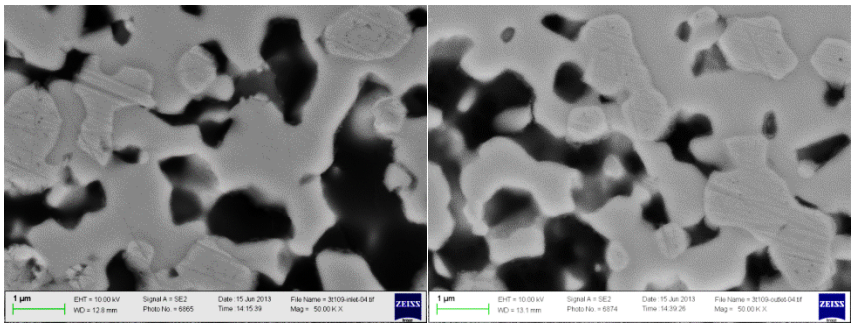

Figure 51. Ni-YSZ electrode of cell T7 after durability test: left) inlet vs. right) outlet

No contact loss between Ni-YSZ was observed for the polished cross-sections of cell T5 (Figure 50) and cell T7 (Figure 51) after durability test.

Voids/impurities inside Ni grains:

Cell T5: Inlet

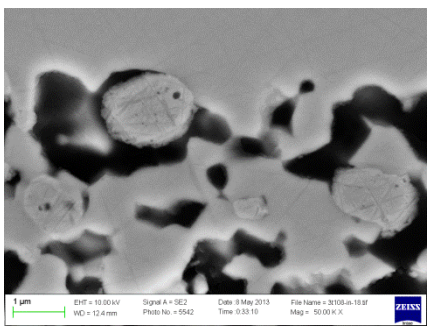

Figure 52. Ni-YSZ electrode of cell T5 after durability test: inclusions in Ni grains

Si impurities were found occasionally in the Ni-YSZ electrode for the cells tested using clean set-ups (without using glass bar sealing), as shown in Figure 52. However, most parts of the Ni-YSZ electrode for these cells (Figure 50 and Figure 51) showed much less amount of impurities than the cells using glass bar sealing. The impurity is therefore expected to make very limited contribution to the degradation of Ni-YSZ electrodes in these cases. As was confirmed by electrochemical analysis, the rapid increase of the Ni-YSZ TPB reaction resistance appeared in the early period of the cell degradation for the normal tests was not observed for the clean tests.

3.1.3 HRTEM/EDS analysis — T2 & T3

3.1.3.1 Ni-YSZ electrode of T2 (-2.0 A/cm^2 for 678 h without gas clean and cooled down at OCV)

<u>Nanoparticles precipitation in the Ni-YSZ electrode:</u>

In order to study the detailed microstructure and composition of the nano-particles, two lamellas was taken by FIB thinning from the Ni-YSZ active electrode of cell T2 at different distances to the YSZ electrolyte and was studied under TEM, as shown in Figure 53. Lamellar Area 1 was from the Ni-YSZ electrode which was ~ 6 µm away from the YSZ electrolyte with a thickness of ~ 100 nm. Lamellar Area 2 was from the Ni-YSZ electrode which was 0 ~ 4 µm away from the YSZ electrolyte. Area 2 was relatively thick (~ 300 nm), but still thin enough for imaging with atomic resolution. In addition, it was possible to study the nanostructures near the cathode-electrolyte interface due to the porous structure of the sample.

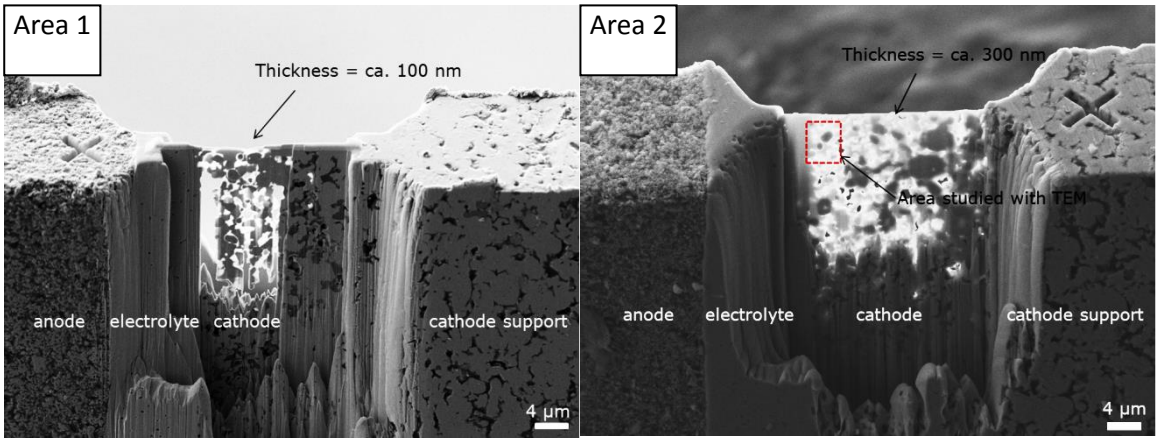

Figure 53. Lamellas of Ni-YSZ active electrode for TEM analysis. Area1: Ni-YSZ at a distance of ~ 6 µm to the YSZ electrolyte and Area 2: Ni-YSZ at a distance of 0 ~ 4 µm to the electrolyte.

Figure 54 shows the nanostructures on a Ni grain approximately 6 µm away from the YSZ electrolyte. A number of nano-particles were observed stacking up loosely over the Ni surface. The nanoparticles were of

a few tens nm in diameter. The entire surface of the Ni grain (Figure 54A & B) was covered by the nano-particles and the Ni grain appeared to be detached from the YSZ bulk. As is shown in Figure 54C, the bulk YSZ at the Ni-YSZ interfacial region close to the TPBs seems to decompose into lots of nanoparticles. Both the TEM and SEM images indicated that the nano-particles were probably originated from the decomposition of YSZ at the Ni|YSZ interface and a subsequent migration to the surface of Ni.

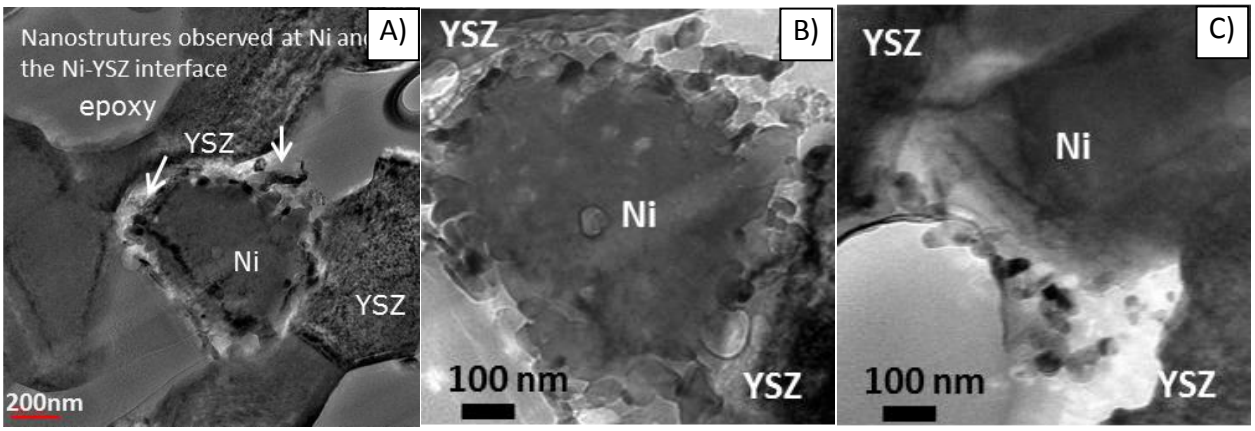

Figure 54. Nanostructures at Ni|YSZ interface and Ni|pore interface observed for the Ni-YSZ active electrodes.

EDS measurements of the Y-to-Zr ratio:

Based on intensive EDS studies the composition of the nanoparticles on the Ni surface and at the Ni|YSZ interface were found to be rich in Zr and Y. A statistical analysis of the Y/Zr ratio for the individual nano-particles was performed for two regions at different distances to the YSZ electrolyte. The nanostructures at the Ni|YSZ interface and Ni|pore interface were found to have similar Y/Zr ratios. The Y/Zr ratio was also similar for the nano-particles at different distances to the YSZ electrolyte (Figure 55). Considering the error level, no significant difference was found in the Y/Zr ratios between the nano-particles and YSZ electrolyte, as is shown in Figure 55. The Y/Zr ratio obtained experimentally was close to the stoichiometric value (0.17) for 8YSZ.

In addition, traces of the following element were found for the zirconia nanoparticles: Al, Si, La, Sr, Mn, etc. However, these elements were considered to mainly come from the contaminations during sampling, e.g. the process of FIB thinning.

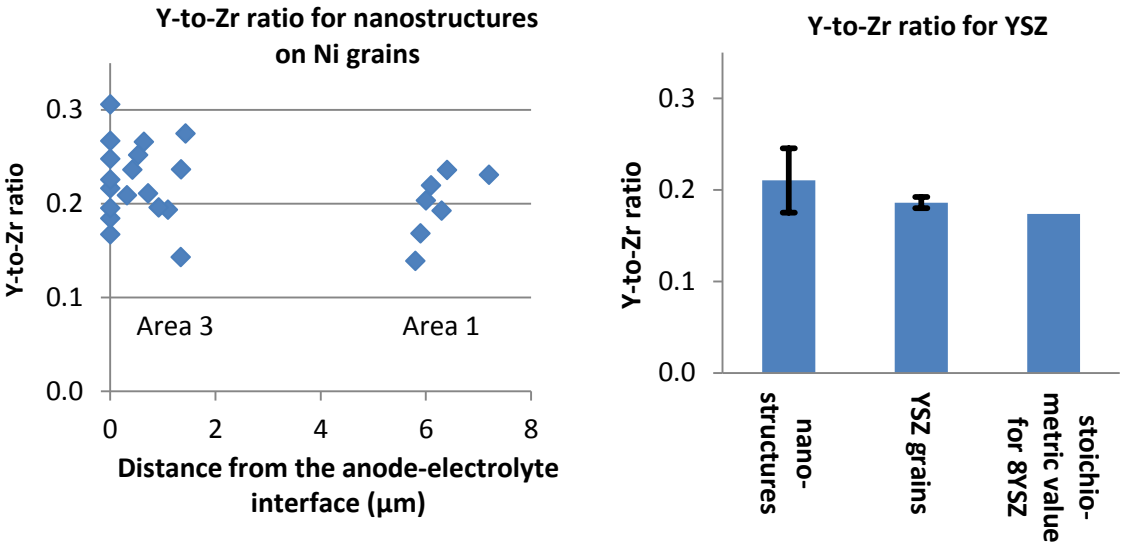

Figure 55. Element ratios of Y to Zr for the nanoparticles formed in the Ni-YSZ active electrodes.

HTREM analysis

The crystal structure of the nano-precipitates has been investigated by HRTEM analysis. Dozens of nano-particles have been analyzed in order to get a general picture of the crystal structure. Figure 56 shows a typical result of the HRTEM analysis for a nanoparticle precipitation from area 1 with the lattice spacing and angle between lattice planes marked on the image. The (hkl) indexes match that of the cubic and tetragonal but not monoclinic phase of zirconia. According to the statistic results of the HRTEM analysis, most of the nanoparticles showed a cubic structure of ZrO_2, which is the structure expected for bulk 8YSZ. Some of the nanoparticles also match with tetragonal phases of ZrO_2. No nanoparticles for area 1 showed large characteristic lattices spacing (3-5 Å) for the monoclinic phase of ZrO_2. Only one of the nanoparticles matched monoclinic ZrO_2 in area 2. Thus, the zirconia nanoparticles exhibited a dominating cubic structure both at the Ni|YSZ interface and the Ni|pore interface.

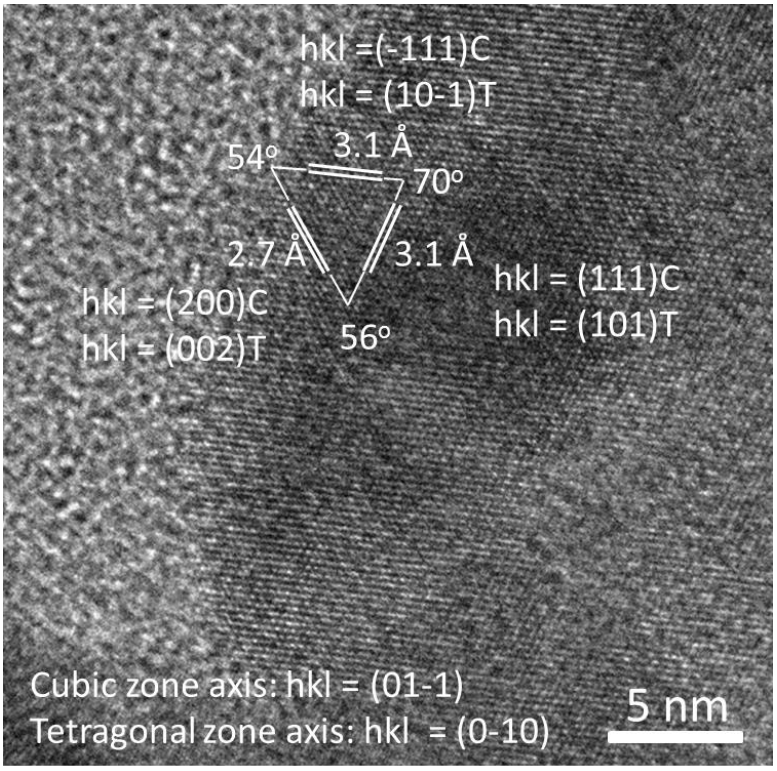

Figure 56. HRTEM analysis for the nanoparticles precipitated in the Ni-YSZ electrode from area 1.

STEM-EDS elemental map (Area 2): Distribution of Ni, Zr and Y at Ni|YSZ Interface

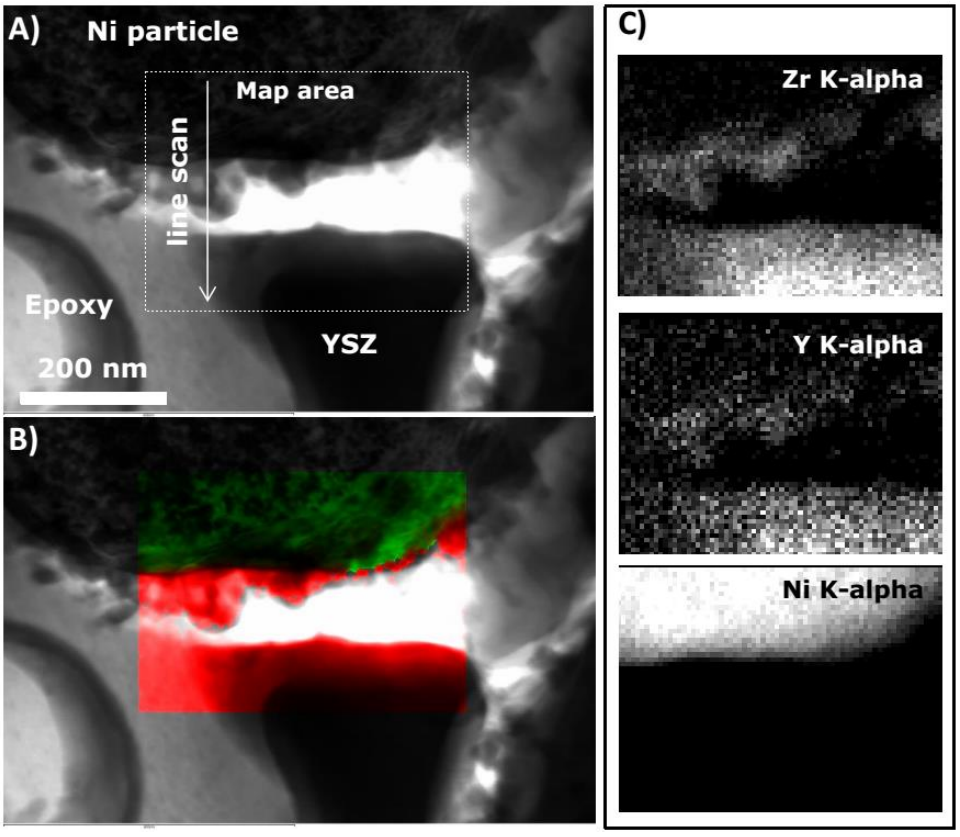

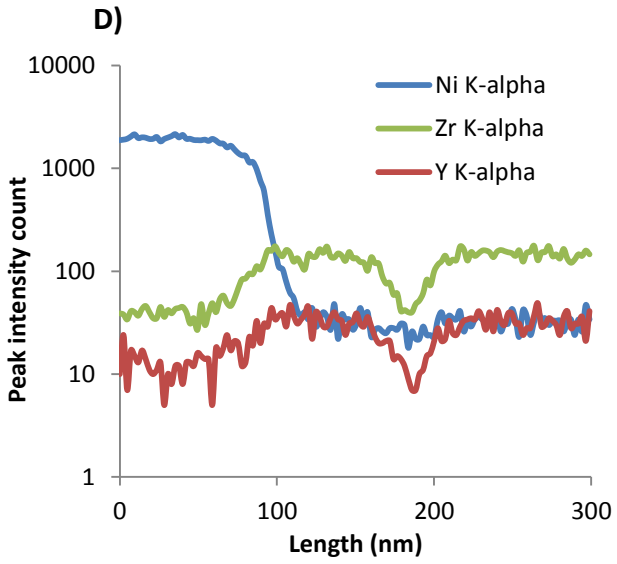

Figure 57. STEM/EDS analysis of the nanoparticles at the Ni|YSZ interface: A) TEM image of nano-precipitates between Ni and YSZ; B) Mix of the Ni and Zr map on the BF STEM image; C) Peak intensity of individual element Ni, Zr and Y for the selected region in A); D) line scan as the arrow indicated in A) across the precipitates

The STEM-EDS elemental maps of the nanostructures in the Ni-YSZ electrode was shown in Figure 57. Nanoparticles with a diameter ranged from ~ 10 to ~ 50 nm were observed on the Ni surface, where Ni particle was detached from the YSZ. The EDS maps and line scans revealed that the nano-particles were composed of Zr and Y rather than Ni. The Y/Zr ratio was found to be similar for the nano-particles and the YSZ electrolyte in four line scans from different regions.

Exclusion of presence of Zr in Ni grain and Ni-Ni interface

Even though the Zr(Y) was dominating on the Ni surface, occasionally some weak signal of Zr (Y) can be observed just beneath the surface of Ni (seen the EDS maps). No Zr (Y) was found for the interior of Ni grains. These results were confirmed by additional TEM analysis in other regions and dominating Zr (Y) was only observed on the surface of Ni. Because the lamella has a thickness of 100 ~ 300 nm, which is significant larger compared to the diameter of the nano-precipitates (a few nm to dozens of nm), the lamella should be regarded as a 3D rather than 2D geometry. Therefore, the Zr signals occasionally observed beneath the Ni surface were likely ascribed to the 3D geometry of the lamella and the tilt under TEM.

No nanoparticles are observed for the Ni-Ni connections for all the examined regions on both lamellas. There is no 'space' between the Ni surfaces. As the '2D' slice through the 3D matrix is random and the

statistics may not be sufficient enough, the possibility of nanostructures in Ni-Ni interfaces cannot be excluded. However, the observations at least indicated that the precipitation of nanoparticle was insignificant at the Ni-Ni interface.

3.1.3.2 A special test: cooling down in H_2 under polarization (cell T3)

From the above tests, it is not clear whether the zirconia nano-particles were generated originally as zirconia or by re-oxidation of Zr-metal from the reduction of YSZ. Because of the high affinity of zirconium with O atoms, the re-oxidation of Zr-metal could occur either during the galvanostatic test or at OCV after test in the gas mixtures containing CO_2 and H_2O. In order to clarify the original state of the nano-precipitates, which is important for understanding the mechanism, a special test was performed by cooling the cell down in H_2 without removal of the polarization after a similar operation at -2.0 A/cm^2 for 502 hours. The cell voltage was kept at the final value of the durability test and H_2 was used to avoid any possible re-oxidation of the metal.

SEM images of cell T3 (Figure 58) revealed that nano-particles were still formed on the Ni surface both at the cell inlet and outlet. The FIB thinning and TEM analysis was carried out for cell T3 the same as for cell T2. The TEM image (Figure 59) shows similar structural and compositional information of cell T3 as obtained for cell T2. The composition of the precipitates during the galvanostatic test was kept the same after test, as having no chance to be oxidized during cooling. This indicates that the nano-particles precipitated as zirconia, instead of Zr-metal.

SEM: Cell T3 Inlet

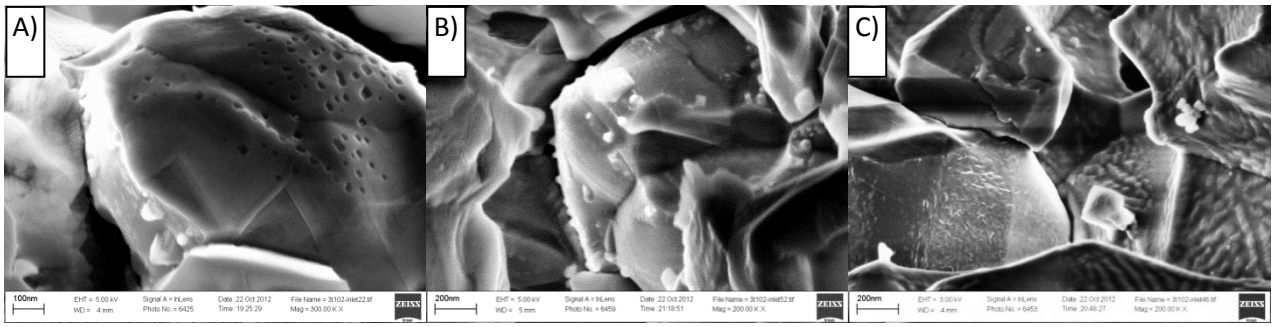

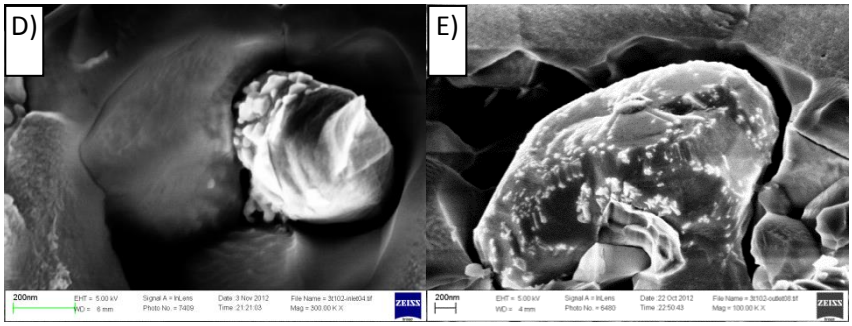

Figure 58. Ni-YSZ electrode of cell T3 after durability test: A) – D) inlet & E) outlet. Cell T3 was cooled down in H_2 with the voltage kept at 1.8 – 1.9 V.

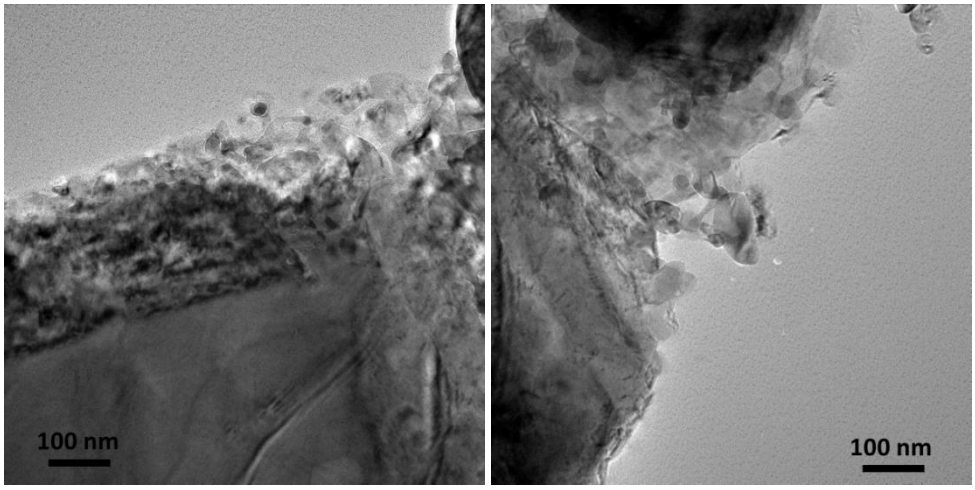

Figure 59. TEM observation for the nanoparticles precipitated in the Ni-YSZ electrode of cell T3 (durability test at -2.0 A/cm^2 for 502 hours; cooled down with cell voltage kept at the final level)

3.1.3.3 Particle size distributions for the nano-zirconia precipitates

Particle size distribution of the zirconia nanoparticles (Figure 60) was obtained based on an analysis of randomly selected 163 particles in cell T2 and 57 particles in cell T3. A single peak distribution was found for the size of these particles. The particle size ranged from ~10 to ~ 80 nm and most of the particles showed a diameter between 30 and 50 nm. The two cells exhibited similar distribution of particle sizes for the nanoparticles observed in the Ni-YSZ electrode.

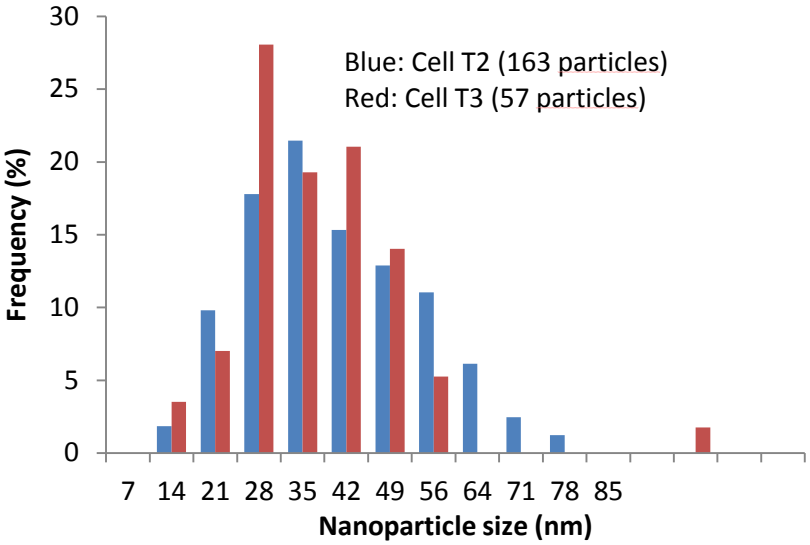

Figure 60. Particle size distribution (PSD) of the nanostructures formed in the Ni-YSZ active electrodes based on TEM observations on cell T2 & cell T3.

3.1.3.4 'Bubble' structured in Ni grains

STEM and line analysis of the bubbles/precipitates inside Ni grains

Cell T2: obvious increase of Si and weak increase of O signal; only evidence for Zr;

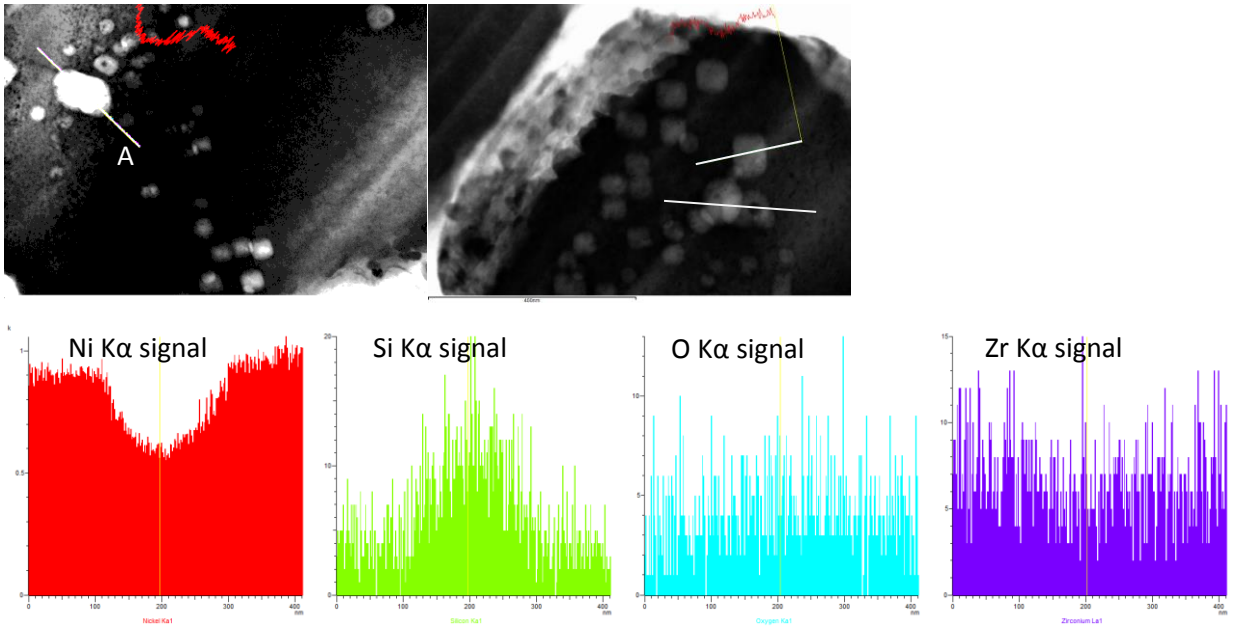

Figure 61. STEM-EDS line scan analysis of the precipitates in Ni grains for the Ni-YSZ electrode of cell T2

Cell T3: obvious increase in both Si and O signal; only evidence for Zr;

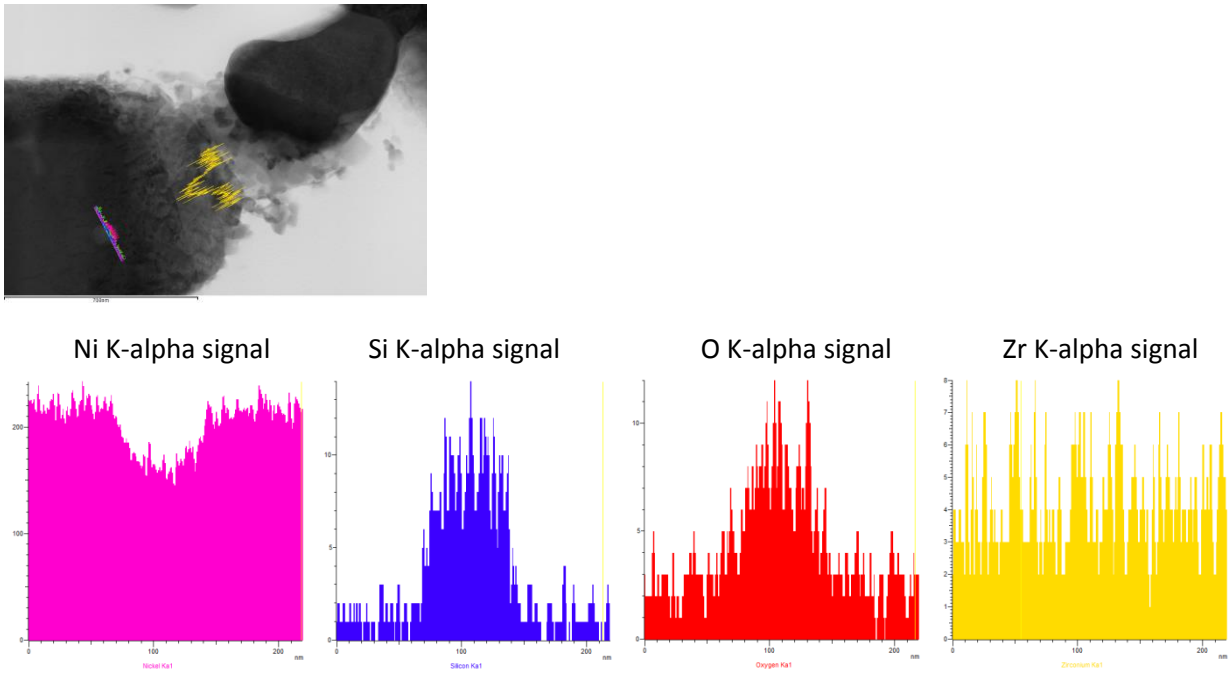

Figure 62. STEM-EDS line scan analysis of the precipitates in Ni grains for the Ni-YSZ electrode of cell T3

As are shown by the TEM images (Figure 61 & Figure 62), a lot of 'bubble' or precipitates with a higher brightness than Ni can be observed in Ni grains close to the YSZ electrolyte, both at the Ni|YSZ interface and the Ni|pore interface. The higher brightness of these regions indicates that the probed area is thinner, e.g. due to a cavity inside Ni grains and/or composed of a lighter material. From the EDS analysis, a loss of Ni signal and meanwhile a clear gain of Si signal were found at the 'bubbles' in Ni grains both for cell T2 and cell T3. The increased Si signal is generally accompanied by a weak increase in the O signal for cell T2 (Figure 61). However, the line scan recorded for sample cell T3 (Figure 61) clearly shows the increase in both O and Si signals. The signal of Zr is also shown for comparison with that of Ni, Si and O. Considering the much heavier atom weight for Zr, it should be more readily detected than Si and O if there is any Zr. The line scan hadn't shown any Zr signal at the 'bubbles' and the interior of the Ni grains. Thus the existence of Zr or zirconia in the bubbles / precipitates in Ni grains should be excluded or neglected. Weak signals from other elements, including Al, Fe, S, Cl, Ca, Na, Co, F, N, Zn, Ti, etc., were also found for the samples and seem not correlated with the 'cavities' either.

3.1.3.5 A summary for TEM analysis

The nanostructure observed at Ni grain surfaces are composed of Zr and Y. The Y/Zr ratio for the nanostructures is similar to that of 8YSZ and independent of the distance to the electrolyte.

The phase of the nanostructures is consistent with that of cubic YSZ and some are also consistent with tetragonal ZrO_2. The phase of the nanostructures is generally less consistent with monoclinic ZrO_2.

The crystalline phase of the nanostructures appears to be independent of the distance to the electrolyte. Same structural and compositional information was obtained for the nanoparticles precipitated at a distance of 0 ~ 1.5 µm and ~ 6 µm away from the electrolyte.

The cell cooled down in H_2 without removal of the polarization showed same structure and composition of the zirconia nanoparticles with that of the cell cooled down at OCV.

3.2 Loss of Ni percolations in the Ni-YSZ electrode

A reference cell without durability test:

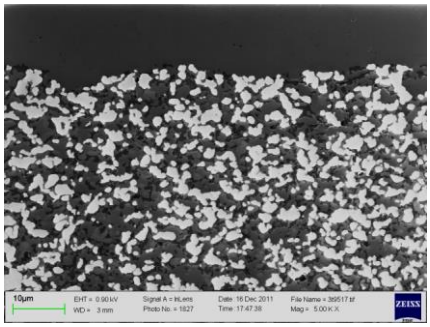

Figure 63. Ni percolations of the Ni-YSZ electrode for a reference cell without durability test

Cell T1: From inlet to outlet

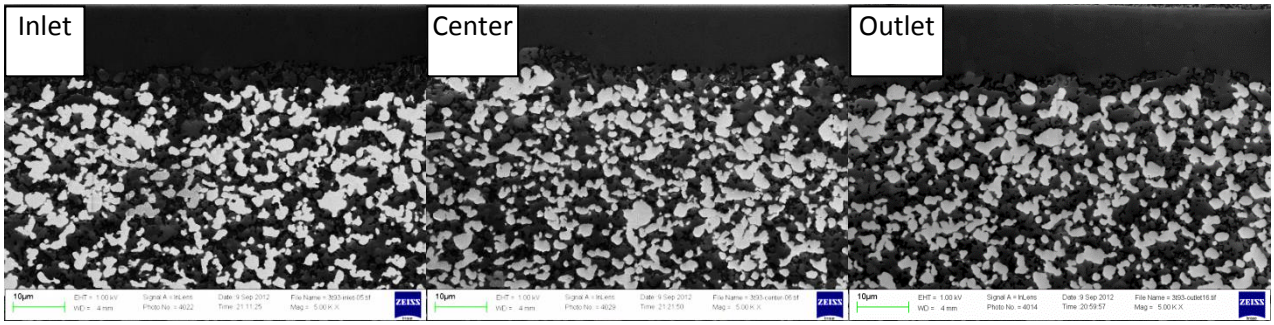

Figure 64. Ni percolations of the Ni-YSZ electrode of cell T1 after durability test: inlet, center and outlet

Cell T2: inlet vs. outlet

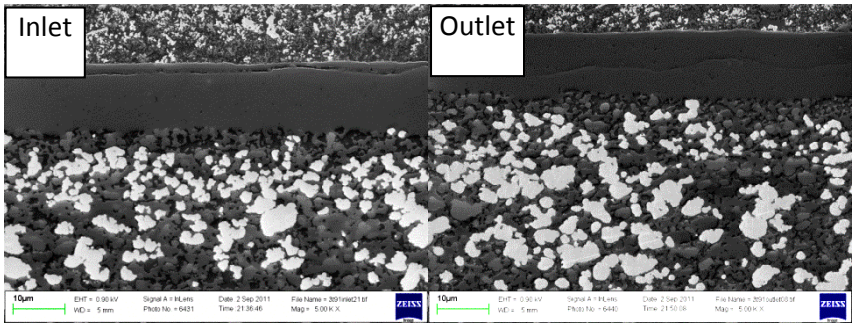

Figure 65 Ni percolations of the Ni-YSZ electrode of cell T2 after durability test: inlet and outlet

Cell T3: From inlet to outlet

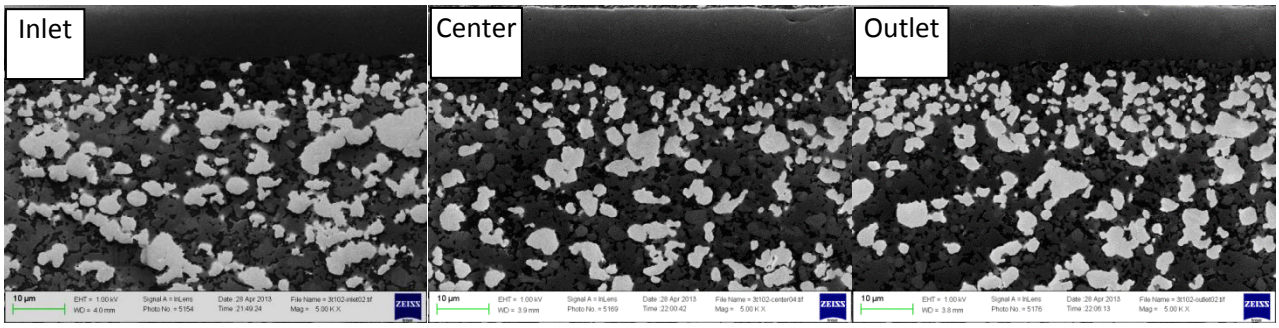

Figure 66. Ni percolations of the Ni-YSZ electrode of cell T3 after durability test: inlet, center and outlet

Cell T4: From inlet to outlet

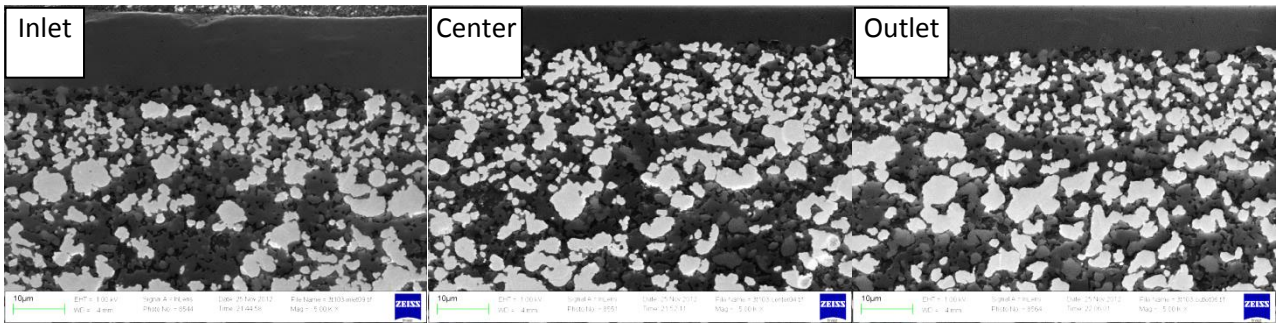

Figure 67. Ni percolations of the Ni-YSZ electrode of cell T4 after durability test: inlet, center and outlet

Cell T7: From inlet to outlet

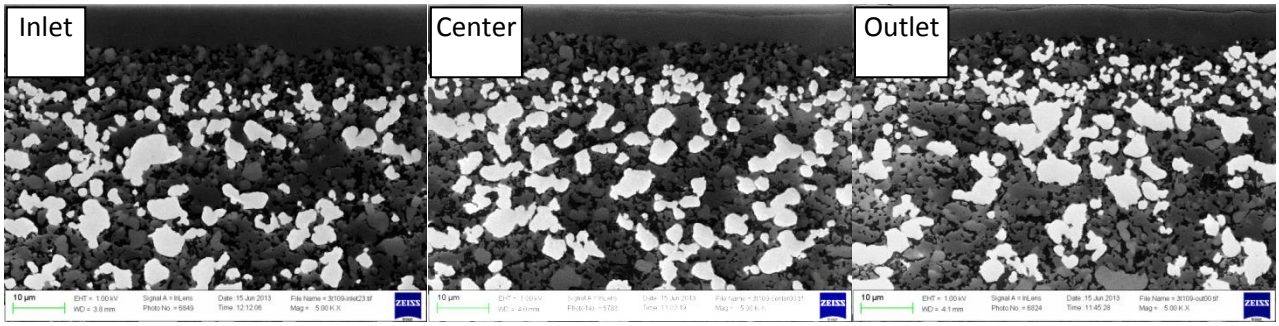

Figure 68. Ni percolations of the Ni-YSZ electrode of cell T7 after durability test: inlet, center and outlet

Cell T8: From inlet to outlet

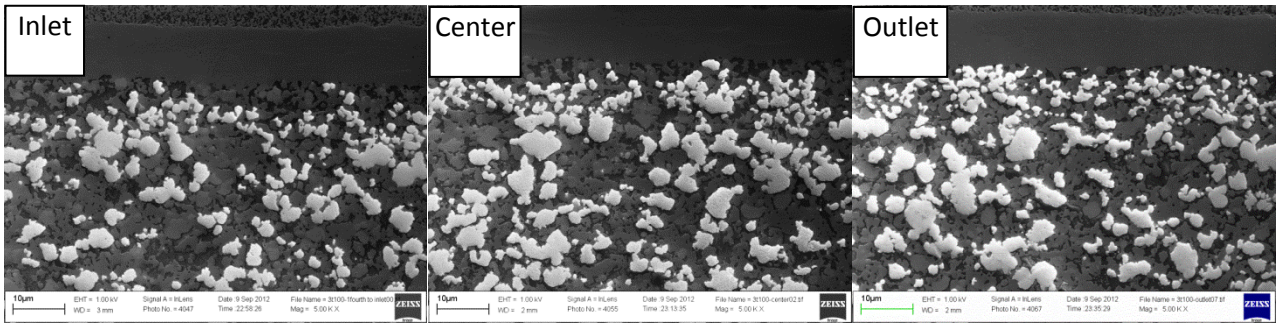

Figure 69. Ni percolations in the Ni-YSZ electrode of the cells T8 after durability test: inlet, center and outlet

Percolation loss of the Ni network in the active Ni-YSZ electrode, especially for that close to the YSZ electrolyte was observed for all the cells after durability test. Figure 63 shows the Ni percolations of the Ni-YSZ electrode for a reference cell without performing any durability test. Figure 64 – Figure 69 show the Ni percolations for the cells after durability test at various conditions. For the cells after 500 – 700 hours test at -1.5 or 2.0 A/cm^2 (cell T1, T2, T3, T7 & T8), severe Ni percolation loss was observed for almost all the Ni particles within ~ 5 um away from the YSZ electrolyte at the cell inlet. Along the gas flow direction, the percolation loss of Ni was observed to be less severe for the outlet than the inlet of cell T1 (Figure 64), cell T3 (Figure 66), T4 (Figure 67), T7 (Figure 68) and T8 (Figure 69). However, cell T2 (Figure 65) showed a severe Ni percolation loss at both the inlet and outlet. Compared with the cells tested for a longer period at -2.0 A/cm^2, cell T4 (Figure 67), which was tested for a much shorter period of 138 hours showed a less severe loss of Ni percolations, especially at the cell center and outlet, indicating an clear evolution of Ni percolation loss from the inlet to the outlet. Percolation loss of Ni in the Ni-YSZ electrode both at the inlet and the outlet was also observed for cell T7 (Figure 68), a LSCF cell tested at -1.5 A/cm^2 for 712 hours with a clean set-up, which showed the lowest degradation for cell voltage and the Ni-YSZ TPB reaction resistance (Chapter Electrochemistry) without any precipitation of zirconia.

No nano-particles at Ni-Ni connections:

Based on intensive SEM observations for both the fractured samples and polished cross-sections, generally there were not nano-particles at Ni-Ni connections of the Ni-YSZ electrodes. Thus, the precipitation of the nano-particles was not related to Ni percolation loss.

3.3 Oxygen electrode and YSZ electrolyte

3.3.1 LSM cells: SEM/TEM/EDS

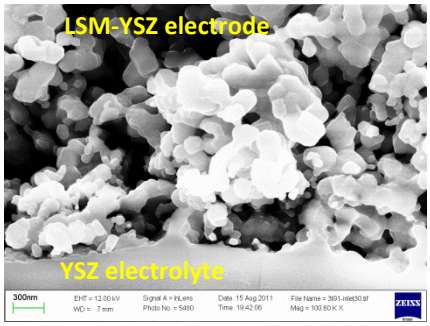

Figure 70. SEM image of the YSZ|LSM-YSZ connections for LSM cell T2 (-2.0 A/cm^2 for 678h)

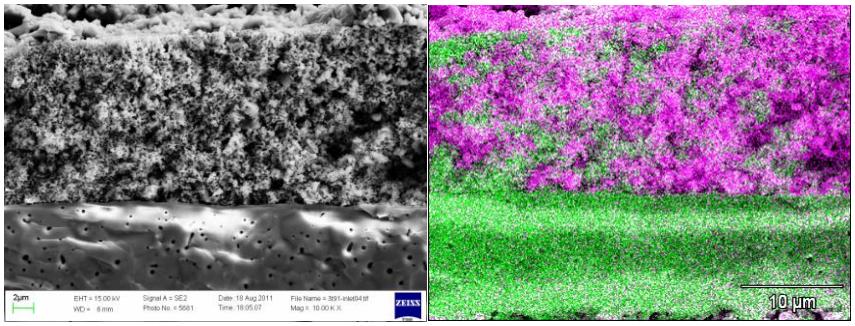

Figure 71. SEM/EDS image of the YSZ electrolyte and LSM-YSZ electrode for LSM cell T2 (co-electrolysis at -2.0 A/cm^2 for 678h): the green color indicates YSZ and violet color indicates LSM

No delamination was observed between the YSZ electrolyte and the oxygen electrode for the LSM cells after durability tests. The LSM-YSZ|YSZ interface of cell T2, as a typical example, is shown in Figure 70. The LSM-YSZ oxygen electrode of cell T2 showed little structural and compositional changes after durability test, as shown in the SEM/EDS images of Figure 71. No detectable changes were observed for the oxygen electrodes of other LSM cells. The microstructure observations were consistent with the results of electrochemical analysis that little performance degradation occur for the oxygen electrode after test.

Similar results were obtained for the oxygen electrode and its adhesion with electrolyte for the LSCF cells after durability test. One example (cell T6) is shown in Figure 72. Delamination was observed neither at the YSZ electrolyte | CGO barrier layer interface, nor between the CGO barrier layer and LSCF-CGO electrode. The microstructure of the LSCF-CGO oxygen electrode maintained almost the same, which is consistent with the stable electrochemical performance during the test (Chapter Electrochemistry).

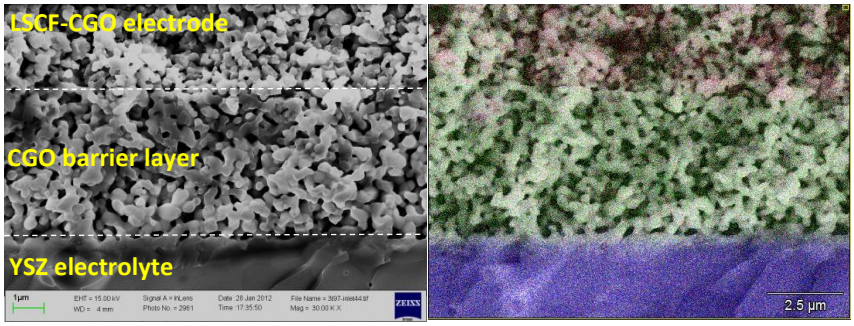

Figure 72. A) SEM image of the connections of YSZ electrolyte | CGO barrier layer |LSCF-CGO oxygen electrolyte for LSCF cell T6 after long-term durability test and B) the corresponding EDS analysis (blue: YSZ; green: CGO; red: LSCF)

3.3.2 Cracks in the center of the YSZ electrolyte

Cell T6: from inlet to outlet

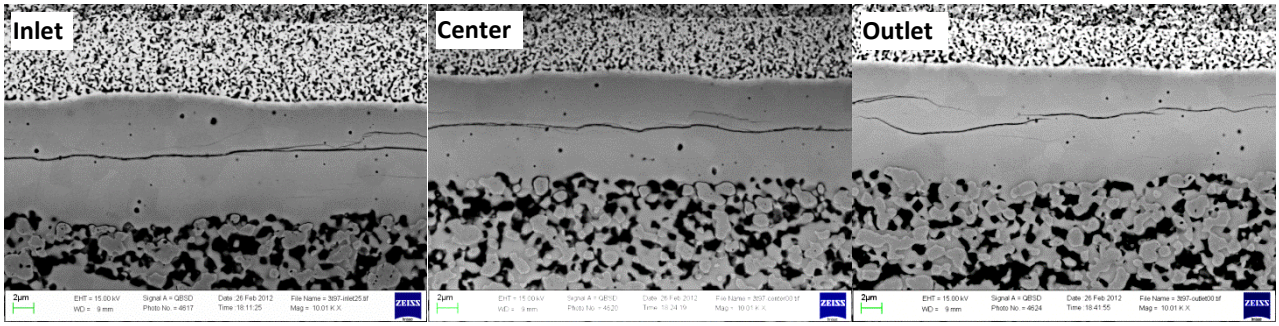

Figure 73. Horizontal cracks in the middle of the YSZ electrolyte for cell T6 after durability test

Similar horizontal cracks can be observed on the polished cross-sections of the cells T6 (Figure 73), T7 and T8 both at the inlet and outlet after tests, but such cracks were not observed on the samples without polishing. As a contrast, no cracks can be observed for the YSZ electrolyte of a reference cell that only experienced initial performance characterization and without any durability test.

A reference cell without durability test:

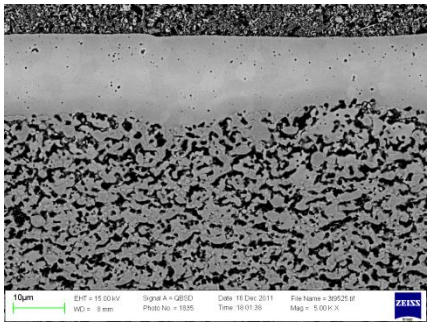

Figure 74. SEM image of the cross-section of a reference cell without any durability test

As a contrast, no cracks can be observed for the YSZ electrolyte of a reference cell that only experienced initial performance characterization and without any durability test.

3.3.3 Bubbles/pits in the YSZ electrolyte close to the LSM-YSZ|YSZ interface

LSM cell T3 outlet:

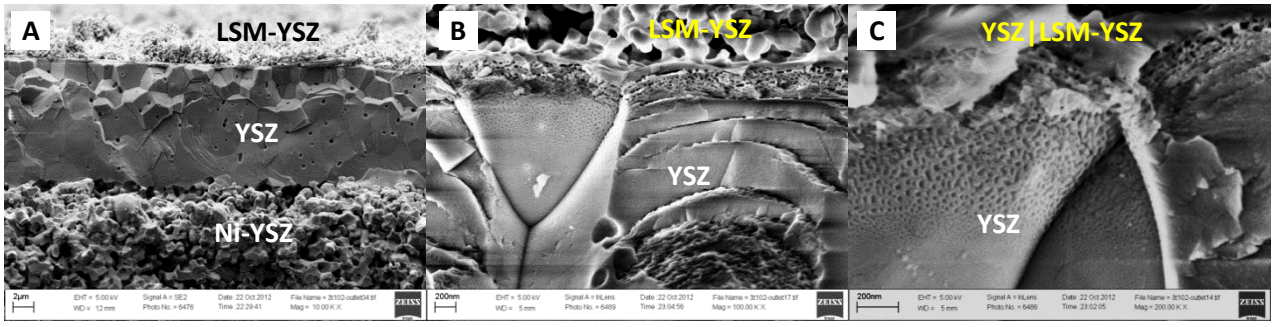

Figure 75. SEM images of the YSZ electrolyte for cell T3 after durability test: A) overview; B) LSM-YSZ electrode and YSZ electrolyte; C) zooming in of the YSZ at LSM-YSZ|YSZ interface

The above post-test microstructural images were taken from the cross-section fractures of the cell T3 without polishing. Careful examination of the YSZ electrolyte (Figure 75A) reveals different fracture morphology at different regions of the electrolyte. The flat surface of the YSZ close to the Ni-YSZ electrode interface indicated an intra-granular fracture, while inter-granular fracture was recognized for the YSZ grains up to ~ 4 µm away from the LSM-YSZ|YSZ interface.

The more clear view of the fracture morphology was showed in Figure 75B & C. A dense layer with a thickness of ~ 100 nm was observed on the interface between the LSM-YSZ electrode and the YSZ electrolyte. This thin layer appears to be structurally intact and good connections between LSM and YSZ were maintained. Beneath this contact region, a ~ 200 nm porous region with horizontally aligned pores exhibited a layered structure. The size and the number of the porosity decreased with increasing the

distance to the LSM-YSZ|YSZ interface. Considerable amount of nano-scaled pores/pits was observed on the bare surface (grain boundaries) of the YSZ grains. The amount and size of the pits decreased with increasing the distance to the interface.

4. Discussions

4.1 Ni-YSZ electrode

4.1.1 Si-impurities

<u>SiO_x inclsuions inside Ni grains:</u>

Even though small amount of the impurities could be ascribed to the raw materials, significantly larger amounts of the SiO_x inclusions were observed (e.g. for cell T1 & T8) in Ni grains close to the YSZ electrolyte than elsewhere. In addition, larger amounts of the impurities were found at cell inlet than outlet, indicating a significant contribution of impurities due to gas flow. For the cells tested in this work, the Si-containing sealing was regarded as the most important sources of the Si impurities. This was confirmed by the post-test microstructural analysis that much more amount of Si was observed for the cells tested using a glass bar sealing (Si-containing) than without the glass bar.

Transportation of Si from sealing glass to Ni-YSZ electrode TPBs has been reported previously for the steam electrolysis in SOECs by Anne Hauch et al.[1,2] During the gas conversions ($H_2O \rightarrow H_2 + ½ O_2$ and $CO_2 \rightarrow CO + ½ O_2$) in the Ni-YSZ electrode of SOECs, there is a decreasing steam partial pressure (pH_2O) and an increasing H_2 partial pressure (pH_2) perpendicular to the cell plane from the bulk gas to the active electrode. Especially in the active Ni-YSZ electrode, the over-potential / current density increases drastically at a closer distance to the YSZ electrolyte, resulting in a much more reducing atmosphere at the TPBs close to YSZ electrolyte than elsewhere. It was hypothesized that Si can be transported by means of the relative volatile $Si(OH)_4$ from sealing glass to TPB sites of the Ni-YSZ active electrode, where it finally deposited as SiO_2 ($SiO_2 + 2\ H_2O \leftrightarrow Si(OH)_4$).[1,2]

However, in this work Si was generally found as inclusions inside the Ni grains close to the electrolyte, in contrast to the previously reported deposition at TPBs.[1–3] The inclusions showed sphere morphology and distributed disorderly in Ni, so they are unlikely to primarily locate along grain boundaries (GBs) of Ni. Thus, the inclusions cannot be explained as a simple migration/segregation process (along GBs of Ni). Note that the important difference lies in the operating conditions: much higher current densities were applied to the cells in this study (-1.5 or -2.0 A/cm^2) than the ones for Anne's tests (-0.5 A/cm^2).[1,2] Thus, for this study the

larger Ni-YSZ electrode over-potential would generate a very reducing atmosphere especially close to YSZ electrolyte, resulting into the reduction of SiO_2. After reduction of SiO_2, Si could be incorporated into Ni grain via bulk diffusion. The SiO_x inclusions could be formed by re-oxidation of Si inside Ni grains, given that O atoms diffuse through Ni grains. O atoms can be provided from the breakdown of the O-containing adsorbates on Ni surface. The oxygen diffusion in Ni is expected to increase at higher temperature and for a cell temperature of ~ 875 ^oC, the diffusivity of oxygen in solid Ni is calculated to be $1.7*10^{-9}$ cm^2/s, according to the following equation:[4]

$$D = 4.9 \times 10^{-2} \exp\left(-\frac{164kJ/mol}{RT}\right) cm^2/s \quad (850 - 1400^oC)$$

Therefore, it is possible that at the test conditions oxygen atoms enter Ni grains by bulk diffusion and precipitate oxides with Si.

The above model can reasonably describe the inclusions which were rich in Si and O. However, the inclusions could also contain Ni, which can form alloys with Si at various ratios from high temperatures to room temperatures (Appendix: Ni-Si phase diagram). Therefore, the possibilities for the precipitation of Si-containing foreign phase in Ni grains in terms of the other compositions (Ni-Si, Ni-Si-O, etc.) cannot be excluded. The inclusions could also contain other elements of such a very low ratio (below 1 % or 2 %) that cannot be confirmed by EDS. The additional impurities are expected to lead to minor, rather than major changes to the above mechanism.

<u>An illustration of the possible mechanism:</u>

A possible mechanism for the formation of inclusions in Ni grains including the transportation was shown as scheme 1 – 4. The silica impurities were mainly ascribed to the Si-containing sealing glass. SiO_2 and steam formed $Si(OH)_4$ (1) at high temperatures, which was transported through gas flow and deposited as SiO_2 (2) at Ni-YSZ TPBs with a low pH_2O. The SiO_2 could be reduced to SiO_x and Si (3) under large cathodic over-potentials. Then Si diffused into Ni grains and was re-oxidized (4) by O atoms which were incorporated in Ni grain by diffusion. The re-oxidation could occur during operation or at OCV after test. According to this mechanism, the Ni particles of the Ni-YSZ electrode could serve as a scavenger for SiO_2 under a large cathodic polarization. An illustration of the mechanism was shown in Figure 76.

SiO_2 (s) + 2 H_2O (g) → $Si(OH)_4$ (g) (1)

$Si(OH)_4$ (g) → SiO_2 (s) + 2 H_2O (g) (2)

SiO_2 (s) + 4 e^- → SiO_x (s) + (2-x) O^{2-} (s) → Si (s) +2 O^{2-} (s) (3)

Si (s) + x O (s) → SiO_x (s) (4)

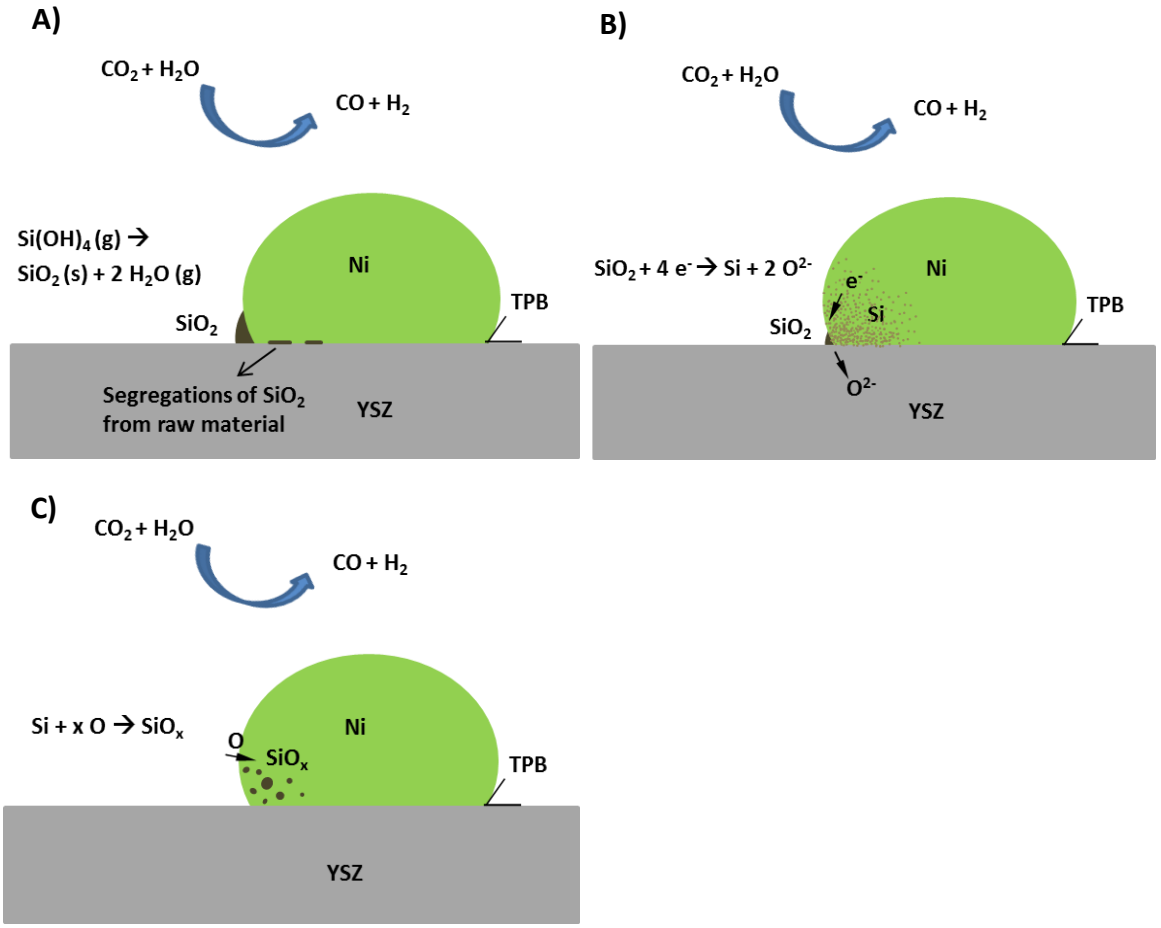

Figure 76. An illustration for the mechanism hypothesized for SiO_x inclusions in Ni grains of the Ni-YSZ electrode under large polarizations: A) Deposition of SiO_2 at TPBs and Ni|YSZ interface; B) Reduction of SiO_2 under large cathodic polarization and diffusion in Ni; C) Re-oxidation of the Si to SiO_x and precipitate in Ni grains

4.1.2 Nano-zirconia precipitations and mechanisms

4.1.2.1 Precipitation of zirconia nanoparticles

<u>Nano-zirconia precipitation for Ni-YSZ electrodes</u>:

Although some nano-zirconia were observed to well bond the surface of Ni (e.g. cell T4), generally the precipitations covered the surface of Ni lossely (a typical structure as shown in Figure 36 for cell T6). The

precipitates poorly bonding to Ni surface indicate these particles were unlikely to precipitated from the bulk of Ni. For cell 6, rough YSZ surfaces was observed for the previous contacting points of Ni-YSZ (Figure 36B & E). Meanwhile, the bumps on YSZ surfaces show a same scale in size with the nanoparticles. Further, based on intensive observations for all the tested cells, gernerally the fewer amounts of nanoparticles were observed on Ni surface with the further distance to the TPB lines or the edge of Ni|YSZ interface. The speculation is the nanoparticles migrated from the Ni|YSZ interface to the TPBs and Ni|pore interface, probably by surface diffusion.

Evolution of the precipitation in Ni-YSZ electrodes:

Considering the uneven distribution of the current densities along gas flow, the precipitates could occur and evolve in a time sequence from inlet to center and outlet. The amount of the nano-precipitates was found to decrease from cell inlet to outlet, as were shown for cell T2 (Figure 35) and T5 (Figure 48). Some larger particles & flake-like particles were probably due to the agglomeration & sintering of the nano-zirconia precipitates, e.g. observed for cell T5 (Figure 47) and T6 inlet (Figure 36). Cell T5 also showed nano-precipitates with a little bit smaller particle size at cell center than that at the inlet (Figure 47). The outlet & center could be viewed as the initial & early stage of the precipitation of the nano-zirconia.

In comparison to the cells tested for a significantly longer duration, cell T4, which was tested only for 138 h at -2.0 A/cm^2, could reveal an initial picture of structural change at the Ni|YSZ interface. The initiation of YSZ decomposition/reduction can be observed at the Ni|YSZ interface (Figure 37A – E) as an uneven reaction front (pits and bumps). The pits/bumps could be ascribed to the unevenness of the reduction and restructuring of YSZ even for the small contacting area between two particles. Generally, no destructive contact loss between Ni and YSZ contact occurred for the Ni-YSZ electrode since it was only initiation stage for the decomposing of YSZ.

Self-adaptive precipitation:

There could be a dynamic adjustment between the microstructure and performance of the cell during durability test. Because the precipitation in Ni-YSZ electrode was attributed to a large cathodic polarization (or a low interfacial pO_2), an increasing resistance for Ni-YSZ TPB reaction with the test means a higher over-potential and lower interfacial pO_2 for the local Ni-YSZ, which would consequently facilitate the precipitation of nano-zirconia. The migration of the zirconia nanoparticles to TPBs (and covering Ni surface) could increase the TPBs sites and decrease the resistance for TPB reactions (activation). The balancing between the degradation contributions and activation contributions would stabilize the electrode

performance. However, due to the continuous (and slowing down) structural changes, probably including coarsening of the nano-precipitates, loss in Ni percolations and impurity segregations, etc., precipitation of the nano-zirconia would also continue (and slowing down) with the durability test. The precipitation of the zirconia nanoparticles depends on the local performance of electrode and will also feed back to the performance, thus it appears to be a self-adaptive process. The stabilization of the Ni-YSZ electrode performance during the long-term galvanostatic test was confirmed by the results of electrochemical analysis (Chapter Electrochemistry).

4.1.2.2 Mechanism hypothesis

As was shown before, the YSZ nano-precipitates were generally observed at the Ni|YSZ and Ni|pore interface close to the YSZ electrolyte. The precipitation seems to be dependent on cell performance and operation. It can occur for a cell operated at very high current densities as short as 11 hours (Chapter CNT) or 138 hours (cell T4) but not necessarily occur for a cell operated at relative lower current densities for a long duration of ~ 700 hours (e.g. cell T7 at -1.5 A/cm^2). Interpretation of the mechanism and process of the precipitations is attempted in this section.

First, the decomposition of YSZ and precipitation of nano-zirconia is unlikely due to the demixing of cations for YSZ electrolyte.[5,6] Y and Zr show different cation diffusion coefficients in YSZ, however, even at 950 ^{o}C, the bulk diffusion coefficients of both cations would be slower than 10^{-19} cm^2/s and chemical decomposition of YSZ by demixing is very slowly.[6] In this study, the precipitation of zirconia was observed for SOECs after a test-duration of ~ 700 hours or even as short as 11 or 138 hours. Therefore, the structural change is not ascribed to kinetics demixing.

Based on the location and morphology of the precipitates, two possible processes / routes can be proposed. One possibility was the formation of Zr(Y) metal by complete reduction of YSZ at the Ni|YSZ interface, followed by diffusion / migration (through Ni grains or along Ni|YSZ interface) to Ni|pore interface, where to be re-oxidized to zirconia. The other possibility is the mechanical disintegration due to partial reduction of YSZ into nanoparticles at the Ni|YSZ interface, followed by migration (diffusion of the nanoparticles) to the Ni|pore interface.

Ni_xZr_y-ZrO_2 model:

As the figure below (Figure 77) illustrates, the YSZ at Ni|YSZ interface is completely reduced to Zr under large cathodic polarizations. Because Ni and Zr can form a variety of alloys with different compositions,[7,8] the Ni_xZr_y alloy could be formed at the Ni|YSZ interface. The interface generally supplies a fast diffusion

route (compared to bulk diffusion). A model based on the diffusion of Zr along Ni|YSZ interface is proposed, as is illustrated in Figure 77B). The metallic Zr will then be oxidized at the TPBs, where has a higher oxygen partial pressure. The metallic Zr of the Ni_xZr_y alloy can also be oxidized when the polarization is removed (Figure 77C), precipitating nanoparticles. The metallic Ni will not be oxidized in the gas atmosphere and will be incorporated into Ni bulk.

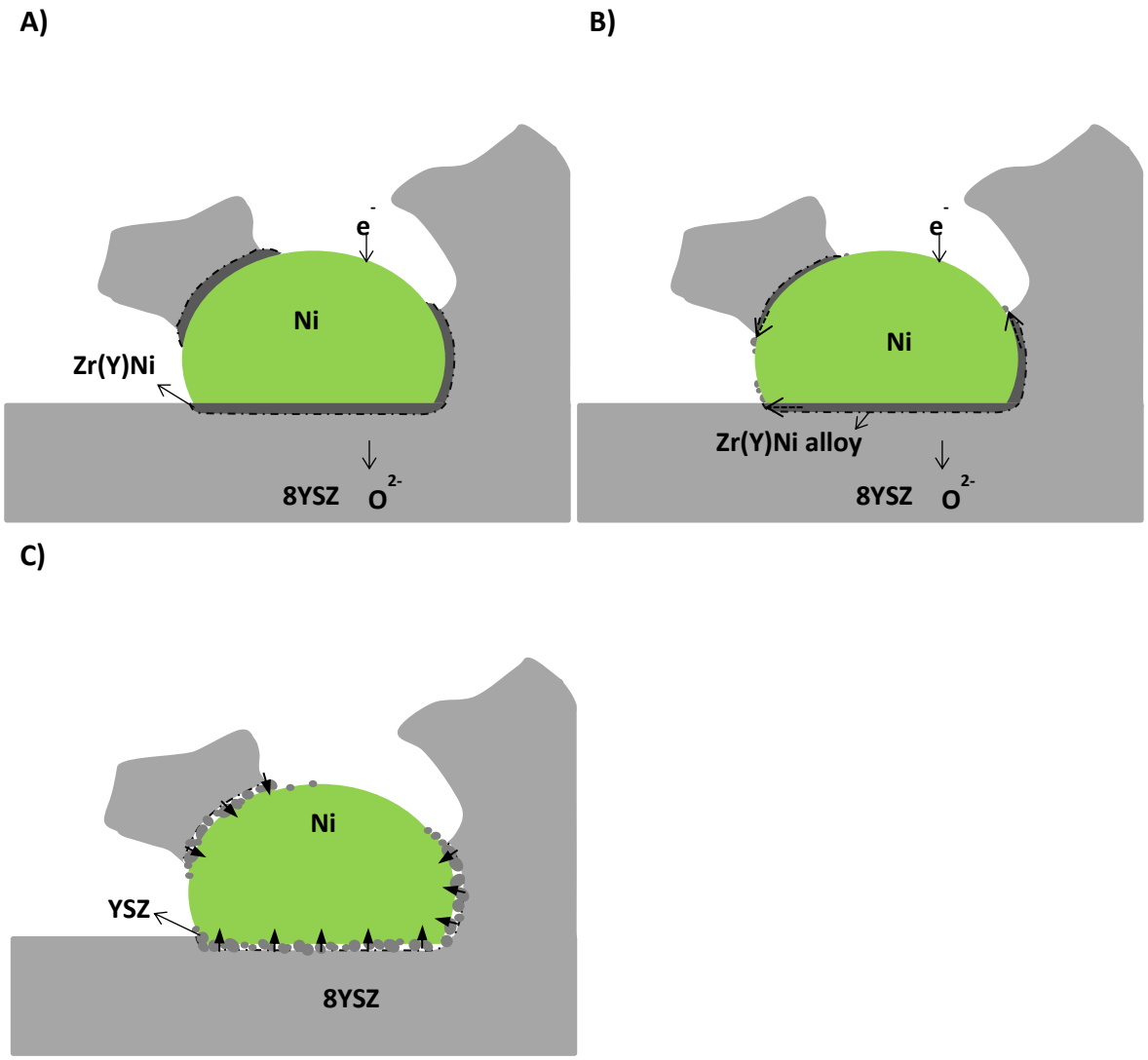

Figure 77. Illustrations of the mechanism hypothesized for the precipitating of nano-zirconia at Ni|YSZ and Ni|pore interface: A) Complete reduction of YSZ to Zr at Ni|YSZ interface; B) Zr diffusion along Ni|YSZ interface and re-oxidation at TPBs; C) In situ re-oxidation of Zr with the removal of polarization (|i| = 0)

Assuming a bulk diffusion of Zr through Ni grain and oxidization at the Ni|pore interface, a model was proposed previously for the explanation of the similar nanostructures observed in the SOECs.[9] The bulk diffusion model can explain the nano-zirconia precipitation at Ni|pore interface without necessity to

interpret the migration of the nanoparticles on Ni surface. But there are some problems with this model. The bulk diffusion of Zr in Ni and oxidation on Ni surface imply that the precipitates would bind strongly to Ni surface. However, SEM and TEM images clearly showed some nano-particles loosely spread over Ni surface, which cannot be explained by this model. In addition, as previously calculated the diffusion coefficient of O atom in solid Ni is $1.7*10^{-9}$ cm^2/s at 875 ^oC, which is much higher than Zr diffusion in Ni ($8.3*10^{-11}$ cm^2/s at 875 ^oC).[10] Therefore, it is expected that O atoms can also diffuse through Ni and form nano-zirconia precipitates inside Ni grains, which however, was not confirmed by observations for any the cells. Instead, the interface diffusion of Zr (Figure 77B) will not lead to precipitation in Ni grains. Metallic Zr would be oxidized as soon as reaching the surface of Ni, followed by the spreading / migration of the zirconia nanoparticles over Ni|pore interface.

Unfortunately, the above model on precipitation via complete reduction of YSZ to Zr-metal was not confirmed by the experimental results that no zirconium was observed at the Ni|YSZ interface for cell T3, a cell cooled down with cell voltage kept at the final value of the durability test. However, the experimental result cannot veto the mechanisms proposed in Figure 77, because the Ni-Zr alloy may already oxidized at room temperature, in particular when it is presented in the form of very thin film.

ZrO_x-ZrO_2 model:

The conductivity study performed by Park and Blumenthal implies an partial reduction of zirconia in the bulk.[11] The formation of low oxidation states was reported for Zr including Zr^{3+}, Zr^{+} and Zr^0 by an in situ XPS study on the blackening / reduction of YSZ.[12] Another study on current-blackening of Sc_2O_3 doped ZrO_2 (SSZ) showed precipitation of nano sub-oxides crystallites without any evidence of presence of metallic Zr.[13] The precipitates were observed to be aggregated at grain boundaries in the electrolyte bulk (differs to that of this study) and the mechanism was still unclear.

A model based on partial reduction of YSZ is proposed for explanation of the precipitation of nano-zirconia in the Ni-YSZ electrode of SOECs, as illustrated below. For the cells operated under large cathodic polarizations, the YSZ at the Ni|YSZ interface could be partially reduced to sub-oxides[13,14] instead of complete reduction to zirconium (Figure 78A). The YSZ under partially reduction could be mechanically unstable due to the unevenness or a dynamic process of reduction / restructuring, or due to defect aggregation. Then YSZ crumbles into many nano crystallites (e.g. loosely stacked crystallites as in Figure 54), followed by migration from the Ni|YSZ interface to Ni|pore interface, as is illustrated in Figure 78B. This model can explain the precipitation of zirconia at the Ni|YSZ interface and Ni|pore interface. It is consistent

with the microstructural observations of the loosely stacked nanoparticles between Ni and YSZ (e.g. cell T2 and T6).

The above model emphasizes a process of partial reduction of YSZ and disintegration. The decomposing of YSZ is probably related to the unevenness of the reduction and restructuring at the Ni|YSZ interface. The unstable reaction front has been previously reported by J. Janek and C. Korte for the electrochemical blackening of YSZ.[15] The pits on the Ni|YSZ interface for cell T4 (Figure 37) in this study can be also deemed as an indicator of the unevenness of the YSZ reduction. In addition, a cell tested at -2.25 A/cm^2 for merely 11 hours showed formation of large numbers of cubic zirconia nanoparticles (and CNTs) at YSZ | Ni-YSZ interface (Figure 79 & Chapter CNT). The porous region of the YSZ electrolyte (Figure 79A) at the previous contacting interface of Ni-YSZ contains many zirconia nanoparticles adhesion to the bulk YSZ, indicating an uneven reaction at Ni|YSZ interface for YSZ reduction / decomposition. The original micron-size YSZ grain of the electrolyte close to the YSZ | Ni-YSZ interface appears to be composed of many nano crystallites after test (Figure 79B). The nano crystallites or rough surface of YSZ were also observed for the other cells (e.g. cell T4 & T6). These features could indicate formation of subdomains and finally nano crystallites in the original grain of YSZ during reduction without formation of Zr-metal.

Further, in comparison to the possible Zr/Y segregations for the Ni_xZr_y-ZrO_2 model, the same composition between the nano-precipitates and the bulk electrolyte (8YSZ) can be predicted by this model, which is in confirmed by the results of TEM analysis. Therefore, it seems that this model well describes the precipitations as observed. However, a clearer / detailed picture on how the partially reduced YSZ physically decompose into nano crystallites is still required.

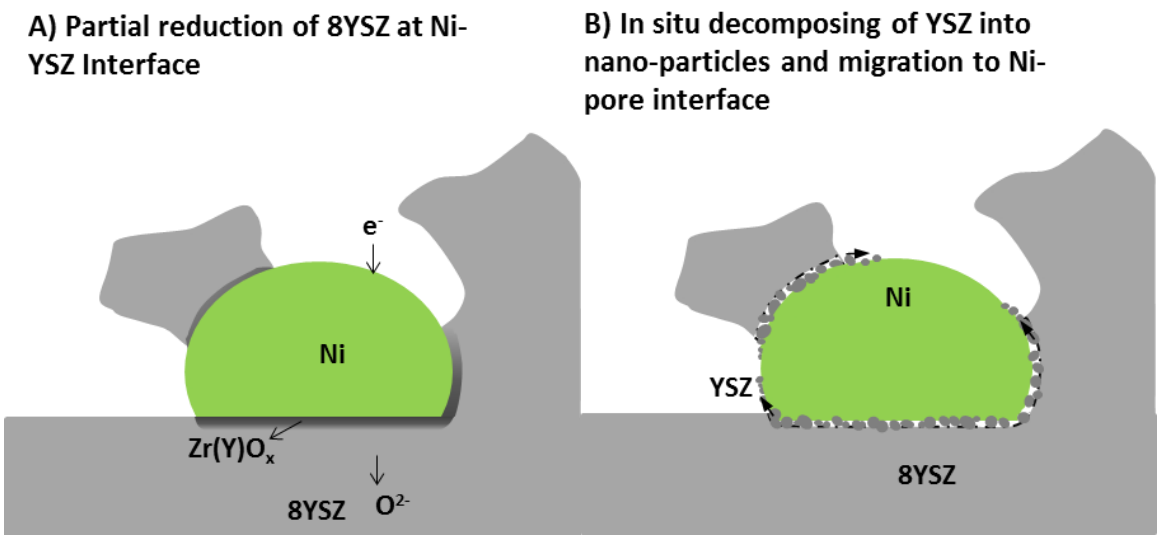

Figure 78. Illustrations of the mechanism hypothesized for the precipitating of nano-zirconia at Ni-YSZ and Ni|pore interface: A) Partial reduction of YSZ at Ni|YSZ interface; B) In situ decomposing of YSZ into nanoparticles and migration to Ni-pore surface

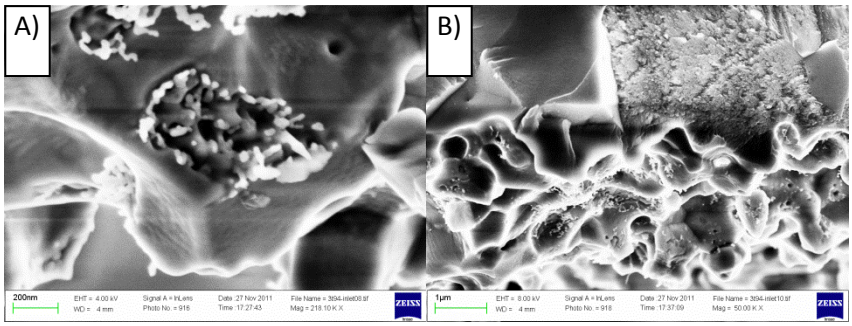

Figure 79. SEM images of the YSZ|Ni-YSZ interface for a cell with CNT formation observed (-2.25 A/cm^2; co-electrolysis; 875 ^{o}C; 11 hours) (See Chapter CNT for more information)

4.1.2.3 Electrochemical condition of the Ni-YSZ electrodes:

Based on Gibbs energy of ZrO_2 and Nernst equation, the oxygen partial pressure was calculated to be 10^{-41} atm for the reduction of ZrO_2 to Zr metal; however, a higher pO_2 of ~10^{-29} atm was estimated based on phase diagram analysis by M. Chen et al.[9] In this study, according to the electrochemical analysis for the cells showing zirconia precipitations (Chapter Electrochemistry), the potential difference (ΔV) of the Ni-YSZ electrode against oxygen electrode in 1 atm O_2 was ~ 1.2 V under operation and the corresponding pO_2 at Ni|YSZ interface is estimated to be 10^{-21} ~ 10^{-22} atm, unlikely for a complete reduction of YSZ to metal. However, the above estimations only refer to the average properties across the cell. The local condition should be much harsher in the Ni-YSZ electrode, considering the uneven distribution of current density / over-potential. Assuming a contribution of three orders higher for the interfacial pO_2, the experimental pO_2 at Ni|YSZ interface is still far away from the condition for Zr formation. On the other hand, estimations can be made based on the LSCF cells, which were operated at relative low cell voltages of no more than 1.52 V (including contributions of all components). Even assuming a ΔV of 1.52 V versus oxygen electrode at 1 atm O_2, the corresponding interfacial pO_2 for Ni-YSZ is estimated to be 2.0*10^{-27} atm, still above the pO_2 expected for a complete reduction of YSZ to metal. Therefore it was less likely for YSZ to be completely reduced to Zr(Y) metal and the nano-zirconia precipitation is more likely to be interpreted by the mechanism model based on partially reduction and in situ volume decomposing of YSZ bulk.

4.1.3 Ni percolation loss: effect of polarization and gas atmosphere

<u>Ni percolation loss vs. nanoparticle precipitation:</u>

As was shown by the SEM images, Ni percolation loss was observed for the Ni-YSZ electrode of all the tested cells, including cell T7, which was operated at relative lower current density (-1.5 A/cm^2) and exhibited the lowest degradation without nano-zirconia precipitation. For the Ni-YSZ electrode showing Ni percolation loss and precipitation of nano-zirconia, precipitation was observed neither for Ni-Ni connections nor for interior of Ni grains. In addition, the percolation loss of Ni (cell T2) at outlet was observed to be as severe as that of inlet, while only limited numbers of precipitates were found for outlet, contrast to the significant amount of precipitates for inlet. Therefore, there is no direct contribution from the precipitation of nano-zirconia to percolation loss of Ni. Ni percolations already start to reduce at mild operation conditions, whereas nano-particle precipitating only occurs at very harsh conditions. For the cells tested in this study, Ni percolations started to decrease from the beginning, while the precipitation initiated sometime later with the degradation of Ni-YSZ electrodes.

Inlet vs. outlet:

LSM cells T2 (maybe also T3) showed equally severe percolation loss of Ni at inlet and outlet after 700 hours test (500 hours for cell T3) at -2.0 A/cm^2. Another LSM cell (cell T4) tested using the same set-up at the same current density but for a much shorter duration (138 hours), showed obvious percolation loss of Ni at inlet and negligible percolation loss at center and outlet. The above results indicated an evolution of Ni percolation loss from inlet to outlet in the Ni-YSZ electrode during the test.

Ni percolation loss and gas composition:

For a Ni-YSZ electrode under operation, transportation of nickel by evaporation/condensation and diffusion mechanisms will lead to changes in surface morphology and particle size.[16] The mass tranport of Ni is highly dependent on the operation conditions (T, pH_2O, etc.). A higher steam ratio of the gas atmosphere is expected to led to more severe Ni-Ni disconnections due to Ni mass loss with the formation and evaporation of $Ni(OH)_2$,[2] or due to the promoted mass tranport and sintering of Ni by Ni_2-OH complex.[17] With the converison of H_2O to H_2 under electrolysis current, the steam partial pressure (pH_2O) decreases along the gas flow direction, i.e. from gas inlet to outlet. Therefore, Ni percolation loss would occur in a much faster rate for the Ni-YSZ electrode close to inlet than outlet, as was observed by SEM.

Ni percolation loss and polarization:

Merely considering the difference of the local gas compositions, Ni percolation loss should have been the lowest at the Ni-YSZ|YSZ interface, where the pH_2O is the lowest. However, an inactive Ni-YSZ layer (a few microns thick) with little percolation of Ni can be observed for the Ni-YSZ electrode close to the YSZ

electrolyte. The more close to the YSZ electrolyte, the more severe percolation loss of Ni can be observed, which was confirmed by all the tested cells. Such severe Ni percolations was not observed in the Ni-YSZ support, where the polarization was zero. The microstructral observations are consistent with the existance of a large over-potential gradient from YSZ|Ni-YSZ interface to the Ni-YSZ electrode. Based on above analysis, the polarization over Ni-YSZ electrode also played an important role for the percolation loss of Ni. Along the cell length, the higher current density/over-potential at cell inlet than outlet (See Chapter VI) could also contribute to the faster/severe percolation loss of Ni at inlet.

Evolutions:

The faster Ni percolation loss at inlet (thus increase of TPB reaction resitance) would cause the local current density (over-potential) decreasing at inlet and increasing at center and outlet.(See Chapter VI) Base on the precious iscussion on Ni percolation loss and over-potential, with the cell degradation Ni percolation loss of the cell at down stream would catch up. And it is expected that if the test duration was long enough, there would be less and less difference in the extent of Ni percolation loss for the Ni-YSZ electrode across the cell, as was confirmed by microstrural analysis (cell T2, etc.). For the severe disconnections of the Ni-Ni particles, the ohmic resistance of the cell will increase, as was shown by the electrochemical analysis.

4.1.4 Ni-YSZ contact loss

Ni-YSZ contact loss:

The contact loss between Ni and YSZ could be mainly ascribed to the formation of the nano-particles. SEM images revealed nanoparticles precipitating at Ni|YSZ interface, insulating the contact of Ni particles with YSZ or even detaching Ni from YSZ electrolyte. For the Ni-YSZ electrode without showing precipitates, including the reference cells without durability test, the gaps between Ni-YSZ were hardly observed. For the Ni-YSZ electrode with only limited amount of precipitations, the Ni-YSZ contact loss was generally insignificant. For the Ni-YSZ electrode at the initiation period of precipitation, Ni particles could still firmly connect with YSZ (e.g. cell T4) and it is postulated that further precipitation will occur for a longer test duration, resulting into deterioration of the Ni-YSZ contact. The Ni-YSZ contact loss is expected to contribute importantly to the increase of Rs during the durability test, which was confirmed by the results of electrochemical analysis. However, the Ni-YSZ contact under operating was not necessarily as poor as the Ni-YSZ gaps observed after test. When cooling down the cell after test, the larger volume shrinkage of Ni particle than that of YSZ due to a higher thermal expansion coefficient (TEC) could contribute to the significant width of gaps between Ni and YSZ.

4.1.5 Microstructural & Electrochemical Evolutions of the Ni-YSZ electrode

Evolution of Ni percolation loss & Nano-precipitates:

Ni particles close to the YSZ electrolyte could lose percolation within a relative short test period, as was observed for the inlet of cell T4 after an operation of only 138 hours. The Ni particles without connections to the Ni networks cannot provide an electron-path for electrochemical reactions, thus turn to be inactive or 'dead' Ni particles. Therefore, the precipitation of nanoparticles must have started as early as before Ni losing Ni-Ni connections. Some zirconia nanoparticles on Ni close to the YSZ electrolyte could be formed even hundreds of hours before the end of the test.

As soon as a Ni particle turned inactive, the local current density / over-potential would drop to zero, not favoring any further decomposing of YSZ. Thus, even if some metallic Zr had been formed during the test, it could be oxidized to zirconia already before stopping the test, given the Ni particle had lost all connections with Ni network. This brings trouble to the investigation of the mechanisms of zirconia precipitation, e.g. the attempt to clarify the presence/absence of metallic Zr in cell T3 by maintaining the cell voltage during cooling. Even though the post-test results confirmed no metallic Zr was observed, probably, the presence of Zr still cannot be excluded.

Percolation loss of Ni particles will result in increase of Rp due to a reduced TPB length. However, for the Ni particles that still connected to the network, the local current density and over-potential will increase (galvanostatic operation). When the critical condition is satisfid locally, nano-particles will start to precipitate. Spreading of the nano-precipitates along TPBs will compensate the increase in Rp to some extent. Rp degradation could also be alleviated by a higher cell temperature due to cell resistance increase. Both compensation effect would contribute to a stabilization of the TPB reaction resistance.

With degradation of the cell in a longer duration, almost all the Ni particles next to YSZ electrolyte lost connections to Ni networks, resulting into not only a Rs increase but also an inactive region for the electrolysis reactions. Instead, the Ni particles or Ni-YSZ TPBs at a further distance to the electrolyte is expected to play a more important role for reactions. The increase in the local current density/over-potential for these new reaction sites will favor the precipitation locally. Therefore, the Rs would continue to increase due to Ni percolation loss and Ni-YSZ contact loss. But the Rp will not necessarily increase a lot due to the compensation effect. Actually, it was experimentally confirmed that an increasing Rs and a stabilized Ni-YSZ TPB reaction resistance were observed for the long term durability test. (See Chapter Electrochemistry)

Due to a high gradient of the current density/over-potential from the Ni-YSZ | YSZ interface to the Ni-YSZ electorde, most of the reactions take place within a region very close to the interface. For the cells with insignificant amount of nano-particles observed (e.g. cell T1 or T5), the precipitates were found only for the Ni grains very close (1 – 2μm) to YSZ electrolyte, indicating a large over-potantial gradient. Based on careful observations by SEM on cell T2, for which a large number of nano-precipitates were observed, no obvious difference in the amount of the precipitates was found for the region 0 – 6 μm to the electrolyte. However, a drop of the amount was observed at the edge (6 – 8 μm) of the precipitating region. The distribution is in good agreement with the above discussions on the structural evolutions (an advancing front for the reactions). The drop of the amount at the edge confirmed again the presence of large gradient of over-potentials.

It can be concluded from SEM that Ni percolatin loss was less severe (i.e. slower degradation) at cell outlet than inlet. No or very limited nano-precipitates were observed at cell outlet, indicating where the critical condition was not satisfied. It implies an uneveness of the current density / over-potential across the cell along gas flow direction. The above results also confirm that a much harsher condition was requied for initiation of the nano-particles formation than for a substantial loss of Ni percolations.

4.2 YSZ electrolyte and oxygen electrode

4.2.1 Horizontal cracks in the YSZ electrolyte

Mechanism hypothesis:

Horizontal cracks was widely observed in the center of YSZ electrolyte for the polished cross-sections of the cells and never found in the fractures without any processing. The cracking was unlikely to occur during operation, or, the cell would not exhibit any performance. The cracks can only occur during the preparation of samples for SEM, when the high hardness SiC and diamond crystallites were used for polishing. However, the horizontal mechanical failure reflects a high internal stress in the YSZ electrolyte perpendicular to the electrolyte plane. Such cracks have never been observed for the SOECs operated at low current densities or the reference cells, therefore, the internal stress can only originate from the heavy load durability test. Across the YSZ electrolyte, the pO_2 and thermal gradient perpendicular to the cell plane could be the reasons for the generation of internal stress.

Oxygen partial pressure (pO_2):

The distribution of the pO_2 across the YSZ electrolyte during SOEC operation is illustrated in

Figure **80**.[18] From the electrolyte center approaching the cathode, the pO_2 decreases dramatically corresponding to a large cathodic polarization. A low pO_2 could result in initiation of the (partial) reduction of YSZ at the Ni-YSZ electrode | YSZ electrolyte interface. On the contrary, the pO_2 increases with approaching the YSZ electrolyte | oxygen electrode interface and the build-up of oxygen activity at the interface could result in oxygen bubble formation at YSZ grain boundaries.[19]

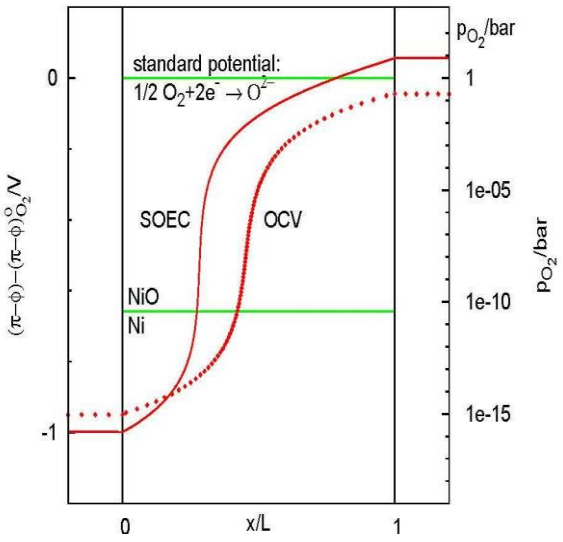

Figure 80. The potential and pO2 course of a SOEC at OCV and under operation

Thermal effect:

Thermal effects of the cell components during SOEC operation could also contribute to horizontal mechanical stress in the YSZ electrolytes. As is shown in the figure below (
Figure 81), the different components of the electrolysis cell exhibit different thermal effects under operation. The ohmic and electrode polarization resistances for the cell operated under a current density i result in positive heating effect according to i^2R. The electrode reaction $2\ O^{2-} \leftrightarrows O_2 + 4\ e^-$ heats/cools much more than $2\ H_2O + 4\ e^- \leftrightarrows 2\ H_2 + 2\ O^{2-}$ and the -TΔS is negative heat (i.e. cooling) for the electrolysis cells. The higher temperature and current density correspond to the stronger cooling effect of the oxygen active electrode. The thermal effect could lead to large thermal gradient and internal stresses in the cell components perpendicular to the cell plane, e.g. in the YSZ electrolyte. As was observed by post-test SEM examination, horizontal cracks were generally observed in the YSZ electrolyte, either in the middle or close to the electrolyte | electrode interfaces.

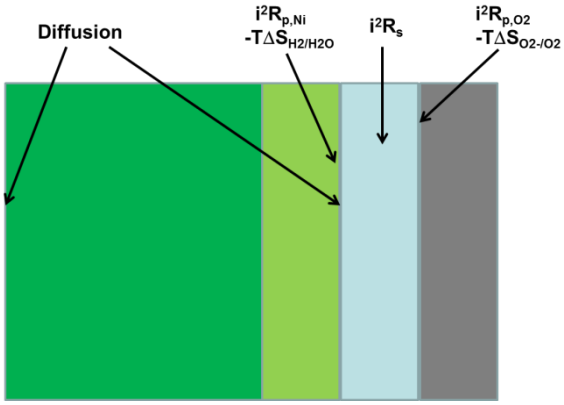

Figure 81. Thermal effects of the electrochemical processes at different cell components

4.2.2 Oxygen bubbles & voids in YSZ

YSZ degradation of cell T3:

The void structure in YSZ electrolyte (Figure 75) was only observed for cell T3 after test. The similar structure of the YSZ electrolyte has been reported by F. Tietz et al on a SOEC cell after 9000 hours' test at -1.0 A/cm^2.[20] They attributed it to the cation diffusion in the electrolyte under large gradient of pO_2 and the pores were regarded as Kirkendall voids. Even earlier, nano-sized pores at the YSZ GBs close to interface were observed on a SOEC tested at -2.0 A/cm^2 for 188 hours by R. Knibbe et al who referred the pores as oxygen bubble.[19] It was hypothesized that oxygen formed at the GBs close to the interface due to a high pO_2 build up under a large oxygen electrode polarization. As is shown in the figure, when approaching the YSZ|LSM-YSZ interface the size and amount of the nano-pores increased at GBs and prevailed inside the YSZ grains, indicating that they were likely of same type of structural degradation but only different extent. The structural changes are unlikely ascribed to cation diffusion due to the short duration.

The horizontal cracks/porous layer structures indicated a potential or pO_2 gradient across the electrolyte causing the structural decomposition of YSZ. However, the void structure of YSZ was not observed for the other cells that experienced a similar galvanostatic operation history. Because the cell voltage of this cell was kept at final operating voltage during cooled down in H_2, the structural degradation of YSZ occur during this process cannot be excluded.

4.2.3 The intact oxygen electrode

Little change was observed for the oxygen electrode after durability test, which is consistent with the electrochemical analysis that no or minor degradation occurred for oxygen electrodes. Good connections were also observed at the oxygen electrode | YSZ electrolyte interface for all the tested cells.

5. Conclusions

Post-test microstructural analysis was performed on the fractures and polished cross-sections of the tested cells by SEM/EDS. Ni percolations at the different regions of the Ni-YSZ electrode were studied by LVSEM. Detailed microstructure and composition of the Ni-YSZ active electrode especially the nano-precipitates were studied by (S)TEM/EDS.

The major structural changes for the cell after durability test occurred in the Ni-YSZ active electrode. The structural and compositional changes of the Ni-YSZ electrode included the accumulation of impurities, the loss of Ni percolation, the precipitation of nanoparticles and the loss of Ni-YSZ contact. Horizontal cracks in the center of the YSZ electrolyte were observed on the polished cross-sections. Little change was found in the oxygen electrode and in its connection with the electrolyte;

For the accumulation of impurities, Si was observed to be the dominating impurity species in the Ni-YSZ active electrode close to the YSZ electrolyte. Si-impurities were observed inside the Ni grain instead of being at the TPBs or at the Ni|YSZ interface. The Si inclusions were revealed to be composed of Si and O by (S)TEM/EDS. The Si inclusions in Ni was likely to be formed according to a deposition-reduction-diffusion-oxidation mechanism: Si transported from the glass sealing by the form of hydroxide followed by deposition to SiO_2 at the Ni-YSZ TPBs; then, SiO_2 was reduced to Si under cathodic polarization; next, Si diffused to the interior of Ni grains; finally, the Si was re-oxidized by O that diffused into the Ni bulk and precipitated as SiO_x.

For the Ni percolation loss, the cell operated at 2.0 A/cm^2 for a short term (138 h) showed severe percolation loss of Ni at the cell inlet and minor percolation loss at the outlet. The cells operated at the same condition for ~ 700 hours showed serious loss of Ni percolation at both the inlet and outlet. These results indicated that an evolution of Ni percolation loss existed along the cell from the inlet to the outlet with the cell degradation. The Ni percolation loss was ascribed not only to the high steam partial pressure of the local gas atmosphere but more importantly to the high cathodic polarization at the TPBs close to the Ni-YSZ|YSZ interface. The Ni percolation loss did not rely on the presence of impurities. No effect was found for the precipitation of nano-zirconia on

the loss of Ni percolation, while the Ni percolation loss resulted in an increase in the Ni-YSZ TPB resistance, indirectly contributing to initiating the precipitation of nano-zirconia;

For the nano-zirconia precipitation, nanoparticle precipitations were observed in the Ni-YSZ active electrode close to the YSZ electrolyte for all the cells except T7. With an increasing amount of the nanoparticles being formed, the precipitates can be found at the Ni|YSZ interface, in the vicinity of TPBs, or even the entire surface of the Ni particles. TEM analysis revealed that the nano-precipitates were yttria doped zirconia with the same composition as that of the YSZ electrolyte. The zirconia precipitates were found to have a dominating cubic phase structure. The particle size of the nanoparticles showed a unimodal distribution and most of the particles were 30 ~ 50 nm. The formation of the nano-zirconia precipitation was proposed to follow three steps: 1) YSZ partial reduction of at the Ni|YSZ interface under large cathodic polarizations; 2) structural breakdown of YSZ and formation of zirconia nanoparticles; 3) migration of the zirconia nanoparticles to the further Ni|pore interface.

For the Ni-YSZ contact loss, Ni-YSZ contact loss can be observed in the active electrode next to the YSZ electrolyte. Because severe Ni-YSZ contact loss was observed for the electrode showing significant amount of nano-zirconia precipitations, while no obvious loss was observed for the Ni-YSZ electrode showing insignificant or small amount of precipitations, the Ni-YSZ contact loss was mainly ascribed to the precipitating of the nanoparticles. The Ni|YSZ contact loss probably indicated a mass loss of YSZ at the Ni|YSZ interface due to the precipitation and transportation of YSZ to the Ni surface.

References

1. A. Hauch, S. H. Jensen, J. B. Bilde-Sørensen, and M. Mogensen, *J. Electrochem. Soc.*, **154**, A619 (2007)

2. A. Hauch, S. D. Ebbesen, S. H. Jensen, and M. Mogensen, *J. Electrochem. Soc.*, **155**, B1184 (2008)

3. A. Hauch, J. R. Bowen, L. T. Kuhn, and M. Mogensen, *Electrochem. Solid-State Lett.*, **11**, B38 (2008)

4. J. Park and C. J. Altstetter, *Metall. Trans. A*, **18**, 43–50 (1987).

5. M. Martin, *Solid State Ionics*, **136-137**, 331–337 (2000)

6. M. Kilo et al., *J. Appl. Phys.*, **94**, 7547 (2003)

7. P. Nash and C. S. Jayanth, *Bull. Alloy Phase Diagrams*, **5**, 144–148 (1984).

8. K. Bhanumurthy, G. B. Kale, S. K. Khera, and M. K. Asundi, *Metall. Trans. A*, **21A**, 2897–2903 (1990).

9. M. Chen et al., *J. Electrochem. Soc.*, **160**, F883–F891 (2013).

10. H. W. Allison and H. Samelson, *J. Appl. Phys.*, **30**, 1419 (1959)

11. J. Park and R. N. Blumenthal, *J. Electrochem. Soc.*, **136**, 2867–2876 (1989).

12. B. Luerßen, J. Janek, S. Günther, M. Kiskinova, and R. Imbihl, *Phys. Chem. Chem. Phys.*, **4**, 2673–2679 (2002)

13. F. K. Moghadam, T. Yamashita, and D. A. Stevenson, *J. Mater. Sci.*, **18**, 2255–2259 (1983).

14. J. Peng et al., *J. Electrochem. Soc.*, **157**, F1 (2010)

15. J. Janek and C. Korte, *Solid State Ionics*, **116**, 181–195 (1999).

16. H. Yokokawa, H. Tu, B. Iwanschitz, and A. Mai, *J. Power Sources*, **182**, 400–412 (2008)

17. J. Sehested, J. A. P. Gelten, I. N. Remediakis, H. Bengaard, and J. K. Nørskov, *J. Catal.*, **223**, 432–443 (2004)

18. T. Jacobsen and M. Mogensen, *ECS Trans.*, **13**, 259–273 (2008).

19. R. Knibbe, M. L. Traulsen, A. Hauch, S. D. Ebbesen, and M. Mogensen, *J. Electrochem. Soc.*, **157**, B1209 (2010)

20. F. Tietz, D. Sebold, a. Brisse, and J. Schefold, *J. Power Sources*, **223**, 129–135 (2013)

Appendix: Ni-Si phase diagram

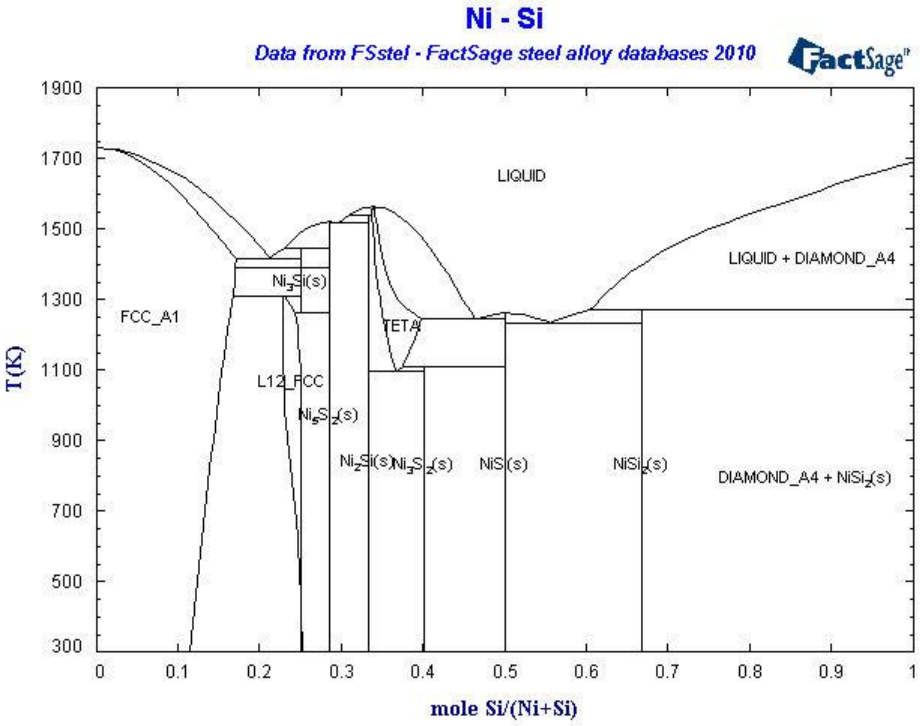

Appendix: Extra results

Cell T2: inlet &outlet

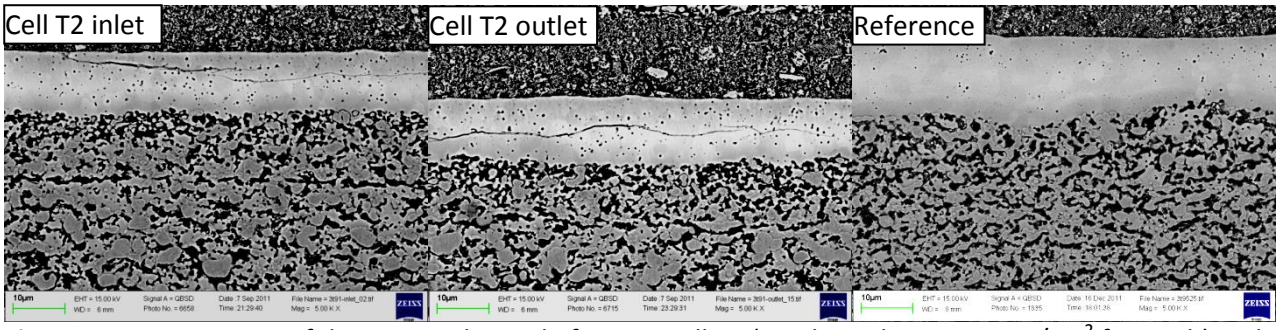

Figure A5-1 SEM image of the Ni-YSZ electrode for LSM cell T2 (co-electrolysis at -2.0 A/cm^2 for 678h) and a reference cell not tested

Ni: round shape after test both for the inlet & outlet

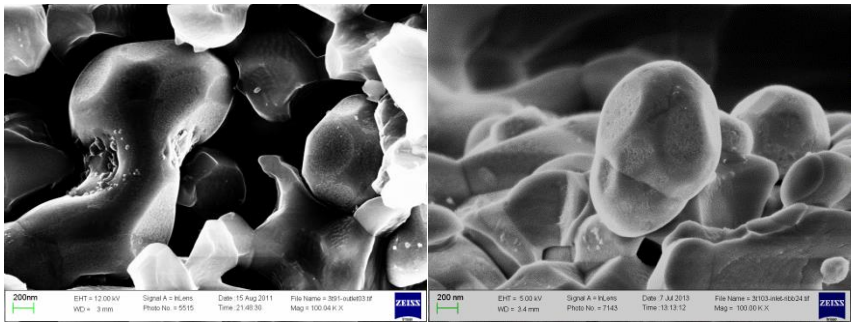

Figure A5-2 SEM images of the Ni particles close to Ni-YSZ|YSZ interface after test: left) cell T2; right) cell T4

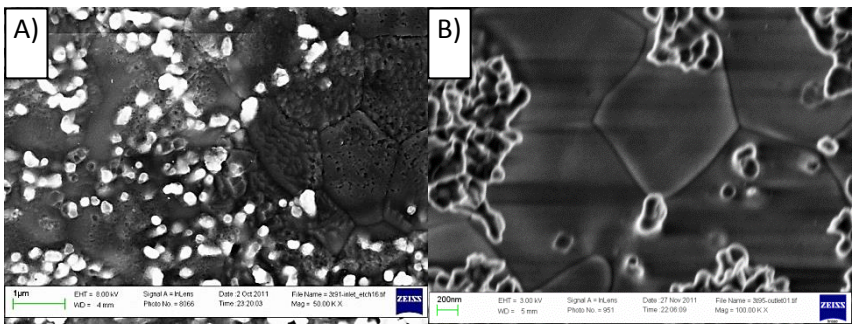

Figure A5-3 SEM image of the HCl etched YSZ|LSM-YSZ interface of A) LSM cell T2 after co-electrolysis at -2.0 A/cm^2 for 678h and B) a reference LSM cell without performing durability test

The inlet part of the cell was soaked in HCl solution for 20min with the LSM electrode etched away; then it was washed with H_2O and ethanol using ultrasonic. The surface of the YSZ electrolyte was observed directly using SEM. As shown in the figure above, apart from the residual YSZ particles, there are some imprints or pits on the YSZ electrolyte surface (both grain surface and grain boundary). Crinkles can also be observed.

Chapter 6 Uneven Distribution of Current Density and Degradation of the Planar Solid Oxide Cells Operated under High Current Densities

1 Introduction

When operating a solid oxide cell at large current, the local gas composition will vary significantly along the gas flow due to gas conversions. The local performance of the cell, e.g. EMF, resistance, current density could be affected and varied depending on the location of the cell. The difference in operating conditions would result in different extent of structural degradation for different regions of a cell after long-term operation. Based on the microstructural analysis in chapter 5, uneven degradation of the Ni-YSZ electrode from inlet to outlet was revealed for the solid oxide electrolysis cells (SOECs) experiencing a few hundred hours' operation at high current densities. The investigation of the variation of the gas composition and current density along the cell is important for the understanding of the uneven performance and degradation.

The uneven performance along the cell can be illustrated by the in-plane voltage between the inlet and outlet of the cell. The measured in-plane voltage indicates different local current densities along the gas flow direction because current will flow through the current collector from the higher resistive part of the cell to the part with lower resistance. Actually, for the SOECs operated at low current densities, the in-plane voltage measurement has been employed for the investigation of the uneven resistance of the Ni-YSZ electrode caused by the impurities(Si or S, etc.).[1,2] At low current densities the impurities plays a major role in the performance changes for the Ni-YSZ elecotrde, and the uneven resistance due to the spreading out of the impurities from inlet to outlet can be revealed by the changes of the in-plane voltage.

In this chapter, both the experimental and modelling work will be performed to study the uneven performance of the cells operated under high current densities. Also, the in-plane voltage measured for the long-term durability test will be interpreted to reveal the evolution of the degradation along the SOECs.

2 Experimental

A planar solid oxide cell, with a configuration of Ni-YSZ support layer (~ 300 µm)|Ni-YSZ active electrode(~ 10 µm) | YSZ electrolyte (~ 10 µm)|CGO barrier layer (~ 5 µm)|LSCF-CGO electrode (~ 20 µm), was tested using the set-up as shown in Figure 82. The albite glass bar was used as sealing on both sides. The cell was heated up to 1000 ^{o}C for reduction of NiO-YSZ in 9 % H_2 + 91 % N_2 and 4 % H_2O + 96 % H_2 and then cooled

down to 850 °C for characterization of the performance. The characterization included the impedance measurement at OCV and i-V scan in various gas compositions. Then, investigation of the uneven performance was carried out for the cell in fuel cell (FC) mode and electrolysis cell (EC) mode. The cell was operated in FC mode at the current density between 0 and 2.5A/cm^2 with 25 L/h 4 % H_2O + 96 % H_2 flown to Ni-YSZ and 140 L/h O_2 flown to LSCF-CGO. Then the cell was operated in EC mode between 0 and -2.5A/cm^2 with 25 L/h 45 % H_2O + 45 % CO_2 + 10 % H_2 flown Ni-YSZ and 140 L/h O_2 flown to LSCF-CGO.

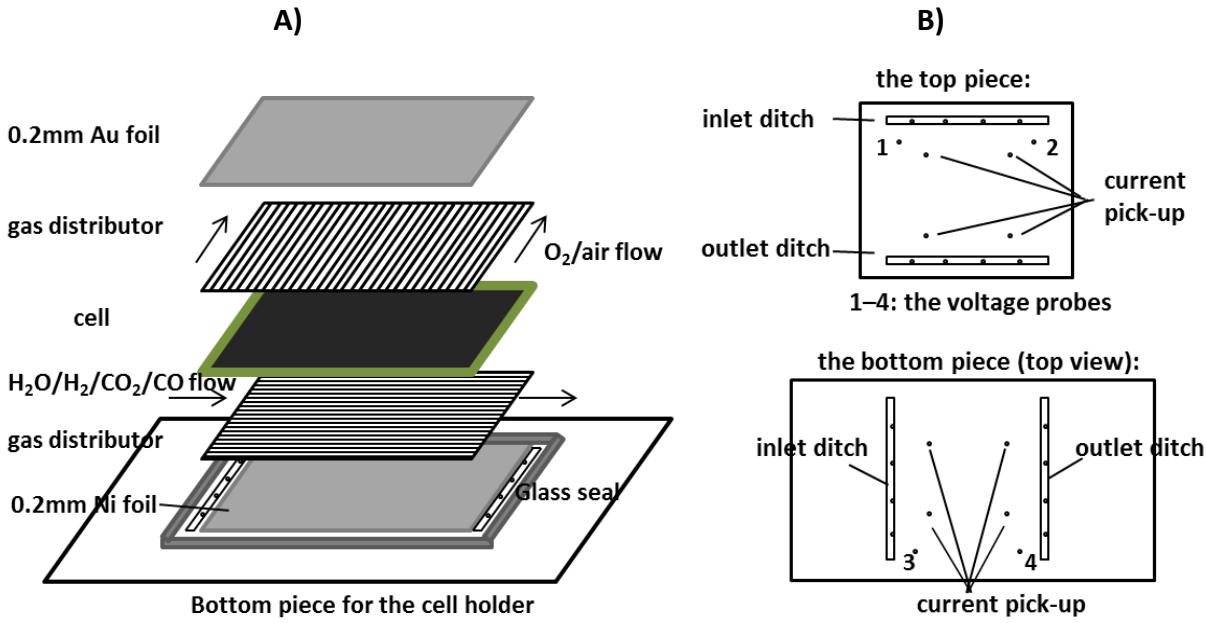

Figure 82 A) sandwich-setup for the test of the cell: the cell, metal foils and the ceramic gas distributors; B) the alumina holder with holes for placing the Pt wires (current pickup and in-plane voltage measurement) and the inlet and outlet ditches for gas flown. Through the holes 1 – 4 the voltage probes are attached to the Au and Ni current collectors. The in-plane voltage is measured between 1 and 2 for the fuel electrode side, or between 3 and 4 for the oxygen electrode side. In addition, for each piece of cell holder there are 4 holes for placing the current pick-up wires.

As is shown in Figure 82, current was collected by the Au and Ni foils (current collectors). Four pieces of Pt short wires were used to pick up the current and then it flows through the main current wire. The four Pt wires have a diameter of 1 mm and an equal length of ~ 10 cm. Both the Au and Ni foils are 0.2 mm in thickness, 4 cm in length and 4 cm in width. The Ni-YSZ and LSM gas distributors have a diamension of 1 mm (thickness) x 4 cm x 4 cm. The voltage probes are attached to the surface of the Au and Ni current collectors. The in-plane voltage is caused by the in-plane current through the current collector and the resistance of the current collector that each pair of probes (1 & 2, or 3 & 4) is attached to. The in-plane

voltage between the inlet and outlet of the cell was measured for FC operation at 0 – 2.5 A/ cm^2 and for EC operation at 0 – -2.5 A/ cm^2. The temperature of the cell at the center and outlet was recorded by two temperature probes which were placed (about 1 mm on top of the oxygen electrode) on the surface of the Au plate.

The long term durability of the solid oxide cells (cell T1, T6 and T8) for electrolysis of CO_2 and steam was studied by operating the cells at a constant current for ~ 700 hours, as was presented in Chapter 4 (Electrochemical analysis) and Chapter 5 (Microstructural analysis). The galvanostatic operation was performed for cell T1 and T6 at -1.5A/cm^2, and for cell T8 at -2.0 A/cm^2. The in-plane voltage was recorded during cell degradation in order to study the current distribution and evolution of the degradations along the cell.

3 Results

3.1. Initial performance in 4 % H_2O + 96 % H_2 (FC mode)

5.1.1 i-V and in-plane voltage measurement

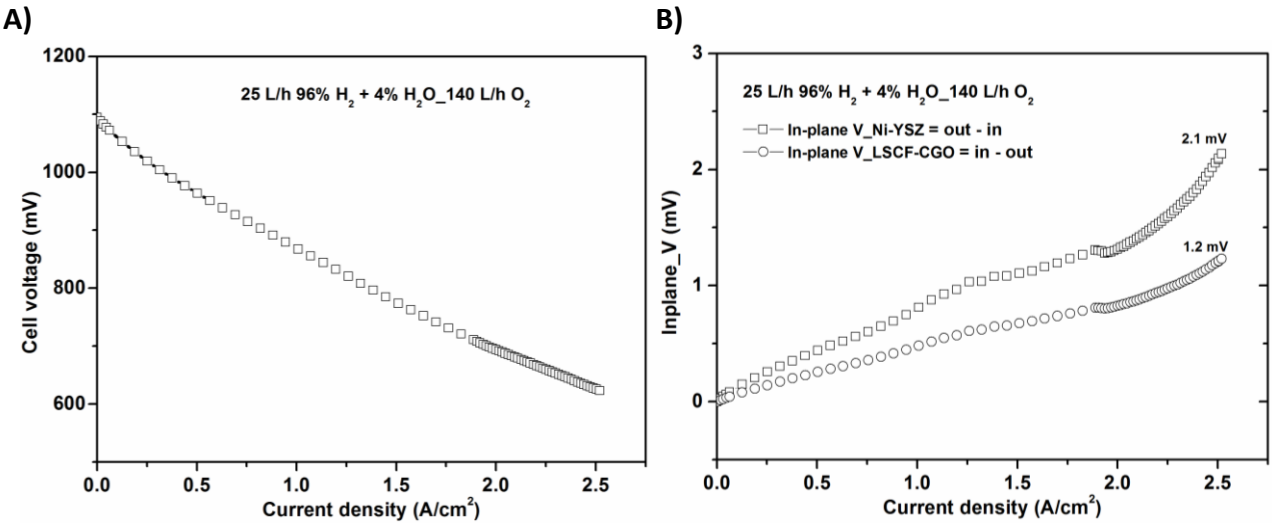

Figure 83 A) the cell voltage and B) in-plane voltage for the Ni-YSZ side as a function of current density for fuel cell operation in 4 % H_2O + 96 % H_2. Here the positive in-plane voltage is shown as $V_{outlet} – V_{inlet}$ for the Ni-YSZ side and $V_{inlet} – V_{outlet}$ for the oxygen electrode side. The in-plane voltages at OCV were calibrated to be 0.

The i-V curve measured for the cell operated in fuel cell mode in 4 % H_2O + 96 % H_2 is shown in Figure 83A). The cell voltage was about 1.09 V at OCV and decreased to about 0.63 V with increasing current density to

2.5 A/cm^2. Figure 83B) shows the in-plane voltage along the current collector for the Ni-YSZ electrode side and oxygen electrode side with increasing current. The measured positive in-plane voltage under operation indicated a higher voltage for the outlet than inlet for the Ni-YSZ side, and at inlet than outlet for the oxygen electrode side. The in-plane voltage increased steadily with increasing the current density from 0 to 2.0 A/cm^2. However, a faster increase was observed for the in-plane voltage when the current density was increased to above 2.0 A/cm^2. The maxium value of the in-plane voltage was measured to be 2.1 mV for the Ni-YSZ side and 1.2 mV for the oxygen electrode side at the maximum current density (2.5 A/cm^2).

5.1.2 Temperature at cell center and outlet during i-V measurement

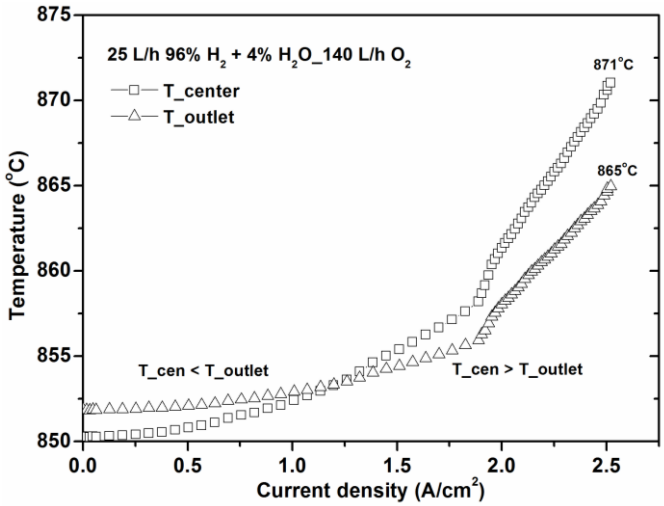

Figure 84 The temperature measured for the center and outlet of the cell during the initial i-V measurement in 4 % H_2O + 96 % H_2.

During the fuel cell operation in 4 % H_2O + 96 % H_2, the temperatures change for the center and outlet part of the cell was recorded with increasing the current density, as is shown in Figure 84. At OCV condition, the temperature measured at the outlet of the cell was 2 ^oC higher than at the center. Increasing current from 0 to 2.0 A/cm^2, both regions showed an increase in temperature. The increase of temperature at the cell center was relatively faster than at the outlet: the center catched up with the outlet at around 1.25 A/cm^2 and then surpass it at the higher current densities. At above 2.0 A/cm^2, both regions showed significant increase in the temperature. The faster increase of temperature was observed for the center than the outlet of the cell. The temperature measured for the cell center was 871 ^oC at 2.5 A/cm^2 (ΔT (vs. at ocv) = +21 ^oC), 6 ^oC higher than the one mesured for the outlet (865 ^oC, ΔT (vs. at ocv) = +13 ^oC).

3.2. Initial performance in 45 % H_2O + 45 % CO_2 + 10 % H_2 (EC mode)

3.2.1. i-V and in-plane voltage measurement

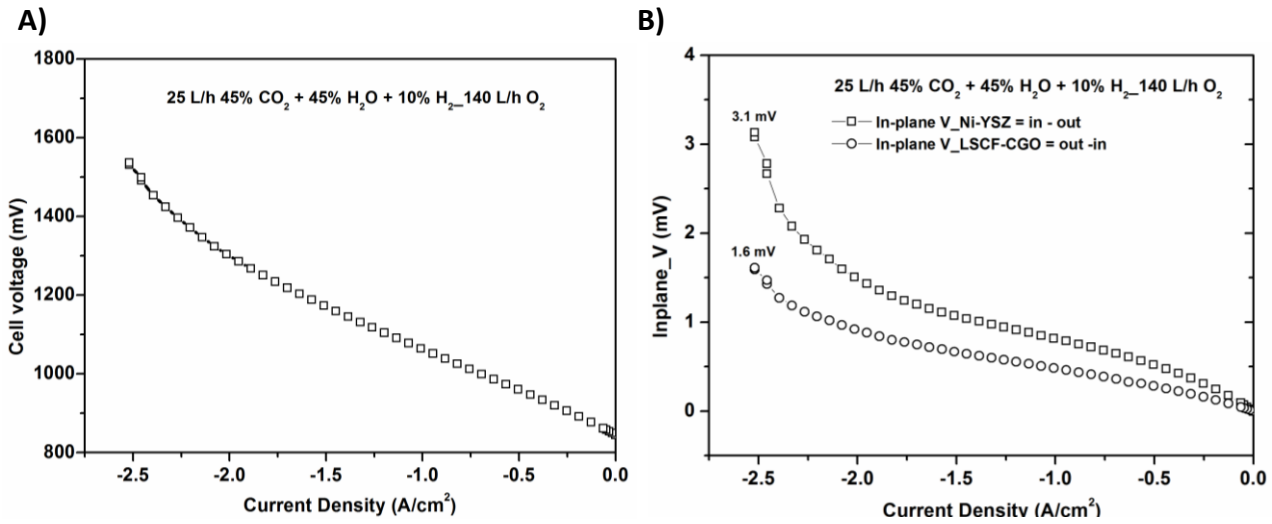

Figure 85 A) the cell voltage and B) in-plane voltage for the Ni-YSZ side as a function of current density for electrolysis operation in 45 % H_2O + 45 % CO_2 + 10 % H_2. Here the positive in-plane voltage is shown as V_{inlet} – V_{outlet} for the Ni-YSZ side and V_{outlet} – V_{inlet} for the LSCF-CGO side. The in-plane voltages at OCV were calibrated to be 0.

Figure 85A) shows the i-V curve measured for the cell operated in electrolysis cell mode in 45 % H_2O + 45 % CO_2 + 10 % H_2. The cell voltage was about 0.85 V at OCV and increased to about 1.54 V at a current density of -2.5 A/cm^2. Figure 85B) shows the in-plane voltages in the current collector at Ni-YSZ side and LSCF-CGO side. The positive values indicated a higher in-plane voltage for the inlet than outlet on the Ni-YSZ side and higher for the outlet than inlet on the LSCF-CGO side. The in-plane voltage increased with increasing the electrolysis current density (|i|). A faster increase was observed for the in-plane voltage at the current density from -2.0 to -2.5 A/cm^2. The maxium value of the in-plane voltage was measured to be 3.1 mV for the Ni-YSZ electrode and 1.6 mV for the LSCF-CGO electrode, corresponding to the maxium electrolysis current denisty (|i| = 2.5 A/cm^2).

3.2.2. Temperature at cell center and outlet during i-V measurement

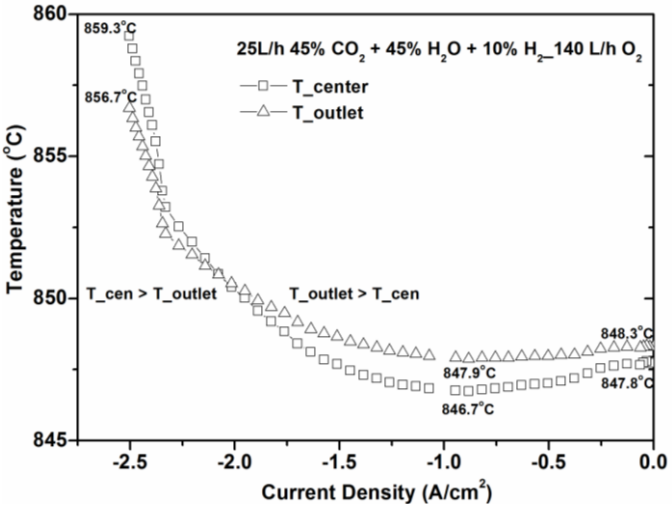

Figure 86 The temperature measured for the center and outlet of the cell during the initial i-V measurement in 45 % H_2O + 45 % CO_2 + 10 % H_2.

Figure 86 shows the temperature at the center and outlet part of the cell recorded as a function of the current density during the electrolysis operation in 45 % H_2O + 45 % CO_2 + 10 % H_2. At OCV, the temperature measured for the cell center was a little lower than the outlet, similar to the situation in 4 % H_2O + 96 % H_2. From 0 to -1.0 A/cm^2, both the center and outlet part of the cell showed a decrease in the temperature. Larger decrease was measured for the center (ΔT = -1.1 ^oC) than the outlet (ΔT = -0.4 ^oC) of the cell. From -1.0 to -2.5 A/cm^2, both regions showed an increase in the temperature with increasing the electrolysis current density (|i|) and the higher the electrolysis current the faster the increase of the cell temperature. The more significant temperature increase was observed for the center than for the outlet of the cell. The maximum temperature increase (T = 859.3 ^oC and ΔT (vs. at ocv) = +11 ^oC) was measured for the cell center at -2.5 A/cm^2.

3.3. In-plane voltage for galvanostatic electrolysis operation

In order to investigate the durability of the solid oxide cells for co-electrolysis of CO_2 and steam at heavy load, the cells were operated at constant current densities (-1.5 or -2.0 A/cm^2) for about 700 hours. Figure 87 shows the cell voltage as well as the in-plane voltage measured on the Ni-YSZ side for the SOEC cells (cell T1, T6 and T8) during the galvanostatic operations. All these cells showed the positive in-plane voltage (V_{inlet} – V_{outlet}) throughout the test for the Ni-YSZ side. After the start of the test, the in-plane voltage decreased rapidly and reached the minimum within one or two hundred hours. Then, for the next 200 ~ 300 hours, the in-plane votlage increased in a relatively slower rate to a level which was lower than the initial in-plane voltage. After that, the in-plane voltage declined again but in an even slower rate.

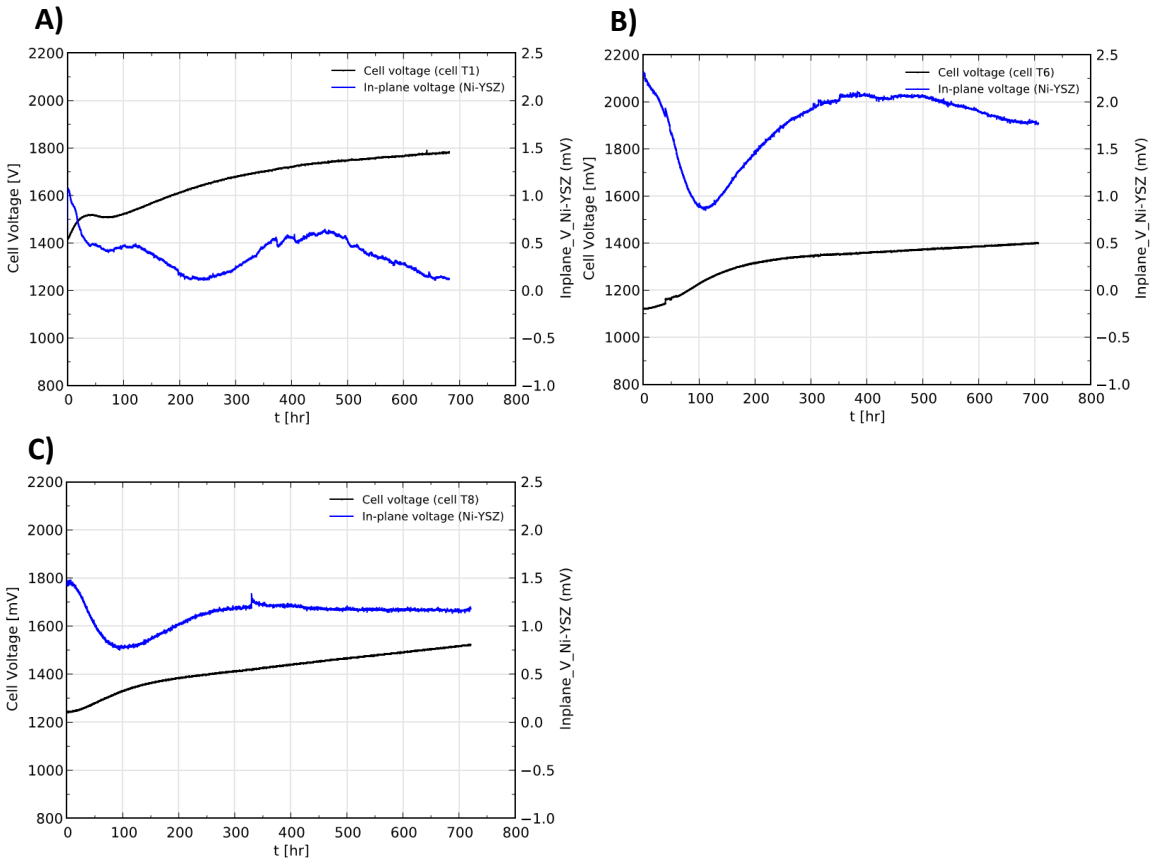

Figure 87 The in-plane voltage measured for the Ni-YSZ side of the cell during the galvanostatic operation: A) cell T1 (-1.5 A/cm^2); B) cell T6 (-1.5 A/cm^2); C) cell T8 (-2.0 A/cm^2). Note the in-plane voltage measured for the Ni-YSZ side is shown as $V_{inlet} - V_{outlet}$.

4 Discussions

4.1. In-plane voltage

The in-plane voltage measurement was first reported by S. H. Jensen et al [1] for the test of SOECs with Si containing glass sealing. It was also employed by S. Ebbesen at al [2] for evidencing the the distribution of the S etc. impurities in the Ni-YSZ electrode. For the planar type SOFCs and SOECs with a plug flow type gas flow, the equivalent circuits can be depicted in Figure 88. The grey region represents the planar cell, which is divided into two parts along the gas flow, the upstream and downstream. In accordance to the test setup of the cell (see experimental), four same resistors were used to represent the resistance of the wires (R_w). R_{OxE} and R_{Ni} are respectively the in-plane resistance for the oxygen electrode side and Ni-YSZ electrode side. The resistance for the upstream and downstream part of the cell are indicated by R_{up} and R_{down} respectively. The total current I flows through the main wire, and $\frac{I}{2}$, a half of the total current flows equally through the

two wire resistors (R_w) on each side, given R_w, R_{up} and R_{down} are much larger than R_{OxE} and R_{Ni}[1] (satisfied for this test). The in-plane voltage can be viewed as an indicator for the unevenness of the current distributions between the inlet and the outlet of the cell. Based on the experimental results (Figure 83B and Figure 85B), the current flow for the cell operated in fuel cell mode and electrolysis cell mode is illustrated respectively in Figure 88A and B. For both the FC and EC operations, larger current flows through the upstream than the downstream part of the cell.

The in-plane voltages and current flow are summarized and listed below:

FC operation (Figure 88A): I_up > I_down, V_out-in (Ni-YSZ) > 0;
Measurement (Figure 83B): V_{max}_out-in (Ni-YSZ) = +2.1 mV at |i| = 2.5 A/cm^2;

EC operation (Figure 88B): I_up > I_down, V_in-out (Ni-YSZ) > 0;
Measurement (Figure 85B): V_{max}_in-out (Ni-YSZ) = +3.1 mV at |i| = 2.5 A/cm^2;

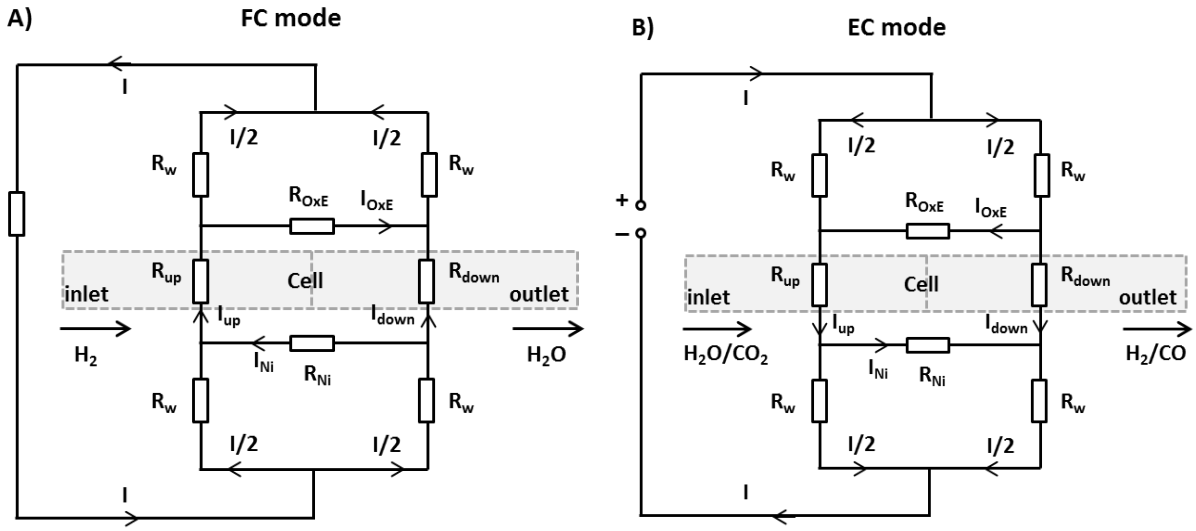

Figure 88 An electric circuit model and current flow for the cell setup which includes a plug flow type reactor for the cell and flat plate current collectors for both electrodes: A) operated in fuel cell (FC) mode in H_2; B) operated in electrolysis cell (EC) mode in H_2O and CO_2. The cell is devided into the upstream and the downstream part according to the gas flow directoin for the Ni-YSZ electrode. (R_w, R_{up}, R_{down} >> R_{Ni}, R_{OxE})

Based on the dimensions of the foils (see experimental) and resistivity of 1 * 10^{-5} Ω cm for Au and 5*10^{-5} Ω cm for Ni, the in-plane resistance is estimated to be 0.5 mΩ for the Au foil and 2.5 mΩ for the Ni foil. The in-plane resistance of the Ni-YSZ gas distributor is estimated to be 4 mΩ based on a resistivity of 2500 S/cm. Thus, corresponding to a parallel connection between the Ni-YSZ gas distributor and Ni foil, the in-plane

resistance for the Ni-YSZ side is estimated to be about 1.5 mΩ. Because of the much larger resistance of the LSM gas distributor, the in-plane resistance of the Au foil is used for the in-plane resistance value for the LSM-YSZ side. From Figure 85B, the in-plane voltage was measured to be 3.1 mΩ for the Ni-YSZ side and 1.6 mΩ for the oxygen electrode side, corresponding to an in-plane current of 2.1 to 3.2 A flowing from the downstream to the upstream part of the cell. The total electrolysis current was -40 A (-2.5A/cm^2), thus, the above in-plane current indicated the current for the upstream was 11 to 17 % larger than for the downstream part of the cell. This difference turns to 7 to 12 % for a total current of -32 A (-2.0 A/cm^2).

4.2. Simulation of the uneven current distribution of an SOEC

In this section, a plug flow reactor (PFR) model is used for the simulation of the uneven performance along the gas flow for a planar solid oxide cell during co-electrolysis of CO_2 and H_2O. Figure 89 shows the PFR model for the cell. Along the gas flow, the cell is separated into many small segments. Reactant is converted by electrolysis reaction in one segment and then flown to the next segment for further reaction. Gas concentration changes along the cell due to electrolysis, meanwhile, perpendicular to the cell plane, the concentration also changes for each segment due to the diffusion of the reactant from the bulk gas (in the gas channel) through the Ni-YSZ support to the active electrode. Typically, the active electrode is a layer of a few microns in depth; for simplification the active electrode is represented as the Ni-YSZ|YSZ interface.

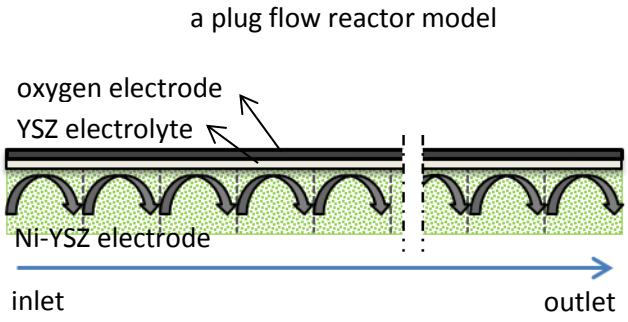

Figure 89 A plug flow reactor model for the planar solid oxide cell with the gas flown along the cell length. For each small segment of the cell, the concentration profile of the reactants from the bulk gas to the electrode active sites. For simplification, the active Ni-YSZ electrode is represented by the Ni-YSZ|YSZ interface.

For each segment of the cell, an equation can be expressed between the cell voltage (*V*) and the contributions:

$$V = E + i \cdot R_{ohm} + i \cdot R_{anod} + i \cdot R_{cath} + i \cdot R_{diff} \qquad [1]$$

Where *E* is the Nernst potential corresponding to the local gas composition for the individual segment, *i* is the local current density, R_{ohm} is the ohmic resistance, R_{anod} and R_{cath} are respectively the resistance of anode and cathode, R_{diff} is the diffusion resistance for Ni-YSZ. Because O_2 is generated at the oxygen electrode and pure O_2 is flown to the oxygen electrode, the O_2 concentration is constant and there could be only an insignificant change in the pressure at the electrolyte interface. Thus, the contribution of the gas variation for the oxygen electrode to the cell voltage is negligible and not included in the calculation. Because the ohmic resistance is independent of gas composition, an even ohmic resistance is used for the whole cell. Also assume an even performance of the R_{anod} and R_{cath} along the cell.

The Nernst potential for the mixture of H_2O + H_2 can be calculated as:

$$E_{H_2O/H_2} = E^0_{H_2O/H_2} - \frac{RT}{2F} ln(\frac{P^{Ni}_{H_2O}}{P^{Ni}_{H_2} P^{½}_{O_2}}) \qquad [2]$$

Where $E^0_{H_2O/H_2}$ is the standard cell potential, *R* is the gas constant, *F* is Faraday constant, *T* is the Kelvin temperature, $P^{Ni}_{H_2O}$ and $P^{Ni}_{H_2}$ are respectively the partial pressure of H_2O and H_2 at the Ni-YSZ|YSZ interface, P_{O_2} is the oxygen partial pressure at the oxygen electrode.

Based on Nernst equation, Faradays Law and Fick's law, the diffusion over-potential for oxidation of H_2 by O_2 has been derived for the fuel cells.[3] Similarly, an equation of the diffusion over-potential for electrolysis of H_2O can be derived and expressed as:

$$\eta^{H_2O/H_2}_{diff} = \frac{RT}{2F} \ln[(1 + \frac{liRT}{2FD^{eff}_{H_2O} P^{bulk}_{H_2}}) \Big/ (1 - \frac{liRT}{2FD^{eff}_{H_2O} P^{bulk}_{H_2O}})] \qquad [3]$$

Where $\eta^{H2O/H2}_{conc}$ is the diffusion over-potential, *R, F* and *T* are as normal, l is the thickness of the electrode, *i* is the current density, $D^{eff}_{H_2O}$ is the effective diffusion coefficient of H_2O, $P^{bulk}_{H_2}$ and $P^{bulk}_{H_2O}$ are the partial pressure of H_2 and H_2O for the bulk gas. The binary diffusion coefficient can be calculated using Fuller correlation, Eq. 2:[4]

$$D_{AB} = 10^{-7} T^{1.75} \sqrt{1/M_A + 1/M_B} / P(\sqrt[3]{V_A} + \sqrt[3]{V_B})^2 \qquad [4]$$

And the multi–component (four components here) gas diffusion coefficient can be calculated using the Maxwell–Stefan equation:[5]

$$D'_A = (1 - y_A)/(y_B/D_{AB} + y_C/D_{AC} + y_D/D_{AD}) \qquad [5]$$

Where y_A, y_B, y_C and y_D are the molar fraction of each component A, B, C and D; D_{AB}, D_{AC} and D_{AD} are the respective binary diffusion coefficients. Assuming a linear change along the gas flow direction, the average of the gas composition before and after the conversion by each segment of the cell was used for the calculations of diffusion coefficients for this segment. The Knudsen diffusion coefficient of the gas diffusion in the Ni–YSZ porous electrode can be expressed as:

$$D_{Knu} = \frac{d_p}{3}\sqrt{8RT/\pi M_A} \quad [6]$$

Where d_p is the pore diameter, R is the gas constant, T is the Kelvin temperature, M is the molar mass of the specific gas molecular. Then the effective diffusion coefficient can be calculated as:

$$D_A^{eff} = p/[t(1/D'_A + 1/D_{Knu})] \quad [7]$$

Where p is the porosity and t is the tortuosity of the porous electrode.

Similarly, the concentration over–potential of CO_2 and CO can be calculated using the above method. For the mixture of the four components in this study, the total concentration over–potential can be estimated as the weighted sum of the over-potential for each group of gas:

$$\eta_{diff} = X_{H_2O+H_2} \cdot \eta_{diff}^{H_2O/H_2} + X_{CO_2+CO} \cdot \eta_{diff}^{CO_2/CO} \quad [8]$$

The concentration over–potential was calculated as a function of the electrode structure parameters (porosity and tortuosity) and current density for co–electrolysis of CO_2 and H_2O (45 % H_2O + 45 % CO_2 + 10 % H_2).

The parameters:

Gas to the oxygen electrode: pure O_2;

Gas to Ni-YSZ: 25 L/h 45 % H_2O + 45 % CO_2 + 10 % H_2;

Pressure: P = 1 atm.;

Cell temperature: T = 1148 K;

Active area of the cell: 16 cm^2;

Thickness of Ni-YSZ support: l = 300 µm;

Pore diameter: d_p = 1 µm;

Tortuosity: t = 3;

Porosity: p = 30 %;

Cell voltage: 1.6 V;

$R_{ohm} + R_{anod} + R_{cath}$: $3*10^{-5}$ Ω m^2

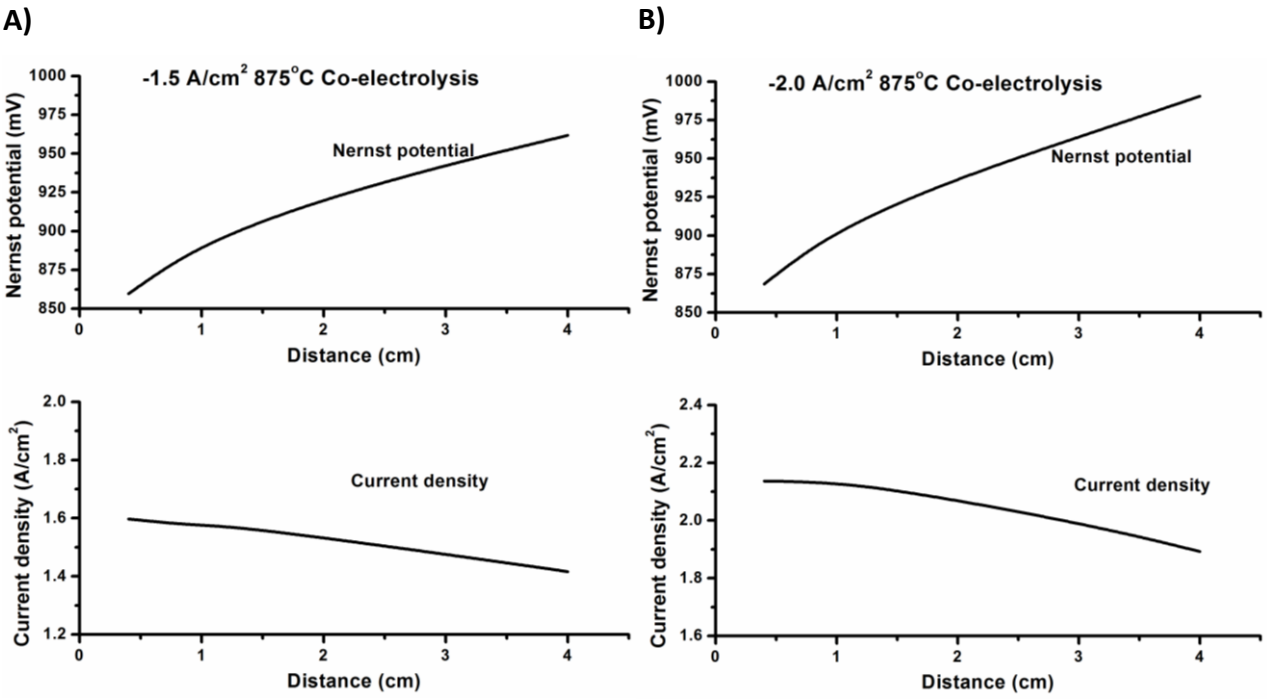

Figure 90 Simulated distribution of the electrochemical performance (Nernst potential and current density) along gas flow direction for the cell operated at -1.5 A/cm^2 A) and -2.0 A/cm^2 B). The dimension of the single cell in gas flow direction is 4 cm.

Figure 90 shows the simulation results of the uneven performance along the gas flow for a SOEC cell operated at -1.5 A/cm^2 and -2.0 A/cm^2. The Nernst potential at the cell outlet is higher than at inlet. The Nernst potential difference is observed to be larger for the operated at the larger current. The local current density decreases for the cell along the gas flow direction. Larger difference in the local current density is observed between the inlet and outlet for the cell operated at the larger current. As is shown in Figure 90B, when the cell is operated at an average current density of -2.0 A/cm^2, the local current density at cell inlet (-2.14 A/cm^2) is 13.2 % larger than that of the cell outlet (-1.89 A/cm^2).

4.3. Temperature distribution

The higher temperature (ΔT = 2 ^{o}C) measured at OCV condition for the outlet than the center of the cell (Figure 84) was due to the closer distance to the heating elements of the furnace. Any heat transport due to gas flow was unlikely the reason, because this temperature difference was also observed for a fresh cell in stagnant gas (before reduction of NiO to Ni). For the fuel cell operation in 4 % H_2O + 96 % H_2, the temperature increase for the cell operated under current densities was ascribed to the ohmic heating and exothermic reaction of hydorgen oxidation. The ohmic heating can be expressed as i^2R or iV, where i is the

local current density, *R* is the local resistance and *V* is the voltage. The exothermic oxidation of hydrogen is also proportional to the local current density *i*. The faster temperature increase for the center of the cell (Figure 84) revealed more heating generated at the cell center than outlet. Considering the cell voltage (V) is equal along the cell, this indicates a higher local current density (i) at the center than outlet of the cell. In addition, at high current densities the temperature difference between the center and outlet of the cell was larger (up to 6 ^{o}C at 2.5 A/cm^2) than at lower current densities (Figure 84), indicating a larger difference of the local current density with increasing the current, as is revealed by in-plane voltage in Figure 83B. It has to be mentioned that the measured temperature change should be smaller than the real change of the cell temperature,[6] due to the distance (~ 1 mm) between the probe and the surface of the cell.

When operating in electrolysis cell (EC) mode in 45 % H_2O + 45 % CO_2 + 10 % H_2, both the ohmic heating of the cell and the endothermic reaction (cooling) of steam and CO_2 electrolysis (as well as the RWGS reaction at the Ni-YSZ electrode and O_2 generation at the oxygen electrode) contributed to the measured temperature changes. In Figure 86, the decreasing temperature at the current density of 0 to ~ -1.0 A/cm^2 indicates a more important and an increasing contribution of the reaction cooling than ohmic heating for the cell. Contrary, the increase of the temperature at higher electrolysis current reveals a more important and an increasing contribution of the ohmic heating than reaction cooling. At the current around -1.5 A/cm^2, the temperature got close to the level at OCV, indicating the equal contributions from the both effects.

The cooling effect only rely on the current densities (the molar number of the reactants). Instead, the ohmic heating rely on both the current density and the voltage (i*V). Considering the increasing voltage with increasing electrolysis current densities, the contribution of the ohmic heating becomes more and more important. At low current densities, the cooling effect was larger than ohmic heating. From OCV to -1.5 A/cm^2, the relative lower temperature measured for the cell center than outlet indicated the relative higher local current density for the cell center, which was confirmed by the in-plane voltage in Figure 85B. At high electrolysis current densities (|i| = 1.5 – 2.5 A/cm^2), the ohmic heating is more important. The larger temperature increase, i.e. the more significant heating for the cell center than outlet indicates the higher local current density for the cell center than outlet. Moreover, it indicates the increasing unevenness of the local current density with increasing electrolysis current densities, which is consistent with the measured in-plane voltage (Figure 85B). The above analysis on current distribution is also consistent with the modelling results showed before.

The higher cell temperature was observed for the cell operated in FC mode than in EC mode at |i|= 2.5A/cm^2. This is because in EC mode the ohmic heating is offset to some extent by the endothermic

reactions, while in FC mode both the ohmic heating and exothermic reactions tend to elevate the cell temperature.

4.4. Evolution of degradation for SOECs along the cell

A typical evolution of the in-plane voltage is depicted in Figure 91A for the cell experiencing a long-term test in 45 % H_2O + 45 % CO_2 + 10 % H_2 at high current densities. The in-plane voltage can be divided into three stages according to the tendency (decrease/increase) of the changes. Corresponding to the four situations for the in-plane voltage (i – iv) in Figure 91A), the current distribution along the cell along gas flow direction is illustrated in Figure 91B). At the beginning of the durability test, for a cell without degradation (at situation 'i'), the large in-plane voltage indicates a significant difference in the local current density between the cell inlet and outlet. According to the experimental and modeling results for a fresh cell, the local current density is higher for the inlet than outlet, which is shown as the situation 'i' in Figure 91B. With the rapid degradation of the Ni-YSZ electrode in the 1^{st} 100 ~ 200 hours, the in-plane voltage decreases rapidly (stage i – ii in Figure 91A), indicating the less and less difference in the local current density between inlet and outlet. Since the total current is constant, the local current density will decrease at inlet and will increase at outlet (i – ii in Figure 91B). Correlating the microstructural and electrochemical analysis (Chapter 4 and 5), this current distribution change reveals that more severe degradation occurred for the Ni-YSZ electrode (TPB process) at the cell inlet than outlet for the initial period. It was confirmed by SEM observations on a short-term tested cell that much more severe Ni percolation loss was observed at inlet than outlet (cell T4 in Chapter 'Microstructure').

The degradation rate of the Ni-YSZ TPB resistance is expected to slow down for the further test, considering a decreasing driving force for Ni coarsening due to particle size increase and a potential TPB activation by nano-zirconia precipitation (Chapter 'Microstructure'). Corresponding to an increase in the in-plane voltage (ii – iii in Figure 91A and B), the local current density start to decrease at outlet and increase at inlet. In this stage, the degradation of the Ni-YSZ electrode continues for the whole cell but the degradation at the outlet appears to catch up. Due to the relative faster degradation rate for the outlet than inlet, the degradation appears to be expanded from inlet to outlet. The Ni-YSZ degradation as a whole is slower for this stage than for the initial stage (i – ii), thus a longer duration is observed for this stage.

As has been discussed in Chapter 'Electrochemistry' and 'Microstructure', the large polarization with the severe reduction in the numbers of Ni-YSZ TPB sites under harsh operations resulted into precipitation of zirconia nanoparticles between Ni and YSZ close to the electrolyte, contributing to the stabilization of the polarization resistance (Rp) and the increase of the ohmic resistance (Rs). Therefore, the difference in the

local Rp would become less significant with the test, while the difference of the local Rs would account more for the unevenness of the cell resistance. The inlet is expected to show a larger increase of Rs than outlet, corresponding to the significantly larger amount of precipitations. Thus, the local current density will decrease relatively for the cell inlet and increase for the outlet, as is shown for the stage of iii – iv in Figure 91. Due to the stabilization of the Rp of Ni-YSZ and the slow precipitation of nanoparticles, the decrease of the in-plane voltage is very slower for this stage.

The in-plane voltage shows the minimum at the situation 'ii', which is still above 0. The positive in-plane voltage indicates the local current density at the cell inlet is higher than that of the outlet throughout the test.

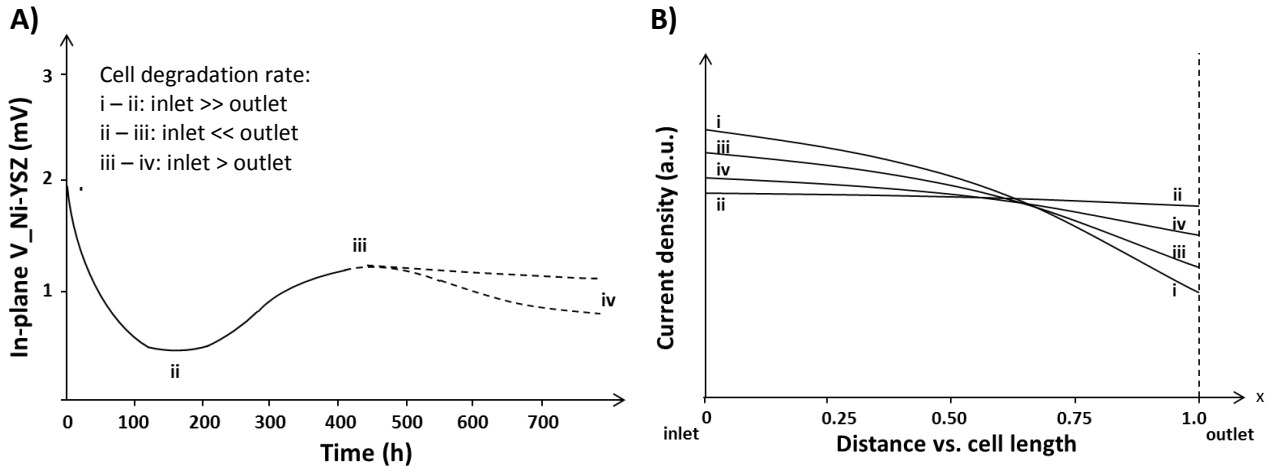

Figure 91 A) A typical evolution of the in-plane voltage for the Ni-YSZ side and B) an illustration of the current distributions along the cell from inlet to outlet. The four situations (i – iV) in B) correspond to the situations in A). The arbitrary scale values of the x- and y-axis in A) are only for convenience of the illustrations rather than for rendering the exact values.

5 Conclusions

The in-plane voltage was measured for the solid oxide cells operated in fuel cell mode and electrolysis mode in a large range of current densities. The larger in-plane voltage was measured at the higher current densities for both modes, indicating the larger unevenness of the current distributions from inlet to outlet. Further, both operations revealed larger local current density for the inlet than outlet of the cell. The changes in the cell temperature were also recorded for the center and outlet of the cell. The fuel cell operation showed a monotonic increase in the cell temperature with increasing current, due to the exothermic reactions. The electrolysis cell operation first showed a decrease and then an increase in cell

temperature with increasing the electrolysis current, which was ascribed to the competitions between the ohmic heating of the cell resistance and the endothermic electrolysis reactions. For both operation modes, the different temperature between the cell center and outlet was consistent with the result of the higher local current density for the cell center than outlet. The uneven current distribution was simulated for a planar cell using a plug flow reactor model. A decreasing current density is obtained for the cell along the gas flow direction, which agrees with the experimental results. The in-plane voltages were measured for the SOECs operated at high current densities during the long-term test. Based on the above study on the uneven performance, the degradation evolution for the SOECs was interpreted by correlating with the microstructural and electrochemical analysis for the durability test. The current distribution between inlet and outlet is speculated to be adjusted dynamically in a 'seesaw' manner, corresponding to the evolution of the local degradation along the cell.

References

1. S. H. Jensen, A. Hauch, P. V. Hendriksen, and M. Mogensen, *J. Electrochem. Soc.*, **156**, B757 (2009)

2. S. D. Ebbesen, C. Graves, A. Hauch, S. H. Jensen, and M. Mogensen, *J. Electrochem. Soc.*, **157**, B1419–B1429 (2010)

3. S. Primdahl and M. Mogensen, *J. Electrochem. Soc.*, **146**, 2827–2833 (1999).

4. J. R. Welty, C. E. Wicks, and R. E. Wilson, *Fundamentals of Momentum, Heat and Mass Transfer*, 3rd ed., John Wiley & Sons, Inc., New York, (1984), p. 490.

5. D. F. Fairbanks and C. R. Wilke, *Ind. Eng. Chem.*, **42**, 471–475 (1950).

6. S. D. Ebbesen and M. Mogensen, *ECS Trans.*, **50**, 167–182 (2013).

Chapter 7 Carbon Deposition in Solid Oxide Cells during Co-Electrolysis of H_2O and CO_2

(Accepted with minor changes for publication in Journal of the Electrochemical Society)

Youkun Tao, Sune Dalgaard Ebbesen, and Mogens Mogensen

Department of Energy Conversion and Storage, Technical University of Denmark, DTU, Risø Campus, Frederiksborgvej 399, Roskilde 4000, Denmark

Abstract

Carbon formation during co-electrolysis of H_2O and CO_2 in Ni-YSZ supported Solid Oxide Electrolysis Cells (SOECs) may occur, especially at high current density and high conversion. In order to evaluate the carbon formation limits, five galvanostatic tests were performed in this work at electrolysis current densities from 1.5 to 2.25 A/cm^2 and reactant (H_2O + CO_2) conversion of up to 67 %. Delamination and carbon nano-fibers were observed at the Ni-YSZ|YSZ interface for two cells with a dense microstructure operated at electrolysis current densities of 2.0 and 2.25 A/cm^2 and a conversion of 59 % and 67 % respectively. Based on the nominal gas composition, carbon formation only occurs, according to equilibrium thermodynamics, at a reactant conversion above 99 %. Therefore, the observed carbon formation is ascribed to a change in gas composition due to the diffusion limitations within the Ni-YSZ support and the active Ni-YSZ electrode. Carbon nano-fibers were only observed close to the YSZ electrolyte, indicating a very reducing atmosphere and a large over-potential gradient in the active electrode, being highest at the interface to the bulk electrolyte and decreasing towards the Ni-YSZ support.

1. Introduction

Solid oxide electrolysis cells (SOECs) have been studied in the past 30 years because of increasing demand for alternatives to fossil fuel.[1–16] Co-electrolysis of H_2O and CO_2 in SOECs yield syngas (H_2 + CO), which can be further converted into various types of synthetic fuels such as methane, petrol and diesel.[17,18] Excellent initial performance has been demonstrated for Ni-YSZ based SOECs for H_2O, CO_2 and co-electrolysis of H_2O and CO_2.[10,12–16] With regard to the cell degradation, impurities play a major role in Ni-YSZ electrode degradation at low current densities.[12,14–16] At high current densities, degradation in the Ni-YSZ electrode and YSZ electrolyte and / or oxygen electrode have been reported for electrolysis of steam[10,19] operated at 1.0 – 2.0 A/cm^2 or co-electrolysis of steam and CO_2 at 1.0 – 1.5 A/cm^2.[13,20] During co-electrolysis of H_2O and CO_2, the ratio of CO and H_2 to CO_2 and H_2O in the Ni-YSZ electrode increases with increasing conversion, leading to a more reducing environment. Thus the risk of carbon deposition increases.[18] Even if not favored by the global gas composition based on total conversion and thereby the gas composition in the outlet, carbon formation may occur locally in the cell due to gas transport limitations.

Nickel is a well-known catalyst for dissociation of carbon containing gases and disproportionation of CO forming solid carbon. Carbon deposition has been regarded as a challenge for utilization of carbon containing fuels in solid oxide cells (SOCs) with a Ni-YSZ composite electrode.[21–23] Formation of small amounts of carbon within the active Ni-YSZ electrode may reduce the amount of active sites, thus leading to a reduced activity.[14] Formation of larger amounts within both the Ni-YSZ support and the active Ni-YSZ electrode will in worst case cause structural damage due to the volume expansion and nickel dusting. In this work, co-electrolysis of H_2O and CO_2 was examined in Ni-YSZ based SOECs operated at electrolysis current densities up to 2.25 A/cm^2 and at a reactant conversion up to 67 % in order to study the limits for carbon formation in these Ni-YSZ based cells.

2. Experimental

Planar Ni-YSZ-supported SOCs of 5 × 5 cm^2 with an active electrode area of 4 × 4 cm^2 were used for all experiments. The cells were produced at DTU energy conversion,[24,25] and have a 10 – 15 μm thick Ni-YSZ cermet electrode (YSZ = Yttria Stabilised Zirconia); a 10 – 15 μm thick YSZ electrolyte and a 15 – 20 μm thick strontium-doped lanthanum manganate (LSM-YSZ) composite LSM-YSZ electrode. The cells are supported by a ~300 μm thick porous Ni-YSZ layer. Ni-YSZ and LSM-YSZ were used as current collectors on the cathode and anode side, respectively. Albite glass bars were used as sealing on both sides. The cell was heated to 1000 °C for sealing and reduction of NiO in 9 % H_2 + 91 % N_2. After reduction, the initial performance was characterized at 850 °C. Characterization of the initial performance include recording of electrochemical

impedance spectra (EIS) and i-V curves, with 4 % H_2O + 96 % H_2, 20 % H_2O + 80 % H_2, 50 % H_2O + 50 % H_2, and 45 % H_2O + 45 % CO_2 + 10 % H_2 flown to the Ni-YSZ electrode, and with either air or pure oxygen flown to the LSM-YSZ electrode. The flow rate to the Ni-YSZ electrode was 25 L/h and the flow rate to the LSM-YSZ electrode was 140 L/h in all cases. A Solartron 1255B frequency analyzer was used for measuring the impedance contribution at frequencies from 82 kHz to 0.08 Hz with 6 data points per decade for cell 1 – cell 4 and with 12 data points per decade for cell 5. The impedance data were corrected using the short-circuit impedance response of the test set-up. Both the Rs and Rp was determined by break-down of the EIS.

After characterization of the initial performance, electrolysis durability was examined with 45 % H_2O + 45 % CO_2 + 10 % H_2 flown to the Ni-YSZ electrode and pure O_2 flown to the LSM-YSZ electrode. The electrolysis current was increased with steps of 0.25 or 0.50 A/cm^2 for cell 2, 4 and 5, and at each step the impedance was measured after a hold-time of 15 min. The current for cell 1 and 3 was increased without measuring impedance to the current density of galvanostatic test. The initial cell temperature at OCV was 850 ^oC which increased to ~ 875 ^oC at an electrolysis current density of 2.0 A/cm^2. During galvanostatic operation, the applied electrolysis current density was 1.5 A/cm^2 for cell 1, 2.0 A/cm^2 for cell 2, 3 and 4, and 2.25 A/cm^2 for cell 5. The corresponding reactant conversion (according to Faraday's law) was 45 % at 1.5 A/cm^2, 59 % at 2.0 A/cm^2 and 67 % at 2.25 A/cm^2. The cells were operated until the cell voltage reached ~ 2.0 V or a duration no more than ~ 700 hours. However, cell 4 was stopped at ~ 2.2 V due to a high degradation rate. After the durability test, EIS characterization was performed at OCV for all the other cells except cell 4. No characterization was performed after the durability test for cell 4, and the cell was cooled directly while flowing hydrogen to the Ni-YSZ electrode.

Data analysis.— DRT analysis (distribution of relaxation times)[26] and ADIS (analysis of the difference in impedance spectra)[27] was performed for the impedance spectra with variations in the gas composition for both the Ni-YSZ and LSM-YSZ electrode, in order to estimate the resistance and characteristic frequency of the individual process. The estimates was used for a subsequent breakdown of the impedance contributions from each of the two electrodes according to the model previously described for this type of Ni-YSZ based SOCs produced at DTU Energy conversion.[28,29] The model consists of one inductance (L), one serial resistance (R_S), one element for the LSM-YSZ electrode at high frequency (LSM_{High}), one element for the Ni-TPB reaction (Ni_{TPB}), one element for the low frequency responds of the LSM-YSZ electrode (LSM_{low}), one element for gas diffusion and one for gas conversion (both for the Ni-YSZ electrode).

Impedance spectra recorded in 4 % H_2O + 96 % H_2 to the Ni-YSZ electrode and with air to the LSM-YSZ electrode (not shown) was used as a basis for the remaining fit as the published values for the developed

model are based on this composition. For the remaining mixtures, first, the contribution to the Ni-YSZ electrode was fitted when changing the gas composition to the Ni-YSZ electrode only, followed by fitting the contribution to the LSM-YSZ electrode. For these subsequent fitting routines the exponents of constant phase element of the respective processes were always kept constant. The exponents of the constant phase elements were kept constant for the electrochemical processes on all the cells and according to literature (0.68 for LSM_{high}, 0.80 for Ni_{TPB}, 0.87 for LSM_{low}, 0.75 for diffusion and 0.9 ~ 1 for conversion process).[28,29] The 'RAVDAV' software was used for the DRT analysis and fitting of the impedance spectra.[30]

The microstructure of the cells after test was investigated by SEM (Supra35). Two samples were prepared for each cell: one fractured sample and one polished sample embedded in epoxy. The fracture sample allowed for examination of the "3D" microstructure to some extent. The polished sample presented the 2D microstructure, which was also used for an estimation of the porosity based on the contrast between the Ni, YSZ and the epoxy filled pores by the Image J software.[31]

3. Results

Characterization of the solid oxide cells.— Figure 92 shows the cell voltage when increasing the electrolysis current to the operating current (1.5 – 2.25 A/cm^2) with 45 % CO_2 + 45 % H_2O + 10 % H_2 supplied to the Ni-YSZ electrode. Pure oxygen was supplied to the LSM-YSZ electrode in order to avoid transients after start-up from OCV due to changes in oxygen stoichiometry of LSM with changes in oxygen partial pressure. The measured open circuit voltage (OCV) in 45 % CO_2 + 45 % H_2O + 10 % H_2 varied from 831 mV (cell 1 and 3) to 844 mV (cell 2), the corresponding theoretical OCV is 852 mV. The lower experimental OCV indicates O_2 leak in to the fuel stream equivalent to approximately 2 ~ 3 % more steam/CO_2 in the gas. When increasing the electrolysis current density above 1.75 A/cm^2, the cell voltage increased drastically for cell 4 and cell 5.

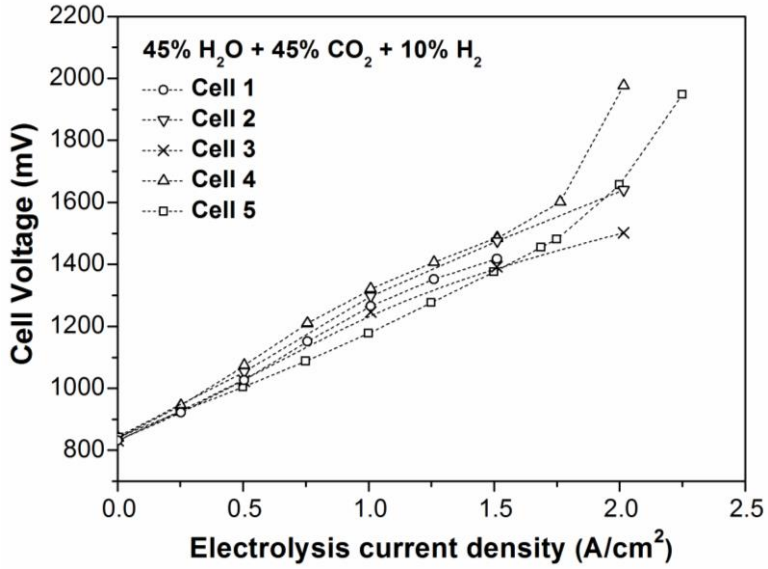

Figure 92 Cell voltage recorded when increasing the electrolysis current to operating current with 45 % H_2O + 45 % CO_2 + 10 % H_2 flown to the Ni-YSZ electrode.

Figure 93a shows EIS spectra measured for each of the five cells at OCV with 45 % H_2O + 45 % CO_2 + 10 % H_2 flown to the Ni-YSZ electrode. The breakdown of the impedance contribution for the individual processes for the five cells are also shown as dot-dash lines in Figure 93a and listed in Table 15. The polarization resistance (Rp) was 0.30 Ω cm^2 (cell 1), 0.32 Ω cm^2 (cell 2), 0.28 Ω cm^2 (cell 3), 0.35 Ω cm^2 (cell 4) and 0.26 Ω cm^2 (cell 5), respectively. Cell 4 showed a significant larger Rp than the remaining cells. Cell 4 and 5 showed larger diffusion resistance (0.07 and 0.06 Ω cm^2, respectively) than the remaining cells. Cell 3 showed the smallest diffusion resistance (0.04 Ω cm^2). The smallest oxygen electrode resistance (LSM_{high} and LSM_{low}) (0.05 Ω cm^2) was observed for cell 5. The cells showed similar conversion resistance, varying from 0.11 Ω cm^2 (cell 3) to 0.12 Ω cm^2 (cell 5).

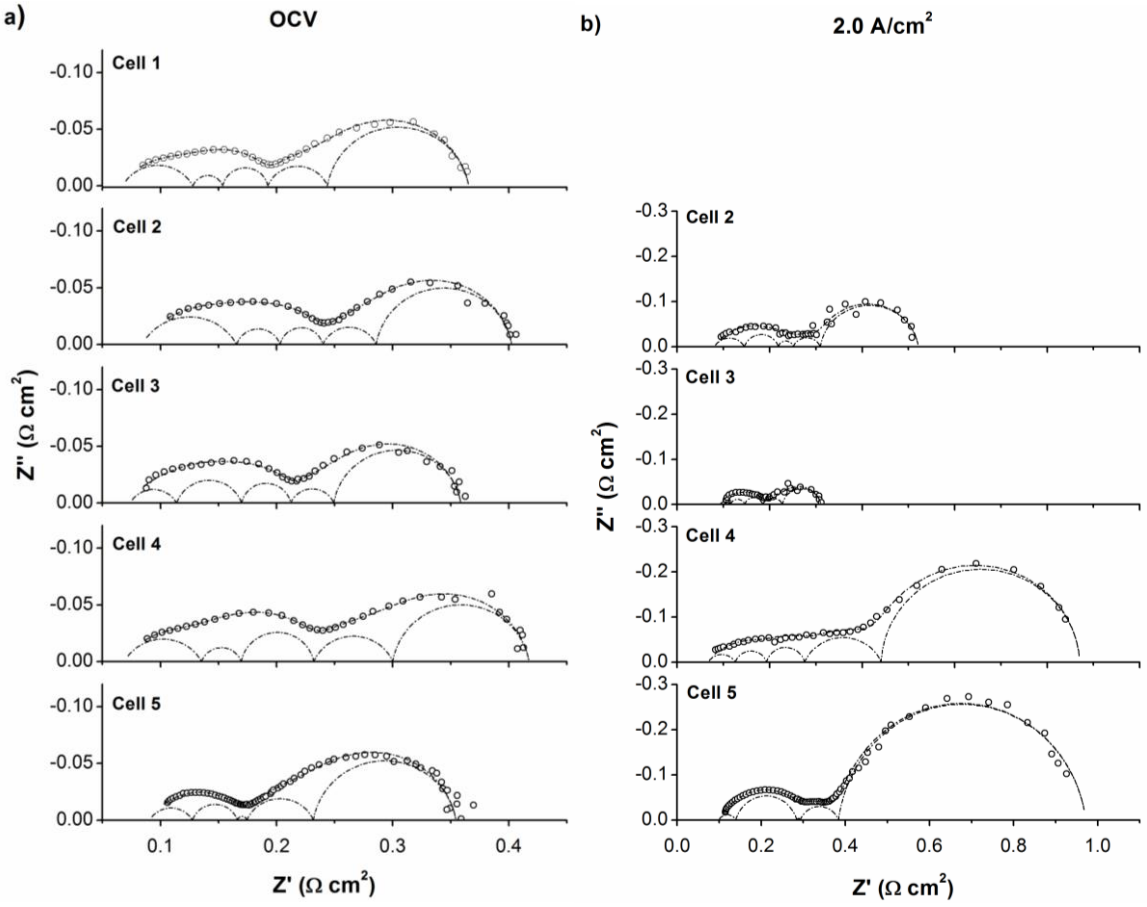

Figure 93 Electrochemical impedance spectra measured at: a) OCV and b) electrolysis current density of 2.0 A/cm^2 with 45 % H_2O + 45 % CO_2 + 10 % H_2 flown to the Ni-YSZ electrode. Open circles: the measured EIS corrected for inductance. Dot-dash lines: total fit and break-down of the EIS spectra with inductance corrected.

Table 15 Area-specific resistance (ASR) of the individual process deduced from the EIS measured at OCV with 45 % H_2O + 45 % CO_2 + 10 % H_2 flown to the Ni-YSZ electrode and O_2 to the LSM-YSZ electrode.

Cell Nr.	*Rs* *(Ωcm²)*	*LSM_{high}* *(Ωcm²)*	*fs* *(Hz)*	*Ni_{TPB}* *(Ωcm²)*	*fs* *(Hz)*	*LSM_{low}* *(Ωcm²)*	*fs* *(Hz)*	*Diff.* *(Ωcm²)*	*fs* *(Hz)*	*Conv.* *(Ωcm²)*	*fs* *(Hz)*	*ASR_{total}* *(Ωcm²)*
1	*0.07*	*0.06*	*29628*	*0.03*	*3197*	*0.04*	*1205*	*0.05*	*17*	*0.12*	*1.2*	*0.37*
2	*0.08*	*0.08*	*30956*	*0.04*	*4060*	*0.04*	*1074*	*0.05*	*16*	*0.12*	*1.5*	*0.40*
3	*0.07*	*0.04*	*29501*	*0.06*	*4860*	*0.04*	*814*	*0.04*	*20*	*0.11*	*1.9*	*0.36*
4	*0.07*	*0.07*	*31090*	*0.03*	*2700*	*0.06*	*817*	*0.07*	*16*	*0.12*	*1.4*	*0.42*
5	*0.09*	*0.04*	*30928*	*0.04*	*9814*	*0.01*	*1042*	*0.06*	*21*	*0.12*	*1.6*	*0.36*

Figure 93b shows EIS spectra measured at electrolysis current density of 2.0 A/cm^2 in 45 % H_2O + 45 % CO_2 + 10 % H_2 for the cells operated at or above 2.0 A/cm^2 (cell 2, 3, 4 and cell 5). The breakdown of the

impedance spectra measured at electrolysis current density of 2.0 A/cm^2 is shown in Figure 93b and the results of the breakdown are shown in Table 16. Although the impedance spectra were rather similar at OCV, when increasing the electrolysis current to 2.0 A/cm^2, the cells showed significant difference in polarization resistance. Cell 3 showed the lowest Rp of the four cells. For cell 4 and 5, the Rp increased dramatically both at high frequency (a few kHz) and low frequency (< ~ 100 Hz). According to the break-down of the impedance at 2.0 A/cm^2, the polarization resistance of cell 2 (0.44 Ω cm^2) and 3 (0.22 Ω cm^2) were much lower than cell 4 (0.80 Ω cm^2) and 5 (0.87 Ω cm^2). The most obvious difference in Rp among the cells was attributed to the conversion resistances. Cell 4 (0.43 Ω cm^2) and cell 5 (0.59 Ω cm^2) showed a conversion resistance a few times larger than that of cell 2 (0.21 Ω cm^2) and cell 3 (0.08 Ω cm^2). Cell 4 and cell 5 also showed a relative larger diffusion resistance. The smallest total oxygen electrode resistance was observed for cell 5 as at OCV. Cell 4 showed the lowest summit frequency at 400 Hz for the low frequency process of oxygen electrode, which was confirmed by the DRT analysis.

Table 16 ASR of the individual process deduced from the EIS measured at an electrolysis current density of 2.0 A/cm^2 with 45 % H_2O + 45 % CO_2 + 10 % H_2 flown to the Ni-YSZ electrode and O_2 to the LSM-YSZ electrode.

Cell Nr.	*Rs (Ωcm^2)*	*LSM_{high} (Ωcm^2)*	*fs (Hz)*	*Ni_{TPB} (Ωcm^2)*	*fs (Hz)*	*LSM_{low} (Ωcm^2)*	*fs (Hz)*	*Diff. (Ωcm^2)*	*fs (Hz)*	*Conv. (Ωcm^2)*	*fs (Hz)*	*ASR_{total} (Ωcm^2)*
2	*0.08*	*0.07*	*19139*	*0.07*	*4055*	*0.03*	*529*	*0.06*	*28*	*0.21*	*0.6*	*0.52*
3	*0.09*	*0.02*	*20961*	*0.03*	*7741*	*0.04*	*1388*	*0.04*	*16*	*0.08*	*0.8*	*0.31*
4	*0.07*	*0.06*	*22604*	*0.07*	*4554*	*0.08*	*400*	*0.17*	*18*	*0.43*	*0.4*	*0.87*
5	*0.10*	*0.04*	*20000*	*0.15*	*3294*	*0.01*	*715*	*0.09*	*60*	*0.59*	*0.3*	*0.97*

In order to visualize the electrode processes and the performance changing with increasing electrolysis current densities, DRT analysis of the impedance measured between 0 and 2.0 A/cm^2 was performed for cell 5 and the results are shown in Figure 94. A consecutive increase in the height of the high frequency peak (a few KHz) was observed, corresponding to the TPB reactions at Ni-YSZ. Beside the resistance increase, a peak shift to lower frequency was observed for the Ni-YSZ TPB reaction with increasing current / polarization. The shift of peak position for Ni-YSZ TPB reaction of cell 5 is clearly visible from the numbers in Table 16 where the summit frequency shifted down to ~3300Hz. The diffusion resistance (50 – 100 Hz) first decreased followed by an increase with increasing current. A rapid increase in the diffusion resistance was

observed when increasing electrolysis current density above 1.75 A/cm^2. Same trend was clearly observed for the conversion peak (below 10 Hz).

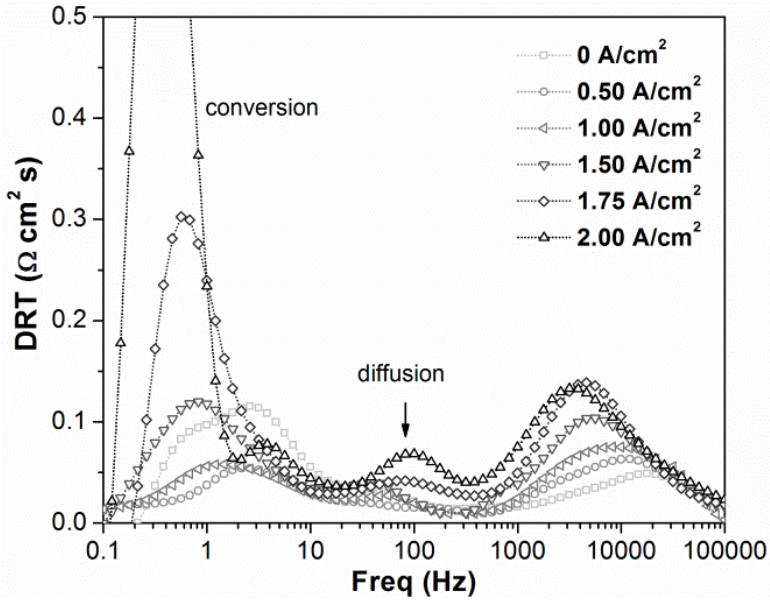

Figure 94 DRT analysis of the impedance measured at electrolysis current densities between 0 and 2.0 A/cm^2 for cell 5 with 45 % H_2O + 45 % CO_2 + 10 % H_2 flown to the Ni-YSZ electrode.

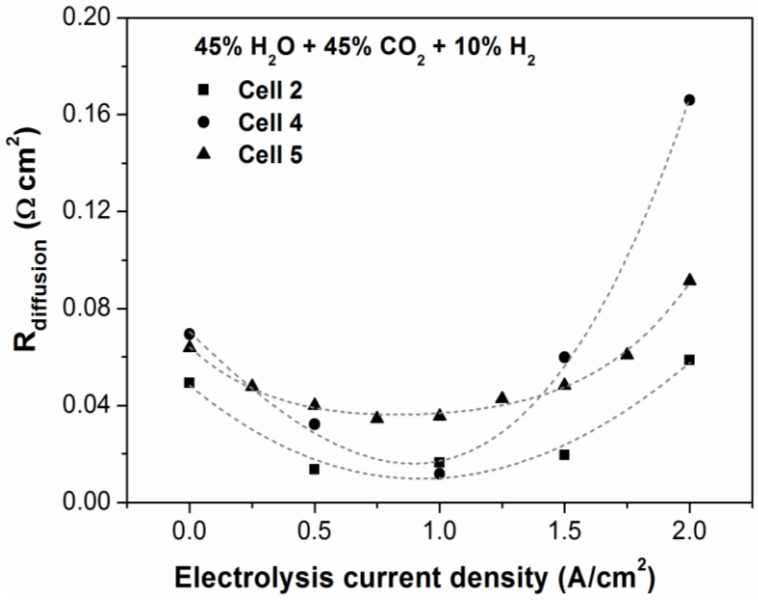

Figure 95 Diffusion resistance of cell 2, 4 and 5 for co-electrolysis of 45 % H_2O + 45 % CO_2 + 10 % H_2 with electrolysis current increase. Markers: diffusion resistance obtained from the breakdown of the impedance spectra; dashed lines: polynominal fit of the obtained diffusion resistance.

Figure 95 shows the diffusion resistance obtained by the breakdown of the EIS measured when increasing the electrolysis current density. All cells showed decreasing diffusion resistance from OCV to around 1.0 A/cm^2 and increasing diffusion resistance with further increasing electrolysis current density to 2.0 A/cm^2. In comparison to cell 2, cell 4 and cell 5 show larger diffusion resistance especially at high electrolysis current densities.

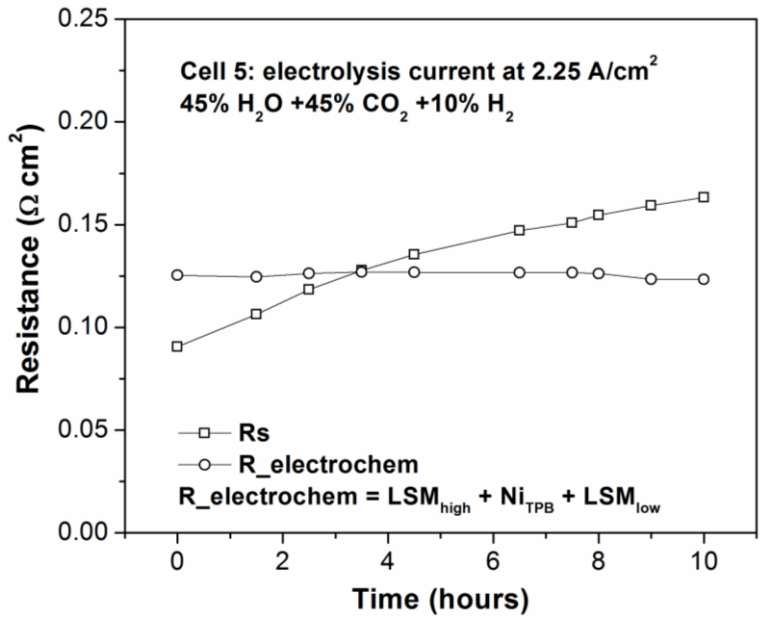

Figure 96 The breakdown results of the impedance for cell 5 during co-electrolysis of 45 % H_2O + 45 % CO_2 + 10 % H_2 at a constant electrolysis current density of 2.25 A/cm^2.

The impedance spectra of cell 5 during the galvanostatic operation at electrolysis current density of 2.25 A/cm^2 were analyzed by breakdown and the results are showed in Figure 96. The electrochemical part of the polarization resistance, including the high frequency O^{2-} transfer (LSM_{high}), the TPB reactions at the Ni-YSZ electrode (Ni_{TPB}) and LSM-YSZ electrode (LSM_{low}), showed limited changes during the short test period, while the serial resistance (Rs) showed significant increase from 0.09 Ω cm^2 to 0.16 Ω cm^2.

Voltage degradation during co-electrolysis.— The evolution of cell voltage during galvanostatic operation is shown in Figure 97. Cell 1 was tested at 1.5 A/cm^2, the lowest electrolysis current density of the five tests. It showed the lowest initial cell voltage (1421 mV) and the lowest degradation rate (0.18 mV/h, during the last 100 hours). Both cell 2 and 3 were tested at an electrolysis current density of 2.0 A/cm^2 and stopped at 2000 mV. Cell 2 was operated for 294 hours and the degradation rate for the final 100 hours was 0.42 mV/h. Cell 3 was operated for 677 hours before reaching 2000 mV and the degradation rate for the final 100 hours was 0.47 mV/h. Although operated at the same electrolysis current density (2.0 A/cm^2) cell 4 showed

much higher initial cell voltage (1977 mV) than cell 2 (1641 mV) and cell 3 (1510 mV) reflecting a much lower performance of the cell in accordance with the measured IS.

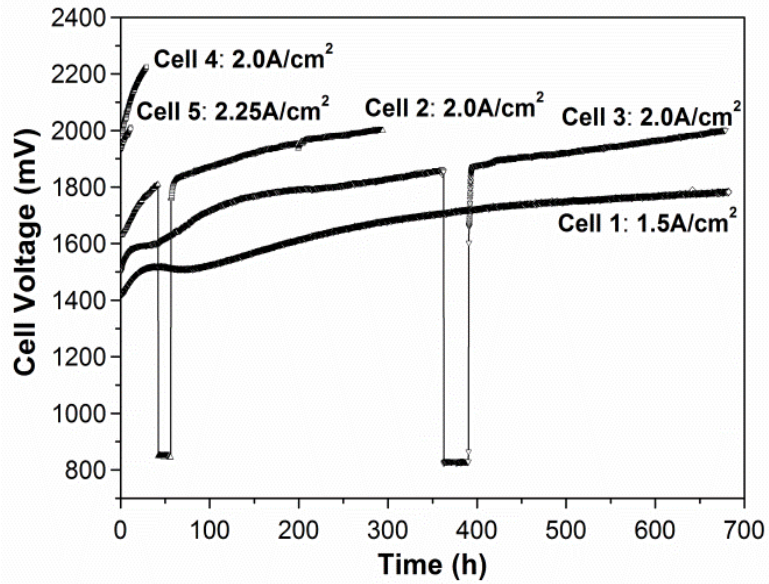

Figure 97 Cell voltage of the SOECs during galvanostatic operation at electrolysis current densities of 1.5 A/cm^2, 2.0 A/cm^2 and 2.25 A/cm^2. 45 % H_2O + 45 % CO_2 + 10 % H_2 was supplied to the Ni-YSZ electrode and O_2 was supplied to the LSM-YSZ electrode. The cell voltage drop for cell 2 and 3 was due to unexpected instrument breakdown.

The voltage degradation of cell 4 was higher than the remaining cells, and therefore the cell was stopped after 29.5 hours only at a cell voltage of 2224 mV. Cell 5 showed an initial cell voltage of 1947 mV at an electrolysis current density of 2.25 A/cm^2 and was stopped at 2006 mV after an operation of 11.2 hours. Due to the short duration, the degradation rate of both cell 4 (8.40 mV/h) and 5 (5.27 mV/h) is calculated as the total degradation of the cell voltage divided by the total duration.

The voltage drop at 40 h for cell 2 and 359 h for cell 3 during the durability test was due to unintended cut off of the current. The cells showed an activation during the unintended period at OCV. When restoring the applied current, the cells degraded rapidly to the level observed just before the period in OCV, whereafter the degradation rate was similar to the degradation rate observed before the period at OCV.

Post-test microstructure of the cells.— Structural damages at the Ni-YSZ|YSZ interface and delamination of the Ni-YSZ electrode (Figure 98a) was observed for cell 4 and cell 5, the two cells with the highest degradation rate. No change was observed at the LSM-YSZ|YSZ interface (Figure 98a). Carbon nano-fibers, which had a diameter of 10 ~ 20 nm were observed in the Ni-YSZ electrode close to the YSZ electrolyte for

both cell 4 and cell 5 (Figure 98b & c). Such structural damage and carbon nano-fiber was not observed in the Ni-YSZ electrode of cell 1, 2 and 3. Nano-particles were observed on the nickel surface as previously observed for Ni-YSZ based cells operated at high electrolysis current densities.[19,20] Besides the nano particles observed at the Ni surface, nano particles were also observed at the end of the carbon fibers (Figure 98c). Further analysis of these nano particles is being performed and will be presented in a separate paper focusing on the formation of carbon fibers in these Ni-YSZ based SOECs. No carbon fiber was found within the Ni-YSZ support. In addition, the amount of carbon fibers was found to be higher at the outlet compared to the inlet of the cell.

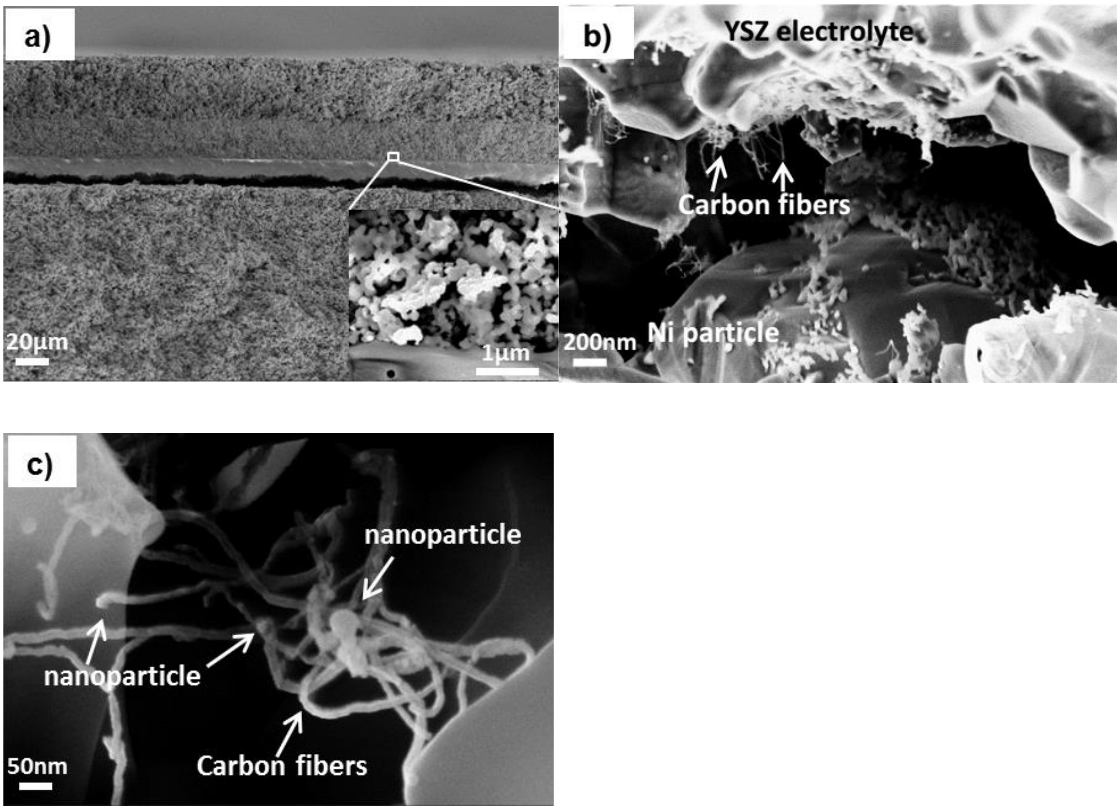

Figure 98 SEM pictures of cell 5 after electrolysis at 2.25 A/cm^2 in 45 % H_2O + 45 % CO_2 + 10 % H_2 at 850ºC, and with a reactant conversion of 67 %. a) Overview of the cell, showing delamination at the Ni-YSZ|YSZ-electrolyte interface, and the inset showing the intact LSM-YSZ|YSZ interface; b) The interface between the Ni particle (lower part) and the YSZ electrolyte (upper part) close to the gas inlet area of the cell and c) showing a clear image of the carbon nano-fibers and nano particles at the Ni-YSZ|YSZ interface.

Based on the image contrast, the porosity of the Ni-YSZ electrode was estimated to be 30 – 40 % for cell 1, 2 and 3. Cell 4 showed the lowest porosity of ~20 % while Cell 5 (~ 25 %) showed a higher porosity than cell

4 but lower than the rest. SEM images of the polished cross-sections of the Ni-YSZ electrode of cell 1 to 5 are shown in Figure 99.

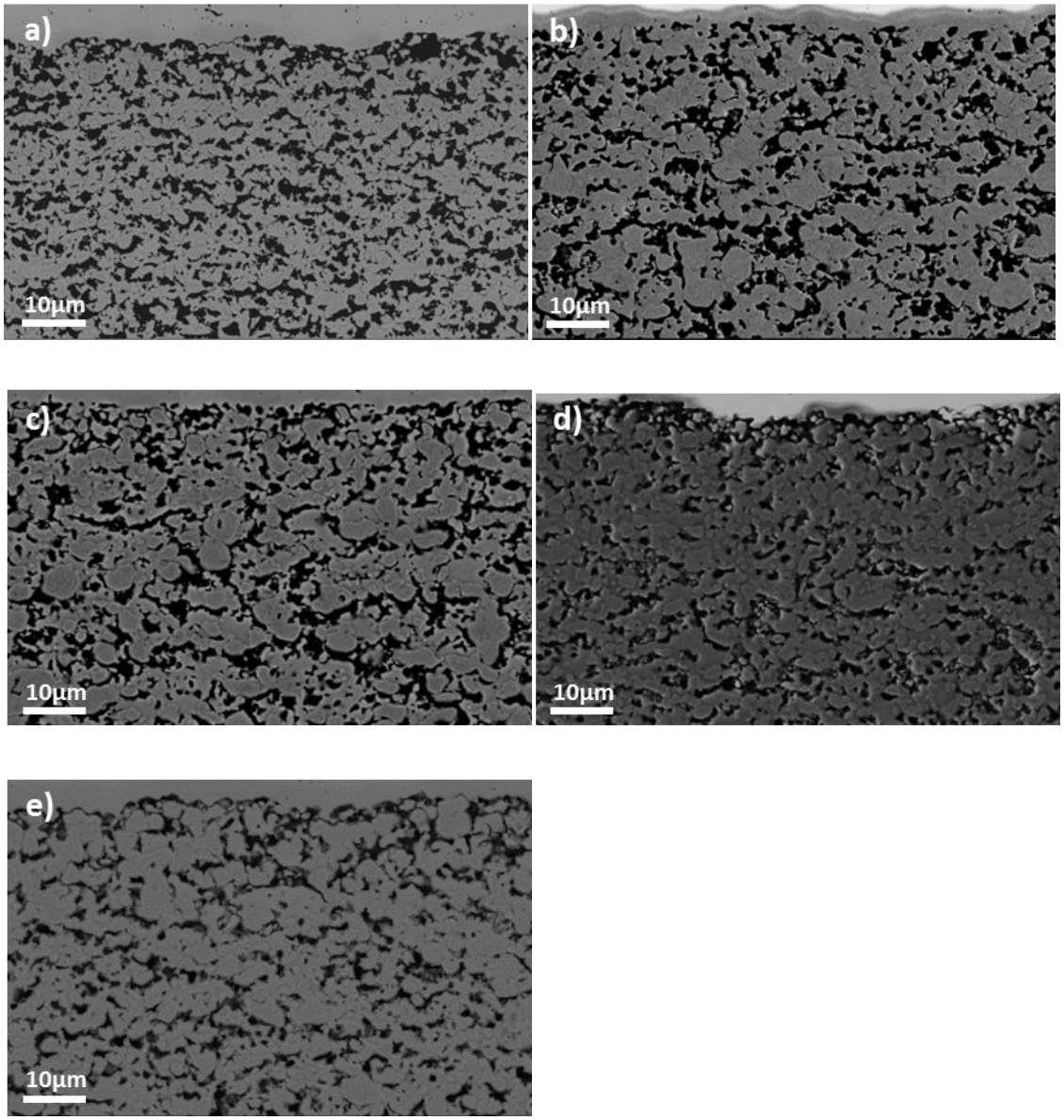

Figure 99 SEM images of the polished cross-section of the Ni-YSZ electrode of a) Cell 1; b) Cell 2; c) Cell 3; d) Cell 4 and e) Cell 5 after durability test.

4. Discussions

Overvoltage and IS recorded when increasing current density to the operating current.— At electrolysis current densities below 1.75 A/cm^2, all cells show similar overvoltage, whereas at electrolysis current densities above 1.75 A/cm^2, a large increase in overvoltage was observed for cell 4 and cell 5 only.

Correspondingly, the conversion resistance of cell 4 and cell 5 was found to be significantly larger than that of cell 2 and cell 3.

The high frequency arcs of the cells reveal the resistance of the electrochemical reaction at TPBs and the low frequency arcs reflect the resistance of the diffusion and conversion processes.[32] The diffusion impedance (10 ~ 100 Hz) reflects the gas transport within the porous support / electrode structure. The conversion impedance (~1 Hz) depends solely on the ratios between the reactants and products.[20] Theoretical, the conversion impedance is lowest when the molar ratio of the reactants ($H_2O + CO_2$) to the products ($H_2 + CO$) is 1, and will increase symmetrically with either increasing or decreasing ratios.[32] It has been speculated that the increased conversion resistance normally observed in electrolysis mode is caused by diffusion to the active Ni-YSZ electrode, depleting the reactants at the active Ni-YSZ electrode, and that the conversion resistance reflects the gas composition at the active Ni-YSZ electrode.[33] The significant increase in conversion impedance for cell 4 and 5 at high current density indicate a very high concentration of either $CO + H_2$ or $CO_2 + H_2O$ in the active Ni-YSZ electrode, consistent with the steep increase in the cell voltages (Figure 92). This increase may be caused by diffusion limitations within the Ni-YSZ support structure.

The diffusion over-potential is caused by a change in Nernst potential due to the different bulk gas composition compared to the gas composition at the active Ni-YSZ[33,34] and is related to the electrode structure (porosity and tortuosity) and the conversion (flux). The modeled diffusion over-potential[33,34] for electrolysis in 45 % H_2O + 45 % CO_2 + 10 % H_2 is shown in Figure 100. The estimated porosity for the cells (18 % – 32 %, see above) and a tortuosity factor between 1.75 (experimentally determined for a good performing cell[33]) and 4 was used for the calculations (a tortuosity factor of 4 was chosen, as it is known that the tortuosity increases with decreasing porosity[35]). Generally, a low porosity and a large tortuosity cause an increase in the diffusion over-potential. Diffusion limitations may occur during co-electrolysis at electrolysis current densities above 1.75 A/cm^2 when the tortuosity is 3 ~ 4 and the porosity is below 30 %.

Because polarization resistance of the cell measured by EIS corresponds to the tangent of the current-voltage curve at that voltage, a numerical integration of the contribution to the diffusion resistance with current increasing from 0 to the operating current i_0 gives the diffusion over-potential $\eta_{diff}(i_0)$ according to the differential equation:

$$d\eta_{diff} / \, di = R_{diff}(i)$$

which implies:

$$\eta_{diff} = \int_0^{i_0} R_{diff}(i)\, di$$

where $R_{diff}(i)$ is the diffusion resistance at a current density of *i*. Therefore, the over-potentials of cell 2, 4 and cell 5 can be obtained from the measured diffusion resistances in this way. The continuous values of R(i) was approximately obtained from a polynominal fit of the experimental measured diffusion resistances (shown in Figure 95). In order to facilitate the comparison with the modeled results based on microstructures and gas species, the diffusion over-potentials obtained from impedances of cell 2, 4 and 5 were also shown in Figure 100. The obtained diffusion over-potentials for cell 4 and 5 exhibit fast increase at high electrolysis current densities and show fair agreement with the theory using a porosity of 18 % – 22 % and tortuosity of 4. The modeled results based on a higher porosity of 28 % and a lower tortuosity of 3, seem close to the experimental obtained diffusion over-potential for cell 2.

However, there is some extent of deviation in the shapes of the obtained diffusion over-potential from integration (based on the experimental results) for the cells from the modeled results, indicating a practically more complicated microstructure than parameters described (porosity, tortuosity and thickness) or gas properties than that used for modeling.

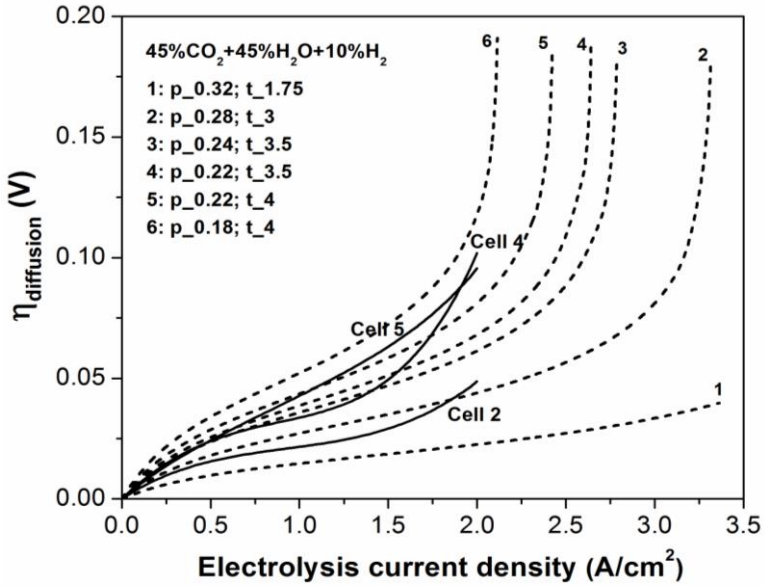

Figure 100 Diffusion over-potential from modeling (dash lines) and numerical integration (solid lines) of the resistances obtained from polynomial fit of the experimental diffusion resistances for cell 2, 4 and cell 5. The modeled diffusion over-potentials are calculated based on the estimated microstructure parameters for the cells (porosity, p and tortuosity, t).

Microstructural changes after test.— Post-test microstructural analysis of cell 4 and 5 which degraded much faster than the remaining cells revealed delamination at the Ni-YSZ|YSZ interface. Most strikingly, carbon fibers were observed at the delaminated interface. The structural damage observed for these cells differed from the previous reported delamination at the LSM-YSZ|YSZ interface, which was ascribed to the build-up of oxygen at the LSM-YSZ|YSZ interface.[10,36]

The interfacial damage results in contact loss between Ni-YSZ electrode and YSZ electrolyte, contributing to the observed significant increase in series resistance (Figure 96). This microstructural damage at the Ni-YSZ|YSZ interface (Figure 98) is ascribed to the growth of carbon fibers which lead to a volume expansion, and thus delamination / a structural change at the electrode/electrolyte interface.

Local conditions favoring carbon formation at the interface.— Thermodynamic calculations (FactSage software[37]) reveals that a reactant conversion above 99 % is needed in order to catalytic form coke (carbon fibers) at 875 ºC. The total reactant conversion applied in the present study was less than 67 %, below the thermodynamic condition for carbon formation. However, the increased cell voltage and conversion arc indicate a high local CO + H_2 concentration. This high local CO + H_2 concentration may be reducing enough to form the observed carbon deposition at the Ni-YSZ|YSZ interface.

The deviation of the local gas composition from the average (in – out) composition could be due to two factors: 1) diffusion limitations in the Ni-YSZ structure and 2) the over-potential / current density gradients away from the Ni-YSZ|YSZ interface into the active Ni-YSZ electrode, enhancing the diffusion limitations since most conversion thus occur close to the Ni-YSZ|YSZ interface and the reactants has to diffuse a longer distance within the low porosity active Ni-YSZ electrode.

For a Ni-YSZ electrode, the ionic conductivity of YSZ is much lower than the electronic conductivity of Ni. The active TPB is limited within a thin layer next to the electrolyte. Therefore, there is a high gradient in the over-potential / current density distributing from the Ni-YSZ|YSZ interface into the active electrode (Figure 101).[38] Even though the penetration depth could be up to 10 microns, most of the reaction takes place in the Ni-YSZ active electrode at TPBs close the YSZ electrolyte, where the reactant concentration drops and product concentration rises sharply. Whether reaching diffusion limit or not, the local current density and the corresponding H_2 + CO molar ratio at TPBs in the vicinity of the electrolyte is much higher than the average (Figure 101).

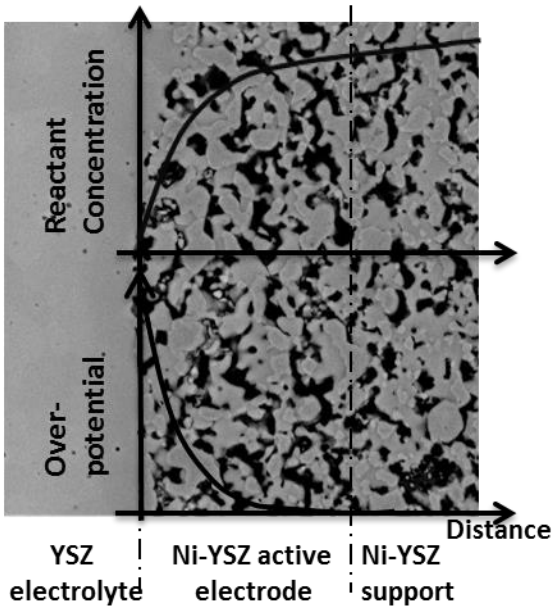

Figure 101 Bottom: over-potential / current density gradients from the electrode | electrolyte interface into the Ni-YSZ active electrode; Top: the concentration profile of the reactant.

Although the total reactant conversion is below 67 %, diffusion limitations and the current gradient may cause the gas composition at the active TPB's close to the electrolyte to be so reducing that the gas composition falls into the carbon formation regime, and consequently form carbon fibers (solid carbon). This is consistent with the SEM observations that the carbon deposition was found mainly at the first 1 or 2 microns of the active electrode next to the electrolyte. For the cells with higher porosity (cell 2 and 3) or when operated at lower current density / conversion (cell 1), the gas composition close to the YSZ electrolyte is, although more reducing than the outlet, still oxidizing enough to prevent carbon formation.

5. Conclusions

Carbon formation was observed in the active Ni-YSZ electrode during co-electrolysis H_2O and CO_2 in low porosity Ni-YSZ based solid oxide cells when operated at 2.0 – 2.25 A/cm^2 with a reactant conversion of only 67 %. Cells with a higher porosity showed no carbon formation.

The low porosity cells for which carbon formation was observed had a significantly larger diffusion and conversion resistance than the remaining cells. Based on the total conversion, the H_2 + CO concentration was below the carbon formation regions. The formation of carbon indicates a very reducing atmosphere at the active TPB at the Ni-YSZ|YSZ interface. The reducing atmosphere and thus the deposition of carbon is ascribed to the diffusion limitations dominating at high electrolysis current densities. The diffusion

limitations may be enhanced by the current density gradients away from the Ni-YSZ|YSZ interface into the active Ni-YSZ electrode, since most conversion thus occurs at the Ni-YSZ|YSZ interface.

Acknowledgment

This work was financially supported by the DTU Mobility Fellowship Program. The support from the staff of the DTU Energy Conversion is highly appreciated.

References

1. W. Doenitz, R. Schmidberger, E. Steinheil, and R. Streicher, *Int. J. Hydrogen Energy*, **5**, 55 (1980).

2. A. O. Isenberg, *Solid State Ionics*, **3/4**, 431 (1981).

3. J. E. O'Brien, C. M. Stoots, J. S. Herring, and J. Hartvigsen, *J. Fuel Cell Sci. Technol.*, **3**, 213 (2006)

4. A. Hauch, S. H. Jensen, S. Ramousse, and M. Mogensen, *J. Electrochem. Soc.*, **153**, A1741 (2006)

5. J. Udagawa, P. Aguiar, and N. P. Brandon, *J. Power Sources*, **166**, 127 (2007).

6. J. Hartvigsen, S. Elangovan, J. O'Brien, C. Stoots, and J. Herring, *ECS Trans.*, **7**, 357 (2007).

7. J. S. Herring, J. E. O'brien, C. M. Stoots, G. L. Hawkes, J. J. Hartvigsen, M. Shahnam, *Int. J. Hydrogen Energy*, **32**, 440 (2007)

8. S. H. Jensen, P. H. Larsen, and M. Mogensen, *Int. J. Hydrogen Energy*, **32**, 3253 (2007)

9. A. Brisse, J. Schefold, and M. Zahid, *Int. J. Hydrogen Energy*, **33**, 5375 (2008)

10. R. Knibbe, M. L. Traulsen, A. Hauch, S. D. Ebbesen, and M. Mogensen, *J. Electrochem. Soc.*, **157**, B1209 (2010)

11. C. M. Stoots, J. E. O'Brien, J. S. Herring, and J. J. Hartvigsen, *J. Fuel Cell Sci. Technol.*, **6**, 011014 (2009)

12. S. D. Ebbesen, C. Graves, and M. Mogensen, *Int. J. Green Energy*, **6**, 646 (2009)

13. C. Graves, S. D. Ebbesen, and M. Mogensen, *Solid State Ionics*, **192**, 398 (2011)

14. S. D. Ebbesen and M. Mogensen, *J. Power Sources*, **193**, 349 (2009)

15. S. D. Ebbesen and M. Mogensen, *Electrochem. Solid-State Lett.*, **13**, B106 (2010)

16. S. D. Ebbesen, C. Graves, A. Hauch, S. H. Jensen, and M. Mogensen, *J. Electrochem. Soc.*, **157**, B1419 (2010)

17. C. Graves, S. D. Ebbesen, M. Mogensen, and K. S. Lackner, *Renew. Sustain. Energy Rev.*, **15**, 1 (2011)

18. X. Sun, M. Chen, S. H. Jensen, S. D. Ebbesen, C. Graves, M. Mogensen, *Int. J. Hydrogen Energy*, **37**, 17101 (2012)

19. F. Tietz, D. Sebold, A. Brisse, and J. Schefold, *J. Power Sources*, **223**, 129 (2013)

20. M. Chen, Y. Liu, J. J. Bentzen, W. Zhang, X. Sun, A. Hauch, Y. Tao, J. R. Bowen, P. V. Hendriksen, *J. Electrochem. Soc.*, **160**, F883 (2013).

21. S. C. Singhal and K. Kendal, *High Temperature and Solid Oxide Fuel Cells Fundamentals, Design and Applications*, 1st ed., Elsevier Ltd., Oxford, UK (2003)

22. A. Atkinson, S. Barnett, R. J. Gorte, J. T. Irvine,S A. J. Mcevoy, M. Mogensen, S. C. Singhal, J. Vohs, *Nat. Mater.*, **3**, 17 (2004)

23. M. Cimenti and J. M. Hill, *J. Power Sources*, **186**, 377 (2009)

24. M. J. Jørgensen and M. Mogensen, *J. Electrochem. Soc.*, **148**, A433 (2001)

25. A. Hagen, R. Barfod, P. V. Hendriksen, Y.-L. Liu, and S. Ramousse, *J. Electrochem. Soc.*, **153**, A1165 (2006)

26. H. Schichlein, A. C. Müller, M. Voigts, A. Krügel, and E. Ivers-Tiffée, *J. Appl. Electrochem.*, **32**, 875 (2002).

27. S. H. Jensen, A. Hauch, P. V. Hendriksen, M. Mogensen, N. Bonanos, T. Jacobsen, *J. Electrochem. Soc.*, **154**, B1325 (2007)

28. R. Barfod, A. Hagen, S. Ramousse, P. V. Hendriksen, and M. Mogensen, *Fuel Cells*, **6**, 141 (2006)

29. R. Barfod, M. Mogensen, T. Klemensø, A. Hagen, Y. Liu, P. V. Hendriksen, *J. Electrochem. Soc.*, **154**, B371 (2007)

30. C. Graves, RAVDAV data analysis software, version 0.9.7, (2012).

31. *Image J. http//rsbweb.nih.gov/ij/*.

32. S. Primdahl and M. Mogensen, *J. Electrochem. Soc.*, **145**, 2431 (1998).

33. S. D. Ebbesen and M. Mogensen, *ECS Trans.*, **50**, 167 (2013).

34. S. Primdahl and M. Mogensen, *J. Electrochem. Soc.*, **146**, 2827 (1999).

35. J. R. Wilson, J. S. Cronin, and S. A. Barnett, *Scr. Mater.*, **65**, 67 (2011)

36. T. Jacobsen and M. Mogensen, *ECS Trans.*, **13**, 259 (2008).

37. C. W. Bale, A. D. Pelton, W. T. Thompson, G. Eriksson, and K. Hack, *FactSage 6.2, Thermfact GTT-Technologies, © 1976–2010*.

38. M. Mogensen, K. V. Hansen, P. Holtappels, and T. Jacobsen, *Proc. 10th Eur. SOFC Forum*, **B04**, 7 (2012).

Chapter 8 Carbon Nanotube Growth on Nano-Zirconia under Strong Cathodic Polarization in Steam and Carbon Dioxide

(This chapter is the manuscript submitted to ChemCatChem)

Youkun Tao, Sune D. Ebbesen, Wei Zhang, and Mogens B. Mogensen

Department of Energy Conversion and Storage, Technical University of Denmark, DTU, Risø Campus, Frederiksborgvej 399, Roskilde 4000, Denmark

Graphical Table of Contents:

This work describes nano-zirconia acting as a catalyst for the growth of CNT during electrochemical conversion of CO_2 and H_2O in a Ni–YSZ cermet under strong cathodic polarization and an electrocatalytic mechanism is proposed for the CNT growth.

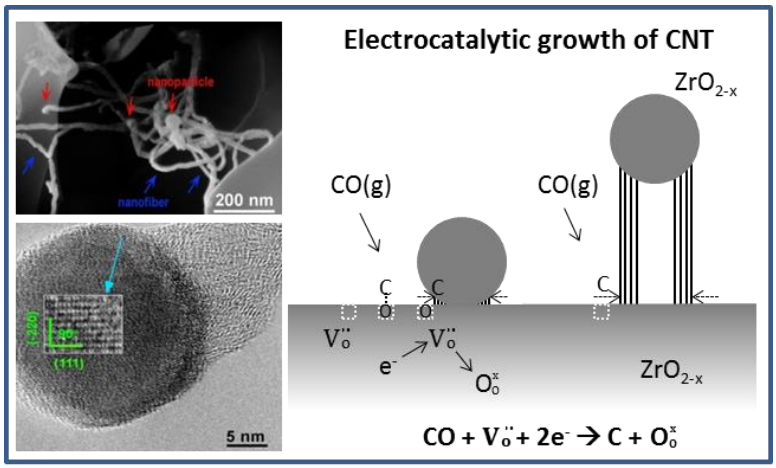

Keywords:

carbon; nanotubes; zirconia; electrocatalysis; solid oxide cells

1. Introduction

A solid oxide electrolysis cell (SOEC) can electrochemically split CO_2 and H_2O into CO and H_2 (syngas)[1] and has potential as a converter of renewable electric energy such as solar, wind and hydropower into syngas, which further may be catalytic converted into CO_2 neutral hydrocarbon fuels.[1b,2] Recently, we found that carbon fibers were formed in the SOEC cathode under heavy load conditions.[3] In this work it is shown that the fibers are carbon nanotubes (CNTs). The purpose of this paper is, therefore, to describe the CNT formation in SOEC and put up a hypothesis for the mechanism behind. This work may reveal additional aspects of the broad picture of CNT formation.

CNTs are generally synthesized by the catalytic chemical vapor deposition (CVD) process from carbon monoxide, methane or other carbon containing gas molecules.[4] Nanoparticles of transition metals, such as Fe, Co, and Ni, have been intensively studied as heterogeneous catalysts for the growth of CNTs during the past decades.[4c,5] A variety of other metal nanoparticles including Au, Ag, Mo, Cu, Pt, Al, Zr, *etc*. have also been added to the list of metal catalysts for CNT growth.[6] Metal oxides, which usually exhibit good stability at high temperatures, are commonly used as the support of the catalysts. For example, zirconia particles has been reported as an inert matrix for dispersing iron catalyst during catalytic growth of CNTs.[7] However, recent research showed that nano-zirconia can act as a catalyst for CNT growth through a thermal CVD process.[8] In addition, several other metal oxides such as MgO,[9] Al_2O_3,[10] SiO_2,[11] and Ta-oxide[12], have been reported to have catalytic activity for CNT growth.

The carbon nanotubes we observed was generated during co-electrolysis of 45% H_2O + 45% CO_2 + 10% H_2 *via* SOEC with a typical composite cathode consisting of Ni and yttria doped zirconia (YSZ). Ni is known as an effective catalyst for hydrocarbon breakdown into carbon, and the deposition of carbon in the Ni–YSZ electrode is usually thought to be catalyzed by Ni.[13] In this paper, the formation of CNTs in the SOEC cathode is studied by detailed microstructure and composition characterization. Unexpectedly, strong indications were found that zirconia, not Ni, nanoparticles serve as the catalyst for CNT growth. Correlating to the electrochemical conditions in SOECs under large cathodic polarizations, an electro-catalytic process rather than the conventional heterogeneous catalysis is proposed for the mechanism behind CNT formations.

2. Experimental

High temperature co-electrolysis of CO_2 and H_2O was performed using a Ni–YSZ based planar solid oxide cell. Feed gas of 25 Lh^{-1} 45 % H_2O + 45 % CO_2 + 10 % H_2 was flown to the Ni–YSZ cathode. The cell was

operated at a constant electrolysis current density of 2.25 Acm^{-2} with the gas conversion of 67 %. The cell temperature was ~ 875 ^{o}C and the test duration was about 11 hours. Additional information on the configuration of the solid oxide cell and detailed test procedures is given in supporting information.

High-resolution SEM (HRSEM) using a field-emission gun scanning electron microscope (Zeiss Supra 35), operated between 5 and 10 kV in in-lens mode was employed to characterize the fresh fracture of the tested cell. Through a large amount of SEM observation, it was verified that CNTs were formed in the part of the cathode at a distance of 1 to 2 μm to the Ni–YSZ | YSZ interface. The nanostructures were carefully collected by scraping the bare surface of a delaminated YSZ electrolyte using a sharp steel blade. The collected CNTs and nanoparticles were dispersed in ethanol and loaded onto lacey carbon film supported by copper grid for transmission electron microscopy (TEM) observation. High-resolution TEM (HRTEM) analysis of the derived CNTs and nanoparticles was performed using a JEM-3000F microscopy equipped with a field-emission gun, operated at 300 kV. The point resolution is 0.19 nm.

3. Results and Discussions

Figure 102a shows the SEM image of the carbon nanostructures in the Ni–YSZ electrode during co-electrolysis of 45 % H_2O + 45 % CO_2 + 10 % H_2 at an electrolysis current density of 2.25 Acm^{-2}. The carbon filament is approximately 20 nm in diameter with a nanoparticle (NP) located both at the end of the fiber, but also embedded in the fiber. It is not clear from the SEM image if it is a dense fiber or a hollow tube, but TEM reveals that they are hollow (Figure 102b). The formation of fibers was only observed in the Ni–YSZ active electrode within 2 μm away from the YSZ electrolyte.[3] It should be noted that fibers were only observed for cells operated in regimes with gas diffusion limitation.

TEM images (Figure 102b) shows CNTs together with zirconia NPs, some of which are situated at one end of the CNT and one is embedded inside a CNT. By EDX analysis, it was confirmed that the NPs are rich in zirconium and oxygen (Figure 102c). Further, from the electron diffraction pattern (Figure 102d) the nanoparticles are identified as cubic zirconia. Based on and HRTEM analysis (Figure 102e and f), the {111} and {-220} planes of cubic zirconia, as well as their characteristic 90^{o} angle, can be identified. A three-wall branch of the CNT can be seen in Figure 102e. NP 1 with a diameter of ~ 5 nm was encapsulated inside the multi-walled CNT. It is not feasible for the zirconia NPs to have migrated into a well-grown closed nanotube or grown inside the CNT. Thus it is reasonable to assume that initially a CNT with a small diameter was growing on NP 1. Later, the growth of the CNT proceeded to contact NP 4, a larger neighboring particle with a diameter of ~ 25 nm. As a result, the thicker multi-wall CNT was grown in a reverse direction with particle NP 1 encapsulated in the final CNT. Clearly, the perpendicular {111} and {-220} crystal planes are

found from NP 4 (Figure 102f). NP 4 is located at the tip of the CNT. NP 2 and 3 are attached to the CNT at the open end (Figure 102e). The morphology appears consistent with the growth from root or base.[14] In addition, for the zirconia NPs with larger diameters, carbon layers covering the zirconia NPs were widely observed.

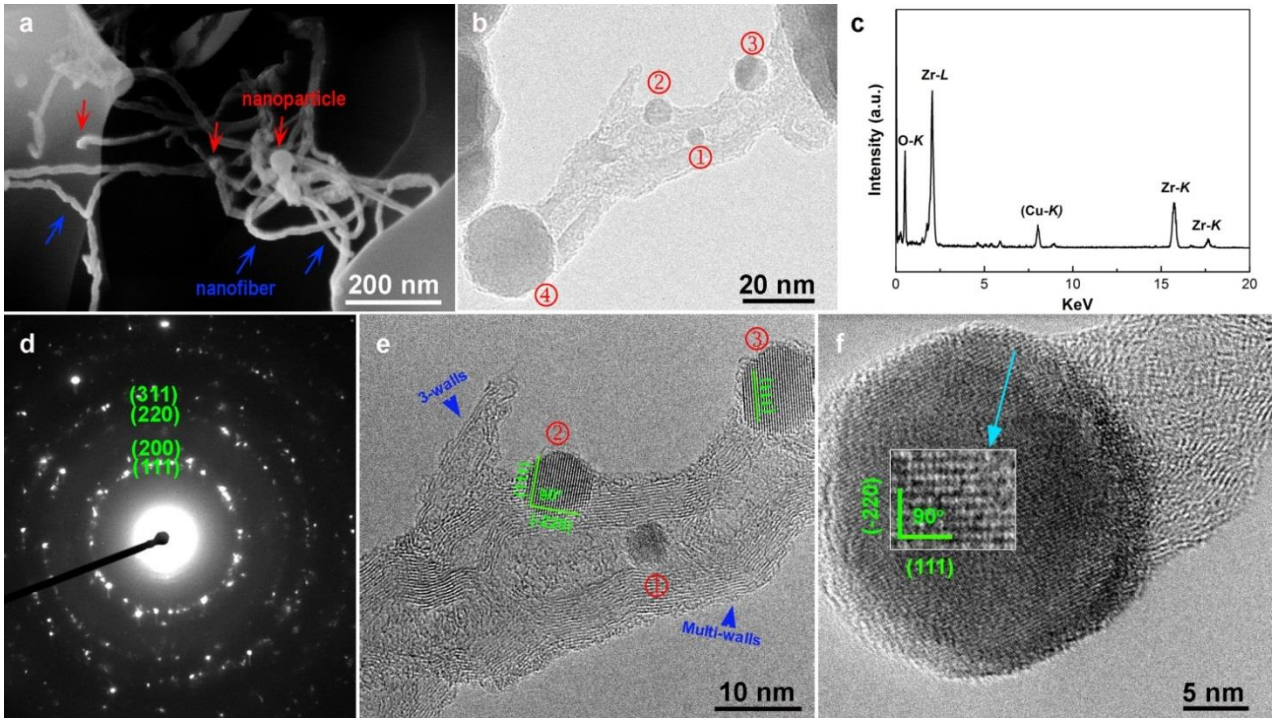

Figure 102 a) SEM image of the nanostructures at Ni–YSZ cathode | YSZ electrolyte interface; b) TEM image of the carbon nanotubes and nano particles, which are numbered; c) EDS and d) Electron diffraction of the nanoparticles; e) and f) HRTEM images of the structures showed in b)

Zirconia nanoparticle as a catalyst for CNT growth: Both zirconium and zirconia have been reported as the heterogeneous catalysts for CNT growth.[8,15] In this study, reduced Zr-metal as the catalyst can be excluded. If the nanoparticle that catalyzed the CNT growth were Zr-metal, which was subsequently re-oxidized to zirconia by steam when the cathodic polarization was removed, the large volume expansion of Zr oxidation to zirconia (approximately 150 %) should result in mechanical stress, leading to mismatch with or detachment from the CNT. The HRTEM observation shows that the zirconia NPs were closely attaches to the nanotube (NP 4 in Figure 102) or matches exactly the inner channel of the nanotube (NP 1). Moreover, the shape of the catalyst particles appear spherical, not pear-like or elongated as reported for the metal catalysts for CNT growth, especially in the case of the metal catalyst encapsulated inside the tube.[16] Thus, the results are taken as strong indicating that the NPs, which served as the catalyst for CNT growth during co-electrolysis of CO_2 and H_2O, actually are zirconia, not Zr-metal or carbide.

Chemical state of the zirconia nanoparticles under cathodic polarization: The observed carbon formation specifically at the Ni–YSZ cathode | YSZ electrolyte interface occurs only when gas diffusion limits the reaction rate.[3] Consequently, a strong cathodic polarization occurs at TPBs in the very vicinity of the electrolyte which facilitates the CNT formation. In a strongly polarized cathode of an electrolysis cell, zirconia NPs could present a different chemical state than the bulk zirconia under normal conditions (high pO_2). By increasing the applied cathodic over-potential, the oxygen partial pressure (pO_2) at the Ni–YSZ cathode | YSZ electrolyte interface may be sufficient low. At conditions milder than for complete reduction of ZrO_2 to Zr-metal ($pO_2 \sim 10^{-40}$, *i.e.* potential ~ 2.3 V vs. 1 atm. O_2) zirconia may undergo partial reduction.[17] The oxygen deficiency of the YSZ at cathode | electrolyte interface depends on pO_2. Based on the operating conditions in this experiment, an interfacial oxygen partial pressure of ~ 10^{-27} atm is estimated. The oxygen deficiency of bulk 8YSZ[18] increases with decreasing pO_2 as is shown in Figure 103a. With respect to the conductivity, at normal conditions, zirconia is a good ion conductor and the electronic conductivity is negligible. Partially reduced zirconia could have considerable electronic conductivity under very low oxygen partial pressure or strong cathodic polarization, according to the relationship: $\sigma_e \propto {pO_2}^{-\frac{1}{4}}$ [18,19] (Figure 103b). The fact that zirconia NPs with mixed ionic and electronic conductivity (MIEC) act as catalyst for CNT growth indicates that they are taking part in the electrochemical catalysis of H_2/H_2O and CO/CO_2 in general.

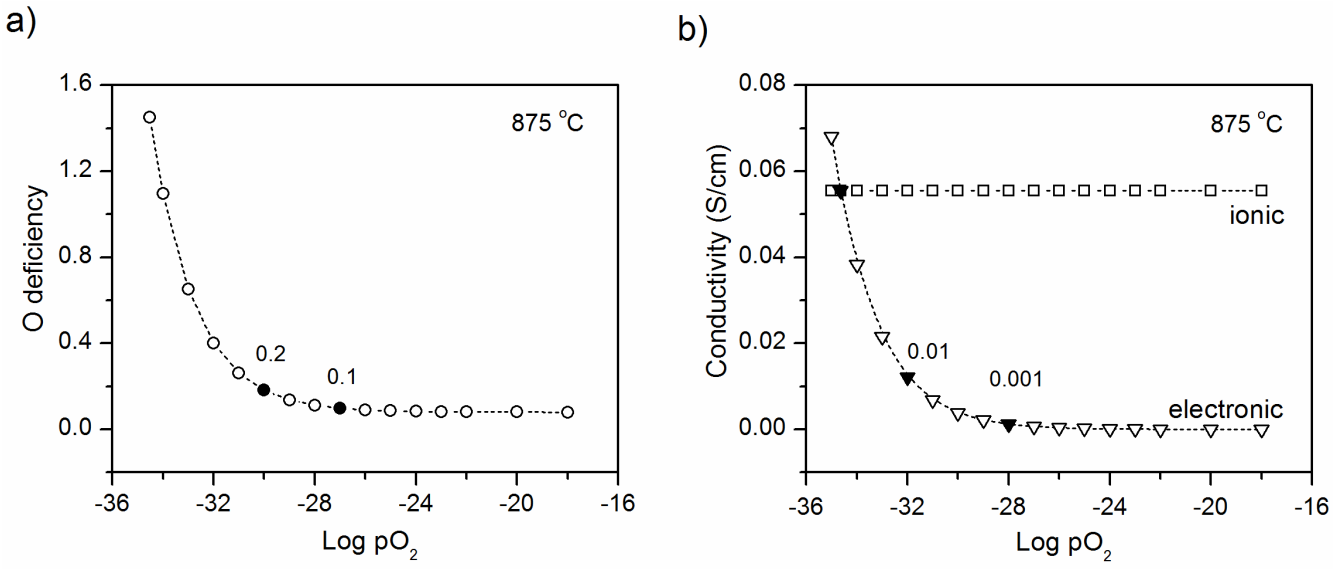

Figure 103 a) Oxygen deficiency and b) electronic and ionic conductivity for 8YSZ as a function of oxygen partial pressure (pO_2).

Gas conversion and electrochemical reduction: In the experiment, the carbon feedstock is CO_2 and the total conversion of CO_2 and H_2O is 66.8 % based on Faraday's Law. Carbon deposition becomes thermodynamically favorable only when the conversion increasing close to 100% (the local gas is composed mainly of H_2 + CO).[3] It is known that zirconia NPs may form under strong cathodic polarization of the Ni–YSZ electrode.[20] A hypothesis is that zirconia NPs are formed by re-oxidation of Zr that has been formed by reduction. However, the detailed mechanism for the formation of zirconia NPs is not clear yet. The fact that the zirconia NPs act as catalyst particles for the CNT growth shows that the Zirconia NPs are formed during the electrolysis in volumes of the Ni–YSZ electrode with very low pO_2 near the bulk electrolyte within significant less than 11h.

A hypothesis of CNT growth on MIEC via an electrocatalytic process: The physical and chemical state of the catalyst particle is important for the elucidation of the CNT growth model. In this work, carbon formation was observed on zirconia NP instead of Ni surface. Zirconia has been reported as a heterogeneous catalyst for CNT growth *via* the typical CVD process.[8] The classical VLS (vapor-liquid-solid) mechanism to describe CVD growth of CNT relies on the diffusion of carbon through catalyst particle.[21] Therefore, a liquid or quasi-liquid state of the catalyst (low melting temperature), and high carbon solubility or formation of carbide intermediate,[22] are necessary for this mechanism. Considering the very high melting point of zirconia (2715 ^{o}C), as well as a high temperature needed for carbide formation (> 1200 ^{o}C) even with nano-scaled zirconia,[23] the VLS mechanism can be ruled out. Furthermore, Ni is one of the best heterogeneous catalysts for CNT growth.[4c,5] If carbon formation occurs *via* the simple heterogeneous catalysis on zirconia NP for a Ni-zirconia composite, it is also expected to deposit on Ni, a catalyst at least no worse than zirconia NP. The large particle size of Ni should not be crucial for this process, because significant amount of carbon can be still formed on Ni particles of submicron or micron scale, as in the case of coking in solid oxide fuel cells.[13] Therefore, the growth of CNT unlikely occurs *via* simple heterogeneous catalysis in these cells.

An electro-catalytic mechanism is proposed for the growth of CNT on zirconia in the SOECs. An illustration of the mechanism model is shown in Figure 104. At the Ni–YSZ cathode | YSZ electrolyte interface under electrolysis as in this experiment, CO molecules could be adsorbed on the surface of zirconia and broken down electrocatalytically, in which process O ions occupy the oxygen vacancies of zirconia and C atoms are produced on the surface. As more carbon atoms precipitate, a graphite nucleus grows and forms around a Zirconia-NP periphery, which is energetically favored.[24] Initially, the bottom surface connecting zirconia support has lower pO_2 and higher electronic conductivity than the top surface; thus it could be the preferntial site for the electrocatalytic reaction (and graphitic nucleation). The particle will be lift up from

the support with the CNT growing (Figure 104). The electrocatalytic reaction could continue on the surface of the support. Via surface migration, carbon atoms are incorporated into the CNT at the root.

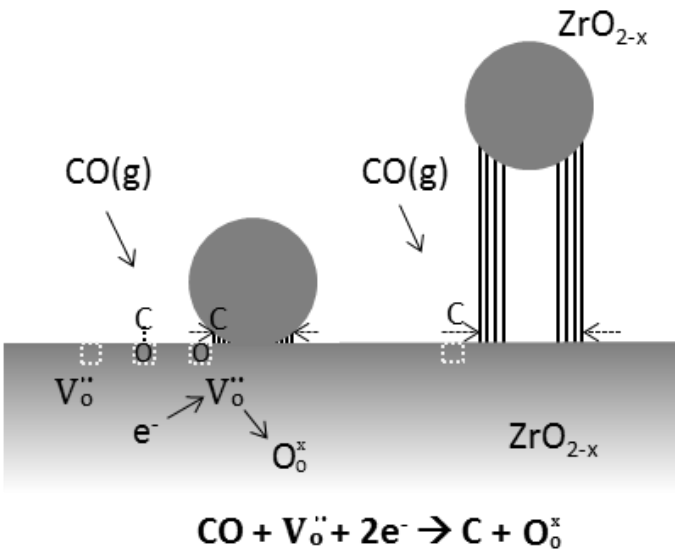

Figure 104 Growth of carbon nanotubes on zirconia nanoparticles *via* an electrocatalytic process. $V_o^{\cdot\cdot}$ and O_o^x denotes respectively an oxygen vacancy and an occupied site of O in zirconia while e^- is an electron.

The role of surface defect and mixed conductivity: Since little contribution comes from the bulk due to the low carbon solubility, the surface property of oxide catalyst is expected to play a crucial role for CNT growth.[16a,25] For the catalytic process, a critical step is the breakdown of the bonds within carbon containing molecules so that carbon atoms can be produced. Surface oxygen vacancies have been identified as the active site of oxide catalysts for dissociative chemisorption of various molecules.[26] More important, the oxygen vacancies has been proposed in the electrochemical oxidation of CO in SOFCs.[27] For the catalytic growth of CNT on zirconia, enhanced properties can be attributed at least partly to the oxygen-deficiencies.[8,28] During the SOEC operation, CNT growth could be promoted by a large cathodic polarization. The deoxygenation of adsorbate on zirconia could take place preferentially at the surface O vacancies.[26a] The electron and oxygen ion transfer are essential for the electrocatalysis. As mentioned previously, zirconia exhibit mixed ionic and electronic conductivity under strong cathodic polarizations, which are crucial for CNT growth in this mechanism. However, Ni or Zr metal nanoparticles cannot play this role because they only have electronic conductivity.

In summary, carbon nanotubes found in the Ni–YSZ cathode of a solid oxide electrolysis cell during electrolysis of CO_2 and H_2O was studied. Results of TEM analysis indicated that cubic zirconia nanoparticles,

which were generated under large cathodic polarization, acted as the catalysts for CNT growth. The zirconia at the cathode | electrolyte interface may exhibit considerable surface defect concentration and mixed ionic and electronic conductivity under SOEC operation condition resulting in CNT growth. An electrocatalytic mechanism is proposed for the growth of CNT on the zirconia nanoparticles. The mixed conductivity of partially reduced zirconia is essential for oxygen ion and electron transfer process of this mechanism. This work provides further understanding not only on the mechanism of the catalytic growth of CNTs, but also on the local electrochemical properties of a highly polarized Ni–YSZ cathode at the micro and nano level.

Acknowledgment

Financial support for this work was provided by the DTU Mobility Fellowship Program. The support from the staff of the DTU Energy Conversion is highly appreciated.

References

[1] a) W. Dönitz, E. Erdle, *Int. J. Hydrogen Energy* **1985**, *10*, 291–295; b) S. D. Ebbesen, C. Graves, M. Mogensen, *Int. J. Green Energy* **2009**, *6*, 646–660; c) A. O. Isenberg, *Solid State Ionics* **1981**, *3/4*, 431–437; d) S. H. Jensen, P. H. Larsen, M. Mogensen, *Int. J. Hydrogen Energy* **2007**, *32*, 3253–3257.

[2] a) C. Graves, S. D. Ebbesen, M. Mogensen, K. S. Lackner, *Renew. Sustain. Energy Rev.* **2011**, *15*, 1–23; b) Z. Zhan, W. Kobsiriphat, J. R. Wilson, M. Pillai, I. Kim, S. A. Barnett, *Energy & Fuels* **2009**, *23*, 3089–3096; c) C. M. Stoots, J. E. O'Brien, J. S. Herring, J. J. Hartvigsen, *J. Fuel Cell Sci. Technol.* **2009**, *6*, 011014; d) S. H. Jensen, P. H. Larsen, M. Mogensen, *Int. J. Hydrogen Energy* **2007**, *32*, 3253–3257.

[3] Y. Tao, S. D. Ebbesen, M. Mogensen, *ECS Trans.* **2013**, *50*, 139–151.

[4] a) K. J. MacKenzie, O. M. Dunens, A. T. Harris, *Ind. Eng. Chem. Res.* **2010**, *49*, 5323–5338; b) A. Moisala, A. G. Nasibulin, E. I. Kauppinen, *J. Phys. Condens. Matter* **2003**, *15*, S3011; c) J.-P. Tessonnier, D. S. Su, *ChemSusChem* **2011**, *4*, 824–847.

[5] a) M. F. L. De Volder, S. H. Tawfick, R. H. Baughman, A. J. Hart, *Science* **2013**, *339*, 535–539; b) K. P. De Jong, J. W. Geus, *Catal. Rev.* **2000**, *42*, 481–510.

[6] a) D. Takagi, Y. Homma, H. Hibino, S. Suzuki, Y. Kobayashi, *Nano Lett.* **2006**, *6*, 2642–2645; b) D. Takagi, Y. Kobayashi, H. Hibino, S. Suzuki, Y. Homma, *Nano Lett.* **2008**, *8*, 832–835; c) D. Yuan, L. Ding, H. Chu, Y. Feng, T. P. McNicholas, J. Liu, *Nano Lett.* **2008**, *8*, 2576–2579; d) J. H. Hafner, M. J. Bronikowski, B. R. Azamian, P. Nikolaev, A. G. Rinzler, D. T. Colbert, K. A. Smith, R. E. Smalley, *Chem. Phys. Lett.* **1998**, *296*, 195–202; e) L. Huang, S. P. Lau, Y. B. Zhang, B. K. Tay, Y. Q. Fu, *Nanotechnology* **2004**, *15*, 663–666; f) M.-Q. Zhao, Q. Zhang, W. Zhang, J.-Q. Huang, Y. Zhang, D. S. Su, F. Wei, *J. Am. Chem. Soc.* **2010**, *132*, 14739–14741; g) Q. Zhang, M.-Q. Zhao, D.-M. Tang, F. Li, J.-Q. Huang, B. Liu, W.-C. Zhu, Y.-H. Zhang, F. Wei, *Angew. Chem. Int. Ed. Engl.* **2010**, *49*, 3642–3645; *Angew. Chem.* **2010**, 122, 3724–3727.

[7] S. Han, T. Yu, J. Park, B. Koo, J. Joo, T. Hyeon, S. Hong, J. Im, *J. Phys. Chem. B* **2004**, *108*, 8091–8095.

[8] S. A. Steiner III, T. F. Baumann, B. C. Bayer, R. Blume, M. A. Worsley, W. J. MoberlyChan, E. L. Shaw, R. Schlögl, A. J. Hart, S. Hofmann, et al., *J. Am. Chem. Soc.* **2009**, *131*, 12144–12154.

[9] M. H. Rümmeli, E. Borowiak-Palen, T. Gemming, T. Pichler, M. Knupfer, M. Kalbác, L. Dunsch, O. Jost, S. R. P. Silva, W. Pompe, et al., *Nano Lett.* **2005**, *5*, 1209–1215.

[10] H. Liu, D. Takagi, H. Ohno, S. Chiashi, T. Chokan, Y. Homma, *Appl. Phys. Express* **2008**, *1*, 014001.

[11] a) B. Liu, W. Ren, L. Gao, S. Li, S. Pei, C. Liu, C. Jiang, H.-M. Cheng, *J. Am. Chem. Soc.* **2009**, *131*, 2082–2083; b) S. Huang, Q. Cai, J. Chen, Y. Qian, L. Zhang, *J. Am. Chem. Soc.* **2009**, *131*, 2094–2095; c) A. Bachmatiuk, F. Börrnert, M. Grobosch, F. Schäffel, U. Wolff, A. Scott, M. Zaka, J. H. Warner, R. Klingeler, M. Knupfer, et al., *ACS Nano* **2009**, *3*, 4098–4104.

[12] B. C. Bayer, C. Castellarin-Cudia, R. Blume, S. A. Steiner III, C. Ducati, D. Chu, A. Goldoni, A. Knop-Gericke, R. Schlögl, C. Cepek, et al., *RSC Adv.* **2013**, *3*, 4086–4092.

[13] a) S. C. Singhal, K. Kendal, *High Temperature and Solid Oxide Fuel Cells Fundamentals, Design and Applications*, Elsevier Ltd., Oxford, UK, **2003**; b) A. Atkinson, S. Barnett, R. J. Gorte, J. T. S. Irvine, A. J. Mcevoy, M. Mogensen, S. C. Singhal, J. Vohs, *Nat. Mater.* **2004**, *3*, 17–27.

[14] R. T. K. Baker, R. J. Waite, *J. Catal.* **1975**, *37*, 101–105.

[15] H.-C. Wu, C.-J. Huang, M.-J. Youh, C.-L. Tseng, H.-T. Chen, Y.-Y. Li, A. Sakoda, *Carbon N. Y.* **2010**, *48*, 1897–1901.

[16] a) M. H. Rümmeli, F. Schäffel, C. Kramberger, T. Gemming, A. Bachmatiuk, R. J. Kalenczuk, B. Rellinghaus, B. Büchner, T. Pichler, *J. Am. Chem. Soc.* **2007**, *129*, 15772–15773; b) S. Helveg, C. López-Cartes, J. Sehested, P. L. Hansen, B. S. Clausen, J. R. Rostrup-Nielsen, F. Abild-Pedersen, J. K. Nørskov, *Nature* **2004**, *427*, 426–429; c) M. Lin, J. P. Y. Tan, C. Boothroyd, K. P. Loh, E. S. Tok, Y.-L. Foo, *Nano Lett.* **2007**, *7*, 2234–2238; d) S. Hofmann, R. Sharma, C. Ducati, G. Du, C. Mattevi, C. Cepek, M. Cantoro, S. Pisana, A. Parvez, F. Cervantes-Sodi, et al., *Nano Lett.* **2007**, *7*, 602–608.

[17] B. Luerßen, J. Janek, S. Günther, M. Kiskinova, R. Imbihl, *Phys. Chem. Chem. Phys.* **2002**, *4*, 2673–2679.

[18] J. Park, R. N. Blumenthal, *J. Am. Ceram. Soc.* **1989**, *72*, 1485–1487.

[19] J. Park, R. N. Blumenthal, *J. Electrochem. Soc.* **1989**, *136*, 2867–2876.

[20] a) M. Chen, Y. Liu, J. J. Bentzen, W. Zhang, X. Sun, A. Hauch, Y. Tao, J. R. Bowen, P. V. Hendriksen, *J. Electrochem. Soc.* **2013**, *160*, F883–F891; b) F. Tietz, D. Sebold, a. Brisse, J. Schefold, *J. Power Sources* **2013**, *223*, 129–135.

[21] a) R. T. K. Baker, M. A. Barber, P. S. Harris, F. S. Feates, R. J. Waite, *J. Catal.* **1972**, *26*, 51–62; b) J. Rostrup-Nielsen, D. L. Trimm, *J. Catal.* **1977**, *48*, 155–165.

[22] A. Rinaldi, J.-P. Tessonnier, M. E. Schuster, R. Blume, F. Girgsdies, Q. Zhang, T. Jacob, S. B. Abd Hamid, D. S. Su, R. Schlögl, *Angew. Chem. Int. Ed. Engl.* **2011**, *50*, 1–6; *Angew. Chem.* **2011**, *123*, 3371–3375.

[23] M. D. Sacks, C.-A. Wang, Z. Yang, A. Jain, *J. Mater. Sci.* **2004**, *39*, 6057–6066.

[24] X. Fan, R. Buczko, A. Puretzky, D. B. Geohegan, J. Y. Howe, S. T. Pantelides, S. J. Pennycook, *Phys. Rev. Lett.* **2003**, *90*, 145501.

[25] B. Liu, D.-M. Tang, C. Sun, C. Liu, W. Ren, F. Li, W.-J. Yu, L.-C. Yin, L. Zhang, C. Jiang, et al., *J. Am. Chem. Soc.* **2011**, *133*, 197–199.

[26] a) G. Lu, A. Linsebigler, J. T. Yates, *J. Phys. Chem.* **1994**, *98*, 11733–11738; b) I. M. Brookes, C. A. Muryn, G. Thornton, *Phys. Rev. Lett.* **2001**, *87*, 266103; c) R. Schaub, P. Thostrup, N. Lopez, E. Lægsgaard, I. Stensgaard, J. K. Nørskov, F. Besenbacher, *Phys. Rev. Lett.* **2001**, *87*, 266104; d) R. Razzaq, H. Zhu, L. Jiang, U. Muhammad, C. Li, S. Zhang, *Ind. Eng. Chem. Res.* **2013**, *52*, 2247–2256.

[27] T. H. Etsell, S. N. Flengas, *J. Electrochem. Soc.* **1971**, *118*, 1890–1900.

[28] S. Noda, K. Hasegawa, H. Sugime, K. Kakehi, Z. Zhang, S. Maruyama, Y. Yamaguchi, *Jpn. J. Appl. Phys.* **2007**, *46*, L399–L401.

Supporting Information

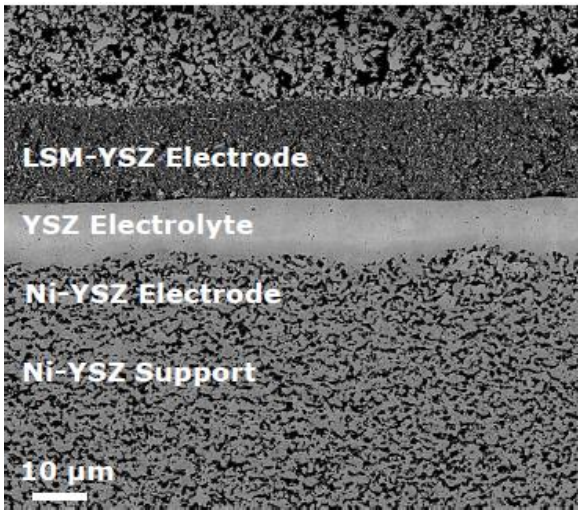

Figure S1. The solid oxide cell consisting of Ni-YSZ support, Ni-YSZ active cathode, YSZ electrolyte and LSM-YSZ anode

The solid oxide cell used in this work was developed at DTU Energy Conversion (former Risø-DTU).[1] The cell before reduction consists of ~ 300 µm NiO-YSZ support layer, 10 ~ 15 µm NiO-YSZ active cathode, ~10 µm YSZ electrolyte and 15 ~ 20 µm LSM-YSZ anode; the active electrode area is 4 x 4 cm^2. Ni-YSZ and LSM-YSZ were used as current collectors on the cathode and anode side, respectively. Albite glass bars were used as sealing on both sides. The cell was first heated to 1000 ^oC for sealing and subsequent reduction of NiO in H_2 to obtain the Ni-YSZ cathode. It was then cooled down to 850 ^oC for characterization of the initial performance, including measurement of electrochemical impedance spectra (EIS) and i-V curves with various gas compositions. Afterwards, co-electrolysis of CO_2 and H_2O was started with a flow of 25 Lh^{-1} 45 % H_2O + 45 % CO_2 + 10 % H_2 at 1 atm. to the Ni-YSZ cathode and pure O_2 as sweep gas to the LSM-YSZ anode. The 10 % H_2 addition was only for the purpose of keeping sufficiently reducing atmosphere to avoid Ni oxidation. The electrolysis current increased with a step of 0.25 Acm^{-2} at which impedance spectra were recorded after a hold-time of 15 min. Finally, an electrolysis current density of 2.25 Acm^{-2} was applied to the cell; the corresponding average conversion of the reactant (according to Faraday's Law) was 67 %. The cell temperature was 850 ^oC at OCV and increased to approximately 875 ^oC at 2.25 Acm^{-2}. The test was

stopped after 11 hours operation with cell voltage reaching 2.0 V, still below the decomposition voltage of ZrO_2 (~ 2.3 V); after impedance characterization again at OCV the cell was cooled down to room temperature in H_2.

References

[1] a) M. J. Jørgensen, M. Mogensen, *J. Electrochem. Soc.* **2001**, *148*, A433–A442; b) P. H. Larsen, C. Bagger, S. Linderoth, S. Mogensen, Mogens Bjerg; Primdahl, M. J. Jørgensen, P. V. Hendriksen, B. Kindl, N. Bonanos, F. W. Poulsen, K. A. Maegaard, in *Proc. Solid Oxide Fuel Cell VII (SOFC VII)* (Eds.: S.C. Singhal, H. Yokokawa), Electrochemical Society, Pennington, NJ, **2001**, pp. 28–37; c) N. Christiansen, J. B. Hansen, H. Holm-Larsen, M. J. Jørgensen, M. Wandel, P. V. Hendriksen, A. Hagen, S. Ramousse, *ECS Trans.* **2009**, *25*, 133–142; d) S. D. Ebbesen, C. Graves, A. Hauch, S. H. Jensen, M. Mogensen, *J. Electrochem. Soc.* **2010**, *157*, B1419–B1429.

Chapter 9 Conclusions

From the results and discussions presented in the previous chapters, the main conclusions of this study can be drawn as followings:

1) The initial characterization of the SOECs at OCV showed that the resistances of Ni-YSZ TPB reaction were similar in the gas atmosphere of 45 % H_2O + 45 % CO_2 + 10 % H_2 and 50 % H_2O +50 % H_2. The Ni-YSZ TPB reaction resistance in 45 % H_2O + 45 % CO_2 + 10 % H_2 increased with increasing the electrolysis current density.

2) Co-electrolysis of H_2O and CO_2 were performed at 865 ~ 875 ^oC for up to approximately 700 hours using SOECs with a LSM-YSZ or LSCF-CGO oxygen electrode under un-cleaned conditions (using albite glass sealing and feed gases as received) and clean conditions (using glass sealing with low impurity and cleaned feed gas) at high current densities (|i| = 1.5 or 2.0 A/cm^2). The feed gas to Ni-YSZ electrodes consisted of 45 % H_2O + 45 % CO_2 + 10 % H_2 and the conversion was 45 % or 60 %. Generally, the LSM cells showed more server degradation in ohmic resistance than the LSCF cells, indicating the effect of the type of the oxygen electrode on the YSZ degradation. Furthermore, transient change of the YSZ resistance, i.e. significant increase/decrease of Rs when applying/stopping the current (-2.0 A/cm^2) was observed for the LSM cells but not for the LSCF cells. Parallel cracks were observed in the electrolyte on the polished cross-sections for all the tested cells, which could be ascribed to the internal stress due to a large thermal gradient in the YSZ electrolyte perpendicular to the cell plane.

3) The major structural changes of the SOECs, including the percolation loss of Ni, the SiO_x inclusions in Ni, the formation of zirconia nanoparticles at Ni|YSZ interface and Ni surface and the contact loss between Ni and YSZ occurred on the Ni-YSZ electrode, especially in the area adjacent to electrolyte during durability test. No delamination of the oxygen electrode from electrolyte was observed for any of the tested cells. The performance degradation of the tested SOECs was mainly due to the significant increase of the ohmic resistance and the Ni-YSZ TPB reaction resistance. Corresponding to the increase of the Ni-YSZ TPB resistance, the summit frequency decreased from a few KHz to ~ 1 KHz or even as low as ~ 600 Hz. The TPB reaction of the oxygen electrode showed minor performance degradation.

4) Si-impurities were observed as the dominate impurities species, appearing as SiO_x inclusions inside the Ni grain adjacent to the electrolyte. A 'deposition/segregation-reduction-diffusion-oxidation' mechanism was proposed to explain the formation of Si-impurities, which included the transport of

silica from sealing or segregation from raw materials, the reduction of silica to Si under cathodic polarization, the diffusion of Si in Ni and the re-oxidation of Si by O that diffused in Ni and inclusion formation.

5) The cell tested for a short-term (138 h) showed a more severe Ni percolation loss at the inlet than at the outlet, while for the cells tested for a longer term (~ 700 h), almost equally percolation loss of Ni was observed at the inlet and outlet, which indicated the evolution of degradation from inlet to outlet (i.e. initially degradation was faster for upstream and then faster for downstream). An inactive Ni-YSZ layer with a thickness of a few microns formed next to electrolyte due to the severe Ni percolation loss, leading to the increase in the TPB reaction resistance and in the ohmic resistance. The severe percolation loss of Ni adjacent to Ni-YSZ|YSZ interface was related to the large cathodic polarization, considering the increasing polarization with approaching the interface. The Ni percolation loss seems not rely on the presence of impurities and the formation of nano-zirconia. The higher impurity (SiO_x) level accelerated the degradation of the Ni-YSZ TPB reaction resistance at the beginning, but did not influence the final value of the TPB resistance significantly, which was probably due to the removal of SiO_x from TPBs under strong cathodic polarization.

6) Zirconia particles of a few tens nm was formed in the Ni-YSZ active electrode close to the YSZ electrolyte with a similar crystal structure and composition to the bulk YSZ. The zirconia nanoparticles were observed at the Ni-YSZ interface and in the vicinity of TPBs, and spread over the entire surface of Ni particles in certain cases. The Ni-YSZ electrodes showed a large cathodic over-potential for zirconia precipitation, equivalent to the potential of -1.19 ± 0.03 V versus oxygen electrode in 1 atm O_2 (or pO_2 of 10^{-21} ~ 10^{-22} atm at the Ni-YSZ|YSZ interface). The formation of metallic Zr seems not to be favored at this condition. The strong cathodic polarizations of Ni-YSZ could lead to a partial reduction of YSZ at the Ni-YSZ interface and a structural decomposition into nanoparticles. Severe precipitating of nano-zirconia impaired the Ni-YSZ interface, led to the Ni detachment from the YSZ electrolyte, resulting into resistance increases both for ohmic and oxygen ion transfer processes.

7) A stabilization of the Ni-YSZ TPB resistance was generally observed for the SOECs after a few hundred hours (e.g. 300 ~ 400h) operation under large current. It could be attributed to the regeneration of TPBs sites accompanying the formation of nano-zirconia around the original TPBs as well as the elimination of the impurities from TPBs (formation of SiO_x inclusions in Ni).

8) During both the SOFC and SOEC operations, the current distribution was observed to be increasingly uneven along the cell with increasing the current. The local current density was measured to be larger

for the cell inlet than for the outlet, which is in agreement with the simulation result based on a plug flow reactor model. The current distribution also resulted in an uneven thermal distribution along the cell, which was confirmed by the temperature measurement at the cell center and outlet. The correlation between the microstructure change and the in-plane voltage change during the durability test revealed a dynamic re-distribution of current corresponding to the evolution of degradation along the cell from the inlet to the outlet.

9) SOECs with different porosities were tested: for the relatively dense Ni-YSZ structure, carbon (CNT) formation was observed at the Ni-YSZ|YSZ interface during co-electrolysis of H_2O and CO_2 at -2.0 and -2.25 A/cm^2 with a reactant conversion ≤ 67 %, while the cells with a more porous Ni-YSZ structure showed no carbon formation. The SOECs with carbon formations exhibited a significantly larger diffusion and conversion resistance at high current densities than the cells without. HRTEM revealed that the cubic nano-zirconia served as the catalyst of carbon formation and an electro-catalytic mechanism was proposed for carbon formation under the test conditions.

Declaration

I hereby declare that this thesis is my own work and effort. I certify that the material has not been submitted, either in whole or in part, for a degree at this or any other university.

Youkun Tao

Roskilde, December 2013